Investigation of Past Habitable Environments through Remote Sensing of Planetary Surfaces

Thesis by

Nathaniel Thomas Stein

In Partial Fulfillment of the Requirements for

the degree of

Doctor of Philosophy

CALIFORNIA INSTITUTE OF TECHNOLOGY

Pasadena, California

2020

Defended May 29, 2020

Nathaniel Thomas Stein
ORCID: 0000-0003-3385-9957

ACKNOWLEDGEMENTS

This thesis would not have been possible without my advisors, mentors, colleagues, friends, and family who supported me. First, I would like to thank my advisors John Grotzinger and Bethany Ehlmann. John, thank you for the opportunities you have given me to work on Curiosity, pursue ambitious projects, and travel to incredible field sites. Bethany, thank you for introducing me to Dawn and giving me the freedom and guidance to pursue questions that I found intriguing. I have appreciated the chance to learn from both of your examples as fantastic scientists and mentors. I also thank my committee members, Woody Fischer and Mike Lamb, for their guidance on this thesis and in the field.

I owe immense gratitude to the people who influenced my scientific path before I came to Caltech. I especially want to thank my middle school science teacher Brian Fisher for his encouragement and kindness. I am also extremely grateful to Ray Arvidson for his mentorship and for introducing me to planetary science. There is no question that his guidance was paramount forging my scientific trajectory. Ray also brought me to Dumont Dunes, CA for rover mobility testing where I met John Grotzinger when I helped to push his car out of the sand.

The work presented in this thesis would not have been possible without help from two amazing science teams. It has been a privilege to help drive a rover on Mars. I benefited greatly from scientific interactions with collaborators from the MSL science team, particularly with Ashwin Vasavada, Chris Fedo, Lauren Edgar, Katie Stack, and Abby Fraeman. Thanks also to the Dawn Science team for letting me jump into the mission and especially to Julie Castillo-Rogez and Carol Raymond for the fruitful scientific interactions. I am also grateful to Mory Gharib, Reza Nemovi, Noel Esparza-Duran, and others for welcoming me to CAST and helping me build amazing things.

Some of the most formative adventures of my time at Caltech were on Little Ambergris Cay in the Turks and Caicos, first on Agouron Institute Field trips and later for follow-up research. Thanks to John Grotzinger, Andy Knoll, and Woody Fischer for organizing the Agouron trips and to a whole cast of characters who made the experiences fun and insightful. Special

thanks to Lizzy Trower, Maya Gomes, and Usha Lingappa for making so much subsequent work possible and helping to tame the Spider Crab. Thanks also to Alistair Hayden for getting stuck in a hurricane with me (and still managing to get the data we came for!).

My experience at Caltech was eased by many peers and colleagues who helped along the way. I was lucky to interact with so many awesome people in the Grotzinger and Ehlmann groups. Thanks especially to Jessica Watkins, Ted Present, Mathieu Lapotre, William Rapin, Rebecca Greenberger, and Valerie Fox for your insight and support. Thanks also to Janice Grancich for your immeasurable help and for saving me in the Turks and Caicos and to other staff members including Jen Shechet, Julie Lee, Margaret Carlos, Ulrika Terrones, Loreta Young, and Irma Black without whom things simply would not happen. Thanks to Jay Dickson for your immeasurable help with data processing and for talking to me about baseball. As far as I can tell, your only shortcoming is that you are a Red Sox fan.

I am not sure I would have gotten through the last five years without the incredible support of my friends. Thanks in no particular order to Peter Gao, Mike Wong, Henry Ngo, Peter Buhler, Danielle Piskorz, Joe O'Rourke, Lulu Pan, Pushkar Kopparla, Daven Quinn, Dana Anderson, Ellen Leask, Peter Martin, Patrick and Erin Fisher, Elizabeth Bailey, Chris Spalding, Shreyas Vissapragada, Aida Behmard, Yayaati Chachan, Cam Buzard, Siteng Fan, Elizabeth Bailey, Nicole Wallack, Eva Scheller, Cecilia Sanders, and many others! Thanks also to the GPS soccer (Cambrian Explosion), softball (Strike-Slip), and back-to-back champ dodgeball (Late Heavy Bombardment) teams for keeping me active.

Finally, I would like to thank my friends and family who have provided so much support from afar. Nancy, I cannot thank you enough for your unconditional support and kindness and for bringing so much joy to my life. Mom, dad, and Emily – thank you for your endless love and encouragement.

ABSTRACT

Planetary surfaces record a history of potentially habitable environments throughout the solar system. This dissertation focuses on the characterization of three planetary surfaces to inform their evolution and past habitability: Earth (Chapter 2), Mars (Chapters 3-4), and Ceres (Chapters 5-6). In chapter 1, we introduce major questions driving the work presented in this thesis. In Chapter 2, we use a combination of UAV-based images and in-situ observations to characterize the processes that control the texture and distribution of modern microbial mats in the Turks and Caicos. We find that the surface texture and distribution of the mats is controlled primarily by subtle differences in elevation that drive significant changes in subaerial exposure time. Sedimentation and mechanical weathering from storm events also play a key role in controlling the distribution of mats. In Chapter 3, we apply a PCA-based regression method to stereo Curiosity Mastcam images to measure the structural orientation of the Murray formation. We constrain the dip to be effectively horizontal, which indicates that the Murray formation predates the creation of Aeolis Mons and is consistent with flat strata being deposited on an equipotential surface in a lacustrine setting. In Chapter 4, we summarize the investigation of networks of reticulate ridges on the surface of several rock slabs in the Murray formation using data from the Curiosity rover. We find that the features are preserved mudcracks that were likely deposited during a lowstand in a lake ~3.2-3.6 Ga. The mudcracks are one of few definitive textural markers of drying in the Murray formation and suggest a history of oscillating lake levels that led to intermittent exposure. In Chapter 5, we catalog bright spots on Ceres and propose mechanisms for their formation. We identify hundreds of Na-carbonate-bearing regions on Ceres. We show with a Monte Carlo impact model that these deposits must have been exposed within the last few hundred Ma. In Chapter 6, we investigate the source of shallow subsurface Na-carbonate deposits. We show that the deposits must have been emplaced in the last ~1 Ga and that the solid-state mobilization of water ice and hydrated Na-carbonates could simultaneously explain the formation of domes and large crater rim Na-carbonate exposures. Chapter 7 synthesizes the major results of this thesis and avenues for future exploration.

PUBLISHED CONTENT AND CONTRIBUTIONS

Chapter 3 is published as: Stein, N.T. et al. (2020), Regional structural orientation of the Mount Sharp group revealed by in situ dip measurements and stratigraphic correlations on the Vera Rubin Ridge. *JGR : Planets*, 123. https://doi.org/10.1029/2019/JE006298.

N. Stein and J.P. Grotzinger conceived the study. N. Stein and D.P. Quinn processed the data and N. Stein performed the analysis and wrote the manuscript with help from all coauthors.

Chapter 4 is published as: Stein, N.T. et al. (2018), Desiccation cracks provide evidence of lake drying on Mars, Sutton Island member, Murray formation, Gale crater. *JGR : Planets*, 46, 515-518. https://doi.org/10.1130/G40005.1.

N. Stein and J. Grotzinger conceived the study. N. Stein and coauthors processed the data. N. Stein performed the analysis and wrote the manuscript with help from J.P. Grotzinger.

Chapter 5 is published as: Stein, N.T. et al. (2019), The formation and evolution of bright spots on Ceres. *Icarus*, 320, 188-201. https://doi.org/10.1016/j.icarus.2017.10.014.

N. Stein and B. Ehlmann conceived the study. N. Stein processed the data and wrote the manuscript with help from B.L. Ehlmann.

TABLE OF CONTENTS

TABLE OF CONTENTS CONT.

TABLE OF CONTENTS CONT.

TABLE OF CONTENTS CONT.

LIST OF ILLUSTRATIONS

Number *Page*

Chapter 3

Chapter 4

LIST OF ILLUSTRATIONS CONT.

Number *Page*

LIST OF TABLES

Number *Page*

LIST OF ACRONYMS

ADM. Asteroid-Derived Model

APXS. Alpha Particle X-ray Spectrometer

BPm. Blunts Point member

ChemCam Chemical Camera

CRISM. Compact Reconnaissance Imaging Spectrometer for Mars

CSFD. Crater Size Frequency Distribution

DCS. Decorrelation Stretch

DEM. Digital Elevation Model

DGPS. Differential Global Positioning System

EPS. Extracellular Polymeric Substances

FC. Framing Camera

HAMO. High Altitude Mapping Orbit

HiRISE. High Resolution Imaging Science Experiment

I/F. Radiance Factor

Jm. Jura member

JPL. Jet Propulsion Laboratory

LAMO. Low Altitude Mapping Orbit

LDM. Lunar-Derived Model

LIBS. Laser Induced Breakdown Spectroscopy

LVLD. Low-Viscosity Low-Density

MAHLI. Mars Hand Lens Imager

MIPL. Multimission Image Processing Lab

ML. Left Mast Camera

MR. Right Mast Camera

MSL. Mars Science Laboratory

Mastcam. Mast Camera

MSAM. Mastcam Stereo Analysis and Mosaics

MWL. Mean Water Level

OLS. Ordinary Least-Squares

OS. Old Soaker

Pancam. Pan Camera

PCA. Principal Components Analysis

PDS. Planetary Data System

PPm. Pettegrove Point member

RGB. Red, Green, Blue

RMI. Remote Micro Imager

RT. Rayleigh-Taylor

SC. Squid Cove

UAV. Unpiloted Aerial Vehicle

VIR. Visible and Infrared Spectrometer

VNIR. Visible and Near-Infrared

VRR. Vera Rubin Ridge

Chapter 1

INTRODUCTION

This thesis addresses three major themes: (1) How do planetary surfaces reflect the physical processes that shaped their evolution? (2) What environments generated the surface features we see today, and were they habitable? (3) How can we interrogate the nature of planetary surfaces using novel remote sensing-based approaches? This thesis investigates these questions through studies on three bodies: Mars (Chapters 2-3), Earth (Chapter 4), and Ceres (Chapters 5-6). Below I briefly review the motivation and context for this research.

1.1 Investigating Past Habitable Environments on Earth and Mars

Over the past few decades of robotic exploration, it has become clear that we stand to learn a great deal about the history and extent of habitable environments through the interrogation of planetary surfaces. Nowhere is this more evident than on Mars, whose surface is strewn with ample geomorphic evidence of past aqueous activity in the form of sedimentary deposits (e.g. Malin and Edgett, 2000), valley networks (e.g. Baker et al., 1992; Craddock and Howard, 2002; Pieri, 1976), open and closed basin lakes (e.g. Cabrol et al., 1999; Fassett and Head, 2008), outflow channels (e.g. Masursky et al., 1977), and perhaps a northern ocean (Parker et al., 1989). Excepting Hesperian outflow channels (Carr and Head, 2010), extensive hydrologic activity on Mars was likely concentrated in the Noachian to Early Hesperian periods (>~3.5 Ga). During the same period, life may have already been established on Earth. Fossilized stromatolites and other microbial textures (e.g. Allwood et al., 2009; Schopf et al., 2006), coupled with geochemical signatures and mineral content indicative of metabolic activity (e.g. Bontognali et al., 2012; Pflüger and Gresse, 1996), reveal abundant Archean life that may have emerged prior to ~3.7 Ga. But as terrestrial life flourished, Mars took a different path than its nearest neighbor; geomorphic evidence for sustained flowing water is scant in the Amazonian period (Ehlmann et al., 2016). Likewise, orbit-based spectrometer measurements of surface mineralogy show widespread clay

mineral formation in the Noachian crust (e.g. Bibring et al., 2005; Ehlmann et al., 2009; Poulet et al., 2005) that became negligible by the Late Hesperian to Early Amazonian period (e.g. Ehlmann and Edwards, 2014). These and numerous other lines of evidence (see Ehlmann et al., 2016; Wordsworth et al., 2016 for more detailed reviews) signal an early, global decline of water and, perhaps, habitability.

At present, it is not known exactly why Earth and Mars diverged. An important piece of the puzzle may lie in plate tectonics, without which hydrogen, carbon, sulfur, and other atmospheric components needed to maintain a thick atmosphere could not be cycled between Mars' surface and interior. Plate tectonics has not been unambiguously identified on Mars, but fortuitously the lack of plate tectonics means that a significant fraction of the martian surface dates back to the ancient past when the planet was wetter and perhaps warmer (Greeley and Guest, 1987; Scott and Tanaka, 1986), an era from which little remains on Earth. Hence, Mars is the premier target to search for signs of early life in the solar system and understand the conditions that sustain habitability over geologic time. NASA's Mars Exploration Program has thus refined its focus from "follow the water" to "seeking signs of past Mars habitability." In tandem with orbit-based remote sensing, landed rover missions have revolutionized our understanding of the habitability of Mars. The verdict is in: Mars was habitable when there was life on Earth (Grotzinger et al., 2014).

The inevitable question that follows looms large on the horizon. Was there life on Mars? It is no longer a far-fetched proposition, but the answer remains elusive for the time being. We can hope that the next Mars rover, Perseverance, brings a swift resolution to this chapter of exploration, but lessons from Earth should fetter optimism. By all indications, Earth has teemed with organisms for billions of years, and yet its oldest signatures of life are often ambiguous (Grotzinger and Knoll, 1999) if preserved at all. Chapter 2 of this thesis will introduce a modern analog for ancient microbial ecosystems in which decimeter-thick microbial mats stretch over several square km. What will be the fate of such an expansive ecosystem? It will be lost, not over billions or even millions of years, but thousands, the victim of its own productivity preventing early lithification. It is difficult to stand knee-deep

in microbial mats and imagine that it will all be lost to time. So too is it challenging to gaze at pictures of Mars' desolate surface and envision a time when there was life to preserve. This is the charge of the planetary geologist: to observe the state of a planetary surface and deconvolve the confounding factors of time. Chapters 3 and 4 of this thesis characterize an ancient lacustrine environment on Mars using data from the Mars Science Laboratory (MSL) Curiosity rover.

1.2 Ceres as an Astrobiological Target

The challenge of discerning past processes, of course, is not exclusive to Earth or Mars. Recent and ongoing exploration of the Jovian and Saturnian moons has revealed a fantastic assemblage of environments (e.g. Carr et al., 1998; Hansen et al., 2006; Stofan et al., 2007). These worlds have expanded our understanding of planetary evolution, the range of planetary processes, and the scope of habitability. A spate of recent and upcoming missions (e.g. Fujiwara et al., 2006; Glassmeier et al., 2007; Lauretta et al., 2017; Russell and Raymond, 2011; Watanabe et al., 2017) has shifted focus to the asteroids, the primordial building blocks that record the conditions of the earliest eon of our solar system.

In addition to Earth and Mars, this thesis investigates a third body, Ceres, the largest asteroid in our solar system. Ceres is geologically primitive and icy, an intermediary between the rocky bodies of the inner solar system and the icy bodies of the outer solar system (McCord and Sotin, 2005). Additionally, our solar system is now thought to contain many ocean worlds (Lunine, 2017) and Ceres, like Mars, may also be a relict ocean world with a protracted history of interactions between water, rock, and organic compounds (Castillo-Rogez et al., 2020). NASA's Dawn mission arrived at Ceres in 2015 with the objective of understanding the conditions in which Ceres formed, the nature of the building blocks of the terrestrial planets, and to contrast its formation and evolution with that of Vesta, another asteroid that followed a distinctive path (Russell and Raymond, 2011). One of the least expected revelations of the Dawn mission is that Ceres is not a static world; it has signs of recent and potentially ongoing geological activity involving liquid water. Two prominent surface features most conspicuously reveal Ceres' active state. The first is the central bright

spot of Occator crater, which formed <20 Ma when brines precipitated salts that include Na-carbonates (De Sanctis et al., 2016). The second is Ahuna Mons, a ~4 km-high mountain that may have formed from the extrusion of brines (Ruesch et al., 2016; 2019) or solid-state deformation (Bland et al., 2019; this thesis). Even in such an exotic place, far from the familiar terrains of Earth or Mars, the prospect of habitability remains tantalizing. Chapters 5 and 6 of this thesis will evaluate the source and timing of recent geological activity on Ceres.

1.3 Key Questions and Thesis Contents

Chapter 2 introduces results from the study of Little Ambergris Cay, an uninhabited island in the Turks and Caicos with broad tracts of well-developed microbial mats. The island is unusual; it contains a rare example of extensive, thick microbial mats, but is situated in a highly energetic environment due to the persistent onslaught of trade wind-driven waves. We attempt to answer two major questions: 1) what factors control microbial mat texture? 2) how did extensive microbial mats develop in such a high-energy environment? We combine in situ observations with UAV-based imaging to map the distribution of microbial mats and quantify their sensitivity to water depth, subaerial exposure, and storm events, demonstrating that the mat textures are controlled by minute differences in elevation. Additionally, we propose a model for the formation of the island and its restricted interior basin in the lee of the adjacent Big Ambergris Cay. Cumulatively, the results provide a framework in which to identify and understand ancient high-energy carbonate depositional environments.

Chapters 3 and 4 turn from Earth to Mars, where we use data from the Mars Science Laboratory Curiosity rover to refine our understanding of an ancient lake system in Gale crater. Broadly, both chapters address the question of what further constraints we can place on the history of habitable environments in Gale crater. In Chapter 3, I summarize a study that utilized stereo images from the Curiosity rover's Mast Cameras to constrain the structural orientation of the Murray formation, a mudstone that was likely deposited in a habitable, predominantly fluviolacustrine setting ~3.6-3.2 Ga (Grotzinger et al., 2014). I applied a principal components-based regression method to measure the dips of Murray

formation strata for the first time. Regional dips were constrained to be within several degrees of horizontal on average, consistent with nearly flat strata deposited horizontally on an equipotential surface. Results also indicate that the Murray formation did not contribute to the primary formation of Aeolis Mons, a ~5-km-high sedimentary mound preserved in the center of Gale crater, consistent with formation that postdates the deposition of the Murray formation.

Chapter 4 summarizes the results of a rover campaign at a peculiar rock slab in the Murray formation called "Old Soaker," utilizing images from the Curiosity rover's Mast Cameras and Mars Hand Lens Imager coupled with Alpha Particle and X-Ray Spectrometer and ChemCam measurements to identify a network of reticulate surface features as mudcracks. The mudcracks, which formed from subaerial exposure of lacustrine facies some 3.6-3.2 Ga, indicate a transition from longer-lived perennial lakes recorded in older strata to younger lakes characterized by intermittent exposure and are one of the few definitive textural indicators of lake drying identified in Gale crater.

In Chapters 5 and 6, we investigate the source and timing of recent geological activity on Ceres using data from Dawn's Visible and Infrared Imaging Spectrometer (VIR) and Framing Cameras (FC). Both papers focus on the following major questions: 1) how and when did Ceres' bright spots form? 2) were or are there transiently habitable environments in Ceres? In Chapter 5, I used FC data to map more than 300 bright spots (faculae) across Ceres, revealing that faculae are widespread. Faculae were found to occur almost exclusively in impact craters. Computational models indicated that the faculae darken and disappear over time scales of hundreds of Ma due to impact-driven lateral mixing, constraining all faculae to have been exposed geologically recently. Chapter 6 investigates the source and timing of Na-carbonate deposits on crater rims. We identified a strong spatial correlation between some crater rim Na-carbonate deposits and domes, suggesting that the processes that mobilize material to form Ceres' domes may be responsible for the emplacement of large subsurface Na-carbonate deposits. We used computational models to constrain the emplacement of subsurface Na-carbonate exposed on crater rims to have occurred within the

last ~1 Ga. Finally, we demonstrated that large crater rim Na-carbonate exposures and domes could have formed without brines via solid-state mobilization of material from Ceres' deep crust.

Chapter 7 summarizes the major findings presented in this thesis and presents promising avenues for future exploration.

References

Allwood, A.C., Grotzinger, J.P., Knoll, A.H., Burch, I.W., Anderson, M.S., Coleman, M.L., et al. (2009). Controls on development and diversity of Early Archean stromatolites. *PNAS*, 106(24), 9548-9555. https://doi.org/10.1073/pnas.0903323106.

Baker, V.R., Carr, M.H., Gulick, V.C., Williams, C.R., & Marley, M.S. (1992). Channels and valley networks. In: Mars. 493-522.

Bibring, J.-P., Langevin, Y., Gendrin, A., Gondet, B., Poulet, F., Berthé, M. et al. (2005). Mars surface diversity as revealed by the OMEGA/Mars Express observations. *Science*, 306, 1576-1581. https://doi.org/10.1126/science.1108806.

Bland, M.T., Buczkowski, D.L., Sizemore, H.G., Ermakov, A.I., King, S.D., Sori, M.M., et al. (2019). Dome formation on Ceres by solid-state flow analogous to terrestrial salt tectonics. *Nature Geoscience*, 12, 797-801. https://doi.org/10.1038/s41561-019-0453-0.

Bontognali, T.R.R., Sessions, A.L., Allwood, A.C., Fischer, W.W., Grotzinger, J.P., Summons, R.E., & Eiler, J.M. (2012). Sulfur isotopes of organic matter preserved in 3.45-billion-year-old stromatolites reveal microbial metabolism, *PNAS*, 109, 15146-15151. https://doi.org/10.1073/pnas.1207491109.

Cabrol, N.A. & Grin, E.A. (1999). Distribution, classification, and ages of martian impact crater lakes. *Icarus*, 142, 160-172. https://doi.org/10.1006/icar.1999.6191.

Carr, M.H., Belton, M.J.S., Chapman, C.R., Davies, M.R., Geissler, P., Greenberg, R., McEwen, A.S. et al. (1998). Evidence for a subsurface ocean on Europa. *Nature*, 391, 363-365. https://doi.org/10.1038/34857.

Castillo-Rogez, J.C., Neveu, M., Scully, J.E.C., House, C.H., Quick, L.C., Bouquet, A. et al. (2020). Ceres: Astrobiological target and possible ocean world. *Astrobiology*, 20. https://doi.org/10.1089/ast.2018.1999.

Craddock, R.A. & Howard, A.D. (2002). The case for rainfall on a warm, wet early Mars. *J. Geophys. Res.*, 107. https://doi.org/10.1029/2001JE001505.

Ehlmann, B.L., Mustard, J.F., Swayze, G.A., Clark, R.N., Bishop, J.L., Poulet, F. et al. (2009). Identification of hydrated silicate minerals on Mars using MRO-CRISM: Geologic context near Nili Fossae and implications for aqueous alteration. *JGR: Planets*, 114, https://doi.org/10.1029/2009JE003339.

Ehlmann, B.L. & Edwards, C.S. (2014). Mineralogy of the martian surface. *Ann. Rev. Earth and Plan. Sci.*, 42, 291-315. https://doi.org/10.1146/annurev-earth-060313-055024.

Ehlmann, B.L., Anderson, F.S., Andrews-Hanna, J., Catling, D.C., Christensen, P.R., Cohen, B.A., et al. (2016). The sustainability of habitability on terrestrial planets: Insights, questions, and needed measurements from Mars for understanding the evolution of Earth-like worlds. *JGR: Planets*, 121(10). https://doi.org/10.1002/2016JE005134.

Fassett, C. I. & Head, J.W. (2008). Valley network-fed, open-basin lakes on Mars: Distribution and implications for Noachian surface and subsurface hydrology. *Icarus*, 198, 37-56. https://doi.org/j.icarus.2008.06.016.

Fujiwara, A., Kawaguchi, J., Yeomans, D.K., Abe, M., Mukai, T., Okada, T. et al. (2006). The rubble-pile asteroid Itokawa as observed by Hayabusa. *Science*, 312, 1330-1334. https://10.1126/science.1125841.

Glassmeier, K.-H., Boehnhardt, H., Koschny, D., Kührt, Ekkehard, & Richter, I. (2007). The Rosetta mission: Flying towards the origin of the solar system. *Space Sci. Rev.*, 128, 1-21. https://doi.org/10.1007/s11214-006-9140-8.

Grotzinger, J. P., Sumner, D. Y., Kah, L. C., Stack, K., Gupta, S., Edgar, L., et al., & MSL Science Team. (2014). A habitable fluvio-lacustrine environment at Yellowknife Bay, Gale Crater, Mars. *Science*, 343(6169), 1242777. https://doi.org/10.1126/science.1242777.

Grotzinger, J.P. & Knoll, A.H. (1999). Stromatolites in Precambrian carbonates: Evolutionary mileposts or environmental dipsticks? *Ann. Rev. Earth Planet. Sci.*, 27, 313-358. https://doi.org/10.1146/annurev.earth.27.1.313.

Hansen, C.J., Esposito, L., Stewart, A.I.F., Colwell, J., Hendrix, A., Pryor, W., et al. (2006). Enceladus' water vapor plume. *Science*. 311(5766), 1422-5. https://doi.org/science.1121254.

Lauretta, D.S., Balram-Knutsom, S.S., Beshore, E., Boynton, W.V., Drouet d'Aubigny, C., DellaGiustina, D.N., et al. (2017). OSIRIS-Rex: Sample return from asteroid (101955) Bennu. *Space Sci. Rev.*, 212, 925-984. https://doi.org/10.1007/s11214-017-0405-1.

Lunine, J.I. (2017). Ocean worlds exploration. *Acta Astronautica*, 131, 123-130. https://doi.org/10.1016/j.actaastro.2016.11.017.

Malin, M. C. & Edgett, K. S. (2000). Sedimentary rocks of early Mars. *Science*, 290, 1927–1937. https://doi.org/10.1126/science.290.5498.1927.

Masursky, H., Boyce, J.M., Dial, A.L., Schaber, G.G., & Strobell, M.E. (1977). Classification and time of formation of martian channels based on Viking data. *J. Geophys. Res.*, https://doi.org/10.1029/JS082i028p04016.

McCord, T.B. & Sotin, C. (2005). Ceres: Evolution and current state. *JGR: Planets*, 110. https://doi.org/10.1029/2004JE002244.

Parker, T.J., Saunders, R.S., & Schneeberger, D.M. (1989). Transitional morphology in West Deuteronilus Mensae, Mars: Implications for modification of the lowland/upland boundary. *Icarus*, 82, 111-145. https://doi.org/10.1016/0019-1035(89)90027-4.

Pflüger, F. & Gresse, P.G. (1996) Microbial sand chips – a non-actualistic sedimentary structure. *Sedimentary Geology*, 102, 263-274. https://doi.org/10.1016/0037-0738(95)00072-0.

Pieri, D. (1976). Distribution of small channels on the Martian surface. *Icarus*, 27, 25-50. https://doi.org/10.1016/0019-1035(76)90182-2.

Poulet, F., Bibring, J.-P., Mustard, J.F., Gendrin, A., Mangold, N., Langevin, Y., et al. (2005). Pyllosilicates on Mars and implications for early martian climate. *Nature*, 438, 623-628. https://doi.org/10.1038/nature04274.

Ruesch, O., Platz, T., Schenk, P., McFadden, L.A., Castillo-Rogez, J.C., Quick, L.C., et al. (2016). Cryovolcanism on Ceres. *Science*, 353, aaf4286-aaf4286. https://doi:10.1126/science.aaf4286.

Ruesch, O., Genova, A., Neumann, W., Quick, L.C., Castillo-Rogez, J.C., Raymond, C.A., et al. (2019). Slurry extrusion on Ceres from a convective mud-bearing mantle. *Nature Geoscience*, 12, 505-509. https://doi.org/10.1038/s41561-019-0378-7.

Russell, C.T. & Raymond, C.A. (2011) The Dawn mission to Vesta and Ceres. In: Russel C., Raymond C. (esd) The Dawn mission to minor planets 4 Vesta and 1 Ceres. Springer, New York, NY. https://doi.org/10.1007/978-1-4614-4903-4_2.

Schopf, J.W. (2006). Fossil evidence of Archaean life. *Phil. Trans. of the Royal Society*, 361, 869-885. https://doi.org/10.1098/rstb.2006.1834.

Stofan, E.R., Elachi, C., Lunine, J.I., Lorenz, R.D.,Stiles, B., Mitchell, K.L. et al. (2007). The

lakes of Titan. *Nature*, 445, 61-64. https://doi.org/nature05438.

Watanabe, S., Tsuda, Y., Yoshikawa, M., Tanaka, S., Saiki, T., Nakazawa, S. (2017). Hayabusa2 mission overview. *Space Sci. Rev.*, 208, 3-16. https://doi.org/10.1007/s11214-017-0377-1.

Wordsworth, R.D. (2016). The climate of early Mars. *Ann. Rev. Earth. Planet. Sci.*, 44, 1-31. https://10.1146/annurev-earth-060115-012355.

Chapter 2

GEOMORPHIC AND ENVIRONMENTAL CONTROLS ON MICROBIAL MAT FABRICS ON LITTLE AMBERGRIS CAY, TURKS AND CAICOS ISLANDS

Nathaniel T. Stein[1], John P. Grotzinger[1], Daven P. Quinn[2], Usha F. Lingappa[1], Theodore M. Present[1], Elizabeth J. Trower[3], Maya L. Gomes[4], Emily Orzechowski[5], Marjorie Cantine[6], Kyle S. Metcalfe[1], Woodward W. Fischer[1], Bethany L. Ehlmann[1], Andrew H. Knoll[7]

[1]Division of Geological and Planetary Sciences, California Institute of Technology, Pasadena, CA 91125, USA.

[2]Department of Geoscience, University of Wisconsin Madison, Madison, WI 53706, USA.

[3]Department of Geological Sciences, University of Colorado, Boulder, CO 80309, USA.

[4]Department of Earth and Planetary Sciences, Johns Hopkins University, Baltimore, MD 21218, USA.

[5]Department of Integrative Biology and Museum of Paleontology, University of California, Berkeley, Berkeley, CA 94720, USA.

[6]Department of Earth, Atmospheric and Planetary Sciences, Massachusetts Institute of Technology, Cambridge, MA 02139, USA.

[7]Department of Organismic and Evolutionary Biology, Harvard University, Cambridge, MA 02138, USA.

2.1 Abstract

To interpret microbially influenced environments in the sedimentary carbonate record, it is crucial to understand what processes control the development and surface morphology of microbial mats in modern carbonate sediments. Here we report results from a multiyear study of Little Ambergris Cay, an uninhabited island floored by broad tracts of well-developed microbial mats on the wave-dominated, high energy Caicos Platform. The purpose of this study was to integrate UAV-based imaging with differential global positioning system topographic surveys and in situ observations to 1) investigate the development and timing of the restricted interior basin on Little Ambergris and 2) identify and quantify the environmental factors that influence the textures of its microbial mats, including their response to large storm events. We found that Little Ambergris developed from the accretion and rapid lithification of carbonate sediment delivered by converging wave fronts in the lee of the adjacent Big Ambergris Cay. A restricted interior and possibly broad tracts of microbial mats developed by *ca* 2000 years ago. We identify three categories of microbial mats differentiated according to surface texture and morphology termed smooth mats, polygonal mats, and blister mats. Mat textures are predominantly controlled by minor elevation differences that drive significant changes in subaerial exposure time; the average elevation of smooth, polygonal, and blister mats is ~-0.14 m, 0 m, and 0.06 m relative to the average water level, respectively, which corresponds to average daily subaerial exposure times of 0 hours, ~21 hours, and ~24 hours, respectively. In addition to elevation, the spatial distribution of mats is controlled by hydrodynamic forces and sediment overprinting during large storm events. Cumulatively, Little Ambergris provides a framework in which to identify and understand ancient high-energy carbonate depositional environments.

2.2 Introduction

Sedimentary fabrics interpreted to result from the interaction of microbial communities with carbonate sediments and cements are ubiquitous throughout the rock record and form major carbonate platforms over the course of Precambrian Earth history (Walter, 1976; Grotzinger, 1989). Stromatolites—attached, lithified sedimentary growth

structures, accretionary away from a point or limited surface of initiation—occur in the rock record since early Archean time and have long been used to probe the fossil record for ancient life (Grotzinger and Knoll, 1999; Schopf, 2006; Allwood et al., 2009; Knoll, 2015). Modern stromatolites are restricted to limited habitats (e.g. Logan, 1961; Reid et al., 1995), but microbial mats and the sedimentary structures they form are distributed worldwide and carry equal significance with stromatolites in the documentation and interpretation of Earth history (Schopf, 2006), making them a good target for modern analog studies.

Evidence of ancient mats commonly relies on mineral content in adjacent sedimentary layers such as black carbonaceous materials (Allwood et al., 2009), pyrite (Pflüger and Gresse, 1996), or a variety of geochemical signatures (e.g. Bontognali et al., 2012; Marshall et al., 2007). Microbial mats also display a wide array of surface morphologies and yield distinctive sedimentary textures that arise syndepositionally from the interaction of mats and biofilms with environmental factors such as desiccation, hydrodynamics, and physical sediment dynamics (Gerdes et al., 2000; Schieber et al., 2007; Noffke et al., 2010). Such textures may be preserved in the rock record as topographic features on bedding planes that hosted the microbial mats (Schieber et al., 2007). Collectively, microbial mats and their associated sedimentary structures in modern environments are considered analogs for similar structures in the rock record (e.g. Dupraz et al., 2009).

To aid interpretation of microbially influenced textures in the sedimentary carbonate record, it is crucial to understand what processes determine the surface morphology of modern microbial mats and to document the range of these textures in carbonate sediments. Several processes determine the surface morphology of microbial mats: 1) microbial community composition, primarily that of the dominant Cyanobacteria (Dupraz and Visscher, 2005; Golubic, 1991; Mobberley et al., 2013; Noffke et al., 2013; Shepard and Sumner, 2010; Visscher et al., 1998) 2) ecological succession and the developmental trajectory of mats toward increasing morphological and compositional complexity (Wanless et al., 1988; Reid et al., 2000); and 3) physical environmental factors such as hydrodynamics,

sedimentation, subaerial exposure, temperature variations, and insolation (Gebelein, 1969; Martin et al., 1993; Andres and Reid, 2006; Mariotti et al., 2014; Trembath-Reichert et al., 2016; Bouton et al., 2016).

Microbial mats occur throughout diverse environments but are relatively uncommon due to ecologic restriction from animal grazing. This study focuses on microbial mats of Little Ambergris Cay, located on the Caicos platform, a wave-dominated high energy environment that is also subjected to frequent storms. Mats in modern carbonate tidal environments have generally been grouped into two morphological classes: flat laminar mats and domical "biscuit" mats (e.g. Wanless et al., 1988; Golubic et al., 1991). Following the impact of Hurricane Kate in 1985, Wanless et al. (1988) postulated that these morphotypes as observed on West Caicos form from organisms that colonize at different rates: *Schizothrix* rapidly colonizes and stabilizes overlying sediment to form flat, smooth mats that inhibit desiccation structures, and *Scytonema* colonizes more slowly to form mats marked by raised desiccation polygons. Subsequent microscopic and genomic studies of flat and domical mats on Little Ambergris Cay, Turks and Caicos revealed that although surface layer cyanobacterial populations are responsible for many of the mat's structural elements, *Schizothrix* and *Scytonema* are genetically similar between mat morphotypes (Trembath-Reichert et al., 2016; Lingappa et al., 2020). As a result, Trembath-Reichert et al. (2016) proposed that the microbial mat morphology is not controlled by the microbes that comprise them, but rather the response of microbial communities to environmental factors.

Although the role of specific environmental factors in the formation and development of microbial mats has been recognized (Gebelein, 1969; Martin et al., 1993; Andres and Reid, 2006; Mariotti et al., 2014; Trembath-Reichert et al., 2016), the relative importance of these factors and their quantification is necessary to better interpret variations in microbial mat morphology. Here, we utilize integrated in situ and UAV-based observations of Little Ambergris Cay, Turks and Caicos Islands collected over several field sessions to identify and quantify the environmental factors that influence the texture and distribution of its microbial mats. Additionally, we report a catalog of microbial induced sedimentary

structures, which are well-documented in modern (e.g. Gerdes et al., 2000; Noffke et al., 2001) and ancient (e.g. Schieber et al., 2007; Noffke et al., 2010) settings.

2.3 Geological Setting

The Caicos platform marks the southern limit of Bahamian platform complexes (Figure 1). The platform is approximately 100 km north-south and 70 km east-west and between 71° 30' and 72° 30' W and 21° and 22° N, subjecting it to relatively stronger easterly trade winds than the northern Bahamian platforms (Wanless et al., 1989; Dravis and Wanless, 2008), with average wind velocities of 8.1 ± 2.6 m/s (Trower et al., 2017). Wind-wave agitation generated by these strong winds promotes widespread formation of Holocene oolitic sands across the platform interior (Dravis and Wanless, 2017; Trower et al., 2017). The Caicos platform has a subarid climate, averaging 50-70 cm/year of precipitation and temperatures consistently between 20-25° C. The tidal range is less than 1 m and tides are semi-diurnal (NOAA/NOS/CO-OPS; Dravis and Wanless, 2017). A string of islands cored by Pleistocene bedrock dominates the northwestern, northern, and northeastern platform margins, having formed during multiple periods of sea-level oscillation (Wanless et al., 1989; Kerans et al., 2019).

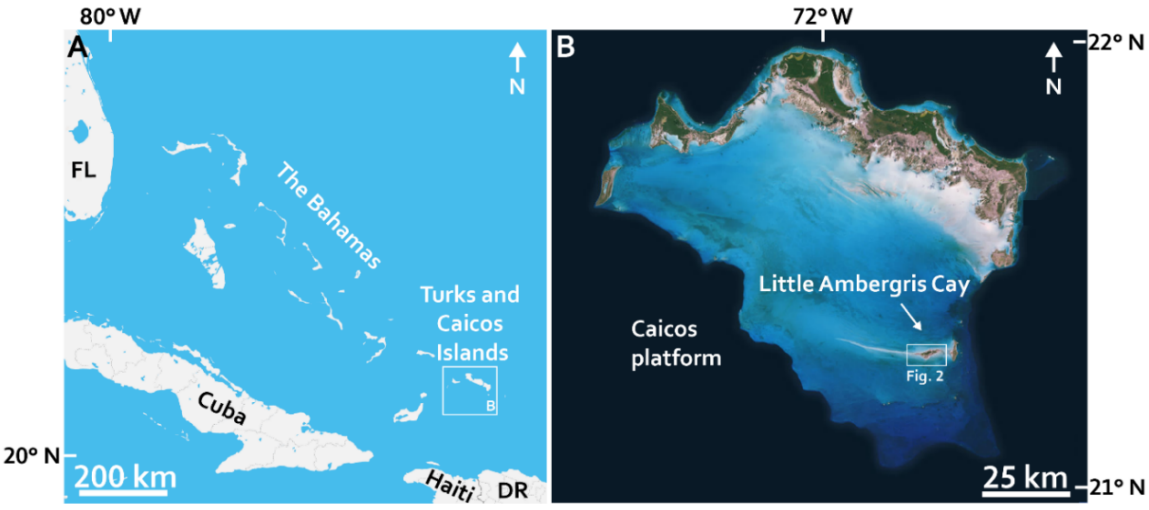

Figure 2.1. (**A**) Location of the Turks and Caicos Islands. (**B**) Satellite perspective of the Caicos Platform. Little Ambergris Cay is shown in the white box.

Figure 2.2. Downsampled version of a UAV-based orthomosaic of Little Ambergris Cay made in July 2016 by combining more than 1,500 RGB images collected over 13 separate flights with a DJI Phantom 4 Pro with a 12-megapixel camera. Flights were performed over seven days. White streaks represent specular reflection of sunlight on shallow water. The images are not radiometrically corrected. Produced using Agisoft Metashape. Locations of vibracore measurements (Figure 2.22) and tide gauge measurements (Figure 2.9) are shown.

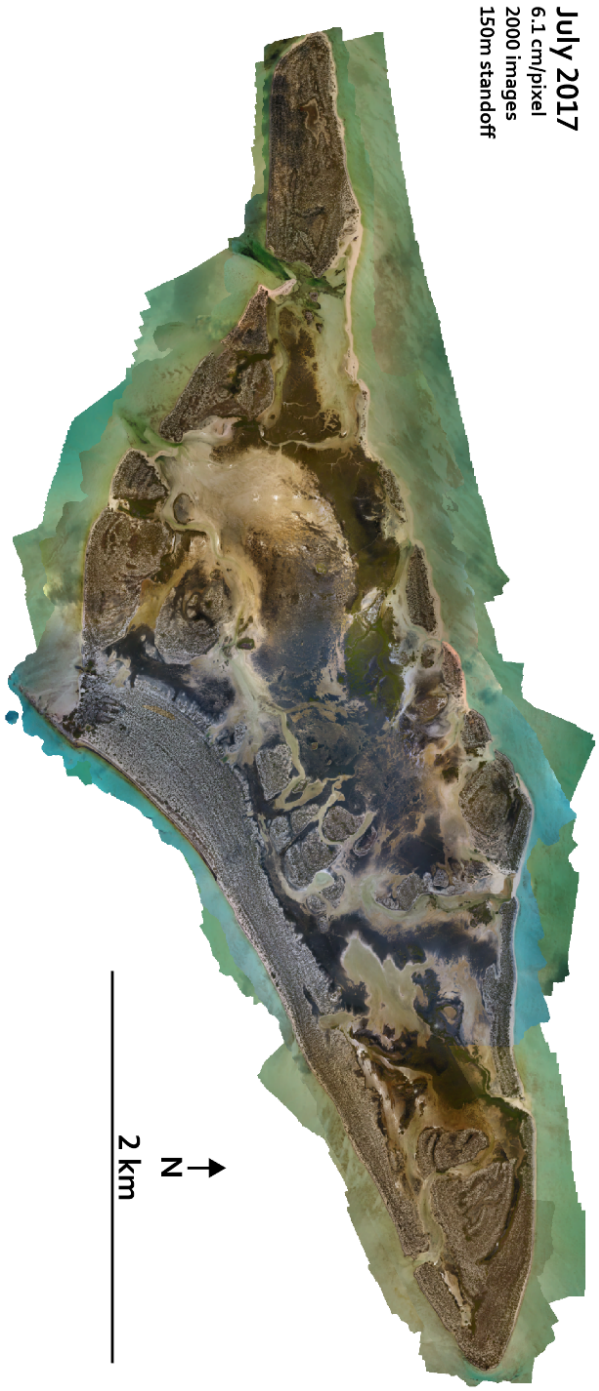

Figure 2.3. Downsampled version of a UAV-based orthomosaic of Little Ambergris Cay made in July 2017 by combining more than 2,000 RGB images collected over 11 separate flights with a DJI Phantom 4 Pro with a 20-megapixel camera. Flights were performed over a five-day period, including variable lighting conditions. The images are not radiometrically corrected. Produced using Agisoft Metashape.

2.3.1 Little Ambergris Cay Physiography

Little Ambergris Cay is a ~6.5 km long, ~1.6 km wide, 6.1 km^2 uninhabited island near the southern margin of the Caicos platform (Figures 2.1, 2.2). The cay sits on a broad bank where ooid-rich sediments influenced by strong easterly trade winds converge in the lee of Big Ambergris Cay to form a linear shallow subtidal shoal extending ~20 km westward from the western tip of Little Ambergris (Wanless et al., 1989; Wanless and Dravis, 2008; Dravis and Wanless, 2017; Trower et al., 2017). Partially lithified upper shoreface to eolian fossiliferous grainstone and rudstone form a ~1-4.5 m high bedrock rim that surrounds an extensive interior tidal marsh. The bedrock rim is breached in seven locations on the north side of the island and two on the south side, allowing tidal flows to flood the interior to shallow depths of generally less than 1 meter.

The interior of the cay is floored by broad tracts of well-developed microbial mats interspersed with mangroves (predominantly *Rhizophora mangle*), ooid hardgrounds, and exposed bedrock and scrubland. The northwestern portion of the cay is covered with a dense network of mangroves floored by luxuriant, polygonal, tufted filamentous Cyanobacteria mats. Mangroves also inhabit interior channels on the southwestern and northeastern portions of the cay. Most of the interior is covered by microbial mats of varying texture (see section 2.5.1) interspersed with exposed ooid hardgrounds. A series of active channels connects tidal inlets on the north and south sides of the island.

2.3.2 Microbial Mats on Little Ambergris Cay

The microbial mats on Little Ambergris Cay can be grouped by surface texture and morphology into three categories termed smooth mats, polygonal mats, and blister mats. Such classification is important because it is these attributes which are imprinted in the rock record of carbonate textures (Demicco and Hardie, 1994). The details of these mat facies are discussed in section 2.4.1. Smooth and polygonal mats are effectively synonymous with the terms “flat mat” and “biscuit mat” (Wanless et al., 1988; Trembath-Reichert et al., 2016), or “*Schizothrix* mat” and “*Scytonema* mat” (e.g. Ginsburg and Hardie, 1975; Neumann et al.,

1970) used in previous literature. We prioritize the term “polygonal mat” in favor of “biscuit mat” as not all mats that are separated by polygon-forming cracks exhibit a convex-up surface.

All mat morphotypes follow a subsurface vertical progression of mm-scale pigmented zonation that typifies photosynthetic microbial mat communities, and their associated heterotrophic and chemotrophic communities, that are stratified due to gradients in sunlight availability and products of biogeochemical processes (Van Gemerden, 1993; Stolz, 2000). The pigmentation progresses from a dark green surface layer to lighter green, then purple, then pink layers sometimes intermixed with mm-thick layers of carbonate sediment (e.g. Figure 2.14). Mat surfaces and/or depressions surrounding them are often covered with tan-colored extracellular polymeric substances (EPS), which provides attachment to the underlying substrate, promotes cell signaling, and protects the mat organisms from external hazards (Wingender, J. et al., 1999; Neu and Laurence, 2010). Below the pigmented mat layers are up to several cm of brown, sometimes laminated organic material. The mats are underlain by ooids and minor to trace carbonate mud.

The mat texture (e.g. Figure 2.14) represents a complex ecosystem that hosts a diverse community of other microorganisms, most notably including Alphaproteobacteria of the Rhodospirillales, Rhodobacterales, and Rhizobiales; Chloroflexi of the Chloroflexales and Anaerolineales; Gammaproteobacteria of the Chromatiales; Deltaproteobacteria of the Myxococcales, Desulfovibrionales, Desulfobacterales, and Syntrophobacterales; Planctomycetes of the Planctomycetales and Phycisphaerales; and Bacteroidetes of the Sphingobacterales (Lingappa et al., 2020). These organisms represent numerous guilds conducting different interconnected metabolisms, including anoxygenic phototrophs, chemolithotrophs, and heterotrophs. The mat communities are stratified with depth based on niche differentiation, generating observable pigmented zonation at a hand sample scale.

2.4 Methods

This study was conducted over six field sessions in June and July of 2016, August of 2017, September of 2017, March of 2018, July of 2018, and July of 2019. Study methods include UAV-based imaging with centimeter-scale topographic surveying and surface geological observations of sedimentary structures, the morphology and distribution of microbial mats, and their temporal variability.

2.4.1 Unmanned Aerial Vehicle Imaging

Orthomosaics and digital elevation models (DEMs) of Little Ambergris Cay were generated in July of 2016 and 2017 using RGB images collected with DJI Phantom 4 Pro unmanned aerial vehicle (UAV). The 2016 full-island orthomosaic (Figure 2.2) was generated from more than 1,500 overlapping nadir images collected from 250 m standoff during manual flights with a 12-megapixel camera, yielding a spatial solution of 13.8 cm/pixel. Images were collected during 13 separate flights spanning multiple days. A corresponding DEM (Figure 2.4A) was created using the same set of images at a vertical resolution of 27.6 cm. The 2017 orthomosaic (Figure 2.3) was generated from more than 2000 overlapping nadir images collected over multiple days from 150m standoff during automated flights with a 20-megapixel camera, yielding a spatial resolution of 6.1 cm/pixel. Low-standoff (<50 m elevation) RGB images were used to digitize the cracks that form polygonal microbial mats to measure their vertex angles and polygon areas and provide additional context for facies mapping.

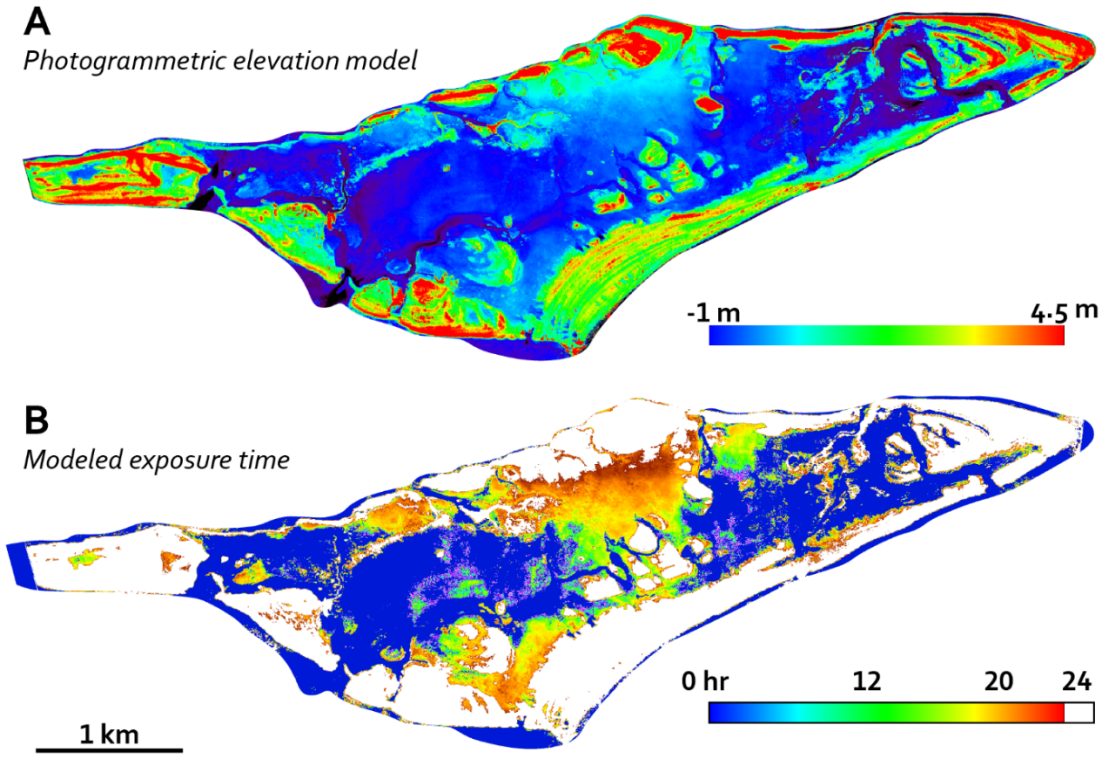

Figure 2.4. (**A**) Elevation model of Little Ambergris Cay made in July 2016 by combining more than 1,500 RGB images collected over 13 separate flights with a DJI Phantom 4 Pro with a 12-megapixel camera. Generated in Agisoft Metashape. (**B**) Map of average number of hours per day that the surface is exposed. Calculated using a spatially weighted average of tide data from three locations on the island (Figures 2.2, 2.10) and the elevation model in (A).

All orthomosaics and DEMs were generated with Agisoft Photoscan software using more than 20 ground control points that were collected with a differential global positioning system (DGPS) unit during transects of the island (see 2.4.2). Long-wavelength distortion in the DEM, which frequently results from alignment errors between overlapping images, was corrected by fitting a three-dimensional polynomial to a downsampled version of the DEM and subtracting it from the original DEM to minimize error relative to in situ survey points (Figure 2.7). The DEM was offset such that an elevation of 0 m is the mean water level (MWL) observed over the course of six days averaged between three tide gauge sites (section 2.4.3).

Hyperspectral images of the interior basin were taken with a Headwall Nano-Hyperspec Visible and Near Infrared pushbroom imaging spectrometer, which has 276 spectral bands between 400-1000 nm. The lens has 640 pixels and a 50.7° angular field of view, yielding ~20 cm resolution from 100 m elevation. The camera was mounted on a DJI Ronin-MX 3-axis powered gimbal and carried by a DJI Matrice 600 Pro UAV. Flights were automated with Drone Deploy software to fly at a constant speed to match the static calibrated frame rate of the spectrometer. Reflectance R was calculated as

$$R = \frac{R_{cal}(W - D)}{W_{cal} - D}, \quad (1)$$

where W is the raw digital number on the detector, D is the dark current measured prior to flight, W_{cal} is the digital number measured averaged from the brightest non-saturated shade of a three-shade calibration target placed in the scene (a 10'x10' tarp), and R_{cal} is the lab-measured reflectance of the calibration target. The resulting product is a set nx640x276 image cubes that are corrected for atmospheric absorption and illumination assuming homogenous atmospheric conditions and illumination across each scene. The images were not orthorectified because there is little topographic relief in the interior basin. Every row of each reflectance cube was independently georeferenced by extracting the GPS-based center location and altitude of the camera corresponding to each frame capture to correct for variation in UAV altitude, heading, and speed. The rows were stitched back into a single mosaic and warped to ground control points selected manually from the visible light orthomosaic. Maps of the band depth of reflectance features corresponding to different characteristic microbial pigments including phycobilins (590 nm), phycocyanin (620 nm), chlorophyll *a* (680 nm), bacteriochlorophyll *c* and/or *d* (720 nm), and bacteriochlorophyll *a* (800-890 nm) were calculated from these cubes (Figure 2.5) (features described in Hubas et al., 2011).

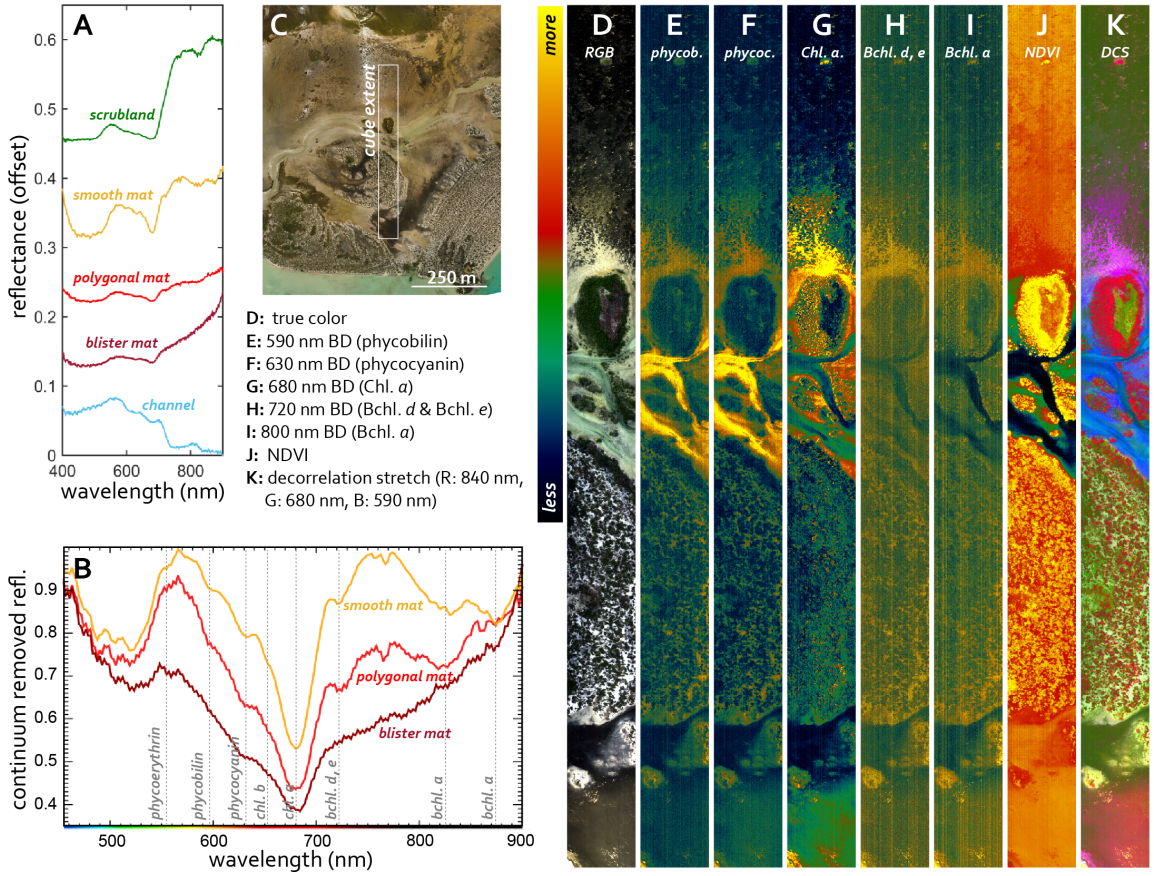

Figure 2.5. (**A**) Averaged overhead reflectance spectra of scrubland, smooth mat, polygonal mat, blister mat, and a channel. (**B**) Continuum removed spectra of the mat facies from (A) with major pigment absorption features labeled. (**C**) Extent of representative hyperspectral image shown in D-K. (**D**) Approximate true color image of scene with each mat morphotype. (**E**) phycobilin absorption depth. (**F**) phycocyanin absorption depth. (**G**) Chlorophyll a absorption depth. (**H**) Bchl. *d* and *e* absorption depth. (**I**) Bchl. *a* absorption depth. (**J**) Normalized difference vegetation index. (**K**) Decorrelation stretch (R: 840 nm, G: 680 nm, B: 590 nm).

2.4.2 Geological Topographic Survey and Facies Mapping

In situ elevation data were collected during June and July and 2016 and August of 2017 using a Total Station and prism and an APS-3 DGPS system. 847 DGPS elevation and facies survey points (Figure 2.6) and 1334 total station elevation points (Figure 2.7) were collected during transects of the island. As with the DEM, all DGPS and total station elevation data were offset such that the MWL is at 0 m elevation.

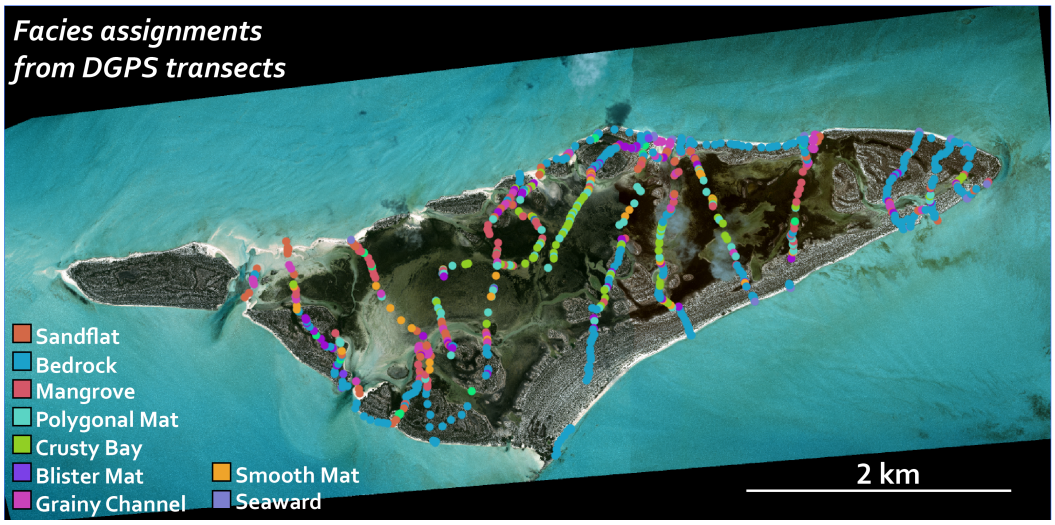

Figure 2.6. Classification of facies during ten transects of Little Ambergris Cay. Facies were classified in situ and positions were marked with a differential GPS (DGPS).

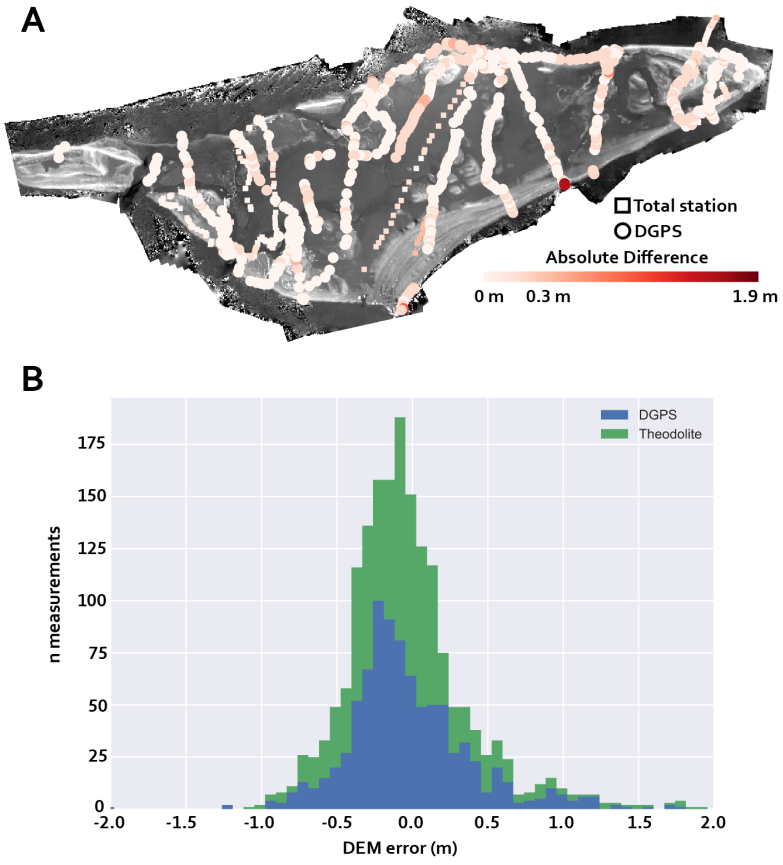

Figure 2.7. (**A**) Absolute elevation difference between the 2016 photogrammetric DEM and total station and DGPS elevation survey points. (**B**) Histogram showing the distribution of DEM errors.

A subset of elevation survey points was used as ground control markers in the generation of the DEM (section 2.4.1) and the remaining points were used to validate DEM accuracy and assess facies elevation. Comparison of in situ elevation survey points with the DEM shows absolute elevation differences of <0.1 m for ~75% of points in the interior (Figure 2.7), indicating that the DEM is approximately representative of true elevations across the island. Most larger elevation deviations are in heavily vegetated areas where photogrammetric elevations are skewed high by the tops of plants.

An island-wide facies map (Figure 2.8) was generated using the 2016 UAV orthomosaic (Figure 2.2) with in situ facies assignments as ground truth (Figure 2.6). Violin plots of the facies elevation distribution were generated by extracting the elevation of each pixel in the facies map from the 2016 DEM (Figure 2.9A, Table 2.1). The violin width is normalized to the sample count of each facies. Long-tailed elevation distributions, which may not be physically realistic for the microbial mat facies, are potentially attributable to four factors: 1) photogrammetric elevation errors in the DEM; 2) systemic DEM error caused by the polynomial surface warping correction; 3) errors in the facies map used to generate the elevation distributions; and 4) true physical elevation variation. Sporadic DEM errors, coupled with the relatively low vertical resolution, produces significant point-to-point elevation variability that contributes to artificially long-tailed elevation distributions. Because the number of points sampled per facies is high (>4.3e6, Table 2.1), however, the mean DEM-derived elevation is likely close to the true mean elevation if the elevations are not shifted by spatially asymmetric DEM warping. The consistently low absolute elevation differences between the DEM and in situ elevation survey points (Figure 2.7) suggest that the DEM is not significantly warped, and thus warping contributes minimally to elevation errors. Misidentification of microbial mats in the UAV orthomosaic due to their similar surface color likely artificially increase the overlap of their elevation distributions. Box plots of the facies elevation distribution (Figure 2.9B, Table 2.1) were generated from the DGPS survey points. The range of facies elevations from DGPS points is likely more accurate than the photogrammetric DEM due to the higher vertical resolution and in situ facies assignment.

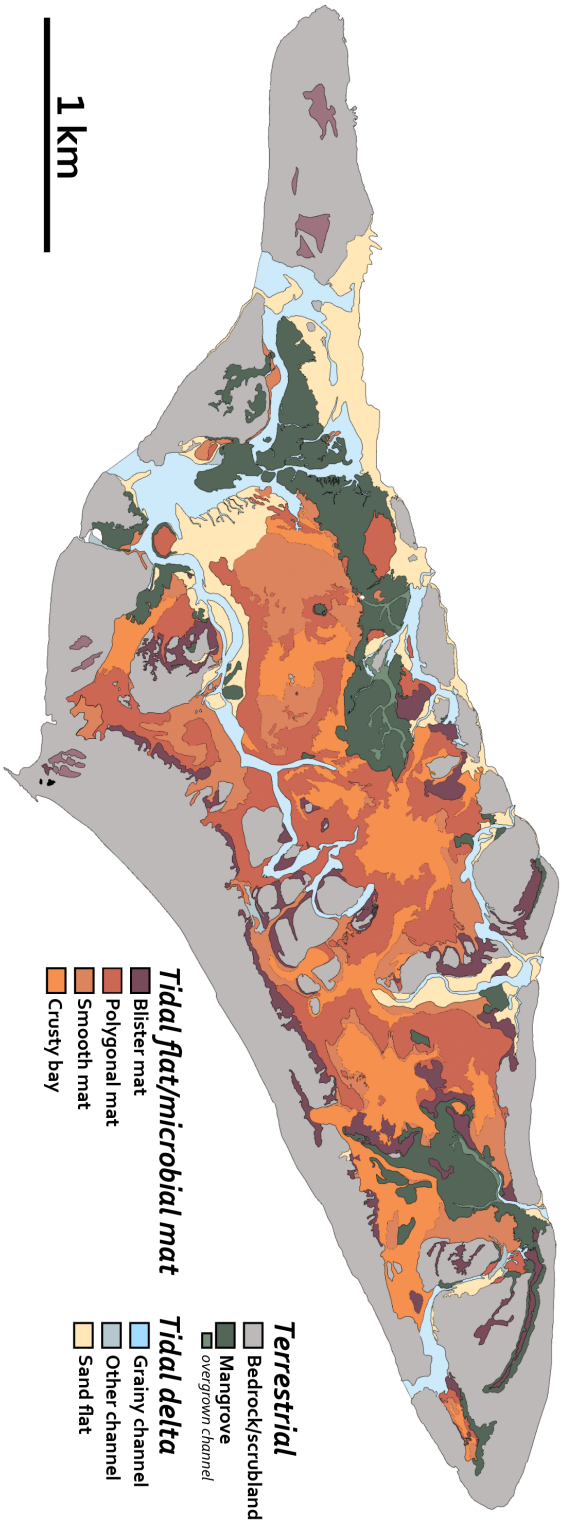

Figure 2.8. Facies map of Little Ambergris Cay, generated by mapping onto the 13.8 cm/pixel orthomosaic in Figure 2.2 and using the DGPS transect classifications shown in Figure 2.6.

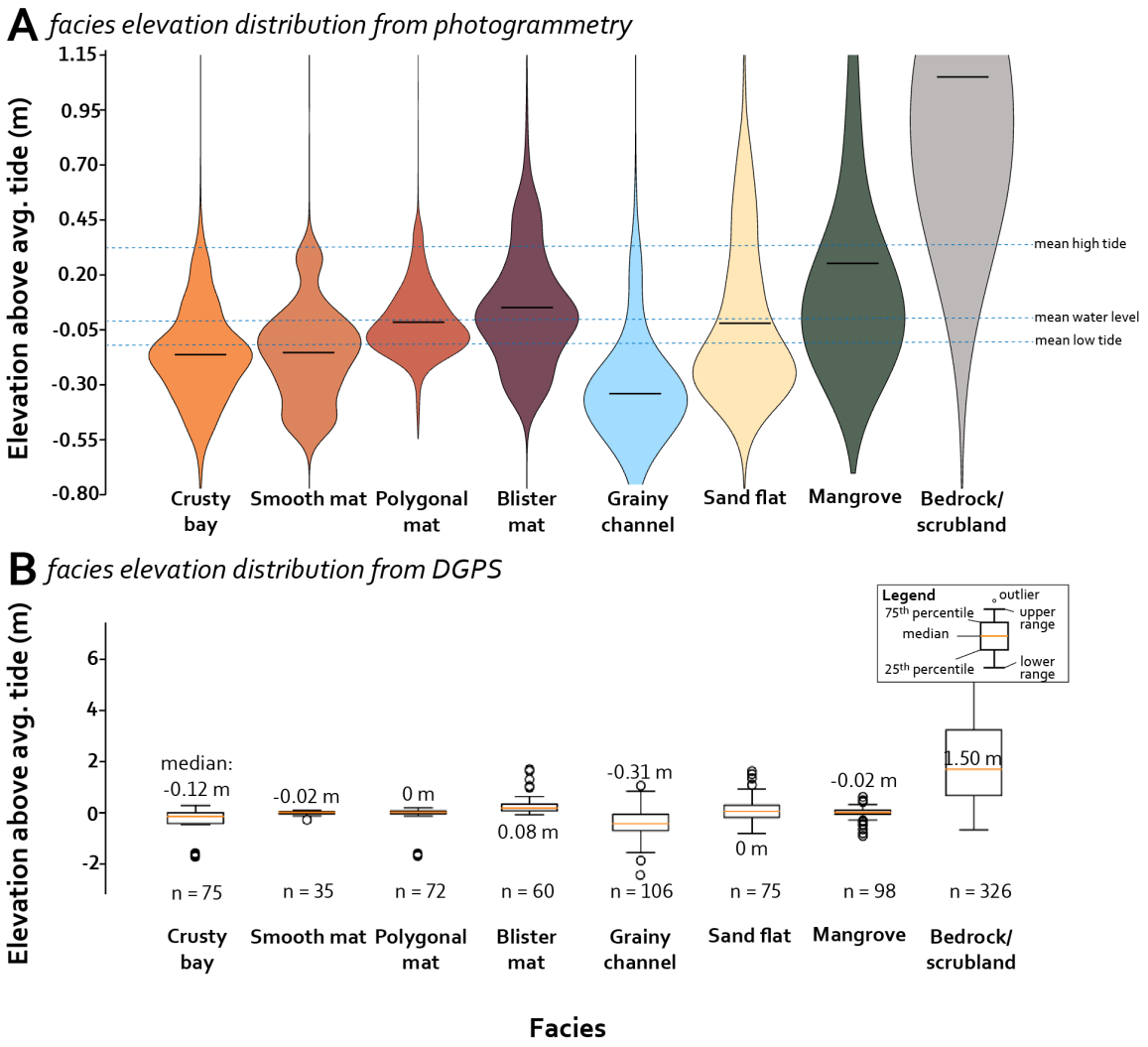

Figure 2.9. (**A**) Violin plot of the elevations of the facies. Elevations are sourced from the 2016 UAV-based digital elevation model (Figure 2.4A) and facies types are sourced from the corresponding facies map (Figure 2.8). A summary of the corresponding statistics is shown in Table 1. The average water depth and low and high tide elevations are derived from the tide data used to generate the modeled exposure time in Figure 2.4B. (**B**) Plot of facies elevation distributions from the DGPS data shown in Figure 2.6. Elevations are relative to the average water level (0 m).

Table 2.1. ELEVATION AND EXPOSURE STATISTICS OF ALL FACIES ON LITTLE AMBERGRIS CAY

Facies	Number of pixels in facies map	Area (km^2)	Mean DEM elevation (m rel. mean water level)	Standard deviation DEM elevation	Median DEM elevation (m rel. mean water level)	Number of DGPS measurements	Median DGPS elevation (m rel. mean water level)
Crusty bay	5611982	0.484	-0.152	0.227	-0.162	75	-0.12
Smooth mat	4713509	0.406	-0.144	0.221	-0.137	35	-0.02
Polygonal mat	8823409	0.761	-0.008	0.160	-0.037	72	0.00
Blister mat	4307242	0.371	0.062	0.277	0.036	60	0.08
Grainy channel	5661462	0.488	-0.327	0.315	-0.346	106	-0.31
Sand flat	4799307	0.414	0.005	0.391	-0.118	75	0.00
Mangrove	7673826	0.662	0.265	0.620	0.107	98	-0.02
Bedrock/scrubland	29300125	2.527	1.109	0.802	0.788	326	1.50

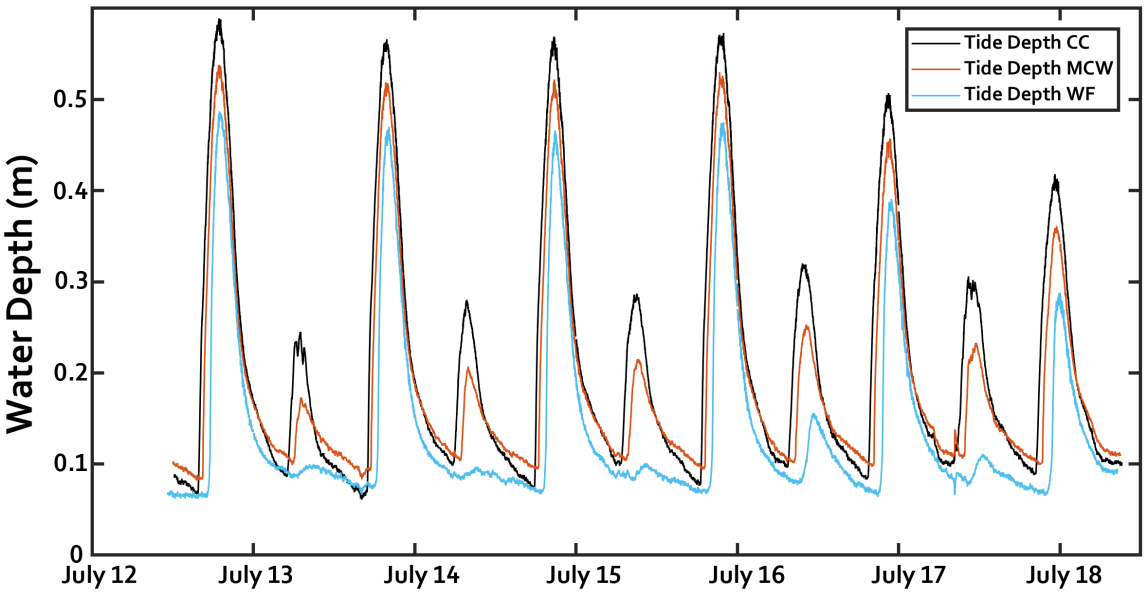

Figure 2.10. Tide data collected at three sites over six days during July 2018. Measurement locations are shown in Figure 2.2.

2.4.3 Tidal Range Measurements and Exposure Time Modeling

Tidal variations in water depth in the island interior were measured with HOBO U20L water depth loggers deployed in the summer of 2018 at three sites in the island interior (Figure 2.10). Data from HOBO loggers were corrected with pressure-corrected with barometric data collected with an additional HOBO U20 logger deployed above water on Little Ambergris Cay. The mean water level was estimated by calculating a temporal average of the water depth at the three logging sites, offset by DEM-measured surface elevation,

assuming no significant tidal lag between their separation distances of 0.8 km, 0.9 km, and 1.7 km. The tide level is similar in elevation and timing at the three sites, indicating that an average of the aggregate dataset is a reasonable estimation of tide levels across the interior.

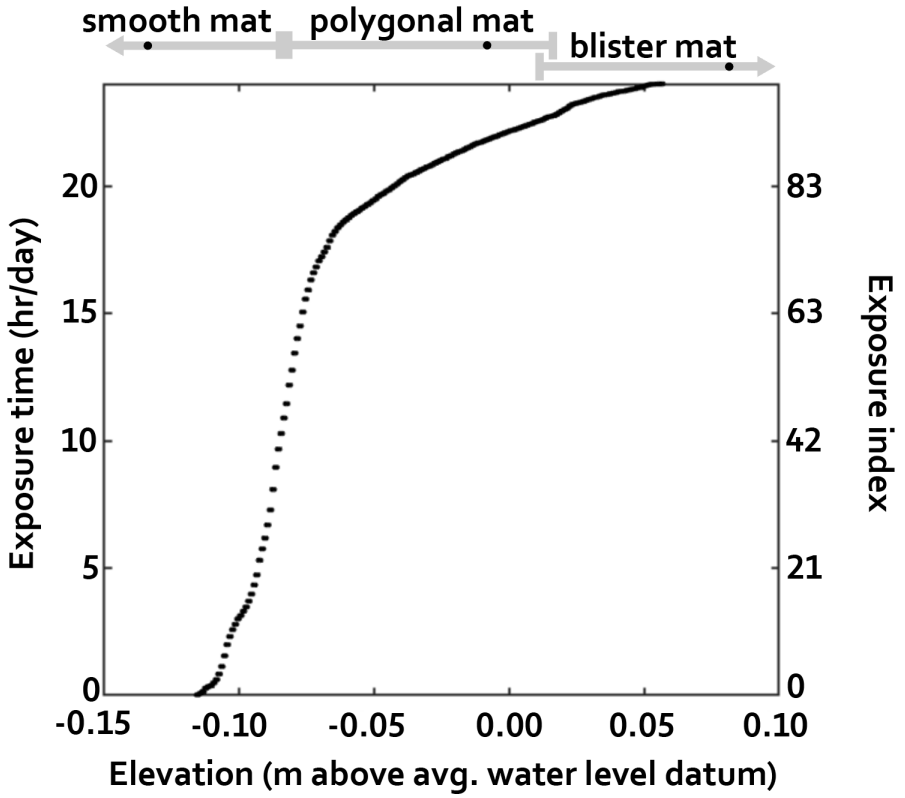

Figure 2.11. Comparison of modeled exposure time (hours per day) and elevation relative to the average water level datum. All DEM points are sampled. The range capturing 95% of elevations for smooth mats, polygonal mats, and blister mats is shown above, as is the DEM-derived mean elevation of each facies (black dot).

Island-wide exposure index, the percent of time a given point is exposed (Ginsburg et al., 1977), was calculated from maps of daily exposure time generated using the DEM and tidal range measurements. A grid with the lateral resolution (13.1 cm/pixel) of the DEM was populated in ten-minute time steps with the distance-weighted average of water depths measured at the three logging sites, offset for local elevation sourced from the DEM. The resulting rasters were time-averaged to calculate the average daily exposure index across the island (Figure 2.4B). The effects of wind tides were not modeled. Because elevations were sourced from the DEM, regions densely populated with mangroves have artificially high

exposure indices because elevations in those areas are skewed by the tops of the plants. The surface of mangrove-populated regions likely experiences similar exposure times to the adjacent basins.

Exposure index and elevation values were plotted for every point on the island to calculate exposure index as a function of elevation (Figure 2.11). The range of exposure indices encapsulating 95% of the points measured for each mat facies was calculated from this curve using the DEM-based mean mat elevations (Figure 2.4A) and DGPS-based elevation ranges (Figure 2.4B).

2.4.4 Subsurface Geology

A 1 cm diameter, 2.5 m long stainless-steel probe was used to measure the depth to basement rock at a 127 point subset of survey points (Figure 2.12). Eight sediment vibracores were obtained by clamping 10' core barrels (3" outer diameter, 0.083" wall thickness aluminum 6063) to a concrete vibrator driven by a portable gasoline motor with an 18' flexible shaft. The vibrating barrels were sunk into the sediment by a team of handlers using guide ropes tied to the top of the barrel and sealed with a 3" gripper plug before recovery. Core recovery was maximized by rapidly extracting cores from the ground without mechanical assistance. Core compaction and recovery were calculated from measurements of core barrel penetration, depth of core top prior to gripper plug emplacement, and length of recovered sediment. Compaction ranged between 11-18% for the samples shown here. Recovered cores were laid flat, excess barrel length removed with a reciprocating hacksaw, and sealed with plastic pipe caps and electrical tape. The barrels were split with a circular saw and the sediment was cleaved open with a wire. Select portions of cores suspected to contain relict mat material were imaged with a Headwall Nano-Hyperspec VNIR imaging spectrometer (see section 2.4.1) using a Thorlabs KMTS50E motorized translation stage.

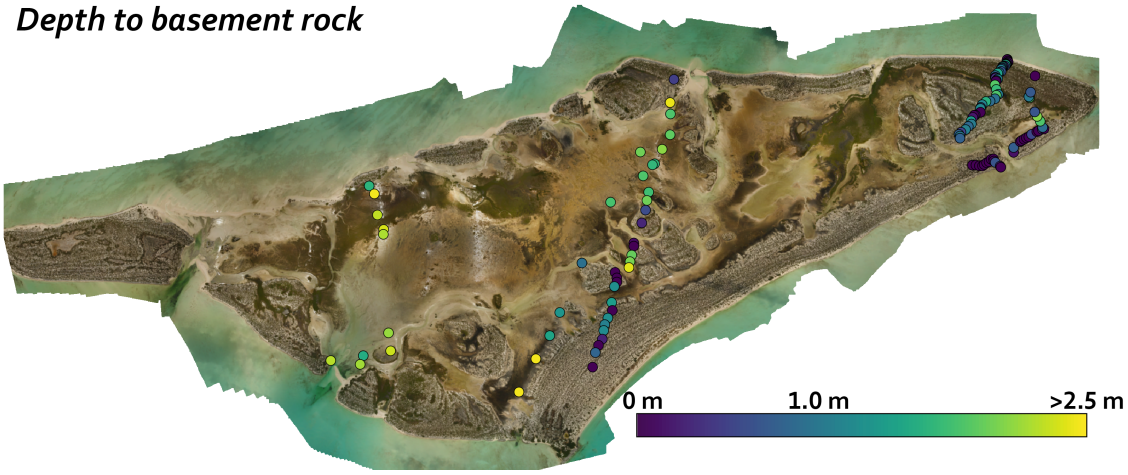

Figure 2.12. Depth to basement rock relative to surface elevation. Measured at 127 sites using a 1 cm diameter, 2.5 m long stainless-steel rod.

2.4.5 Radiocarbon Dating

Strombus (conch), cerithid gastropods, and bivalve fragments were sampled from three cores and multiple sites along the bedrock rim (Figure 2.2). The samples were leached with dilute HCL prior to hydrolysis with 85% phosphoric acid. Analyses were performed at the University of California Irvine Keck Carbon Cycle AMS Facility. Radiocarbon concentrations are given as fractions of the modern standard, D14C, and conventional radiocarbon age following the convention of Stuiver and Polach (1977) (Table 2.2). Sample preparation backgrounds were subtracted based on measurements of ^{14}C-free calcite. All results were corrected for isotopic fractionation following Stuiver and Polach (1977) with δ^{13}C values measured on prepared graphite using an AMS spectrometer.

2.5 Results

2.5.1 Surface Geology and Microbial Mat Facies Descriptions

Eight facies were identified across the island including: bedrock with scrubland, sand flats, channels, ooid hardground-floored bay, mangroves, and three microbial mat facies distinguished based on surface texture: smooth mats, polygonal mats, and blister mats. Most facies occur within an overlapping range of elevations (Figure 2.9), leading to lateral equivalence of some facies components.

Carbonate lithofacies that comprise the rim include seaward-dipping low angle stratification, oolites with keystone vugs, bioturbation and fossiliferous lags, rudstones with imbricated beachrock boulders, and high-angle trough cross bedding reaching ~1-4.5 m above MWL (Figure 2.13) (Orzechwski et al., 2016). Much of the bedrock rim is onlapped by imbricated boulder sized clasts of the bedrock, torn up during storms. The rim is overgrown with higher plants and vegetation. Sand flats are grain-dominated flood-tide delta deposits at or just above MWL with common cm-scale subaqueous wave oscillation ripples exposed at low tide, lags of cerithid gastropods, and seagrass patches. Most channels in the island interior are lined with disaggregated organic material, large mat rip-up clasts, longitudinal bars, and wave-modified transverse bedforms and reach depths of up to -1.5 m MWL. Much of the interior basin, termed "crusty bay," is floored with patchy, cm-thick ooid hardgrounds, *Batophora*, and disaggregated organic material, typically either exposed over large areas such as in the western interior basin or concentrated in m-scale scour pits in areas otherwise floored with smooth or polygonal mats. The mean elevation of the crusty bay facies in DGPS data is -0.12 m, putting it ~5 cm below the mean low tide level and 10 cm below the mean DGPS smooth mat elevation. The mean elevation of the crusty bay facies in DEM data is -0.152 m, ~8 cm below the mean low tide level and ~1 cm below the mean DEM smooth mat elevation. Mangrove-dominated regions typically contain luxuriant polygonal mats of variable thickness with sparse halophytes including sawgrass and *Salicornia*. Mangroves have an average DGPS elevation of -0.02 m MWL, comparable to that of smooth and polygonal mats. The elevation distribution of mangroves in DEM data should be disregarded because it is skewed by the tops of vegetation.

TABLE 2.2. RADIOCARBON AGES OF SHELL FRAGMENTS IN LITTLE AMBERGRIS CAY BEDROCK AND INTERIOR BASIN SEDIMENT CORE SAMPLES

Sample Description	UCIAMS #	Fig. 2 ID #	Sample Name	Fraction Modern	±	$D^{14}C$ (I)	±	^{14}C age (BP)	±
modern beach shell	181089	A1	BBm-1	0.9494	0.0014	-50.6	1.4	415	15
modern beach (*Strombus*)	181094	A1	BBm-2	1.0479	0.0016	47.9	1.6	-370*	15
bivalve fragment	181086	A1	BBwf-1	0.8629	0.0016	-137.1	1.6	1185	15
Oliva	181087	A1	BBwf-2	0.9760	0.0015	-24.0	1.5	495	15
Strombus	181088	A1	BBwf-3	0.8886	0.0014	-111.4	1.4	950	15
Strombus	181090	A1	BBfD-1	0.8886	0.0013	-111.4	1.3	950	15
Strombus	181091	A1	BBfD-2	0.8877	0.0014	-112.3	1.4	955	15
Strombus	181093	A1	BBfD-3	0.8591	0.0013	-140.9	1.3	1220	15
Strombus	181092	A1	Bsil-1	0.9020	0.0015	-98.0	1.5	830	15
Strombus	181095	A1	Bsil-2	0.8397	0.0013	-160.3	1.3	1405	15
cores and core top	218520	-	Modern 1 A cerithid	0.8852	0.0017	-114.8	1.7	980	20
cores and core top	218521	A2	CC-J18-30 cerithid	0.8994	0.0017	-100.6	1.7	850	20
cores and core top	218522	A2	CC-J18-68 cerithid	0.8258	0.0016	-174.2	1.6	1535	20
cores and core top	218523	A2	CC-J18-155-162 cerithid	0.7904	0.0015	-209.6	1.5	1890	20
cores and core top	218524	A3	FML-J18A-84 shell frag	0.8257	0.0016	-174.3	1.6	1540	20
cores and core top	218525	A3	FML-J18A-144 cerithid frag.	0.7907	0.0016	-209.3	1.6	1885	20
cores and core top	218526	A3	FML-J18A-162 shell frag	0.7727	0.0015	-227.3	1.5	2070	20
cores and core top	218527	A4	VC03-030C shell frags	0.8811	0.0017	-118.9	1.7	1015	20
cores and core top	218528	A4	VC03-070 shell frags	0.8598	0.0016	-140.2	1.6	1215	20
cores and core top	218529	A4	VC03-180 shell frags	0.7303	0.0015	-269.7	1.5	2525	20
bedrock *(Strombus)*	218532	A5	8/8 LI-1A shell	0.8998	0.0017	-100.2	1.7	850	15
bedrock *(Strombus)*	218533	A5	8/8 LI-1B shell	0.9388	0.0020	-61.2	2.0	505	20
bedrock *(Strombus)*	218534	A6	8/9 BB-5B shell.1	0.8593	0.0018	-140.7	1.8	1220	20
bedrock *(Strombus)*	218535	A6	8/9 BB-5B shell 2	0.8643	0.0019	-135.7	1.9	1170	20
bedrock *(Strombus)*	218536	A7	8/9 BB01-A shell	0.8636	0.0016	-136.4	1.6	1180	20
bedrock *(Strombus)*	218537	A8	8/5 BB-1B shell	0.9391	0.0018	-60.9	1.8	505	15
bedrock *(Strombus)*	218538	A8	8/5 BB-1A shell	0.9417	0.0018	-58.3	1.8	480	20
bedrock *(Strombus)*	218539	A9	West of (FA)-1C shell	0.8892	0.0017	-110.8	1.7	945	20
bedrock *(Strombus)*	218540	A9	West of (FA)-1B shell	0.8986	0.0017	-101.4	1.7	860	20
bedrock *(Strombus)*	218541	A10	FA-3A (breccia) shell 1	0.9153	0.0018	-84.7	1.8	710	20

*Excess ^{14}C from mid-20th century atmospheric thermonuclear weapons tests

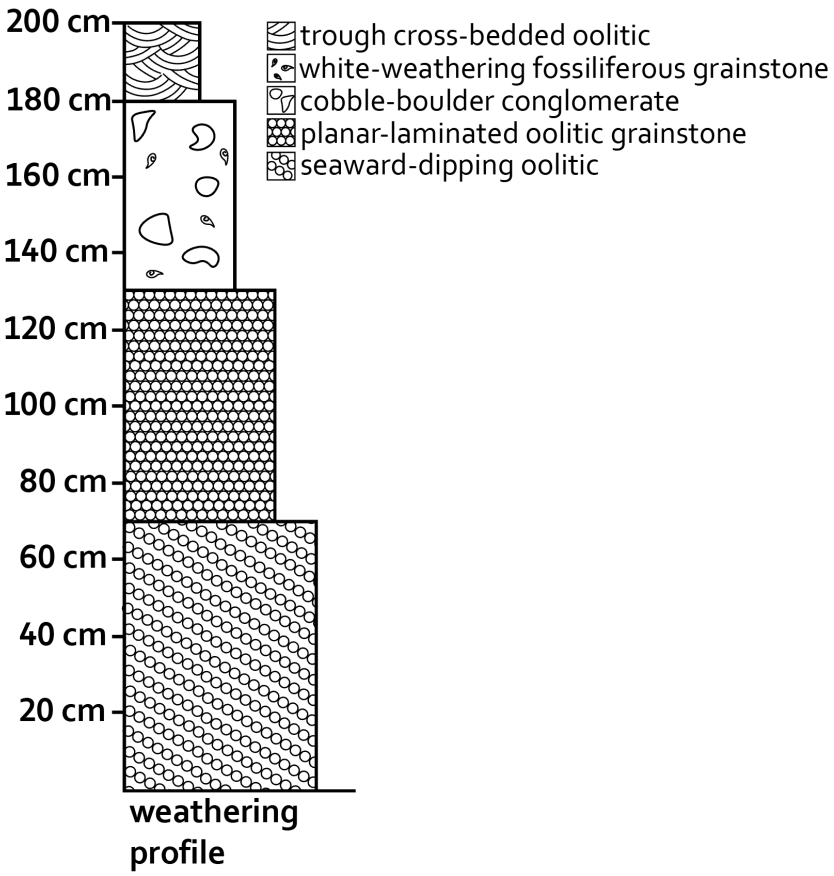

Figure 2.13. Representative stratigraphic column of Little Ambergris bedrock rim.

Microbial mats are widespread in the island's interior, comprising an area of more than 2.3 km^2, developed even in mangrove thickets. Representative examples of these three types are shown in Figure 2.14.

Smooth microbial mats are 4-25 cm thick and form laterally extensive sheets that overlie ooids and ooid hardgrounds and are typically submerged under water. They are developed best in the open interior basin and its margins and exhibit several variants: 1) smooth, cm-dm-thick, EPS-covered, low cohesion mats (Figure 2.14I); 2) smooth, cm-thick, EPS-covered, highly cohesive mats; 3) smooth, mm-thick, tufted mat with a dark green surface; and 4) smooth, often EPS-covered (sometimes dark green), highly cohesive, 3-5 cm-thick mat with incipient, low-lying cracks forming incomplete polygons (Figure 2.14H).

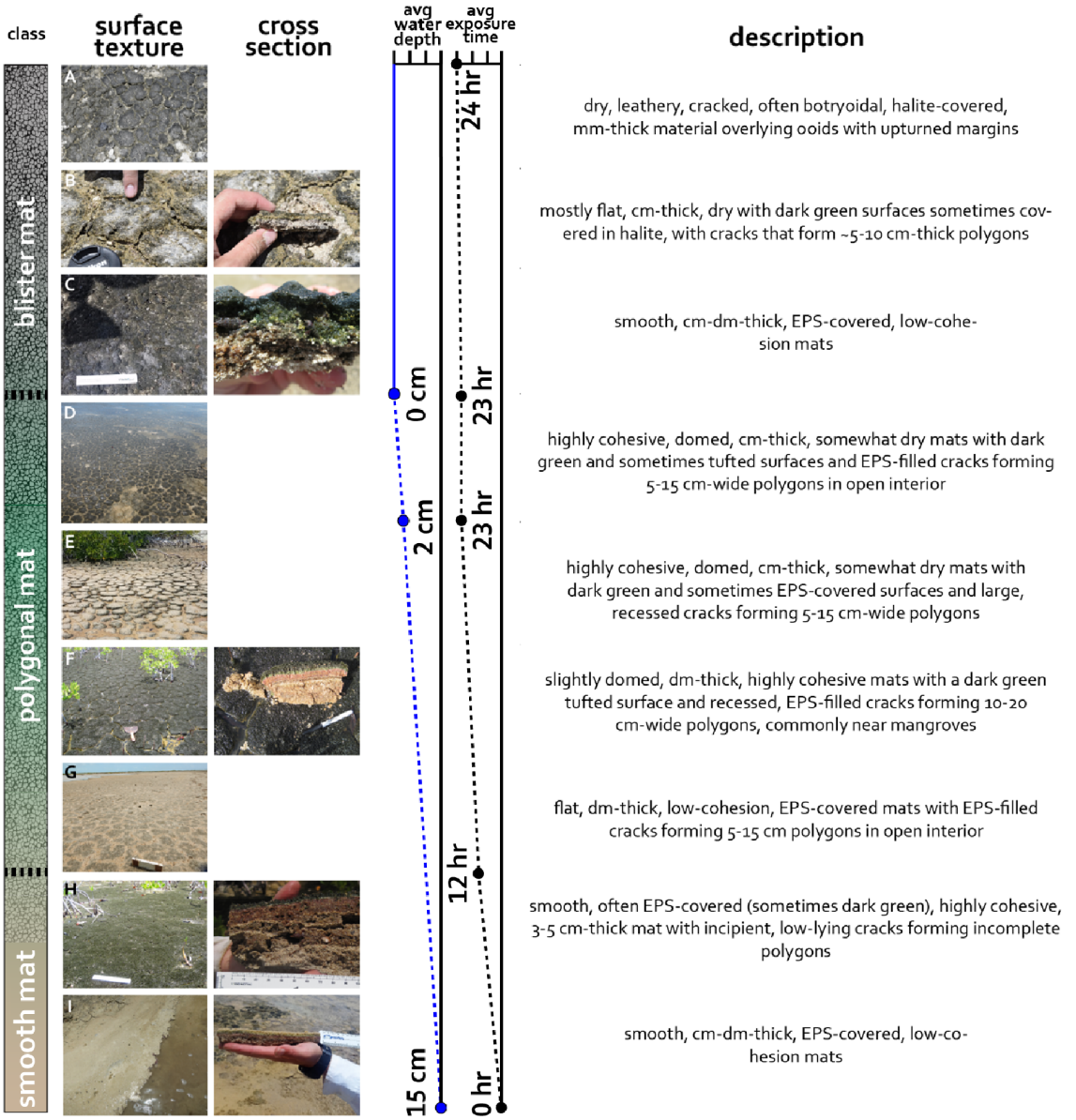

Figure 2.14. Surface and cross-sectional images of representative mat morphologies grouped into the major morphotypes: blister mat (**A-C**), polygonal mat (**D-G**), and smooth mat (**H** and **I**). The average water depth of each mat morphotype is denoted based on three measurements, shown by the blue dots, of the average water depth of the major morphotypes (see Figure 2.9). The average exposure time is denoted based on five measurements, shown by the black dots, of the average exposure time of the equivalent mat morphotypes based on the exposure map shown in Figure 2.4B.

Polygonal mats are typified by deeply penetrating cracks with polygonal geometry, occur commonly in the open interior basin and in prolifically in mangrove thickets, and are intermittently submerged under water. Several variants are expressed: 1) flat, dm-thick, low-cohesion, EPS-covered mats with EPS-filled cracks forming 5-15 cm polygons in the open island interior (Figure 2.14G); 2) slightly domed, dm-thick, highly cohesive mats with a dark green tufted surface and recessed, EPS-filled cracks forming 10-20 cm-wide polygons, most commonly found near mangroves (Figure 2.14F); 3) highly cohesive, domed, cm-thick, somewhat dry mats with dark green and sometimes EPS-covered surfaces and large, recessed cracks forming 5-15 cm-wide polygons (Figure 2.14E); 4) highly cohesive, domed, cm-thick, somewhat dry mats with dark green and sometimes tufted surfaces and EPS-filled cracks forming 5-15 cm-wide polygons, found in the open interior (Figure 2.14D); and 5) mostly flat, 1-2 cm-thick, somewhat dry mats with dark green surfaces and cracks forming 5-15 cm-wide polygons.

Blister mats have dark, cohesive, and usually rough or colloform surfaces. They are rarely submerged under water, although they are often wet due to capillary rise of shallow groundwater. Blister mats are expressed in several ways: 1) dry, leathery, black, often botryoidal, sometimes tufted surface, cm-thick, overlying ooids and sometimes covered in halite with occasional mat chips and domes from outgassing (Figure 2.14C); 2) mostly flat, cm-thick, dry mats with dark green surfaces that are sometimes covered with halite and cracks that form ~5-10 cm-thick polygons (Figure 2.14B); and 3) dry, leathery, cracked, often botryoidal, halite-covered, mm-thick material overlying ooids with upturned margins and interspersed mat chips (Figure 2.14C).

2.5.2 Water Depth and Exposure Time of Microbial Mat Facies

Primary physical environmental factors that may influence the morphology of microbial mats on Little Ambergris Cay include hydrodynamic energy, exposure of mats above water, and sediment flux.

Water depth modeled from tide gauge data and the photogrammetric DEM provides a proxy for hydrodynamic energy and exposure time. The average DEM-based elevations of smooth, polygonal, and blister mats are -0.144 ± 0.221 m, -0.008 ± 0.16 m, and 0.062 ± 0.277 m MWL, respectively (Figure 2.9A, Table 2.1). The reported uncertainty is one standard deviation. The corresponding range of elevation distributions is unrealistically large, owing mostly to the low vertical resolution of the DEM (27.6 cm). Assuming vertical resolution is the primary source of elevation error (section 2.4.2), the average elevations in Figure 2.9A should closely represent the true average because each microbial mat facies is sampled from more than 4.3e6 DEM pixels.

Facies elevations measured with DGPS more accurately represent the true elevation range but are averaged over tens to hundreds of measurements instead of millions, making the mean more susceptible to outliers. The DGPS elevations of smooth, polygonal, and blister mats is -0.02 ± 0.03 m, 0.00 ± 0.04 m, and 0.08 ± 0.24 m MWL, respectively (Figure 2.9B, Table 2.1). The reported uncertainty is one standard deviation.

Collectively, the best estimate of mean facies elevation and elevation range is sourced from a combination of these data using DEM-based means and DGPS-based ranges, which reconciles the strengths and weaknesses of each method. Smooth mats occur on average ~14 cm below MWL and 1-2 cm below the mean low tide measured during 2018. 95% of DGPS smooth mat elevations are between -0.20 to -0.08 cm MWL, which closely mirrors in situ observations and corresponds to a modeled average daily exposure time of 0-12 hours and an average water depth of up to ~0.5 m at high tide for the lowest mats. The average smooth mat elevation was never exposed during our measurement periods. Polygonal mats occur on average ~1cm below MWL, corresponding to an average daily exposure time of 21 hours. 95% of polygonal mats are between -0.08 to 0.02 cm, yielding average daily exposure times of ~12-23 hours. The average elevation of blister mats is ~0.06 cm above MWL, which is on average exposed 24 hours per day. 95% of blister mats are between 0.01 and 0.30 cm, which ranges in daily exposure time from 22 to 24 hours. The elevation distribution of blister mats is skewed high relative to the other mat types, consistent with the presence of blister mats at

relatively high elevations abutting bedrock or in inactive or abandoned channels that are only wet during spring tides or storms (e.g. Figure 2.15). Few mats of any morphotype were identified below -0.2 m MWL, which is close to the average elevation of the ooid hardground floors the interior basin.

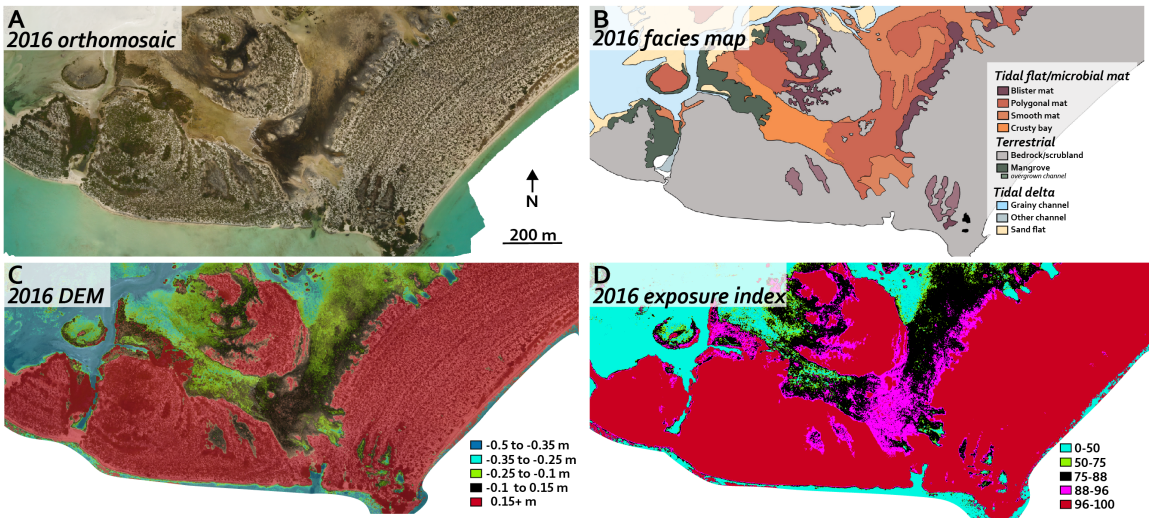

Figure 2.15. (**A**) Subset of the 2016 Little Ambergris RGB UAV orthomosaic showing a region with the three major mat morphotypes. (**B**) Facies map of the same region. (**C**) UAV-based elevation model binned by elevation and overlaid on the RGB orthomosaic. (**D**) Modeled exposure time of the same region binned by hours exposed per day.

Hyperspectral imaging also reveals a link between elevation and the abundance of photosynthetic pigments. The surfaces of smooth mats have the highest chlorophyll *a* abundance of any features on the island, including mangroves and shrubs (Figure 2.5G, 2.16A), indicating high primary productivity. Surficial chlorophyll *a* abundance is lower for polygonal mats and blister mats as evidenced by a consistently shallower 680 nm absorption feature (Figure 2.5B, 2.5G, 2.16A). Chlorophyll *a* abundance has a moderate negative correlation (~-0.6) with elevation (Figure 2.17) consistent with the trends in Figure 2.16A, indicating higher productivity with decreasing exposure. Figure 2.16B shows smooth mats limited to zero exposure in a representative image also have the highest surficial chlorophyll *a* abundance. A second chlorophyll a peak at continuous exposure is due to terrestrial vegetation. The distribution of other photosynthetic pigments is more difficult to measure due to their lower abundance and the interference of water absorption. Regardless, smooth

mats also have a demonstrably higher abundance of phycobilin, phycocyanin, and bacteriochlorophylls *a*, *d*, and *e* (Figure 2.16 E,F,H,I) relative to polygonal mats, which in turn have a higher abundance of these pigments than blister mats. Indeed, the abundance of these pigments also has a weak to moderate negative correlation with elevation (Figure 2.17). The relative abundance of each pigment is positively correlated (Figure 2.17). Although the spectrometer did not overlap with the wavelength of UV-screening compounds like scytonemin (Fleming and Castenholz, 2007), mat surfaces were observed to darken with increasing elevation, evidenced by a consistent decrease in reflectance between flat, polygonal, and blister mats.

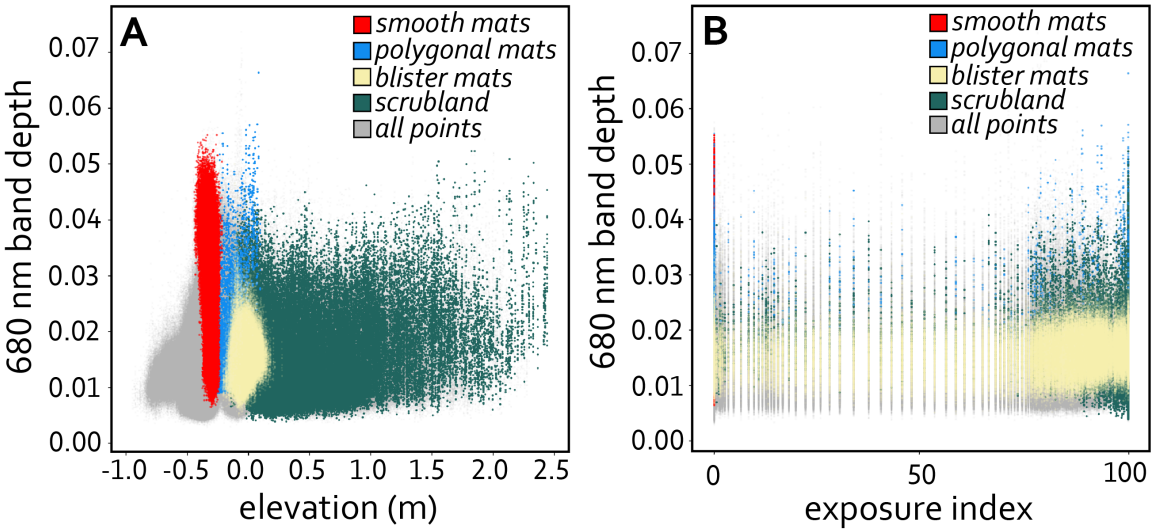

Figure 2.16. (**A**) 680 nm band depth (Chl. *a* abundance) as a function of elevation extracted from the representative scene in Figure 2.5. Smooth mats, polygonal mats, blister mats, and scrubland are color coded. Scrubland includes a mixture of shrubs and bedrock. (**B**) 680 nm band depth as a function of exposure index from the same scene.

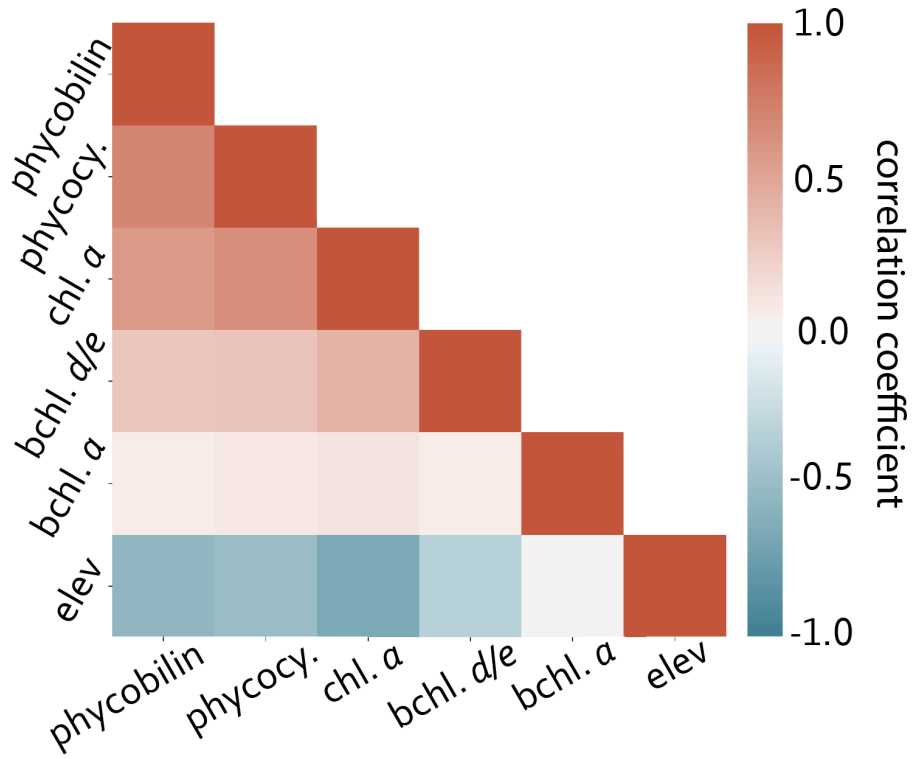

Figure 2.17. Correlation coefficient between the major pigment abundance and elevation measured from the representative scene in Figure 2.5.

2.5.3 Impact of Mechanical Stresses on Mat Texture

Mechanical stresses that modify biostabilized surfaces on Little Ambergris Cay include: 1) erosion and scouring; 2) gas pressure; and 3) desiccation.

The erosion and scouring of microbial mats occur most commonly during storms when hydrodynamic forces overwhelm cohesive forces within the mats or between the mats and underlying substrate. A common result of erosion in the interior basin is the creation of erosional windows up to several m in diameter bordered by sharp 2-15 cm high edges delineating adjacent microbial mats (Figure 2.18A). The erosional windows coalesce in some areas, leaving behind irregularly shaped patches of polygonal microbial mats that rise above the oolitic substrate; their margins are aligned with the preferential current flow during large storm events. Most storm-related erosional work on mats occurs in the interior basin, principally because that is their site of preferred development. However, tidal channels cut back into tidal flats with microbial mats during major storm events indicating mats do not

provide significant resistance to erosion, likely due to the absence of early mat lithification. Their erosion creates microbial mat intraclasts via undercutting during storm-induced channel migration and expansion (Figure 2.18B).

Mat intraclasts (e.g. Figure 2.18C, D) are thin, angular to rounded intraclasts of biostabilized sediment that break free from mat stabilized ripples, domes, folds, or roll-up structures. They form when hydrodynamic forces increase and then undercut biostabilized sediment, but individual textural elements that comprise the mat fragment (clast) remain intact. Mat intraclasts that break free from polygonal mats during strong storms are rounded during transport to form ellipsoidal, highly cohesive, 10-20 cm-wide clasts that are redeposited in the interior basin (Figure 2.18D, E). They are typically deposited upside-down, i.e. with the most recent layer on bottom and older, degraded filaments on top, due to their density profile. Thousands of mat intraclasts were observed throughout the basin following Hurricane Irma in areas where the current flow slowed, such as in erosional depressions in the interior basin, along margins of bedrock, in the roots of mangroves, and as lag deposits along overwash fans. Angular mat intraclasts observed after the storm (Figure 2.18C) likely have similar provenance but experienced less erosion during transport.

If mat intraclasts come to rest in the intertidal zone, subsequent microbial growth may occur in or on the structures. In March, 2018, six months after Hurricane Irma, the overturned rounded mat intraclasts were covered with new cyanobacterial growth and a mm-thick EPS layer (Figure 2.19F). Rounded, overturned mat intraclasts from previous storms, such as those observed after Hurricane Kate in 1985 (Wanless et al., 1987), are preserved in thick polygonal mats on the west side of the island where they are overgrown by several cm of subsequent microbial mat (Figure 2.19G, H), indicating that the production and recycling of mat intraclasts has occurred repeatedly on Little Ambergris.

The production and diffusion of microbially-generated gas provides pressure against the cohesive surface from below, deforming the surface upward. Gas formed within mats migrates toward the surface until it meets cohesive, impermeable microbial structures at the surface that inhibit gas escape. Resulting structures include 3-10 cm diameter, 1-5 cm-high

domes with a hollow center that is susceptible to collapse (Figure 2.18G) and elongated, 1-5 cm-high folds (Figure 2.18H, I).

Shrinkage cracks form in response to tensile stresses within a stratum that result from contraction following the loss of moisture or heat (Shorlin et al., 2000). In most parts of the interior basin, subaerial exposure and rewetting of microbial mats occurs tidally, with mats being submerged for several hours during high tide and exposed the rest of the day (section 2.5.2). Desiccation of mat surfaces due to repeated exposure above water produces polygonally arranged cracks in response to stresses produced when the mats lose water and shrink. The cracks range in width from ~0.5-2 cm and penetrate as far as the underlying substrate (typically ooid hardground), although in some cases penetrate only 1-2 cm into the underlying organic substrate. In uniform material, new cracks turn to converge with other cracks orthogonally to minimize stress, resulting in junctions that preferentially form angles of 90° (Shorlin et al., 2000). Measurements of >1,500 mat polygons imaged via UAV (e.g. Figure 2.20A) indicate that the desiccation cracks meet at an average vertex angle of 120° (Figure 2.20B), forming polygons that range in area from 50 to 350 cm^2 (Figure 2.20C). The average vertex angle of 120° is consistent with multiple wetting and drying cycles, which modify cracks that originally meet at 90° angles (Goehring et al., 2010). The polygon interiors are often domed in response to differential drying, producing a characteristic "biscuit" morphology (Figure 2.18D-F, 2.19E). Despite being more desiccated, not all blister mats are cracked, likely because the mats are thin and overly ooid sand that lacks the cohesion necessary for cracks to develop (e.g. Figures 2.18F, 2.21D).

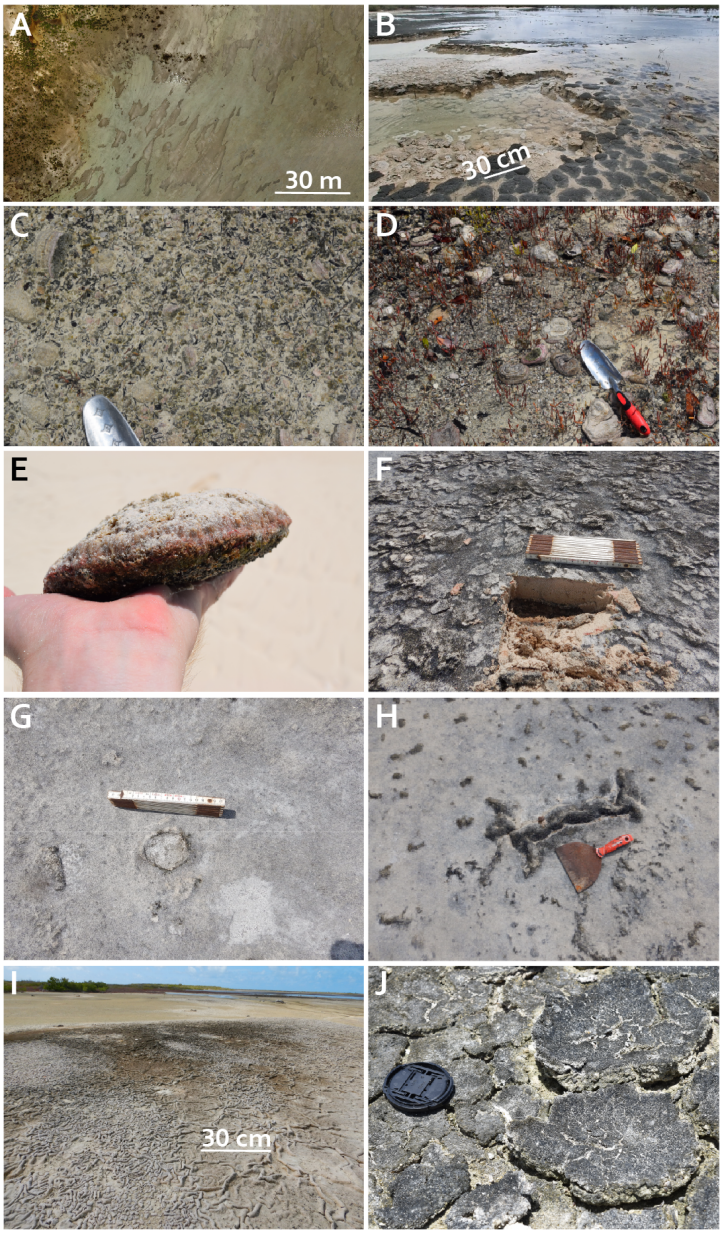

Figure 2.18. Microbial signatures arising from mechanical stress acting on biostabilized surfaces (Table 2.3C). (**A**) Aerial view of scoured sections of microbial mat in the island interior following Hurricane Irma in September, 2017. (**B**) Incised, mat-stabilized channel formed during Hurricane Irma in September, 2017. (**C**) Angular, cm-scale microbial mat intraclasts mixed with ooids, carbonate mud, and organic debris. (**D**) Rounded microbial mat intraclasts formed by the erosion of polygonal microbial mat in strong currents. (**E**) Close-up view of a single rounded microbial mat intraclast, which are typically deposited with the most recent surface layer on bottom, as shown, due to its relatively high density. (**F**) Mat chips embedded in ooids and bound in a matrix of subsequent microbial growth. (**G**) Collapsed gas dome. (**H**) A mat fold from gas pressure. (**I**) Area with ubiquitous mat folds. (**J**) Desiccated mat with upturned edges that break off as rollup structures.

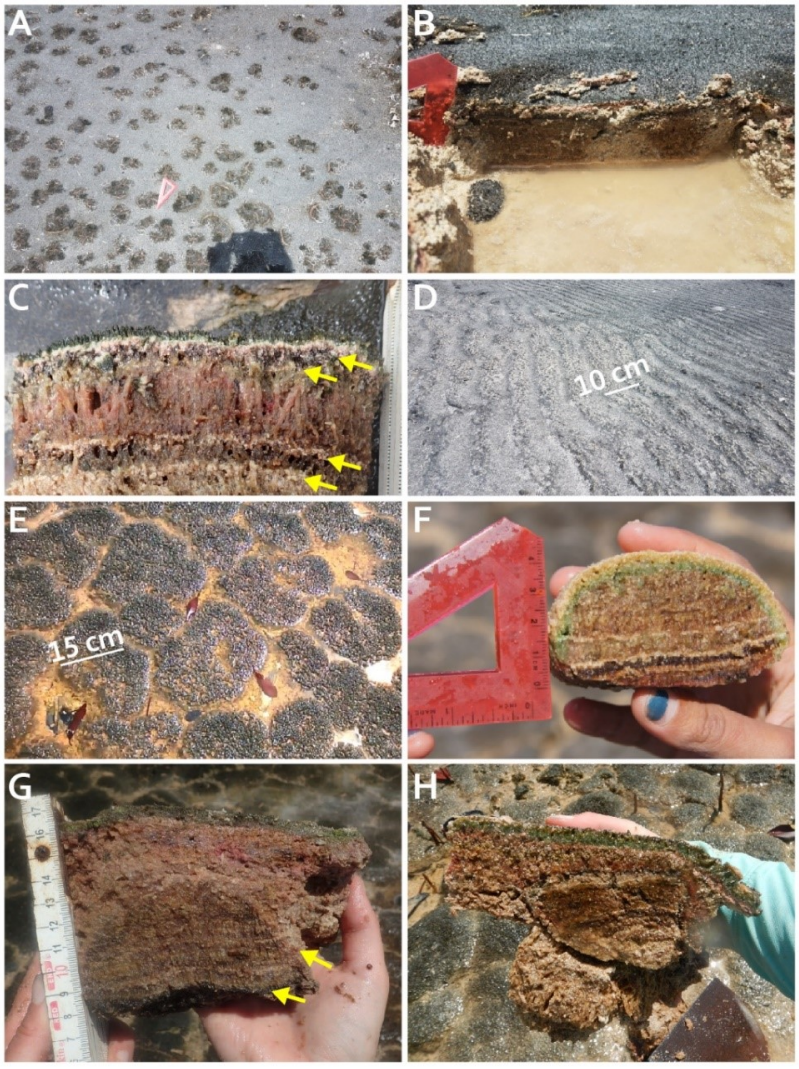

Figure 2.19. Examples of microbial structures arising from a biological response to mechanical stresses (Table 2.3D). (**A**) A level surface created by microbial growth on sediment deposited on polygonal mats. (**B**) Cross-sectional view of (A) showing mature polygonal microbial mats separated and overtopped by sediment and covered in new microbial growth. (**C**) Layers of bound irregular carbonate grains in a mature microbial mat. The yellow arrows denote four separate layers of bound grains, with the uppermost being deposited during Hurricane Irma in September, 2017. (**D**) Sand ripples with ~10 cm wavelength and rounded crests stabilized by subsequent microbial growth. (**E**) Mature polygonal mats. (**F**) A green cyanobacteria and overlying tan EPS layer growing in filaments of a rounded and overturned mat intraclast (see Figure 2.18D, E). (**G**) Mature polygonal microbial mat overgrowing a rounded, overturned mat intraclast. The boundary between the intraclast and new growth is denoted by the upper arrow. The lower arrow shows the overturned cyanobacteria layer of the intraclast, which still exhibits tufts. (**H**) Another example of mature polygonal microbial mat overgrowing a rounded mat intraclast.

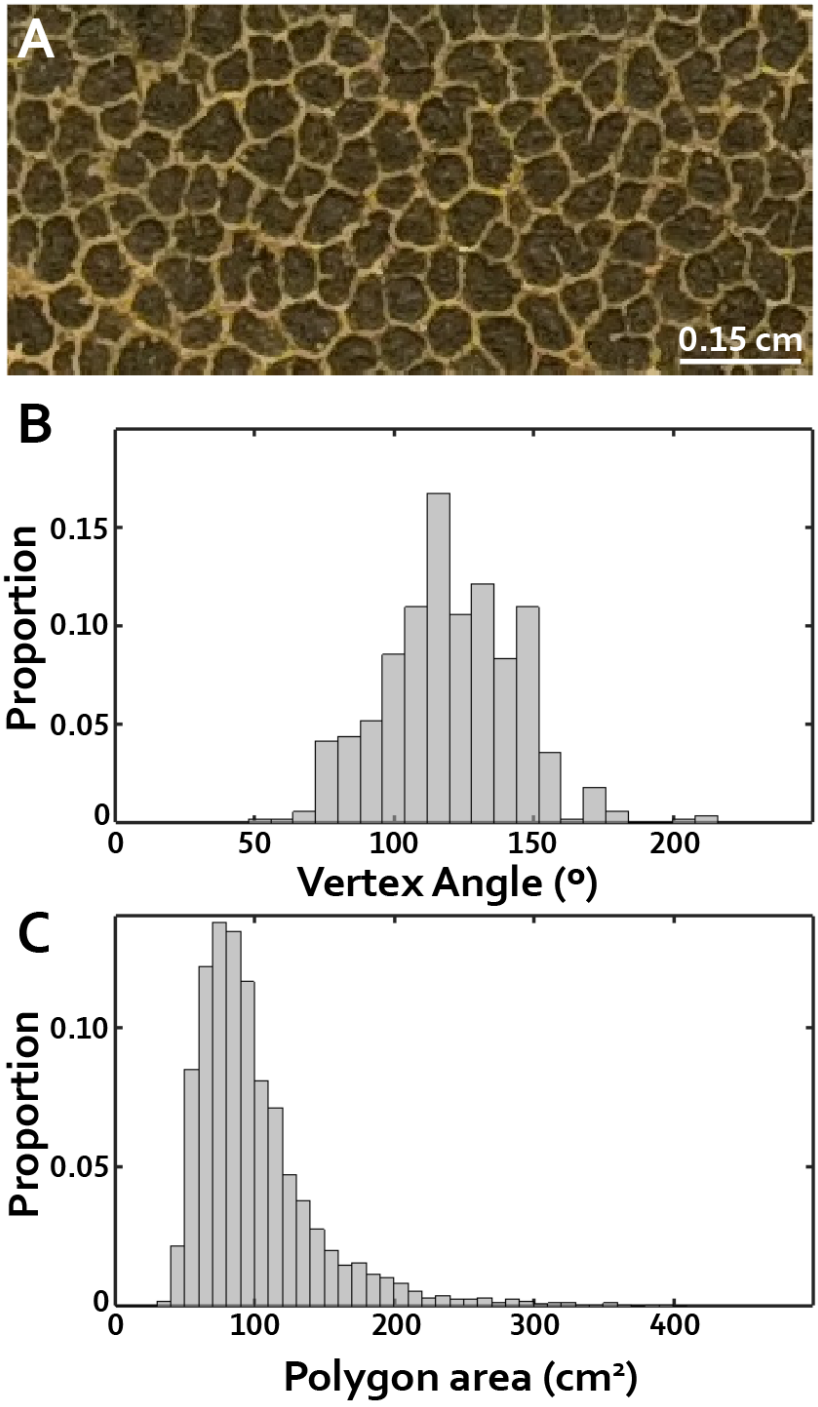

Figure 2.20. (**A**) Subset of UAV-based RGB image of polygonal mats on Little Ambergris Cay. (**B**) Vertex angles formed by >1500 junctions of the cracks that create polygons. (**C**) Distribution of the area of polygons.

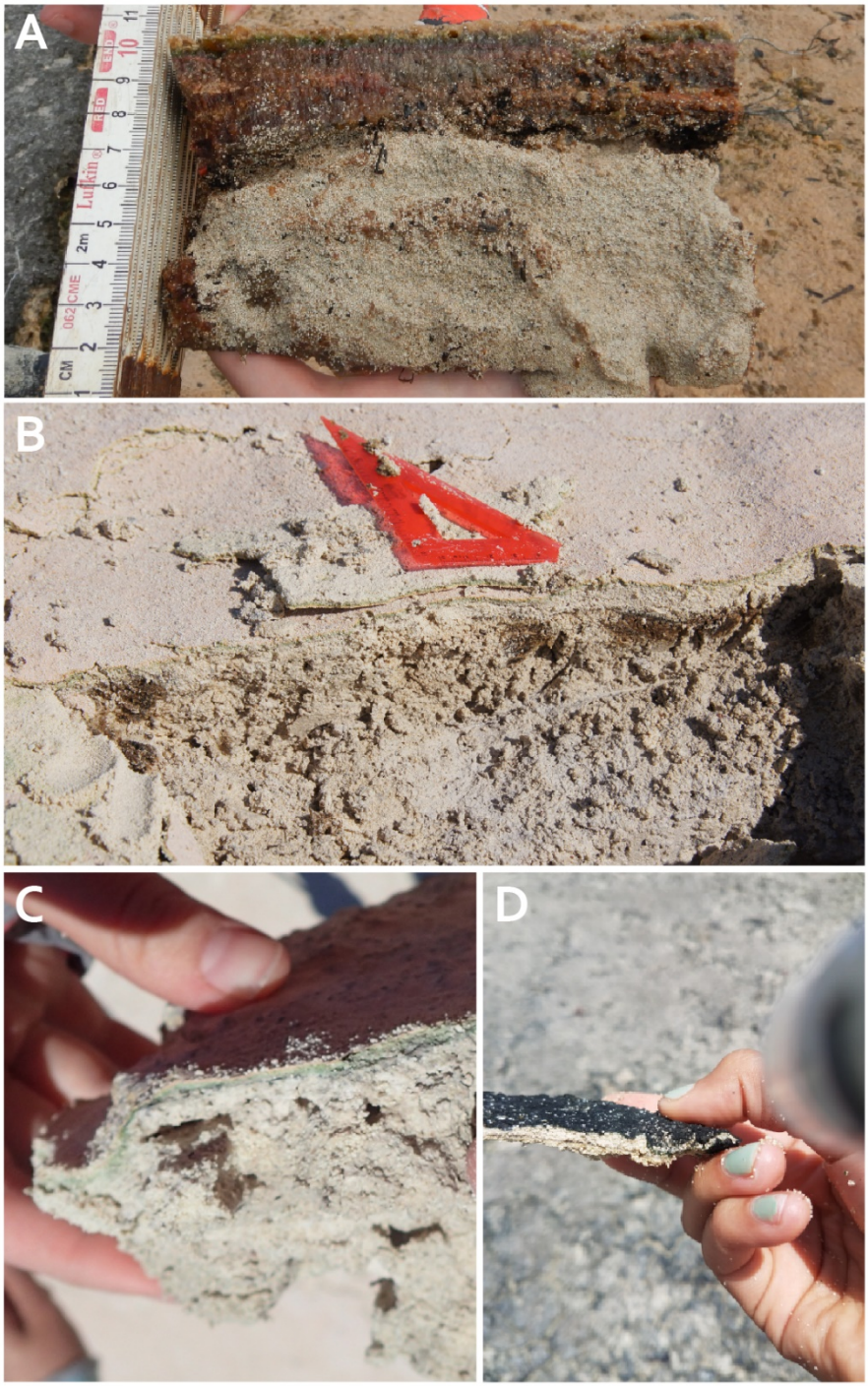

Figure 2.21. Microbial growth on substrate (Table 2.3A). (**A**) Stereotypical, well-developed smooth mat overlying ooids. (**B**) Incipient, sub-mm-thick pink-toned organic material and green-toned cyanobacteria overlying ooids in the island interior. (**C**) Close-up view of B. (**D**) Dark toned, sub-mm-thick cyanobacteria overlying ooids in the island interior.

Table 2.3. CATALOG OF MICROBIAL SIGNATURES IN CARBONATE SEDIMENTS OBSERVED ON LITTLE AMBERGRIS CAY

	Type of microbial signature	Resultant structure	Representative figure(s)
A.	**Microbial growth on substrate** **1.** Microbial mat **2.** Incipient growth	**1.** Flat, laminar, EPS-covered microbial mat overtopping ooids **2.** Cohesive ooids with pigmented organic-rich layers	**1.** 2.18A **2.** 2.18B, C, D
B.	**Trapping and binding** **1.** Sedimentation	**1.** Mat layer-bound irregular carbonate grains	**1.** 2.21C
C.	**Mechanical stress acting on biostabilized surfaces** **1.** Erosion/scouring **2.** Gas pressure **3.** Crystallization pressure **4.** Desiccation	**1A.** Erosional pockets of sand or hardground **1B.** Mat roll-up structures **1C.** Angular mat intraclasts **1D.** Rounded, inverted mat intraclasts **1E.** Mat chips **2.** Domes and folds/wrinkle structures **3.** Evaporite deposits **4.** Desiccation cracks	**1A.** 2.19A, B **1B.** 2.19J **1C.** 2.19C **1D.** 2.19D, E **1E.** 2.19F **2.** 2.19G, H, I **3.** 2.19J **4.** 2.19J
D.	**Biological response to physical disturbances** **1.** Sedimentation **2.** Desiccation **3.** Influx of mat chips or intraclasts	**1A.** Mat layer-bound irregular carbonate grains **1B.** Laminated leveling structures **1C.** Mat-stabilized ripples **2A.** Tufted, domed polygonal microbial mat with EPS-filled cracks **2B.** Growth protruding outward over cracks **3.** New growth in or on deposited mat chips or intraclasts	**1A.** 2.21C **1B.** 2.21A, B **1C.** 2.21D **2A.** 2.21E **2B.** 2.21E **3.** 2.19F; 2.21F, G, H
E.	**Post-burial processes and preservation** **1.** Organic matter decomposition	**1.** Faintly laminated pigmented grains	**1.** 2.22B
F.	**Grazing**	**1.** Cerithid gastropod shells	**1.** 2.14C

2.5.4 Recovery of Microbial Mats Following Sediment Blanketing Storms

Although mat surface texture is dominated by long-term response to subaerial exposure, stochastic storm events modify biostabilized surfaces and influence the spatial distribution of microbial mats, making them a significant control on microbial fabrics. Powerful storms are not uncommon in the Turks and Caicos; on average Little Ambergris experiences hurricane-force winds every 5.5 years (Landsea and Franklin, 2013). These storms produce significant hydrodynamic forces that modify biostabilized surfaces (section

2.4.4) and spread sediment throughout the interior basin, both as a thin veneer of ooid sand (transported in suspension in the storm surge) that coats the entire interior basin and as thicker, locally emplaced layers of sediment such as washover fans (Jamison-Todd et al., 2020; Wanless et al., 1987). The significance of these events is that the distribution, thickness, and duration of deposited sediment critically influences the recovery of microbial mats. Mats can be smothered by a critically thick layer of sediment. Below this critical thickness filamentous Cyanobacteria can migrate upward between ooid grains and spread laterally, trapping the underlying grains in place (Grotzinger and Knoll, 1999). Above this critical thickness, the underlying mats are smothered and subsequent mat growth may require renucleation (e.g. Figure 2.21B, C). The predominant textural evidence of biological responses to sedimentation includes trapped and bound carbonate grains, laminated leveling structures, and mat-stabilized ripples.

Mat-layer bound grains arise when organisms respond to the influx of sediment by migrating upward toward the new surface and spreading laterally, stabilizing the thin layers of sediment below and leaving behind alternating stacks of sediment and microbial sheathes that represent former mat surfaces (e.g. Figure 2.19C). Rapid recolonization over thin storm layers was also observed by Wanless et al., 1987. The recolonization process repeats during subsequent sedimentation events, leaving sediment and sheath couplets with biomass layers of variable thickness depending on the duration of the quiescent period. Hurricane Irma, which directly impacted Little Ambergris Cay as a Category 5 Hurricane in 2017, deposited a ~1-2 cm-thick layer of ooids and carbonate grains over much of the interior with localized deposits >50 cm thick. Tidal currents removed this layer from most of the interior basin by March 2018 except in mangrove-dominated areas with higher tidal friction. Cross sections of the polygonal mats from these areas reveal at least four mm-thick lags of irregular carbonate grains separated by varying thicknesses of remnant biomass (Figure 2.19C). The uppermost grain layer, deposited during Hurricane Irma, had been overgrown by a mm-thick layer of new cyanobacterial tufts by July 2019.

When sediment instead fills and levels depressions between polygonal microbial mats, subsequent microbial growth results in a level mat surface (Figure 2.19A) expressed in cross section as laterally distinct sets of laminated mat fabric and disaggregated sand (Figure 2.19B). Sand ripples deposited in the lower supratidal zone at the end of storm events that are low enough to remain wet from groundwater capillary rise are sometimes colonized at the surface and stabilized by cyanobacteria (Figure 2.19D). Once stabilized, the ripples can withstand moderate hydrodynamic forces during storms and high tides. Organisms may preferentially colonize the lower ripple troughs, and subsequent preferential erosion of the ripple crests produces flat-topped ripples. Erosion of mat-stabilized ripples produces ubiquitous mat chips deposited down-current of the ripples.

2.5.5 Subsurface Geology, Post-burial Processes, and Preservation

The depth to lithified bedrock, which we infer to be Pleistocene in age, ranges within the interior basin from >250 cm to less than 20 cm below the surface with a median of 70 cm (Figure 2.12). Three representative cores collected at sites with each mat facies are shown in Figure 2.22 (see Present et al., 2020 for remaining cores). Beneath the most recent layer of microbial mat, the subjacent deposit was composed of sparsely fossiliferous ooid sands, mostly unlithified, except for sparse, small concretions. The ooid sands show textural evidence of dissolution (Present et al., 2020). Skeletal grains include high-spired gastropods, cerithid gastropods, coralline algae, bivalves, and *Halimeda*, primarily indicative of an upper shoreface or high-energy shoal assemblage (Present et al., 2020). The presence of angular crust intraclasts and cerithid gastropods indicates that most core deposition occurred in a restricted, evaporative environment (Present et al., 2020). Only scant traces of formed intercalated microbial mats were preserved; one core (VC-05, Figure 2.22E) that was buried under several cm of sediment during Hurricanes Irma (2017) and Ike (2008) contains a faintly laminated, ~1 cm-thick pigmented horizon 60 cm below the surface (Figure 2.22B). The VNIR spectrum of the organic material contains characteristic absorption features at ~680 nm and between 775 nm and 900 nm consistent with chlorophyll *a* and bacteriochlorophyll *a*, respectively (Hubas et al., 2011).

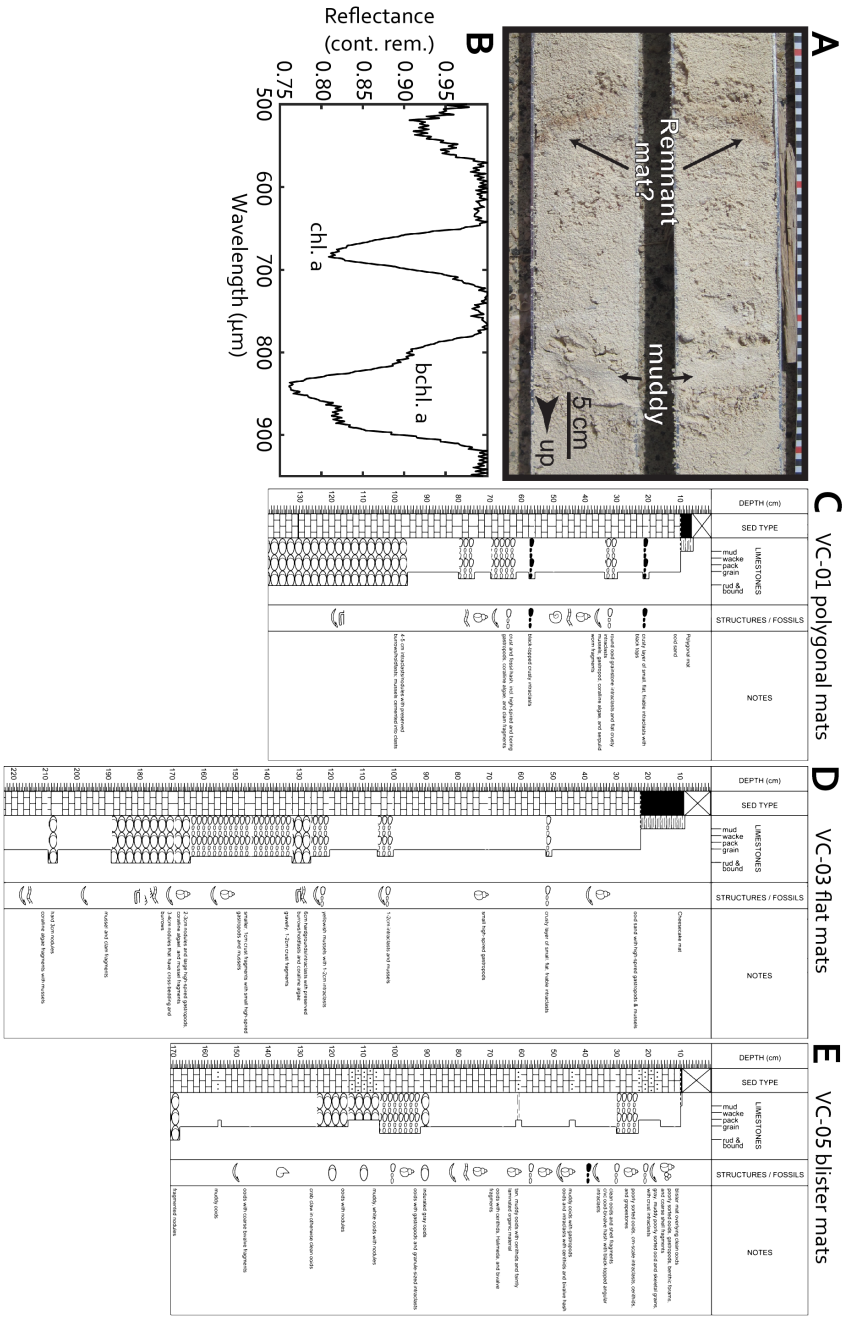

Figure 2.22. (**A**) Cross-section of the only core with potential preservation of faintly laminated microbial mat material down core, ~60 cm below the surface (VC-05C). (**B**) Continuum removed reflectance spectrum of the putative preserved organic material in (A) showing characteristic absorption features of chlorophyll *a* and bacteriochloropyll *a*. (**C**) VC-01 sediment core of area covered by polygonal mats with no preserved mat material below the surface. (**D**) VC-03 sediment core of area covered by smooth mats with no preserved mat material below the surface. (**E**) VC-05 sediment core of area covered by blister mats with putative preserved mat material ~60 cm below the surface. Core locations are shown in Figure 2.

2.6 Discussion

2.6.1 History of Microbial Mats on Little Ambergris

The growth of microbial mats in the high-energy platform environment surrounding Little Ambergris Cay was enabled through accretion of a bedrock rim that created a sheltered interior basin. Accretion was (and still is) driven by persistent easterly trade winds, which control Holocene patterns of carbonate sedimentation across Caicos Platform (Dravis and Wanless, 2017). Shallow subtidal ooid shoals on the Caicos Platform, including the Ambergris Shoal, are oriented parallel to the easterly trade winds (Rankey et al., 2008; Dravis and Wanless, 2017; Trower et al., 2008). Consistent wind-wave agitation maintains the motion of grains that feed Ambergris Shoal. Wave fronts impinge Big Ambergris Cay, a >25 m tall Pleistocene island 2 km east of Little Ambergris Cay, approximately parallel to its eastern shoreline and are refracted, creating two wave sets that converge approximately orthogonal to the northern and southern shorelines of Little Ambergris Cay, and then nearly obliquely to each other on the main shoal (Figure 2.23A) (Wanless and Dravis, 2008; Trower et al., 2017).

Strata that comprise the Little Ambergris rim are interpreted to have formed in an upper shoreface to foreshore depositional setting (Orzechowski et al., 2016). Shoreface accretion of oolitic sand likely initiated in the lee of Big Ambergris thanks to consistent delivery of sediment by converging wave fronts, akin to tombolo or salient formation (Figure 2.23A, B). Continuous bedrock accretion began recently; ^{14}C ages of *Strombus* shells collected from the most seaward exposures of the bedrock rim range from 480 ± 20 to 1220 ± 20 years before present (Table 2.2). Samples were not collected from more inland or eastern portions of the bedrock rim, which may be older. Indeed, ^{14}C ages of cerithid gastropods from sediment cores collected in the interior basin range from 850 ± 20 to 2525 ± 20 years before present (Table 2.2). The presence of gastropods down core, which graze on mats, indicates that at portions of the interior basin have been restricted for at least ~2000 years. These ages do not account for the marine reservoir effect, and thus may be several hundred years younger than shown. Wave baffling in the lee of initial bedrock ridges may have

promoted rapid sedimentation and growth of southwest- and northwest- trending beach ridge complexes that extended the island westward across the platform, eventually partially enclosing an intertidal interior basin (Figure 2.23B-E). Dravis and Wanless (2017) proposed a similar interpretive scenario for the evolution of upper Pleistocene and Holocene oolitic ridges of West Caicos, which likely formed due to ooid sand refraction around and subsequent longshore transport behind preexisting Pleistocene ridges. Another possible scenario is that Little Ambergris formed from the maturation of a double tombolo/salient (e.g. Owens, 1984) that enclosed a restricted region. Sedimentation in the lee of impermeable manmade breakwaters is commonly focused within distances shorter than their length (e.g. Mangor et al., 2017), as is the case with Little and Big Ambergris. ^{14}C ages of bedrock on the western tip of Little Ambergris are as recent as 505 ± 20 (8/8 LI-1B shell) and 480 ± 20 (8/5 BB-1A shell) years before present (Table 2.2), supporting the notion that Little Ambergris has quickly extended westward. Outward progradation of the oolitic beach ridges and eventually dunes extended the bedrock rim to the north and south orthogonal to the direction of wave convergence (Figure 2.23D-F). This progradational process may be been supported by one or more Holocene sea-level stands. The close overlap between faunal richness of the bedrock and modern beach unsurprisingly suggests analogous environmental settings between the two. Additionally, progradation is rapid and ongoing; comparison of recent drone orthomosaics with British aerial survey photos from February 1961 shows 10s of m of seaward progradation on the south side of the island over the last 60 years (Figure 2.23).

The sensitivity of mats to elevation could indicate that they are a recent phenomenon on Little Ambergris arising only after sediment infill raised the elevation of the interior. However, ample evidence of cerithid gastropods, angular crust intraclasts, and mangrove debris unique to an interior basin suggest that microbial mats may have been present in a restricted environment for hundreds or thousands of years (Present et al., 2020). This interpretation faces some challenges. First, little organic material is preserved in cored sediment. Rapid decay of buried mats was also evident months after Hurricane Irma (e.g. Figure 2.21B). Present et al. (2020) propose that the microbial mats are not preserved because

dissolution of carbonate sand driven by aerobic respiration and sulfide oxidation inhibits lithification. In this scenario, ironically, rapid respiration driven by highly productive microbial ecosystems may decrease their preservation potential. Second, although mats exist within a limited elevation range (~-0.2 to 0.3 m MWL), the depth to Pleistocene basement exceeds 2 m across much of the interior (Figures 2.12, 2.22). For mats to have persisted in a restricted environment, sediment accumulation would have to be balanced by denudation from some combination of eustasy, subsidence, dissolution, compaction, and sediment transport. Holocene sea-level change is well documented in the Caribbean (Fleming et al., 1998; Toscano and Macintyre, 2003; Milne et al., 2005). Toscano and Macintyre (2003) infer an average sea level rise of 0.93 mm/yr for 2000 years before present, which would yield a ~2-2.5 m sea level increase since the oldest sediment core ^{14}C ages. Khan et al. (2017) arrive at a similar sea level increase of 1.4 ± 0.5 m in the Bahamas over the last 2000 years. Hence, mats could have grown over a long period in a restricted intertidal environment well below the modern absolute elevation of the interior basin. Other processes could have acted to lower the surface elevation of the basin. Modest thermal subsidence of 0.1 mm/yr (Maloof and Grotzinger, 2012) would have lowered the basin by 0.2 m over the same period. Additionally, carbonate grain dissolution observed in the sediment cores (Present et al., 2020), compaction, and eolian and tidal current sediment transport could plausibly cumulatively offset sedimentation to permit persistent, unpreserved mat growth for potentially thousands of years.

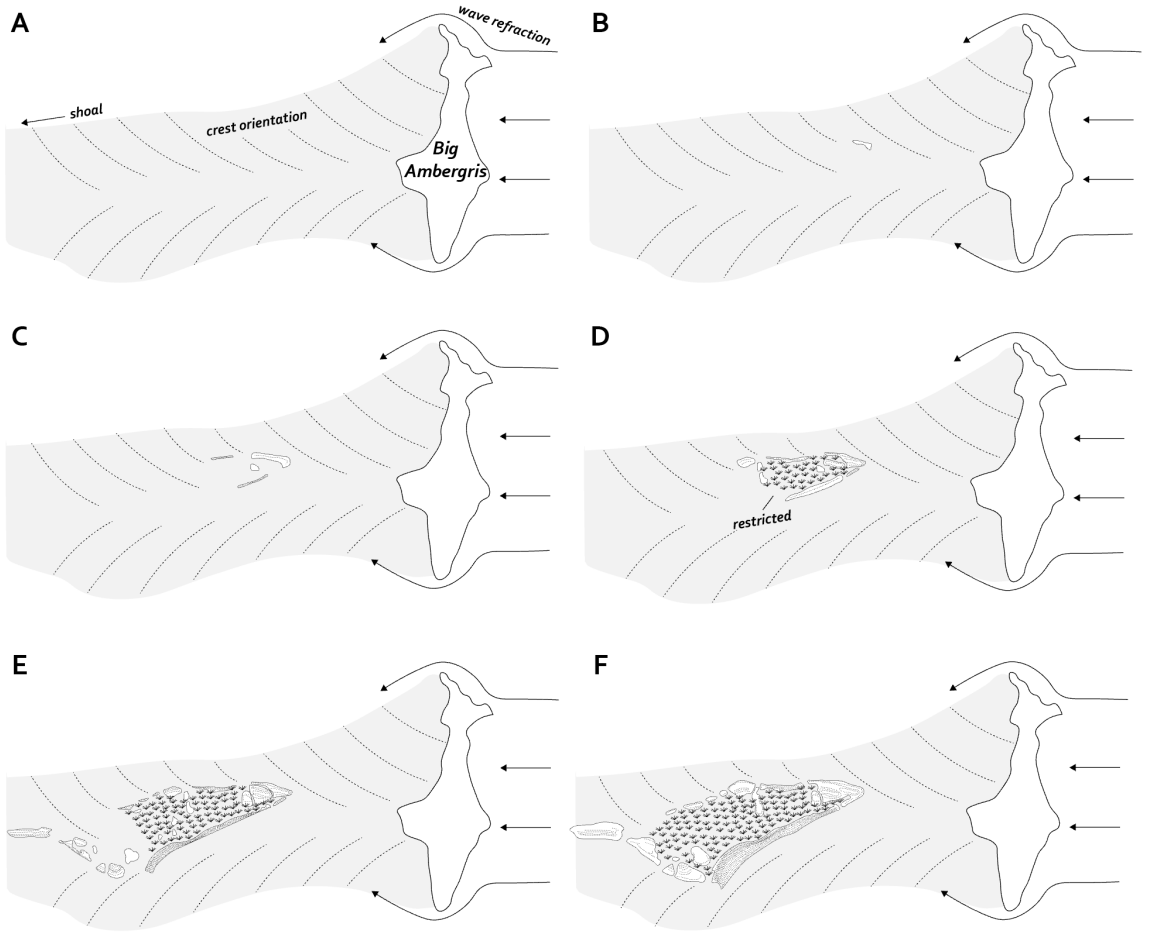

Figure 2.23. Interpretive scenario for the initiation and evolution of Little Ambergris Cay. (**A**) Waves driven by consistent easterlies refract around Big Ambergris and converge in the lee. (**B**) Sediment accumulates in the lee of Big Ambergris, initiating shoreface accretion of oolitic sand. (**C**) Wave baffling in the lee of initial bedrock ridges promotes further sedimentation to the west. (**D**) Oolitic beach ridges and dunes prograde outward orthogonal to the direction of wave convergence, partially enclosing a restricted region. (**E**, **F**) Progradation and westward growth continue until the island reaches its present form.

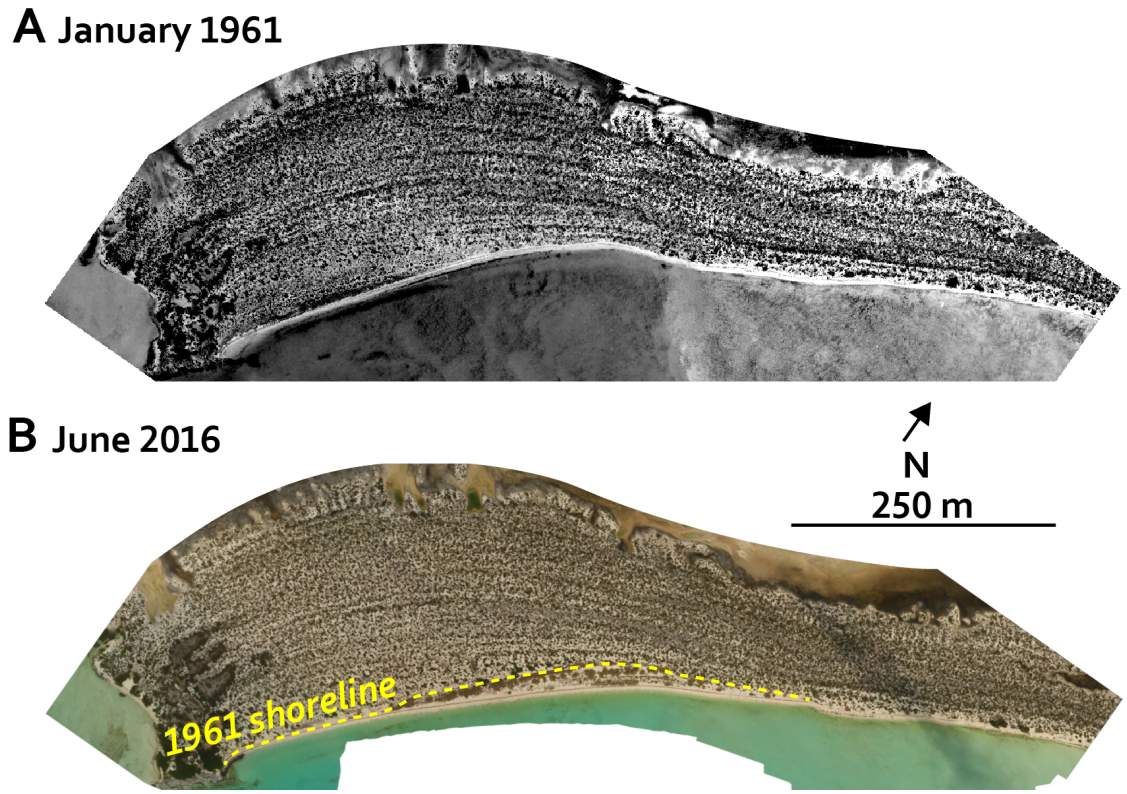

Figure 2.24. (**A**) British aerial survey photo of bedrock on the south side of Little Ambergris taken in February 1961. (**B**) The same location imaged by UAV in June 2016 with a trace of the shoreline from A.

2.6.2 Controls on Microbial Mat Extent and Texture

Multiple observations indicate that hydrodynamic forces and subaerial exposure are the primary factors that determine the texture and distribution of microbial mats on Little Ambergris Cay: 1) the three mat morphotypes have distinctive elevation ranges that correspond to different water depths and daily exposure time and 2) multiple surface textures consistent with desiccation or organic decomposition are observed in conjunction with increasing exposure time.

Based on survey elevation data, smooth mats are found only in the subtidal and lower intertidal zones and experience limited subaerial exposure. Few smooth mats are found below -0.2 m MWL (~0.55 m below mean high tide), likely because relatively high hydrodynamic forces prohibit attachment to the underlying substrate and/or rip up extant

mats. As a result, much of the western interior basin is floored by extensive ooid hardgrounds. Polygonal mats are more desiccated, located on average 14 cm higher than smooth mats and inhabiting portions of the lower and upper intertidal zones, especially in mangrove-dominated areas. Despite their modestly higher elevation, polygonal mats are exposed subaerially for an average of 10 hours each day ranging up to 23 hours, compared to the average of no exposure for smooth mats. Such a drastic change, which is responsible for the formation of domed polygons, is a direct consequence of the delicate sensitivity of exposure time to water depth; daily exposure time differs by as much as 15 hours over elevation differences of less than 5 cm (Figure 2.11). Blister mats are more desiccated still, exposed for 22 to 24 hours per day and sitting up to 30 cm above MWL where they exhibit surface textures resulting directly from desiccation (cracks, convex-up margins, evaporites) and organic decomposition (gas domes and folds). Reflectance spectra show that the smooth mats exhibit generally deeper Chl. *a* and Bchl. *a*, *d*, and *e* absorption features than the more exposed mats, consistent with higher productivity. Reexamination of the microbial community composition of the mat morphotypes shows surprising uniformity (Lingappa et al., 2020). While subtle differences due to the relative abundances of rare taxa – most notably within the Cyanobacteria – distinguish the microbial communities between mat morphotypes, their dominant taxa remain consistent (Lingappa et al., 2020). Hence, the wide diversity and textures and sedimentary structures observed in mats on Little Ambergris is primarily attributable not to microbial community composition or ecological succession, but rather desiccation resulting from elevation differences of less than ~50 cm.

Exposure time alone cannot account for the full range of microbial structures observed on the island; powerful storms play a critical role in the mechanical weathering and distribution of mats and in delivering sediment to the interior basin. In parts of the basin, thick (often recurring) storm deposits completely smother underlying mats, which are unable to migrate upward and rapidly decay. Elsewhere, thinner sediment deposits either quickly dissipate or are traversed and recolonized by underlying motile microorganisms, leading to the trapping of mat layer-bound irregular carbonate grains. Mechanical weathering during the strongest storms rips up broad tracts – up to hundreds of m^2 per event – of mats in the

open interior basin and redeposits them as mat intraclasts. In cross-section, the most spectacular mats display mat intraclasts from previous storms overgrown by multiple cm of cyanobacterial sheaths and several couplets of carbonate grain storm lags and biomass.

2.7 Synthesis and Conclusions

Environments with broad tracts of thick (>10 cm) luxuriant mats are relatively rare globally, and seemingly more widespread in peritidal lagoons (e.g. anchialine pools, Des Marais et al., 1992; Gavish et al., 1985) than in tidal flats subject to periodic hydrodynamic forces (Gerdes and Krumbein, 1994). Little Ambergris is a rare example of luxuriant microbial mats growing in a high-energy intertidal setting. Mats in the restricted interior basin are protected from persistent converging wave fronts driven by strong easterly winds. The same energetic setting was responsible for the development of the restricted environment at least *ca* 2000 years before present as converging wave fronts deposited sediment in the lee of the adjacent Big Ambergris Cay in a tombolo-like process. The precise events by which the restricted basin developed are unclear; perhaps outward progradation began nearly contemporaneously from many points, or perhaps the elongated northern and southern shorelines developed akin to a double tombolo that quickly enclosed an interior region. Regardless, rapid cementation likely played a crucial role in stabilizing the bedrock rim against storm overprinting and permitting further accretion. Early cementation, and thus the development of a similar restricted setting conducive to the development of luxuriant microbial mats, may be less likely in high-energy siliciclastic environments. In addition to the bedrock rim, some mats in the interior are further shielded by mangroves. The most luxuriant mats grow among mangrove roots, which protect the mats during powerful hurricanes that rip up broad tracts of less developed mats from the interior. Indeed, carbonate grain lags from multiple storms are observed in mats throughout the mangroves, indicating that they have survived multiple hurricanes (including the eye wall of Category 5 Hurricane Irma).

Although ubiquitous, it is possible that none of the microbial mats or diverse microbial textures on Little Ambergris will enter the rock record (Present et al., 2020). So

what lessons are there to learn for interpreting ancient microbialites? Perhaps most importantly, Little Ambergris indicates that there may be scant evidence of microbial processes preserved from similar ancient environments. While examples of high-energy settings with extensive, luxuriant microbial mats are rare in modern and perhaps Phanerozoic time, such environments may have been common in Precambrian time when ancient intercratonic seas and tropical carbonate platforms were likely frequently subjected to easterly paleotrade winds (Dravis and Wanless, 2017). Hence, the geomorphic setting that permits mat development on Little Ambergris may be applicable to the reconstruction of ancient paleoenvironments that contained widespread, productive, structurally diverse, and now unpreserved microbial mats.

2.8 Acknowledgments

We thank the Agouron Institute for funding. Thanks to the Turks and Caicos Islands Department of Environment and Coastal Resources for permitting this research. We thank the Tarika family, P. Mahoney, J. Seymour, and J. Grancich for logistical support. Thanks to J. Dickson for analytical support. J. Alleon, A. Bahniuk, A. Hayden, C. Howard, H. Grotzinger, S. Jamison-Todd, T. Mahseredjian, K. Metcalfe, D. Morris, I. Overeem, C. Sanders, E. Sibert, J. Strauss, M. Tarika, S. O'Reilly, L.A. Riedman, and M. Thorpe assisted fieldwork.

References

Allwood, A.C., Grotzinger, J.P., Knoll, A.H., Burch, I.W., Anderson, M.S., Coleman, M.L., et al. (2009). Controls on development and diversity of Early Archean stromatolites. *PNAS*. 106. 9548-9555. https://doi.org/10.1073/pnas.0903323106.

Bontognali, T.R.R., Sessions, A.L., Allwood, A.C., Fischer, W.W., Grotzinger, J.P., Summons, R.E., et al. (2012). Sulfur isotopes of organic matter preserved in 3.45-billion-year-old stromatolites reveal microbial metabolism, *PNAS*, 109, 15146-15151. https://doi.org/10.1073/pnas.1207491109.

Demicco, R.V. & Hardie, L.A. (1994). Sedimentary structures and early diagenetic features of shallow marine carbonate deposits, *Atlas 1: SEPM*, 265 p.

Des Marais, D.J., D'Amilio, E., Farmer, J.D., Jørgensen, B.B., Palmisano, A.C., & Pierson, B.K. (1992). Case study of a modern microbial mat-building community: The submerged mats of Guerrero Negro, Baja California. In: Schopf J., Klein, C. (eds) The Proterozoic biosphere. Cambridge University Press.

Dravis, J.J. & Wanless, H.R. (2008). Caicos platform models of Quaternary carbonate deposition controlled by stronger easterly trade winds – applications to petroleum exploration, *SEPM*, 22. https://doi.org/10.2110/pec.08.22.

Dravis, J.J. & Wanless, H.R. (2017). Impact of strong easterly trade winds on carbonate petroleum exploration – relationships developed from Caicos Platform, southeastern Bahamas. *Marine and Petroleum Geology*, 85, 272-300. https://doi.org/10.1016/j.marpetgeo.2017.04.010.

Dupraz, C. & Visscher, P.T. (2005). Microbial lithification in marine stromatolites and hypersaline mats. *Trends in Microbiology*, 13, 429-438. https://doi.org/10.1016/j.tim.2005.07.008.

Dupraz, C., Reid, R.P., Braissant, O., Decho, A.W., Normal, R.S., & Visscher, P.T. (2009). Processes of carbonate precipitation in modern microbial mats. *Earth Science Reviews*, 96, 141-162. https://doi.org/10.1016/j.earscirev.2008.10.005.

Fleming, E.D. & Castenholz, R.W. (2007). Effects of periodic desiccation on the synthesis of the UV-screening compound, scytonemin, in cyanobacteria. *Environmental Microbiology*, 9, 1448-1455. https://doi.org/10.1111/j.1462-2920.2007.01261.x.

Fleming, K., Johnston, P., Zwartz, D, Yokoyama, Y., Lambeck, K., & Chappell, J. (1998). Refining the eustatic sea-level curve since the last glacial maximum using far- and intermediate- field sites. *EPSL*, 163, 327-342. https://doi.org/10.1016/S0012-821X(98)00198-8.

Gebelein, C.D. (1969). Distribution, morphology and accretion rate of recent subtidal algal stromatolites, Bermuda. *J. Sediment. Petrol.*, 39, 49-69. https://doi.org/10.1306/74D71BE0-2B21-11D7-8648000102C1865D.

Gehling, J.G. (1999). Microbial mats in terminal Proterozoic siliciclastics: Ediacaran death masks. *Palaios*, 14, 40-57. https://10.2307/3515360.

Gerdes, G. & Krumbein, W.E. (1994). Peritidal potential stromatolites – a synopsis. In: Bertrand-Sarfati J., Monte C. (eds) Phanerozoic Stromatolites II. Springer, Dordrecht.

Gerdes, G., Klenke, T., & Noffke, N. (2000). Microbial signatures in peritidal siliciclastic sediments: a catalogue. *Sedimentology*, 47, 279-308.

Ginsburg, R.N. & Hardie, L.A. (1975). Tidal and storm deposits, northwestern Andros Island, Bahamas. In: Ginsburg R.N. (eds) Tidal Deposits. Springer, Berlin, Heidelberg. https://doi.org/10.1007/978-3-642-88494-8_23.

Ginsburg, R.N., Hardie, L.A., Bricker, O.P., Garrett, P., & Wanless, H.R. (1977). Exposure index: a quantitative approach to defining position within the tidal zone. *Johns Hopkins Univ. Press*, Baltimore, MD., 22, 7-11.

Goehring, L., Conroy, R., Akhter, A., Clegg, W.J., & Routh, A.F. (2010). Evolution of mud-crack patterns during repeated drying cycles. *Soft Matter*, 6, 2562-2567. https://doi.org/10.1039/B922206E.

Golubic, S. (1991). Microbial mats of Abu Dhabi. Environmental evolution, effects of the origin and evolution of life on planet Earth. Cambridge, MIT press. 103-130.

Grotzinger, J.P. (1989). Facies and evolution of Precambrian carbonate depositional systems: Emergence of the modern platform archetype. In: *Controls on Carbonate Platforms and Basin Development* (Eds P.D. Crevello, J.L. Wilson, F. Sarg, and J.F. Read), *SEPM Spec. Publ.* 44.

Grotzinger, J.P. & Knoll, A.H. (1999). Stromatolites in Precambrian carbonates: evolutionary mileposts or environmental dipsticks? *Annual Review of Earth and Planetary Sciences*, 27, 313-358. https://doi.org/10.1146/annurev.earth.27.1.313.

Hagadorn, J.W. & Bottjer, D. (1997). Wrinkle structures: Microbially mediated sedimentary structures common in subtidal siliciclastic settings at the Proterozoic-Phanerozoic transition. *Geology*, 25, 1047-1050. https://doi.org/10.1130/0091-7613(1997)025<1047:WSMMSS>2.3.CO;2.

Hubas, C., Jesus, B., Passarelli, C., & Jeanthon, C. (2011). Tools providing new insight into coastal anoxygenic purple bacterial mats: review and perspectives. *Research in Microbiology*, 162, 858-868. http://10.1016/j.resmic.2011.03.010.

Jamison-Todd, S., Stein, N., Overeem, I., Khalid, A., & Trower, E.J. (2020). Hurricane deposits on carbonate platforms: A case study of Hurricane Irma deposits on Little Ambergris Cay, Turks and Caicos Islands. In revision.

Kendall, C.G.S.C. & Skipwith, P.A.D.E. (1968). Recent algal mats of a Persian Gulf Lagoon. *J. Sed. Petrol.*, 38, 1040-1058. https://doi.org/10.1306/74D71AF5-2B21-11D7-8648000102C1865D

Kerans, C., Zahm, C., Bachtel, S.L., Hearty, P., & Cheng, H. (2019). Anatomy of a late Quaternary carbonate island: Constraints on timing and magnitude of sea-level

fluctuations, West Caicos, Turks and Caicos Islands, BWI. *Quaternary Science Reviews*, 205, 193-223. https://10.1016/j.quascirev.2018.12.010.

Khan, N. S., Ashe, E., Horton, B.P., Dutton, A., Kopp, R.E., Brocard, G., Engelhart, S.E., Hill, D.F., Peltier, W.R., Vane, C.H., and Scatena, F.N. (2017). Drivers of Holocene sea-level change in the Caribbean, *Quaternary Science Reviews*, 155, 13-36. https://dx.doi.org/10.1016/j.quascirev.2016.08.032.

Knoll, A.H. (2015). Paleobiological perspectives on early microbial evolution. *Cold Spring Harb. Perspect. Biol.*, 7. https://10.1101/cshperspect.a018093.

Lingappa, U.F., Metcalfe, K.S., Stein, N.T., Grotzinger, J.P., Orphan, V.J., Knoll, A.H. et al. (2020). In prep.

Logan, B. (1961) Cryptozoon and associate stromatolizes from the recent, Shark Bay, Western Australia. *J. Geology*, 69, 517-533. https://doi.org/10.1086/626769.

Lokier, S.W., Andrade, L. L., Court, W. M., Dutton, K.E., Head, I.M., van der Land, C., et al. (2017). A new model for the formation of microbial polygons in a coastal sabkha setting. *The Depositional Record*, 3. https://doi.org/10.1002/dep2.33.

Landsea, C.W. & Franklin, J.L. (2013). Atlantic hurricane database uncertainty and presentation of a new database format. *Mon. Wea. Rev.*, 141, 3576-3592. https://doi.org/10.1175/MWR-D-12-00254.1

Maloof, A.C. & Grotzinger, J.P. (2012). The Holocene shallowing-upward parasequence of north-west Andros Island, Bahamas. *Sedimentology*, 59, 1375-1407. https://doi.org/10.1111/j.1365-3091.2011.01313.x.

Mangor, K., Drønen, N.K., & Kristensen, N.E. (2017). Shoreline management guidelines (4th ed.). Horsholm, Denmark: DHI Water & Environment.

Mariotti, G., Pruss, S., Perron, J., & Bosak, T. (2014). Microbial shaping of sedimentary wrinkle structures. *Nature Geoscience*, 7, 736-740. https://10.1038/NGEO2229.

Marshall, C.P., Leuko, S., Coyle, C.M., Walter, M.R., Burns, B.P., & Neilan, B.A. (2007). Carotenoid analysis of halophilic archaea by resonance Raman spectroscopy. *Astrobiology*, 7, 631-643. https://doi.org/10.1089/ast.2006.0097.

Martin, J.M., Braga, J.C., & Riding, R. (1993). Siliciclastic stromatolites and thrombolites, late Miocene, SE Spain. *Journal of Sedimentary Petrology*, 63, 131-139. https://doi.org/10.1306/D4267AAA-2B26-11D7-8648000102C1865D.

Mobberly, J., Khodadad, C.M., & Foster, J. (2013). Metabolic potential of lithifying cyanobacteria-dominated thrombolytic mats. *Photosynthesis Research*, 118, 125-140. https://doi.org/10.1007/s11120-013-9890-6.

Milne, G.A., Long, A.J., & Bassett, S.E. (2005). Modelling Holocene relative sea-level observations from the Caribbean and South America. *Quaternary Science Reviews*, 24, 1183-1202. https://doi.org/10.1016/j.quascirev.2004.10.005.

Neu, T.R. & Lawrence, J.R. (2010). Extracellular polymeric substances in microbial biofilms, Microbial Glycobiology. Elsevier, Burlington, MA, 735-758.

Neumann, A.C., Gebelein, C.D., & Scoffin, T.P. (1970). The composition, structure, and erodibility of subtidal mats, Abaco, Bahamas, *J. Sediment. Petrol.*, 40, 274-297. https://doi.org/10.1306/74D71F2D-2B21-11D7-8648000102C1865D.

Noffke, N., Gerdes, G., Klenke, T., & Krumbein, W.E. (2001). Microbially induced sedimentary structures indicating climatological, hydrological, and depositional conditions within recent and Pleistocene coastal facies zones (Southern Tunisia), *Facies*. 44, 23-30. https://doi.org/10.1007/02668164.

Noffke, N., Eriksson, K.A., Hazen, R.M., & Simpson, E.L. (2006). A new window into Early Archean life: Microbial mats in Earth's oldest siliciclastic tidal deposits (3.2 Ga Moodies Group, South Africa). *Geology*, 24, 253-256. https://doi.org/10.1130/G22246.1.

Noffke, N. (2010) Geobiology: Microbial mats in sandy deposits from the Archean era to today. Berlin Heidelberg, Springer-Verlag. 166 p.

Noffke, N., Christian, D., Wacey, D., & Hazen, R.M. (2013). Microbially induced sedimentary structures recording and ancient ecosystem in the ca. 3.48 billion-year-old Dresser Formation, Pilbara, Western Australia. *Astrobiology*, 13, 1103-1124. https://doi.org/10.1089/ast.2013.1030.

Orzechowski, E., Strauss, J., Knoll, A., Fischer, W., Cantine, M., Metcalfe, K., et al. (2016). Age and construction of Little Ambergris Cay bedrock rim, southeastern Caicos Platform, British West Indies. *American Geophysical Union Fall Meeting.*

Owens, E.H. (1982). Tombolo. In: Beaches and coastal geology. Encyclopedia of earth science. Springer, Boston, MA. https://doi.org/10.1007/0-387-30843-1.

Pflüger, F. & Gresse, P.G. (1996). Microbial sand chips – a non-actualistic sedimentary structure. *Sedimentary Geology*, 102, 263-274. https://doi.org/10.1016/0037-0738(95)00072-0.

Present, T.M., Grotzinger, J.P., Gomes, M.L., Trower, E.J., Stein, N.T., Lingappa, U.F. et al. (2020). Non-lithifying microbial ecosystem, Little Ambergris Cay, Turks and Caicos Islands. In prep.

Rankey, E., Reeder, S., & Correa, T. (2008). Geomorphology and sedimentology of Ambergris ooid shoal, Caicos Platform: Developing models and analogs for isolated carbonate platforms. *Proceedings Holocene and Pleistocene Carbonates of Caicos Platform, British West Indies, SEPM, Core Workshop*, 22, 127-132. https://doi.org/10.2110/pec.08.22.0127.

Reid, R.P., Macintyre, I.G., Browne, K.M., Steneck, R.S., & Miller, T. (1995). Modern marine stromatolites in the Exuma Cays, Bahamas: Uncommonly common, *Facies*, 33, 1-17. https://doi.org/10.1007/BF02537442.

Reid, R.P., Visscher, P.T., Decho, A.W., Stolz, J.F., Bebout, B.M., Dupraz, C., et al. (2000). The role of microbes in accretion, lamination and early lithification of modern marine stromatolites, *Nature*, 406, 989-992. https://doi.org/10.1038/35023158.

Sarkar, S., Choudhuri, A., Mandal, S., & Eriksson, P.G. (2016). Microbial mat-related structures shared by both siliciclastic and carbonate formations. *Journal of Palaeogeography*, 5, 278-291. https://doi.org/10.1016/j.iop.2016.05.001.

Schieber, J., Bose, P.K., Eriksson, P.G., Banerjee, S., Sarkar, S., Altermann, W., et al. (2007). Atlases in Geoscience. Elsevier. 307p.

Schopf, J.W. (2006). Fossil evidence of Archaean life. *Philos. Trans. R. Soc. Long. B. Biol. Sci.*, 361, 869-885. https://10.1098/rstb.2006.1834.

Shepard, R.N. & Sumner, D.Y. (2010). Undirected motility of filamentous cyanobacteria produces reticulate mats. *Geobiology*, 8, 179-190. https://doi.org/10.1111/j.1472-4669.2010.00235.x.

Shorlin, K.A., de Bruyn, J.R., Graham, M., & Morris, S.W. (2000). Development and geometry of isotropic and directional shrinkage-crack patterns. *Physical Review E: Statistical Physics, Plasmas, Fluids, and Related Interdisciplinary Topics*, 61, 6950-6957, https://doi.org/10.1103/PhysRevE.61.6950.

Stuiver, M. and Polach, H. A. (1977). Discussion reporting of ^{14}C data. *American Journal of Science*, 19, 355-363. https://doi.org/10.1017/S0033822200003672.

Toscano, M.A. & Macintyre, I.G. (2003). Corrected western Atlantic sea-level curve for the last 11,000 years based on calibrated 14C dates from *Acropora palmata* framework and intertidal mangrove peat. *Coral Reefs*, 22, 257-270. https://doi.org/10.1007.s00338-003-0315-4.

Trembath-Reichert, E., Ward, L.M., Slotznick, S.P., Bachtel, S.L., Kerans, C., Grotzinger, J.P., et al. (2016). Gene sequencing-based analysis of microbial-mat morphotypes, Caicos Platform, British West Indies. *Journal of Sedimentary Research*, 86, 629-636. https://doi.org/10.2110/jsr.2016.40.

Trower, E.J., Cantine, M.D., Gomes, M.L., Grotinzger, J.P., Knoll, A.H., Lamb, et al. (2018). Active ooid growth driven by sediment transport in a high-energy shoal, Little Ambergris Cay, Turks and Caicos Islands. *Journal of Sedimentary Research*, 88, 1132-1151. https://doi.org/10.2110/jsr.2018.59.

Visscher, P.T., Reid, R.P., Bebout, B.M., Hoeft, S.E., Macintyre, I.G., & Thompson, J.A. (1998). Formation of lithified micritic laminae in modern marine stromatolites (Bahamas): the role of sulfur cycling. *American Mineralogist*, 83, 1482-1493. https://doi.org/10.2138/am-1998-11-1236.

Walter, M.R., Goode, A.D.T., & Hall, W.D.M. (1976). Microfossils from a newly discovered Precambrian stromatolitic iron formation in Western Australia. *Nature*, 261, 221-223. https://doi.org/10.1038/261221a0.

Wanless, H.R., Tyrrell, J.M., Tedesco, L.P., & Dravis, J.J. (1988). Tidal-flat sedimentation from Hurricane Kate, Caicos Platform, British West Indies. *Journal of Sedimentary Petrology*, 58, 724-738. https://doi.org/10.1306/212F8E2C-2B24-11D7-8648000102C1865D**.**

Wanless, H.R., Dravis, J.J., Tedesco, L.P., & Rossinsky Jr., V. (1989). Carbonate environments and sequences of Caicos platform: Caicos, British West Indies to Miami, Florida. *AGU Field Trip Guidebook*, 374. https://doi.org/10.1029/FT374.

Wingender, J., Neu, T. R., and Flemming, H. C. (1999). Microbial Extracellular Polymeric Substances. Berlin, Heidelberg: Springer-Verlag.

Chapter 3

REGIONAL STRUCTURAL ORIENTATION OF THE MT. SHARP GROUP REVEALED BY IN-SITU DIP MEASUREMENTS AND STRATIGRAPHIC CORRELATIONS ON THE VERA RUBIN RIDGE

N. Stein[1], D. P. Quinn[2], J. P. Grotzinger[1], C. Fedo[3], B. L. Ehlmann[1,4], K. M. Stack[4], L. A. Edgar[5], A. A. Fraeman[4], R, Deen[4]

[1]Division of Geological and Planetary Sciences, California Institute of Technology, 1200 E California Blvd., Pasadena, CA 91125

[2]Department of Geoscience, University of Wisconsin Madison, Madison, WI, 53706

[3]Department of Earth and Planetary Sciences, University of Tennessee, Knoxville, TN 37996

[4]Jet Propulsion Laboratory, California Institute of Technology, 4800 Oak Grove Drive, Pasadena, CA 91104

[5]United States Geological Survey Astrogeology Science Center, Flagstaff, AZ, 86001

This chapter was published as:

Stein, N.T. et al. (2020), Regional structural orientation of the Mount Sharp group revealed by in situ dip measurements and stratigraphic correlations on the Vera Rubin Ridge. *JGR: Planets*, 123. https://doi.org/10.1029/2019/JE006298.

3.1 Abstract

Ground-based bedding orientation measurements are critical to determine the geologic history and processes of sedimentation in Gale crater, Mars. We constrain the dip of lacustrine strata of the Blunts Point, Pettegrove Point, and Jura members of the Murray formation using a combination of regional stratigraphic correlations and bed attitude measurements from stereo Mastcam images taken by the Mars Science Laboratory Curiosity rover. In situ bed attitude measurements using a PCA-based regression method reveal a wide range of dips and dip azimuths owing to a combination of high stereo errors, post-depositional deformation of strata (e.g. fracturing, rotation, impact cratering), and different primary depositional dips. These constrain regional dips to be within several degrees of horizontal on average. Stratigraphic correlations between targets observed in the Glen Torridon trough and at the Pettegrove Point – Jura member contact of Vera Rubin ridge (VRR) constrain dips to be between three degrees southeast and two degrees northwest, consistent with nearly flat strata deposited horizontally on an equipotential surface. The Jura member is determined to be stratigraphically equivalent to the northern portion of the Glen Torridon trough. Rover-based dip magnitudes are generally significantly shallower than the orientation of VRR member contacts measured from HiRISE-based traces, suggesting the sedimentary strata and VRR member contacts may be discordant.

3.2 Introduction

The orientation of sedimentary strata records information about their processes of deposition and subsequent deformation and is one of the most fundamental measurements of structural geology. In Gale crater, Mars, stereo images collected by the Mars Science Laboratory (MSL) Curiosity rover permit quantification of bedding attitudes of outcrops exposed along the rover's traverse. These measurements are useful for establishing sediment transport directions recorded by cross bedding, revealing patterns of deformation, and creating the basis for regional stratigraphic correlation. Collectively, ground-based bedding orientation measurements are critical to determine the history and processes of sedimentation and deformation in Gale crater.

On Earth, bedding orientation measurements are frequently made in situ using a geological compass. On Mars, attitudes must be measured using remotely sensed data consisting of at least one image and a corresponding digital elevation model (DEM). Numerous studies have pursued bedding orientations, particularly dips, using orbital mapping of layered rocks on Mars (e.g., DiBiase et al., 2013; Fraeman et al., 2013; Fueten et al., 2005; Goudge et al., 2017; Hynek & Phillips, 2008; Kite et al., 2013, 2016; Le Deit et al., 2013; Lewis & Aharonson, 2006, 2014; Lewis, Aharonson, Grotzinger, Kirk, et al., 2008; Metz et al., 2010; Milliken et al., 2010; Okubo, 2010; Okubo et al., 2008; Quinn & Ehlmann, 2019a, 2019b; Stack et al., 2013). Orbiter-based dip measurements are constrained by resolution to layered deposits that often extend for hundreds to thousands of meters, whereas bedding orientation estimates or measurements at the centimeter to meter scale are possible using rover-based stereo images (e.g., Arvidson et al., 2011; Barnes et al., 2018; Banham et al., 2018; Hayes et al., 2011; Lewis, Aharonson, Grozinger, Squyres, et al., 2008; Lewis & Turner, 2019; Lewis et al., 2020; Squyres et al., 2004; Turner & Lewis, 2019; Watters et al., 2011).

Prior to Curiosity's arrival at Vera Rubin ridge (VRR), structural orientation measurements of inferred fluviolacustrine strata along the traverse were restricted primarily to visual assessments of dip directions (i.e., azimuths) (e.g., Grotzinger et al., 2015) due to the limited extent of outcrops. Most quantified rover image-based structural orientation measurements reported to date have been made in the Stimson formation (Banham et al., 2018) and more recently in the Murray formation in VRR and Glen Torridon (Lewis & Turner, 2019; Turner & Lewis, 2019). The resistant strata that comprise VRR (defined in section 2.3), first encountered on Sol 1809, are the first beds within the Murray formation with sufficient exposure to measure numerous attitudes from stereo Mastcam images over a wide region. These strata were also investigated earlier from orbit (Fraeman et al., 2013), making them the first to be independently assessed in situ following orbiter-based predictions. The relationship between VRR and adjacent units was unclear from orbital data (Fraeman et al., 2016; Stack et al., 2017) prior to Curiosity's in situ investigation of the ridge. Hence, a major motivation for measuring the bedding

orientation of VRR strata is to place it in stratigraphic context with the rest of the Mount Sharp group.

Another key motivation for quantifying the bedding orientation of strata in the Mount Sharp group is to constrain hypotheses regarding the origin of Mount sharp and other large sedimentary mounds in Martian craters, a significant problem in sedimentary geology that is likely unique to Mars (Grotzinger & Milliken, 2012; Kite et al., 2016). As described in Kite et al. (2016), mechanisms for mound formation generally invoke either (1) flat-lying or shallowly dipping strata that eroded to their present morphology (Andrews-Hanna et al., 2010; Day & Kocurek, 2016; Kite et al., 2013; Malin & Edgett, 2000) or (2) deposition of sediment on preexisting topography that grew mounds in place (Kite et al., 2013, 2016). The latter scenario, also called anticompensational stacking, is supported by numerous orbiter-based layer orientation measurements from sedimentary mounds on Mars including in and above the sulfate-bearing unit in Gale crater that show downslope layer attitudes (Kite et al., 2016). Characterization of the dips of VRR strata may inform which of these hypotheses is supported by the lowermost strata that compose Mount Sharp.

Here we analyze the orientation of 487 beds exposed along VRR using stereo Mastcam images taken at 24 sites to investigate the overall structure of the strata that make up VRR (section 2.5), place VRR in stratigraphic context with the rest of the Mount Sharp group, and investigate the origins of the lower portions of Mount Sharp. We compare the results of stereo image-based attitude measurements with independent assessments of the larger-scale structural orientation of units by making stratigraphic correlations between VRR and the Glen Torridon region (section 2.5.1). Results are compared with orbiter-derived attitude measurements of VRR (section 2.6.2).

3.3 Geological Setting

During its approximately 7-year mission so far on the Martian surface, the Curiosity rover has ascended more than 400 m of the lower slopes of Aeolis Mons (informally known as Mount Sharp), a ~5-km-high mound of sedimentary rocks preserved in the center of

Gale crater. Along this traverse, strata consisting of fluvial, deltaic, lacustrine, and eolian sediments have been documented (Banham et al., 2018; Edgar et al., 2017; Fraeman et al., 2016; Grotzinger et al., 2014, 2015; Minitti et al., 2019; Stack et al., 2019; Rivera-Hernandez et al., 2019, 2020; Williams et al., 2013) (Figure 3.1). These strata form three stratigraphic groups: (1) the Bradbury group, which sits at the base of Mount Sharp; (2) the Mount Sharp group, which interfingers with and overlies the Bradbury group; and (3) the Siccar Point group, which unconformably overlies the Mount Sharp group (Banham et al., 2018; Fraeman et al., 2016). The rover traverse through the Mount Sharp group has kept Curiosity within the Murray formation, a package of predominantly lacustrine mudstone with uncommon intercalated cross-stratified sandstones of prodeltaic, fluvial, or eolian origin (Edgar et al., 2017; Fedo et al., 2018; Grotzinger et al., 2015; Gwizd et al., 2019; Hurowitz et al., 2017; Rivera-Hernandez et al., 2020; Siebach et al., 2019; Stack et al., 2019). The Murray formation, which is at least 300 m thick, has been divided into seven members, the (presently) uppermost three of which are measured in this study. These seven members include, in ascending order, the Pahrump Hills member, Hartmann's Valley member, Karasburg member, Sutton Island member, Blunts Point member, Pettegrove Point member, and Jura member (Figure 3.1). The Pahrump Hills member is dominated by thinly laminated mudstone interpreted to be deposited by hyperpycnal plumes in a freshwater lake (Grotzinger et al., 2015; Stack et al., 2019). The Hartmann's Valley member is characterized by decimeter- to meter-scale cross-stratified deposits indicative of eolian or fluvial reworking (Fedo et al., 2018; Gwizd et al., 2019). The Sutton Island member is a heterolithic mudstone-sandstone that largely consists of broken-up meter-scale blocks and contains textural evidence of periodic dry conditions in the form of desiccation cracks and sulfate enrichments (Rapin et al., 2019; Stein et al., 2018).

The strata measured in this study are limited to three members: the Blunt's Point member (BPm), the Pettegrove Point member (PPm), and the Jura member (Jm), due to their superior exposure relative to other members. The BPm consists of finely laminated mudstone interpreted to result from low-energy deposition of suspended mud in a lacustrine environment (Fedo et al., 2018; Bennett et al., this issue; Edgar et al., 2020;

Rivera-Hernandez et al., 2020). Strata of the PPm and Jm form VRR, a ~200-m-wide, ~6.5-km long erosion-resistant topographic rise on the northwest flank of Mount Sharp (Fraeman et al., 2013, 2016; 2020). Although VRR is topographically distinct from surrounding strata, the Jm, PPm, and BPm are all dominated by finely laminated mudstones and thus assigned to the Murray formation. While the BPm-PPm and PPm-Jm contacts occur with well-exposed outcrops and clear topographic expressions, they do not follow elevation contours (Edgar et al., 2020). The same is true for the SIm-BPm contact, which lies far below VRR. Present understanding of these contact trends is most consistent with postdepositional deformation (C. Fedo et al., personal communication, September 2019) or lateral facies variations (Edgar et al., 2020).

Additional regional geologic context is provided by considering the relationship between strata that comprise VRR and surrounding units. Since leaving VRR, Curiosity began to explore Glen Torridon, a region directly south of VRR characterized by detection of smectite clay minerals in data from the Compact Reconnaissance Imaging Spectrometer for Mars (Fox et al., 2019). The northern part of Glen Torridon, traversed by Curiosity through Sol 2439, is composed of laminated mudstones with uncommon cross-bedded sandstones shaped into smooth, northeast trending ridges (Bennett et al., 2019, 2020) interpreted as periodic bedrock ridges (Stack et al., 2019). At least a portion of northern Glen Torridon, which is topographically lower than parts of VRR, is likely stratigraphically equivalent to the Jm (this paper). Orbital data show the clay-bearing strata of Glen Torridon are overlain by hydrated sulfate-bearing strata that may represent a transition to drier environments in Gale crater (Grotzinger & Milliken, 2012; Grotzinger et al., 2015; Fraeman et al., 2016; Fox et al., 2019; Milliken et al., 2010), and these strata are referred to as the sulfate-bearing or fractured-intermediate unit in this paper.

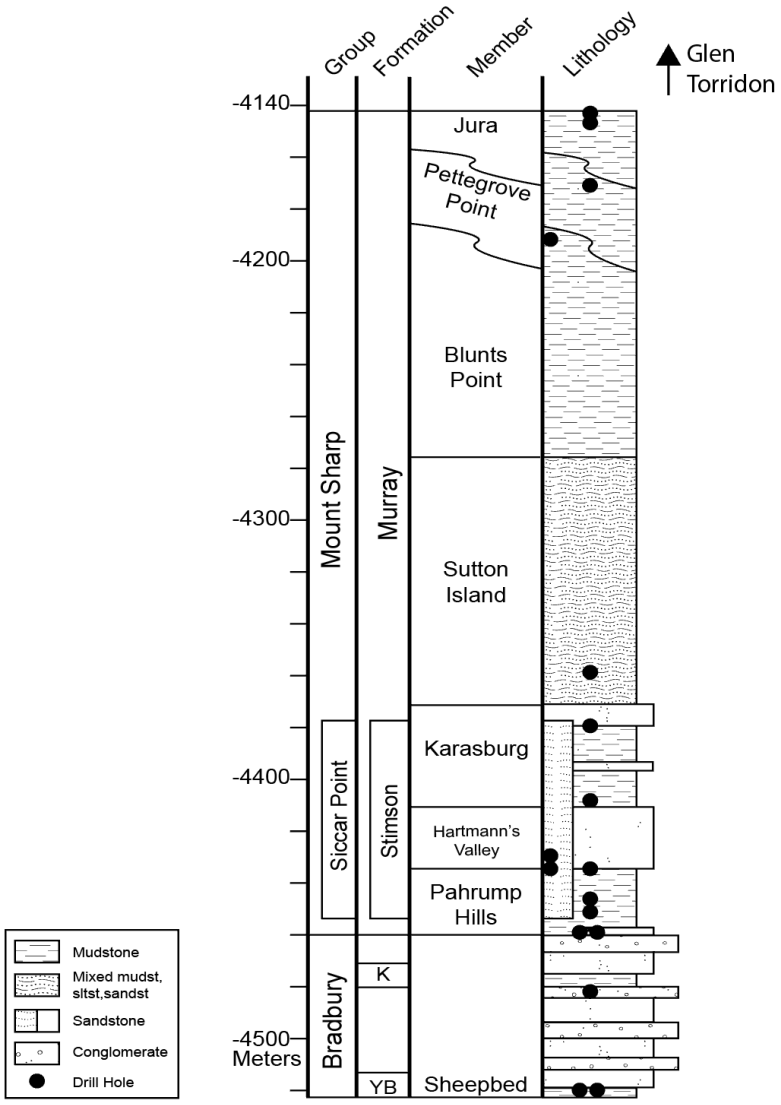

Figure 3.1. Stratigraphic column along Curiosity's traverse.

3.4 Methods

3.4.1 Plane Fitting using PCA

3.4.1.1 Point Extraction

The Curiosity rover collects stereo images from two sets of cameras: Navigation cameras (Navcams) and Mast Cameras (Mastcams). The Mastcams consist of two cameras with different focal lengths and a stereo baseline of ~24.5 cm (Bell et al., 2017; Malin et al.,

2017). The left Mastcam (ML) has a focal length of ~34 mm and collects images at up to 450 μm/pixel from 2 m, and the right Mastcam (MR) has a focal length of ~100 mm and collects images at up to 150 μm/pixel from 2 m (Bell et al., 2017; Malin et al., 2017). Each Navcam camera pair is separated by a 42.4 cm stereo baseline, thus offering ~2.15 times better stereo range error than Mastcams (Maki et al., 2012), but ~3.73 times lower spatial resolution. Mastcam and Navcam stereo images can be used to digitally trace bedding planes for orientation measurements. This study focuses on stereo Mastcam images because their color and higher angular resolution generally yields more accurate traces than Navcam images. Attitudes calculated from Mastcam-based traces were validated against Navcam-based traces in some instances. For each stereo Mastcam pair, coregistered rasters of (x,y,z) points and (x,y,z) errors were generated using JPL's Multimission Image Processing Lab (MIPL) stereo pipeline (Abarca et al., 2019; Alexander and Deen, 2018).

Bedding traces are digitized from RGB images, typically using higher resolution MR images, and the elevations and errors of their constituent points are generated from coregistered elevation models. The (x,y,z) points are defined in site frame, a Mars-fixed rover operations coordinate frame in which +x is defined as north, +y as east, and +z as gravity nadir (down). The result is an array of three-dimensional points that collectively represent a bedding plane and a second array that represents the stereo range error of each point along the trace projected into Cartesian space.

3.4.1.2 Finding the Nominal Plane

Previously, rover-based assessments of bedding orientations were performed visually (e.g. Arvidson et al., 2011; Grotzinger et al., 2015) or calculated via ordinary least-squares (OLS) regression (e.g. Lewis et al., 2008; Lewis and Turner, 2019) or principal-component analysis (PCA) regression (e.g. Hayes et al., 2011). OLS regression, in which planar geologic surfaces are modeled by fitting sets of coordinates to a best-fitting plane, is perhaps the most popular technique for quantifying attitudes in remotely sensed data. A drawback of OLS regression is that it effectively imparts all errors to a dependent variable, typically the vertical plane, which may be unreasonable if errors are not chiefly vertical (Quinn and Ehlmann,

2019b). Our study utilizes a PCA regression method developed by Quinn and Ehlmann (2019b) which simultaneously fits errors along all axes, making it especially relevant when errors are non-vertical, which is known to be the case for stereo Mastcam images in which primary errors are along the range axis (see section 3.4.1.1).

In this section, we detail fundamental aspects of the PCA model as it pertains to this work. More information about the model and its derivation can be found in Quinn and Ehlmann (2019b).

PCA converts observations of putatively correlated variables into sets of linearly uncorrelated variables, or principal components. PCA is commonly used for dimensionality reduction, e.g. for identifying or reducing the set of explanatory variables. When fitting the orientation of planes, however, PCA simply rotates orthonormal spatial coordinates (x,y,z) into a frame aligned with the planar fit ($\bar{x}_1, \bar{x}_2, \bar{x}_3$). Hence, the method does not entail any dimensionality reduction (Quinn and Ehlmann, 2019b).

The application of PCA for bedding-plane fits starts with a digitized bedding trace, which yields an $n \times 3$ data matrix **D** containing the three-axis coordinates of points along the trace in site frame (e.g. Figures 3.3, 3.7). The number of independent observations, n, that comprise the bedding trace typically ranges from several dozen to hundreds of points in Mastcam images. **D** is centered by subtracting the mean along each axis, $\boldsymbol{\mu_D}$, as

$$\mathbf{M} = \mathbf{D} - \boldsymbol{\mu_D}, \tag{3.1}$$

yielding the mean-corrected n x 3 data matrix **M**. Fundamentally, the PCA can be computed by performing an eigenvector decomposition of the sample covariance matrix. Quinn and Ehlmann (2019b) implement the PCA using singular value decomposition (SVD) to produce an orthonormal coordinate basis $\bar{\mathbf{x}}$, which is aligned with the directions of greatest variability within the data. $\bar{x}_1$ and $\bar{x}_2$ are within the best-fitting plane through the data, while $\bar{x}_3$ is normal to the plane, and scatter along $\bar{x}_3$ represents error in the plane fit. The equation of the nominal plane is

$$\mathbf{n}\,\mathbf{x} + \mathbf{x} \cdot \boldsymbol{\mu}_{\mathbf{D}} = 0, \tag{3.2}$$

where $\mathbf{n}$ is the normal vector of the nominal plane, defined as $\mathbf{n} = \boldsymbol{v_3}$ (the third eigenvector row of $\mathbf{V}$), and $\mathbf{x}$ is the set of points within the nominal plane. The strike and dip of the nominal plane are then calculated as

$$(\text{strike}, \text{dip}) = \left(\tan^{-1}\frac{n_1}{n_2} - \frac{\pi}{2}, \cos^{-1}\frac{n_3}{\|\mathbf{n}\|}\right). \tag{3.3}$$

This PCA framework immediately provides a means of assessing quality of fit. $\bar{x}_1$ and $\bar{x}_2$ define the extent of the plane to be fit. If $\bar{x}_2 << \bar{x}_1$, the fit is for a line rather than a plane, and such cases should be excluded. In contrast, planes with sufficient extent in $\bar{x}_1$ and $\bar{x}_2$ are well fit with errors lying in $\bar{x}_3$ (see also 3.4.1.4).

3.4.2 Error Quantification

3.4.2.1 Error Sources and Representation

To fully contextualize structural measurements considering often unpredictable errors and variable terrain, we adopt the PCA-based error approach of Quinn and Ehlmann (2019), which provides a method that simultaneously treats different error structures. A major advantage of PCA for plane fitting is that it accounts for errors along all axes simultaneously, which allows for fitting of planes that drape surfaces with varying error structures, including non-vertical errors (Quinn and Ehlmann, 2019b).

In performing geological orientation measurements with remotely sensed data, two predominant types of error arise: (1) measurement errors in bedding traces and (2) errors resulting from outcrop geometry or improper interpretation of bedding surfaces. Errors of the second type are discussed further in section 3.4.3. There are several sources of measurement errors, chiefly error in the construction of the photogrammetric DEM resulting from image misregistration, an especially difficult problem for Mastcam stereo images because the cameras have different focal lengths. Other major sources of measurement error

include resampling error, sampling error due to inexact digitization of measured features, and downslope bias.

In Cartesian space, orientation errors in regression of a best-fit plane can be represented by two hyperboloids that bound the set of all possible planes fitting the dataset, which vary around the nominal regression solution, or as a set of normal vectors perpendicular to each plane solution (Figure 3.2A). Regression errors can be readily mapped from Cartesian to spherical coordinates. In spherical coordinates, orientations are frequently represented as pairs of angles (e.g. strike and dip or dip and dip direction). Errors are sometimes also parameterized in terms of strike and dip (e.g. Lewis and Aharonson, 2006), although orientation errors are not necessarily aligned with strike and dip and may be especially inaccurate in the case of near-horizontal bedding (Quinn and Ehlmann, 2019b).

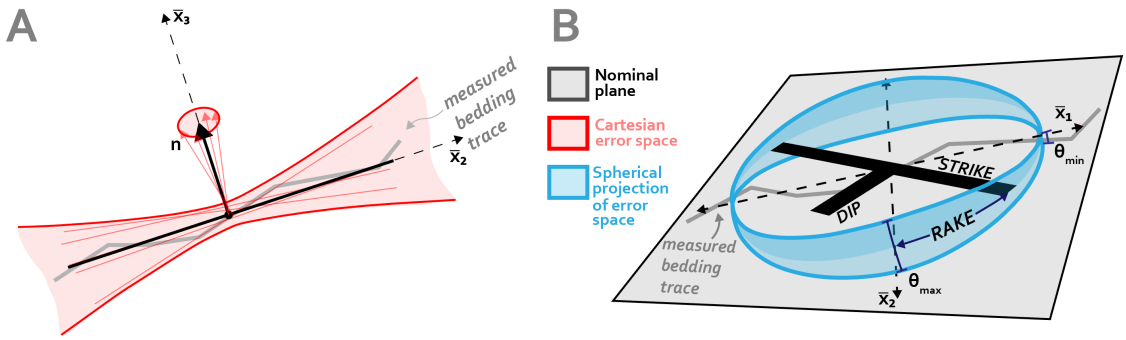

Figure 3.2. (**A**) Schematic representation of an $\bar{x}_2$-$\bar{x}_3$ slice of the nominal plane fit and errors in the Cartesian coordinate system. **n** is the normal vector of the nominal plane, which falls along $\bar{x}_3$. The shaded red region denotes the hyperbolic error space comprised of plane fits with different orientations. (**B**) Schematic representation of the error space to the plane (denoted by θ_{min} and θ_{max}) and rake angle in spherical coordinates. After figure from Quinn and Ehlmann (2019b).

After being mapped to spherical coordinates, the hyperbolic errors to the nominal plane defined in Cartesian coordinates define a spherical girdle of errors. In the convention of Quinn and Ehlmann (2019b), the span of this girdle is described by θ_{max}, the maximum angular error to the plane, and θ_{min}. θ_{max} is not necessarily parallel to the strike or dip. Instead, the orientation of θ_{max} with respect to the nominal plane solution is described by

the rake angle between θ_{max} and the strike of the nominal plane (Figure 3.2B). In this study, errors are reported using this spherical framework because it allows for their conceptually straightforward visualization.

3.4.2.2 Error Quantification and Representation

Regression errors are modeled using a "variance-limited" framework in which the orientation of the PCA regression is equivalent to the PCA eigenvalues, i.e. $\left[\frac{\lambda_3}{\lambda_1}\ \frac{\lambda_3}{\lambda_2}\right]$. In the variance-limited framework, the variance of the input dataset provides a lower bound on errors to the nominal plane; plane fits to data sets with high variance yield high errors regardless of data density (Quinn and Ehlmann, 2019b). Because the precision of the mean of the dataset is modeled by its variance, which is inversely proportional to n – 1, small angular errors might be reported in mean-limited cases for datasets with large sample sizes despite inherently high variance (Quinn and Ehlmann, 2019b). Hence, the adoption of a variance-limited framework allows comparison of planes with different sampling statistics and sanctions the adoption of a Monte Carlo approach for the incorporation of stereo Mastcam errors (section 3.4.2.3) without skewing error statistics.

3.4.2.3 Incorporation of Axially Asymmetric Stereo Errors

Errors for photogrammetric datasets typically depend on the viewing geometry of the input images; oblique (near parallel to terrain) images predominantly produce errors in the line of sight. For MSL, these errors are typically expressed in the x- and y-axes in site frame, which frequently have errors more than an order of magnitude higher than those along the gravity nadir (z) axis. In these cases, if the input data matrix **D** from eq. 3.1 contains only (x,y,z) coordinates from each bedding trace, the contribution of horizontal stereo errors would be systematically underestimated, which could lead to acceptance of solutions strongly biased by stereo errors along one axis. Instead, equation 3.1 is adjusted to ingest a modified input data matrix **D'**:

$$\mathbf{M} = \mathbf{D}' - \boldsymbol{\mu}_{\mathbf{D}}, \tag{3.4}$$

where

$$D' = \begin{bmatrix} x_1 + \delta_{1x} \sim N(0, x_{1e}) & y_1 + \delta_{1y} \sim N(0, y_{1e}) & z_1 + \delta_{1z} \sim N(0, z_{1e}) \\ \vdots & \vdots & \vdots \\ x_1 + \delta_{qx} \sim N(0, x_{1e}) & y_1 + \delta_{qx} \sim N(0, y_{1e}) & z_1 + \delta_{qx} \sim N(0, z_{1e}) \\ \vdots & \vdots & \vdots \\ x_n + \delta_{qx} \sim N(0, x_{ne}) & y_n + \delta_{qx} \sim N(0, y_{ne}) & z_n + \delta_{qx} \sim N(0, z_{ne}) \end{bmatrix}_{qn \times 3} \quad (3.5)$$

is a *qn* x 3 matrix containing (x,y,z) points perturbed by normally distributed samples $(\delta_{qx}, \delta_{qy}, \delta_{qz})$ of stereo errors (x_e,y_e,z_e) generated for each Mastcam image. *q* denotes the number of resampled points for each coordinate and *n*, as before, is the number of independent measurements that comprise a bedding trace. (x_e,y_e,z_e) is the estimated stereo error along each site frame axis, calculated by projecting the range error (error in the downrange and cross-range directions from the camera) along the axes (Deen et al., 2019). The range error e is calculated as

$$e = \frac{r^2 ic}{b}, \quad (3.6)$$

where r is the range from the camera, i is the instantaneous field of view, c is the correlation accuracy, and b is the stereo baseline. For each set of points (x_1,y_1,z_1) and their corresponding stereo errors (x_{1e},y_{1e},z_{1e}), *q* new sets of points are generated by adding the original coordinates to a sample of a normal distribution with a mean of 0 and a standard deviation sourced from (x_{1e},y_{1e},z_{1e}) (e.g. Figure 3.3). *q* must be sufficiently large for **D'** to plausibly contain the true (x,y,z) locations of each point in a bedding trace. *q* was set to 1,000 for this study, as increases beyond 1,000 showed no significant changes to the computed error. A major advantage of utilizing the variance-limited error framework is that the addition of resampled points to the input data matrix does not artificially reduce the maximum angular error, as would be the case in a mean-limited framework (Quinn and Ehlmann, 2019b), allowing stereo errors to be handled with a bootstrap Monte Carlo approach without adversely affecting the accuracy of reported errors.

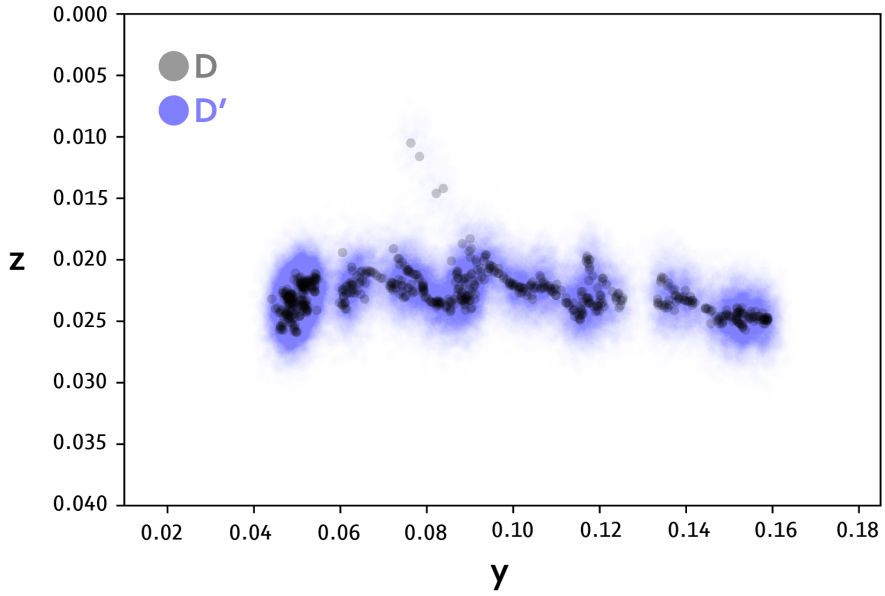

Figure 3.3. An example of all (x,y,z) points (**D**, in black) along a single bedding trace in the y-z plane and the set of points generated from stereo errors (**D'**, in blue). The blue points represent the dataset that is fed to the PCA model. The average magnitude of y errors in this scene is approximately four times that of the z errors.

The Monte Carlo approach to incorporating stereo errors also relies on assumptions about the underlying structure of Mastcam stereo errors, namely that they are represented by a normal distribution with a standard deviation of (x_e,y_e,z_e). In this study, we generate **D'** using different standard deviations and report results for each case: (1) an aggressive approach, and upper bound on error, where (x_e,y_e,z_e) represents one standard deviation of the normally distributed sample $(\delta_{qx}, \delta_{qy}, \delta_{qz})$; (2 and 3) less aggressive approaches where (x_e,y_e,z_e) represents three or five standard deviations of the normally distributed sample $(\delta_{qx}, \delta_{qy}, \delta_{qz})$.

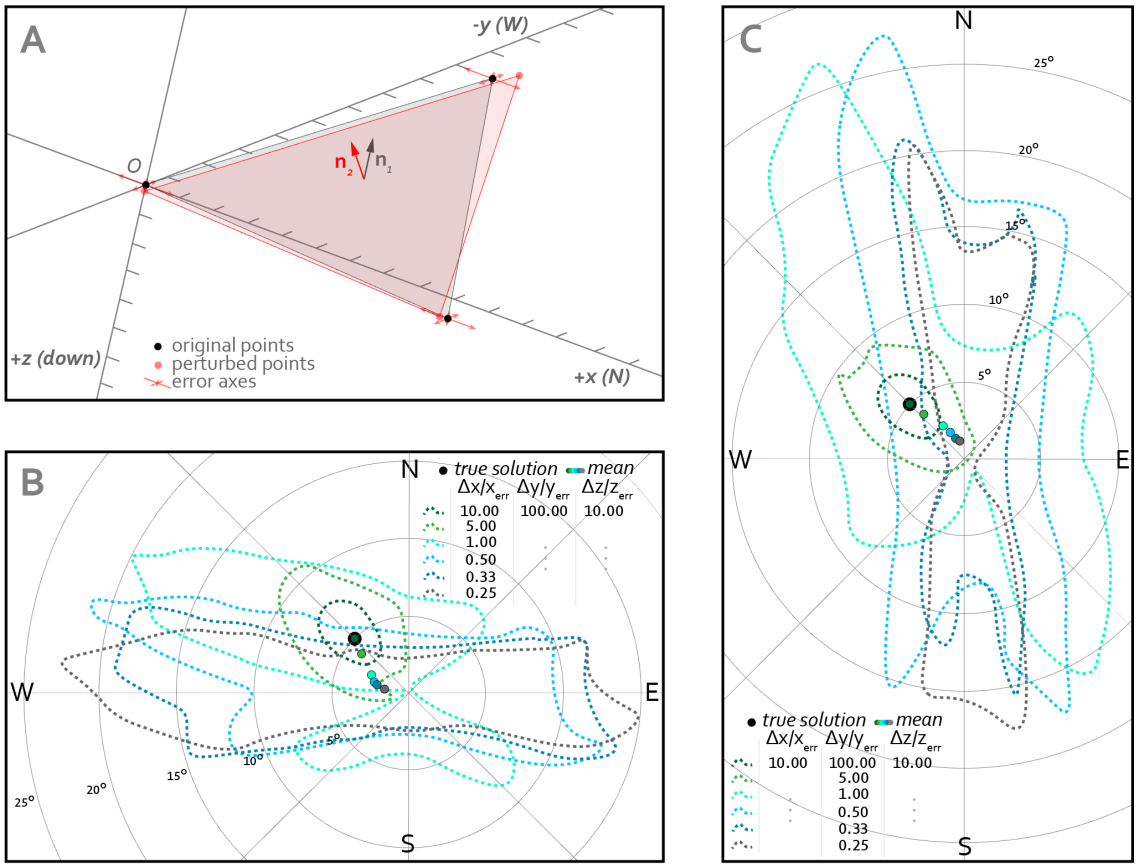

Figure 3.4. Example showing impact of stereo errors on solution uncertainty. (**A**) Schematic showing three points (black) in site frame that define a plane dipping 5° NW (the true solution in panels B and C), their axial errors (red arrows), and a set of perturbed points that defines a new solution. The axes are defined according to site frame. (**B**) Six different solution sets where the ratio of the extent of the bedding trace in the x-direction to x errors ($\Delta x/x_{err}$) changes and $\Delta y/y_{err}$ and $\Delta z/z_{err}$ are constant. Dots denote the average solution. Dashed lines denote the range of possible solutions. Solutions are generated using the PCA-based Monte Carlo bootstrapping approach of section 3 where x_{err}, y_{err}, and z_{err} represent 1σ of the error. (**C**) Six different solution sets where ($\Delta y/y_{err}$) changes and $\Delta x/x_{err}$ and $\Delta z/z_{err}$ are constant.

3.4.2.4 Impact of Stereo Errors on Plane Fits

Perhaps the greatest challenge of rover-based dip measurements is that the spatial extent of outcrop traces is generally low relative to their stereo errors. Even for exceptional outcrops, the ratio of trace extent to error along the first and second principal component axes may be one to two orders of magnitude lower than in traces performed using High Resolution

Imaging Science Experiment (HiRISE) images because beds visible in HiRISE images can frequently be traced for hundreds of meters. Hence, stereo errors may comprise a significant fraction of the variance along bedding traces. Any trace with a high ratio of error to trace extent (δ_d/d) along a given axis is subject to two effects: (1) the solution space of the plane fit will trend toward an axis orthogonal to the direction with the greatest error and within the plane as (δ_d/d) increases; (2) the average dip of the solution space of the plane fit will decrease as (δ_d/d) increases. These effects are demonstrated in Figure 3.4, where a set of three points defining a plane dipping 5° toward 315° (NW) is perturbed by ever-increasing errors along the x- (Fig. 3.4B) and y- (Fig. 3.4C) axes using the approach of section 3.4.2.3 and the corresponding solution space is shown for each case. Similar effects can be seen in Mastcam-derived attitudes for small or distant traces (see section 3.5.1.1).

3.4.2.5 Joint Fitting of Parallel Bedding Planes

Even on VRR, which has some of the largest continuous outcrop exposures in the Murray formation, the lack of continuous exposures and/or bedding planes exposed in multiple dimensions is a common problem. As a result, many individual bed traces in Mastcam stereo images barely exceed stereo errors along one or more trace axes. However, in many scenes, closely spatially associated beds cut topography in different directions, yielding traces with varying coverage and orientation error structures. Hence, although the three-dimensional definition of all individual bedding traces within a scene may yield poor fits, the traces in aggregate may contain enough spatial definition for a high-quality planar fit. Under the assumption that bedding is parallel, based on visual observation of the measured beds, multiple traces are combined and fit jointly. The input data matrix **D'** for each bedding trace is centered on its mean and stacked with other mean-centered matrices to form a combined matrix that contains orientation information for each bedding trace independent of their relative locations. This combined data matrix is regressed using the same PCA technique (Quinn and Ehlmann, 2019b). Results of jointly fit bedding planes are shown for each scene in this study in addition to individual plane fits.

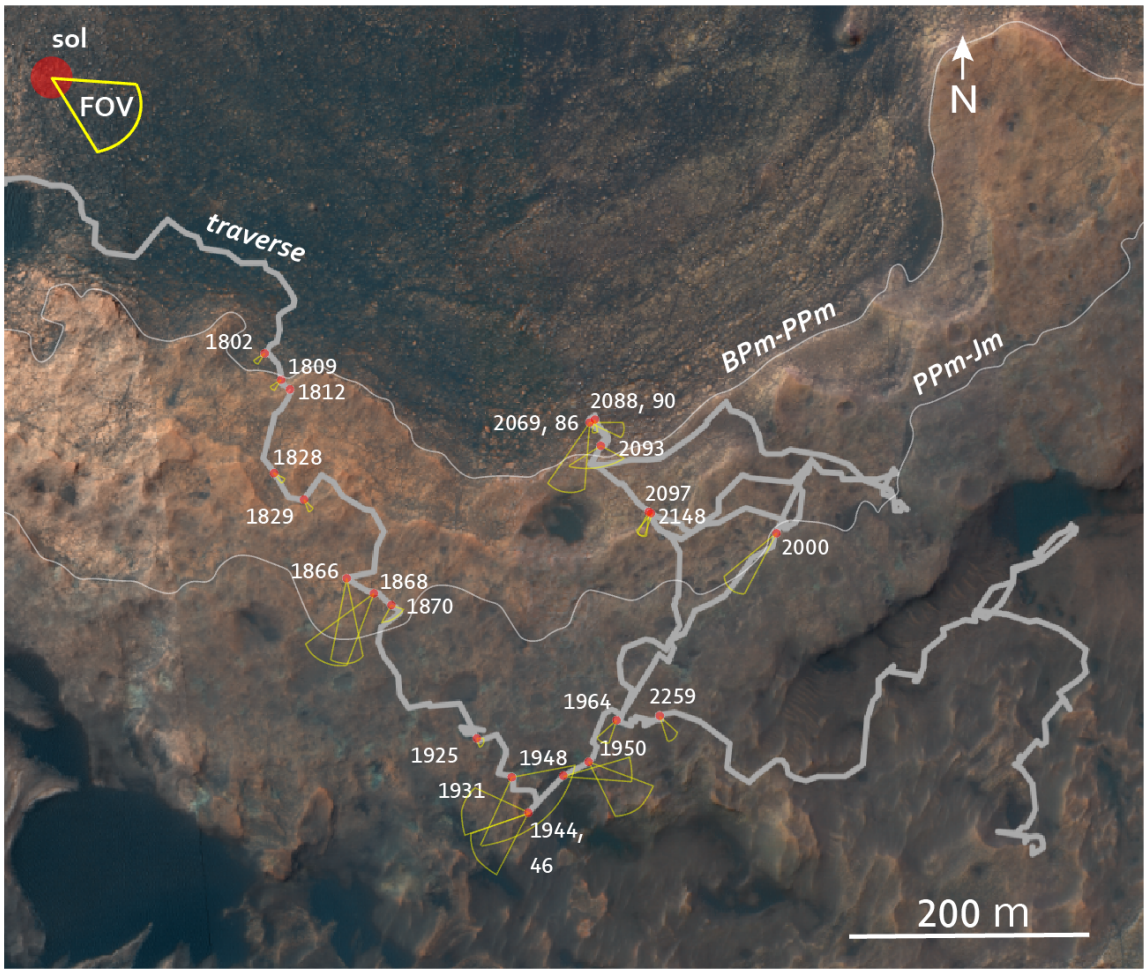

Figure 3.5. HiRISE overview showing sites with stereo Mastcams used in this study, labeled by sol. Yellow arcs denote the approximate field of view (FOV) of each image pair. The Blunts Point member – Pettegrove Point member (BPm – PPm) and Pettegrove Point member – Jura member (PPm – Jm) contacts are traced in white. The rover traverse is shown in gray.

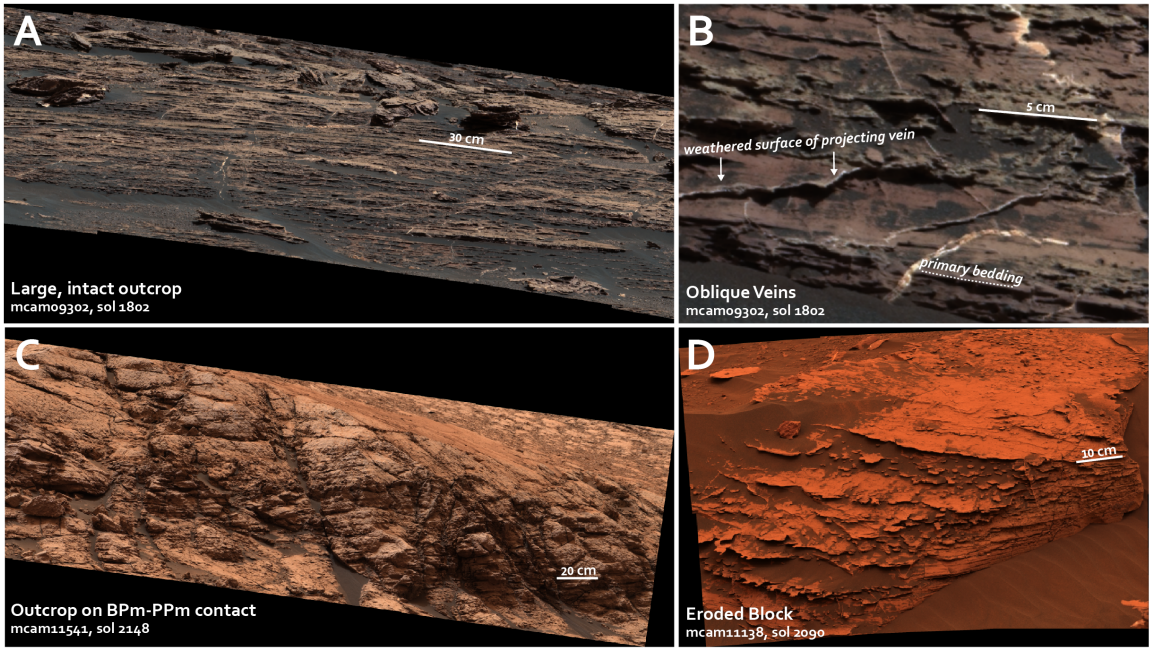

Figure 3.6. Examples of common outcrop geometries with traceable bedding on VRR. (**A**) A large, intact outcrop encountered on sol 1802. (**B**) A portion of the same image showing low-angle weathered surfaces oblique to primary lamination. (**C**) A large, intact outcrop on the BPm – PPm contact imaged on sol 2148. (**D**) A large, possibly rotated block with fine, parallel lamination imaged on sol 2090.

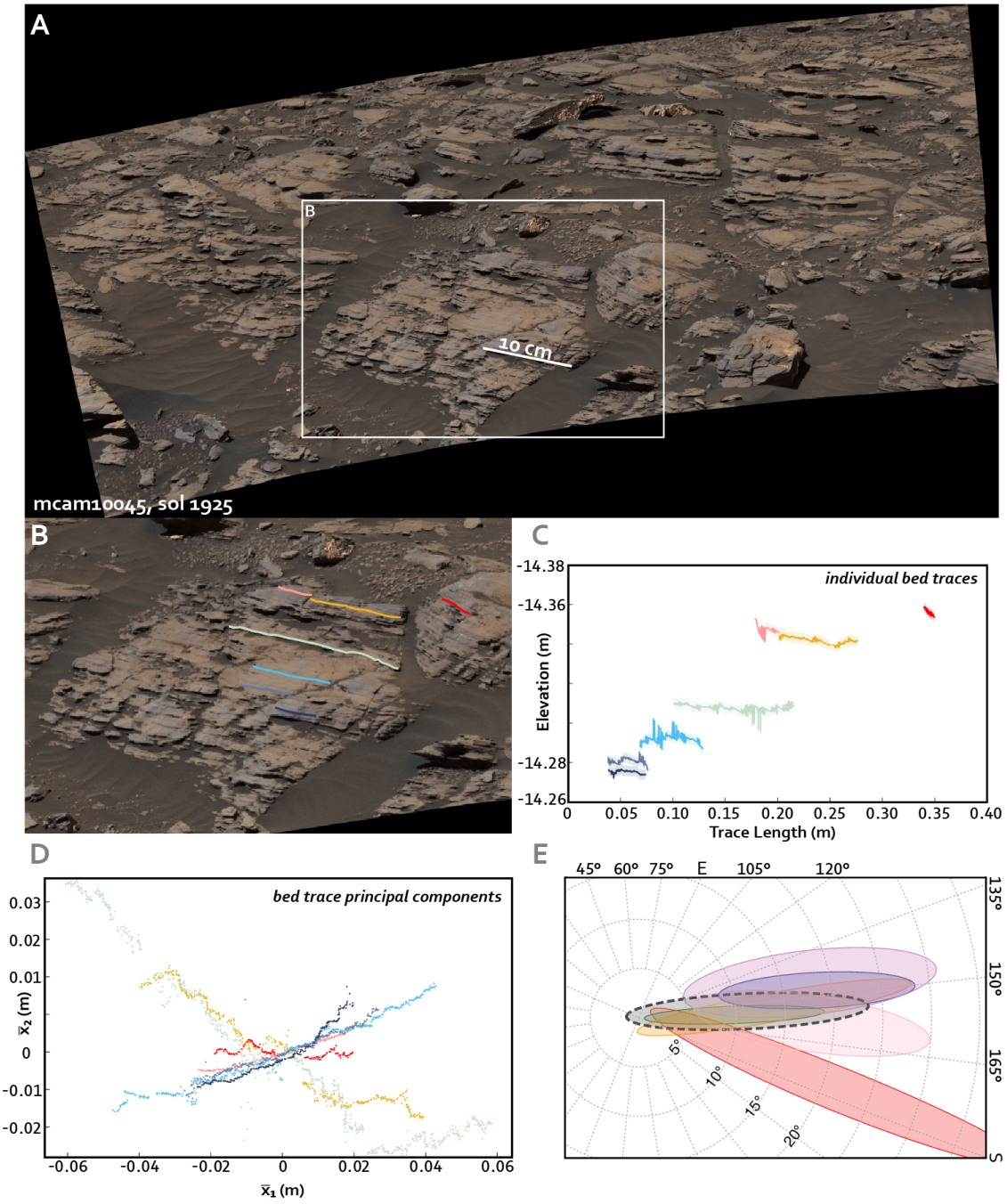

Figure 3.7. Representative example of bedding traces and resulting PCA plane fits. (**A**) Intact outcrop imaged in the Jura member on sol 1925. (**B**) enlarged portion of (A) with colored bedding traces. (**C**) elevation (m) as a function of trace length, color coded by trace. (**D**) each trace projected along its first and second principal components. (**E**) azimuthal plot of uncertainties in dips and dip directions for each example trace.

3.4.3 Outcrop Selection

This study uses Mastcam stereo pairs collected at 24 different sites across VRR between sols 1802 and 2259 (Figure 3.5). Of these, five are in the Blunts Point member (BPm), three are in the Pettegrove Point member (PPm), nine are in the Jura member (Jm), four are on the BPm – PPm contact, and three are on the PPm – Jm contact. The distance to the measured outcrops ranged from ~2-20 m, and no outcrops were excluded from measurement based on range alone. Instead, specific measurements were dismissed based on the ratio of trace to error extent (sections 3.4.2.4 and 3.5.1.1), a metric implicitly related to outcrop range. The number of traces performed at each site is not constant; sites with greater exposure generally have more measurements. In total, 487 beds were traced with an average trace length of 14 cm and a median of 83 points per bed prior to Monte Carlo repopulation (section 3.4.2.3). Stacked bedding traces were also performed at every site where multiple parallel beds could be measured.

Errors resulting from improper interpretation of bedding surfaces are a significant source of uncertainty in remotely sensed bedding orientation measurements. Poorly expressed bedding surfaces may not accurately capture primary depositional orientations for multiple reasons including: (1) rotation, faulting, or other forms of deformation and (2) traces of weathered surfaces, fractures, and/or diagenetic features that resemble but differ from primary bedding. To limit these sources of uncertainty, most measurements were performed on relatively large, intact outcrops (e.g. Figure 3.6A) that were less likely than individual blocks to have rotated during weathering but which may still have experienced regional post-depositional deformation that could result from multiple processes including impact cratering and differential compaction (Grotzinger et al., 2015). Most of these exposures are relatively oblique (e.g. Figures 3.6A, 3.7A), except along contacts (e.g. Figure 3.6C). Traces at seven of the sites were performed on blocks (Figure 3.6D) that may have rotated since deposition, although rotation was not obvious at any of the selected sites based on visual inspection alone. Beds that were obviously affected by localized deformation, such as near small impact craters on the ridge, were excluded. A potential error source especially prevalent on VRR is

the accidental inclusion of low-angle cross-cutting veins, which occur in the geomorphic transition to the ridge (Edgar et al., 2020; Fedo et al., 2018) and are locally difficult to distinguish from primary bedding where it becomes concordant (Figure 3.6B). All cross-cutting features were excluded from analysis in this study. Beds were traced over the longest visibly contiguous span not affected by fractures or other cross-cutting features. An example of a typical intact outcrop in the Jura member, associated bedding traces, and their plane solutions is shown in Figure 3.7.

3.5 Results

3.5.1 Bedding Orientation Results

3.5.1.1 Aggregate Orientation Results for Individual Bedding Planes

The dip and dip direction of all 487 individual beds is shown in Figure 3.8 for the 3σ stereo error case (section 3.2.3). Because uncertainties of individual bedding planes are often large, and because the distribution of sites and the number of traces performed at each site is non-uniform, the aggregate of individual solutions reported in Figures 3.8 and 3.9 should not be interpreted to necessarily correspond to a bulk regional orientation. In aggregate, the average orientation of individual plane fits is highly variable and generally dips between 0 and 10°. The average dip of all individual beds in the 3σ and 1σ stereo cases are shown in Figures 3.A1 and 3.A2. In the 1σ stereo case, the average dip clusters along E-W and N-S axes and around 0° dips, symptomatic of the effects of large, axially asymmetric stereo errors discussed in section 3.4.1.4. Indeed, these solutions generally correspond to traces with low extent to error ratios (white points). In the 3σ case (Figures 3.8A, 3.A1), attitudes do not cluster as strongly along E-W and N-S axes because stereo errors comprise a smaller fraction of the variance along $\bar{x}_3$. The uncertainties associated with the 1σ stereo error case are unrealistically high, and therefore the 3σ stereo error case is likely more physically realistic. Traces whose spatial extent did not exceed the error by at least a factor of three along $\bar{x}_1$ or $\bar{x}_2$ were removed from subsequent analysis. The factor of three was chosen to capture

solutions clearly dominated by stereo errors without removing a significant number of "good" fits, although all accepted solutions are skewed at least somewhat by stereo errors.

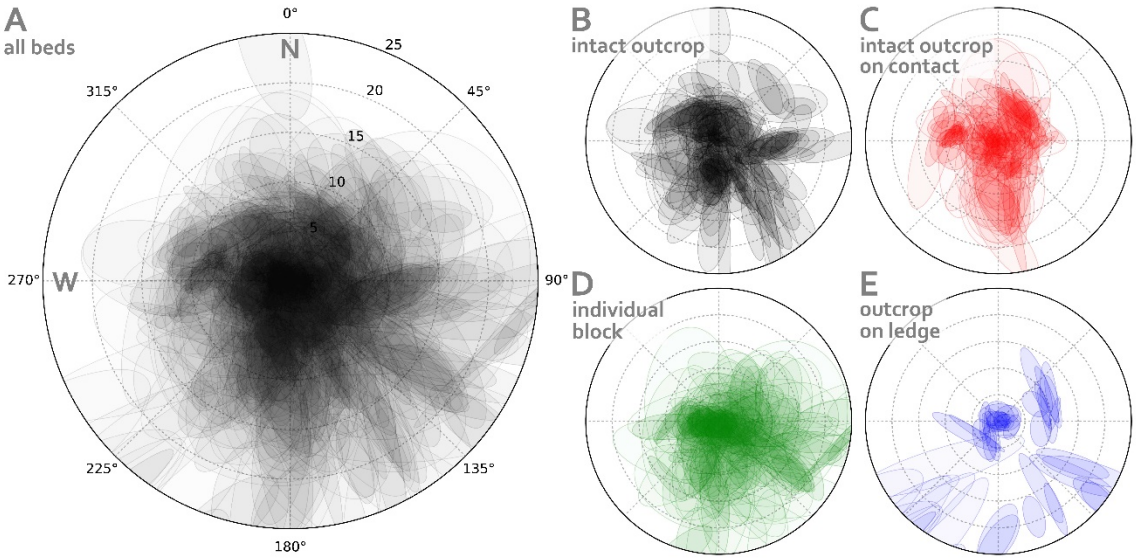

Figure 3.8. (**A**) Dip angle and dip direction of every bed measured in this study using the 3σ stereo error case. Each ellipse represents the range of possible solutions for one bedding plane. (**B-E**) Classification of the solutions from (**A**) according to whether the bed is part of an intact outcrop (**B**), an intact outcrop on a contact (**C**), an individual block (**D**), or an outcrop on the side of a ledge, defined here as a regional slope >20° (**E**).

Figure 3.8B, again presented without uncertainties, shows the broad classification scheme corresponding to each plane fit for accepted solutions from Figure 3.8A: (1) large, intact outcrops (e.g. Figure 3.6A,B, Figure 3.7A); (2) large, intact outcrops that are also on member contacts; (3) individual blocks that may be more subject to rotation during weathering; (4) large, intact outcrops on slopes exceeding 20°, which may also be on member contacts. These categories were selected because they may be subject to different amounts of post-depositional deformation or modification and because they show systematically distinct orientation solutions. Most beds that dip to the north are found on the BPm – PPm or PPm – Jm contacts, which themselves dip north as mapped by HiRISE (Tables 3.1, 3.2), although dips measured on those contacts do not exclusively dip northward. Most beds with an average dip solution of more than 10-15° in any direction are on topographic slopes of at

Table 3.1. DIP MEASUREMENTS OF VRR MEMBER CONTACTS FROM HIRISE AND STACKED DIP MEASUREMENTS FROM STEREO MASTCAM VRR IMAGES (3σ STEREO ERROR CASE)

Sol or ID	Member	Outcrop Type	Reg. Slope	Reg. Dip Direction	n	Trace L (m)	Dip	Dip Direction	$\boldsymbol{\theta}_{min}$	$\boldsymbol{\theta}_{min}$	Rake	$\mathbf{d}/\boldsymbol{\delta}_{\mathbf{d}}$ PC 2
Traces of VRR member contacts from HiRISE												
BPm – PPm contact	BPm – PPm	-	-	-	352	3873	7.30°	334.4°	0.30°	3.74°	91.3°	-
PPm – Jm contact	PPm – Jm	-	-	-	140	1076	6.56°	332.1°	0.22°	1.11°	71.7°	-
Joint fitting of parallel bedding planes on VRR												
1802	BPm	Intact	18.9°	32.0°	1119	0.51	5.82°	317.9°	5.69°	13.34°	30.76°	3.86
1809	BPm – PPm	Intact	18.5°	7.6°	1689	0.14	3.47°	214.6°	1.50°	4.28°	52.50°	4.98
1812	PPm (on ledge)	Intact	20.6°	353.9°	1262	0.06	10.85°	236.4°	7.08°	19.39°	121.11°	14.30
1828	PPm	Intact	8.0°	316.0°	468	0.21	14.37°	52.1°	2.74°	10.60°	20.82°	6.76
1829	PPm (on ledge)	Blocks	36.3°	327.6°	827	0.13	3.40°	261.9°	1.79°	10.31°	175.83°	2.96
1866	PPm – Jm	Intact	18.7°	10.0°	1781	0.25	6.64°	32.1°	2.97°	6.07°	25.22°	33.08
1868	PPm – Jm	Intact	12.4°	3.8°	320	0.20	9.75°	160.9°	4.67°	13.95°	107.69°	4.40
1870	Jm	Intact	15.3°	330.4°	808	0.11	8.96°	96.1°	4.77°	10.62°	60.85°	2.72
1925	Jm	Intact	14.3°	337.1°	1615	0.13	15.57°	149.2°	2.57°	14.49°	89.57°	14.90
1931	Jm	Blocks	18.5°	351.6°	-	-	7.65°	66.7°	7.14°	12.65°	34.58°	3.68
1944	Jm	Intact	15.7°	79.6°	878	0.79	0.57°	320.2°	2.47°	2.72°	90.48°	4.21
1946	Jm	Intact	18.3°	92.8°	1436	0.18	5.07°	192.9°	3.43°	5.09°	0.46°	2.95
1948	Jm	Blocks	12.8°	257.3°	348	0.84	8.33°	190.3°	3.76°	12.84°	73.35°	1.88
1950	Jm	Intact	17.9°	261.8°	527	0.47	6.24°	219.7°	3.46°	4.72°	73.89°	4.77
1964	Jm	Block	8.0°	346.2°	419	0.04	7.39°	170.6°	12.08°	29.01°	87.08°	2.71
2000	PPm – Jm	Intact	18.5°	355.8°	1576	0.25	7.83°	284.5°	1.69°	3.26°	34.43°	10.51
2069	BPm	Intact	18.3°	340.9°	1459	0.74	4.03°	22.4°	5.84°	8.60°	45.42°	3.19
2086	BPm	Intact	18.0°	336.1°	517	0.87	1.82°	279.8°	1.23°	7.90°	32.84°	16.90
2088	BPm	Block	19.7°	357.8°	-	-	-	-	-	-	-	-
2090	BPm	Block	-	-	1190	0.06	2.89°	155.9°	7.06°	11.02°	81.78°	5.87
2093	BPm – PPm	Intact	18.0°	344.7°	614	0.36	5.40°	296.4°	5.44°	19.34°	20.04°	4.46
2097	BPm – PPm (on ledge)	Intact	24.1°	32.3°	659	0.46	9.72°	63.9°	2.21°	9.41°	3.42°	6.54
2148	BPm – PPm (on ledge)	Intact	48.0°	358.4°	502	0.13	1.76°	95.0°	3.67°	4.48°	154.80°	1.51
2259	Jm	Blocks	6.6°	54.4°	720	0.16	10.17°	66.2°	9.47°	13.02°	125.43°	2.04

Table 3.2. ORBITER-BASED ATTITUDE MEASUREMENTS OF VRR OR LOWER GALE MOUNT SHARP STRATA

Study	Trace Location	Dip	Dip Direction	Comments
This study	BPm – PPm contact	7.30°	334.4°	-
This study	PPm – Jm contact	6.6°	332.1°	-
Milliken et al. (2010)	Lower member	1-6°	285-30°	Strata are above sulfate-bearing unit
Stack et al. (2013)	Lower member	7.9°	315°	Strata are above sulfate-bearing unit
Fraeman et al. (2013)	BPm	6.3-7.8°	~315°	-
Fraeman et al. (2013)	VRR	5.7-14.1°	~315-45°	-
Fraeman et al. (2013)	Glen Torridon	5.8-8.6°	~310-350°	-
Fraeman et al. (2013)	Sulfate-bearing unit	3.6°	345°	-
Kite at al. (2013)	Lower Gale mound	2.5-4.5°	~330°	Strata are below sulfate-bearing unit
Kite et al. (2016)	Lower Gale mound	3.1-4.2°	~330°	Strata are below sulfate-bearing unit

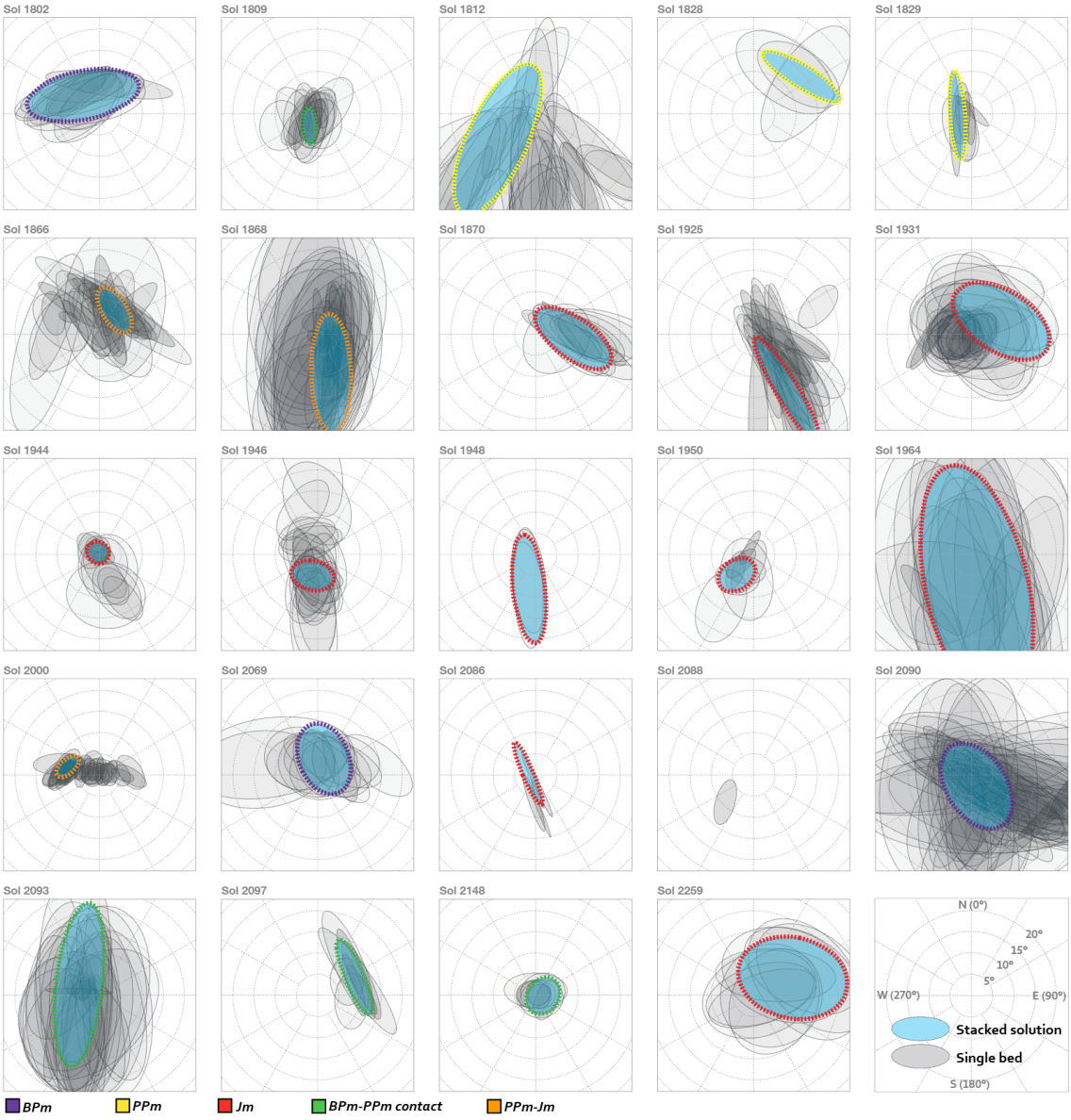

Figure 3.9. Range of possible dip and dip azimuth solutions at different sites, grouped by sol. Gray ellipses denote the solution space of individual bed traces. Blue ellipses denote the solution space of stacked traces from that sol (see Table 1). Not all individual traces shown were necessarily used to produce the stacked solutions for a given sol. All single bed solutions shown had trace extent to error extent ratios of at least five along the first and second principal component axes. Using 3σ error case.

least 20°, which include but are not limited to member contacts in some areas, or in individual blocks. The average dip angle and azimuth of beds measured in intact outcrops not associated with member contacts is also variable, but mostly ranges from 0°-10° SE. Although the

uncertainty of most plane fits for individual beds is generally high, regional bedding attitudes can be constrained by consideration of the most exceptional outcrops (3.5.1.2).

3.5.1.2 Site-specific Orientation Results for Individual and Stacked Bedding Planes

Figure 3.9 shows the projection of errors to bedding poles for all measured beds accepted in section 3.5.1.1 using the 3σ stereo error case discussed in section 3.4.2.2. Corresponding plots for the 1σ and 5σ stereo error case are shown in supplementary Figures 3.A3 and 3.A4, respectively. Solutions corresponding to stacked traces, which represent either a subset or the full set of traces within a scene, are also shown in Figure 3.9, and the probability distribution of the dip magnitude of each stacked solution is shown in Figure 3.10. Although the dip azimuth of individual bed solutions is collectively high (Figure 3.8), dip azimuths typically cluster more tightly within individual scenes, consistent with the expectation that beds within a given scene should dip in similar directions if they are parallel-stratified lacustrine mudstone. It is also possible that bedding comprises topographic features such as mounds or depressions larger than the scale of outcrops observed by the rover, but smaller than the scale over which orbit-based measurements are made, in which case the assumption of consistent dip azimuths within individual scenes remains valid. More credence should be lent to stacked solutions than individual solutions because they have larger trace extents in $\bar{x}_1$ and $\bar{x}_2$ and buffer against the inclusion of poor or otherwise unrepresentative traces. All stacked measurements are summarized in Table 1 for the 3σ stereo error case.

In seven of the 24 scenes, even stacked bedding traces do not exceed the trace to error threshold of a factor of three (Table 3.1, section 3.5.1.1) and should be regarded with skepticism because the dip magnitude and azimuth are likely more heavily influenced by stereo errors than in other scenes. Caution should be taken in comparing the average dip of each scene (Table 3.1) because the uncertainties of plane fits in some scenes is so large as to be effectively unconstrained, thus making it possible that the true attitude and average solution differ significantly. There is no clear correlation between the stacked dip azimuth and regional slope in a scene, which indicates that downslope bias is not a major contributor to the plane solutions.

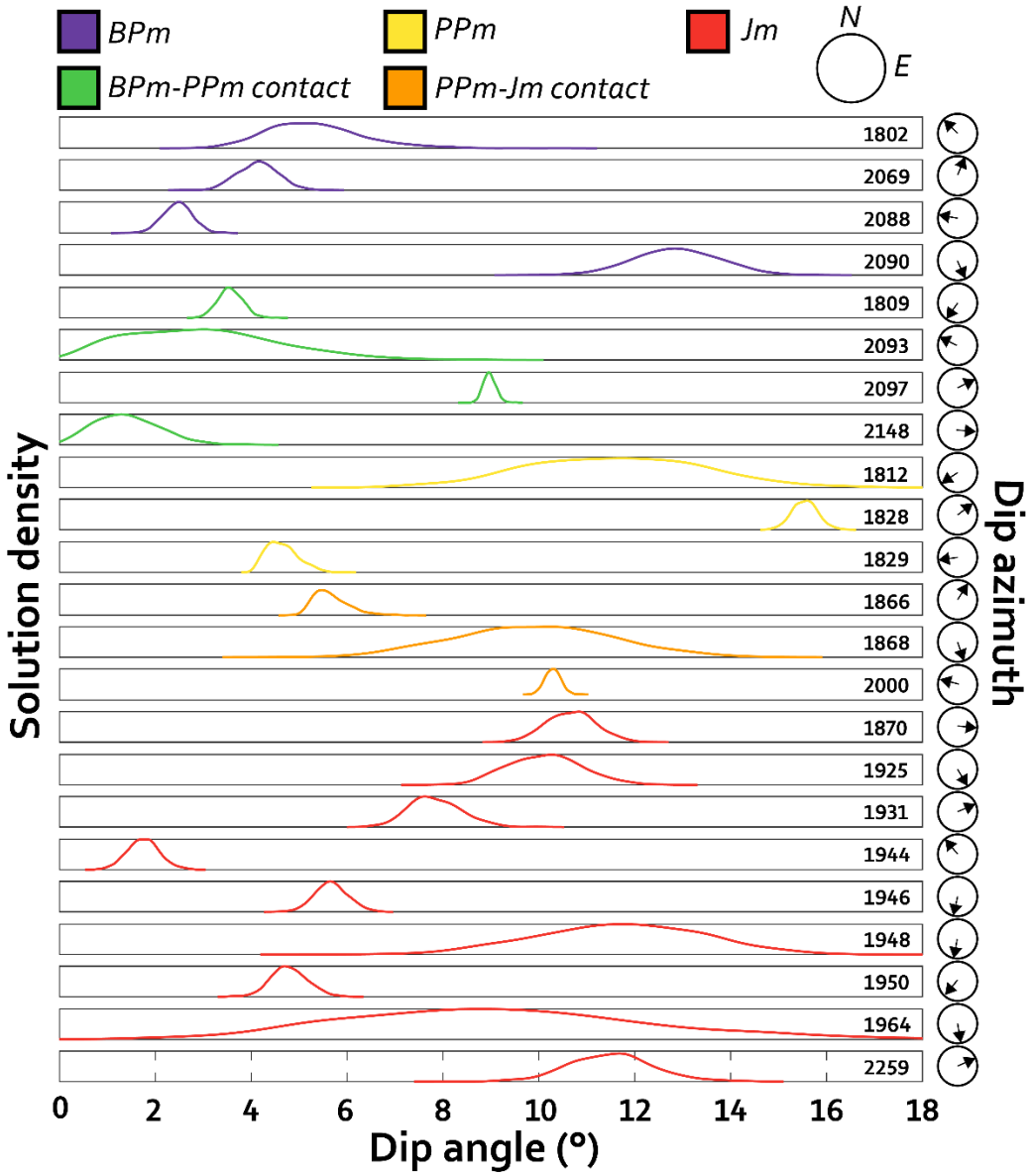

Figure 3.10. Probability density functions for each stacked solution displayed in Figure 3.9, grouped according to member. The average dip azimuth of each stacked solution is shown to the right. The ratio of trace to error extents is variable between solutions (see Table 3.1).

The smallest stacked error ellipses, which represent the best constrained attitudes, occur in scenes from sols 1809, 1829, 1866, 1944, 1946, 1950, 2000, 2086, and 2148. The sol 1866 and 2000 mosaics record the PPm – Jm contact and reveal average dips of ~6.5° toward 32° and ~7.8° toward 285°, respectively, which are close to the dip of the entire

contact (6.56° toward 332.1°), though other, worse constrained measurements (sol 1868) on the PPm – Jm contact dip S. The sol 1809 and 2148 mosaics record the BPm – PPm contact and have median dips of ~3.5° toward 215° and ~1.8° toward 280°, respectively, which differ from the dip of the entire contact (7.30° toward 334.4°). The sol 2086 scene sits in the BPm and has a median dip of ~1.8° toward 279.8°. The median dip solutions of other scenes in the BPm range from ~3° S to ~6° NW, but have significantly larger error ellipses that encompass many solutions within that range. The sol 1829 scene sits in the PPm and has a median dip of ~3.4° toward 262°, although the stacked traces were performed on a block and other beds in the PPm show a wide range of dips (e.g. sol 1828, Table 3.1). The sol 1944, 1946, and 1950 scenes are in the Jm and have median dips of ~0.6° toward 320.2°, ~5.1° toward 192.9°, and ~6.2° toward 219.7°. Several scenes in the Jm are likely proximal to small impact craters, but care was taken to exclude obviously deformed beds in these scenes. Other beds measured in the Jm dip predominantly ~0-15° south with larger error ellipses that encompass a wide range of solutions.

3.5.2 Constraints on Bedding Orientation from Regional Geology

Due to the large uncertainties of plane fits for individual beds (Figures 3.9, 3.10), changes in topography across the ridge, and asymmetric imaging and bed trace sampling, it is difficult to report a cumulative average dip direction and magnitude for the strata that comprise VRR based solely on individual plane traces with a confidence better than several degrees. It is possible, however, to validate rover-based bedding orientations and further constrain regional dips by analyzing the elevations where facies present on VRR reappear in the Glen Torridon trough, a much larger spatial scale of structural analysis.

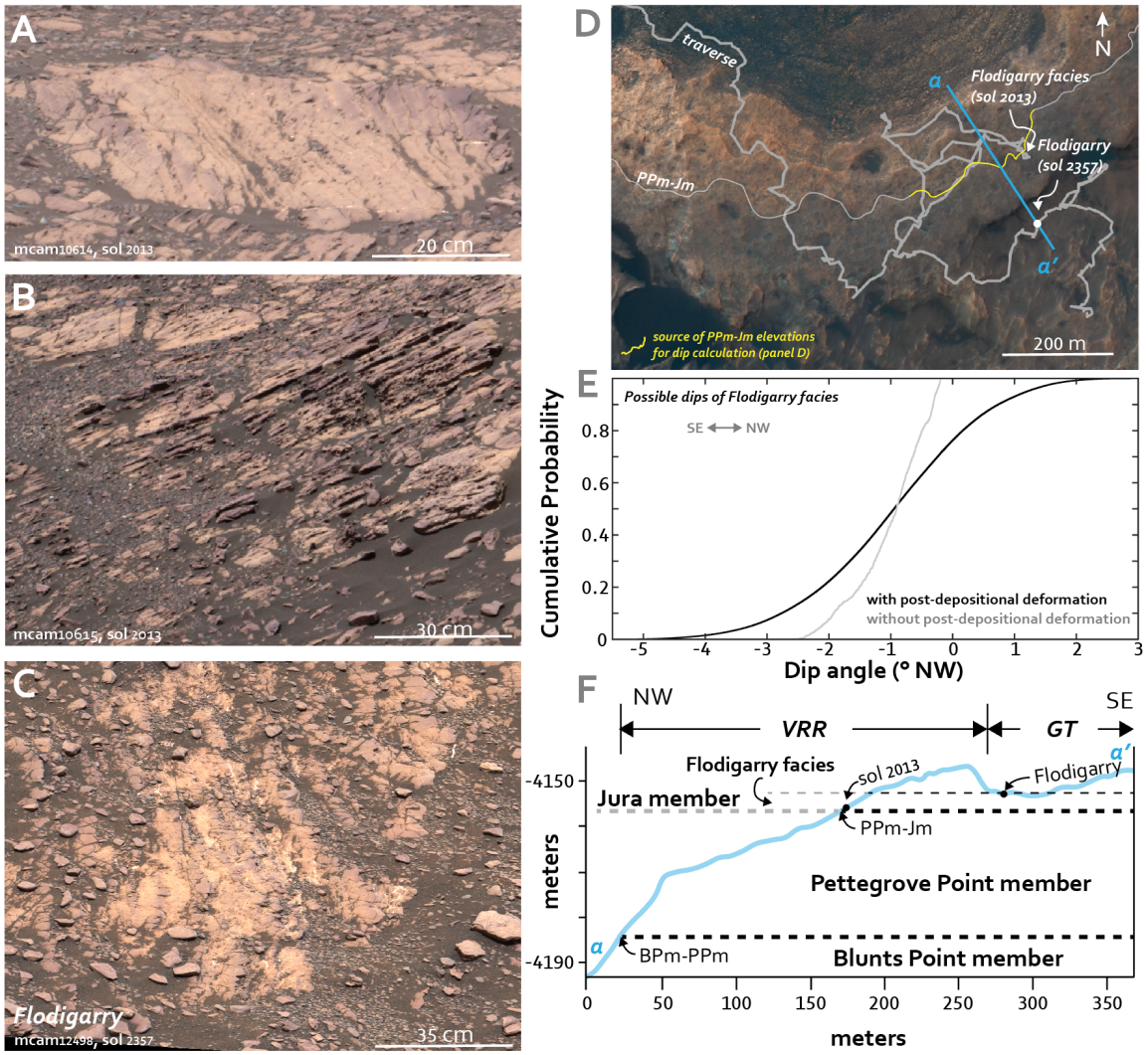

Figure 3.11. (**A**) and (**B**) Recessive tan- and purple-toned beds above the PPm – Jm contact (sol 2013). (**C**) Recessive tan- and purple-toned beds of the Flodigarry target (sol 2357). (**D**) a-a' profile in (E) and location of images in (C) and (D). The portion of the PPm – Jm contact used to calculate dips of the Flodigarry facies is gold. (**E**) (gray line) set of angles between the Flodigarry target and the gold portion of Jm-PPm contact using a Flodigarry target elevation offset by -5m; (black line) same set of angles as the gray line, but allowing the Flodigarry facies to have deformed at scales similar to those observed on member contacts. (**F**) Transect across VRR and into the Glen Torridon trough showing the relative locations of the BPm – PPm and PPm – Jm contacts and the Flodigarry facies.

3.5.2.1 Dip of the Flodigarry Facies

On VRR, a ~5-7 m-thick laminated mudstone with distinct, alternating resistant (purple) and recessive (tan) beds defines the base of the Jura member of the Murray formation (Edgar et al., 2020). This characteristic "Flodigarry facies" sits at the PPm – Jm contact, which occurs at an elevation of -4155 m at the easternmost part of the traverse (sol 2013; Figure 3.11D,F). On sol 2357, Curiosity encountered similar alternating resistant and recessive, tan- and purple-shaded beds at the target *Flodigarry* near one of the deepest parts of the Glen Torridon trough at an elevation of -4152 m (Figure 3.11D). Due to its similar lithology to the rocks at the base of the Jura member of VRR, *Flodigarry* is interpreted to be part of the same stratigraphic interval (Edgar et al., 2020; Fedo et al., 2020). Using the elevations of the base of the Jura member and of the *Flodigarry* target, which collectively comprise an informally recognized Flodigarry facies, the regional bedding attitude of the Flodigarry facies can be evaluated. Notably, this estimate of bedding attitude is independent of both orbiter- and rover-based dips, which are based on local geometry.

Estimating the attitude of the Flodigarry facies requires knowledge of the elevations of the *Flodigarry* target and the PPm – Jm contact, the distance between them, and the position of the *Flodigarry* target within the stratigraphic interval. To account for different elevations along the PPm – Jm contact (Fedo et al., 2019), the dip of the Flodigarry facies was calculated using elevations sampled from a large portion of the contact (yellow line Figure 3.11D). To account for possible post-deposition deformation, the elevation of *Flodigarry* was perturbed by elevations equivalent to the magnitude of elevation variation measured along many 150 m segments of the PPm – Jm contact (the average distance between the PPm – Jm contact and *Flodigarry*) (black line, Figure 3.11E). Because the *Flodigarry* target is shallowly exposed, slopes were calculated under the assumption that the target occurs near the top of the facies and that the facies thickness varies minimally between 5-7 m as observed on VRR. Because the PPm – Jm contact defines the bottom of the facies on top of VRR, possible slopes of the Flodigarry facies can be estimated by tracing lines between points on the PPm – Jm contact and the elevation 5-7 m below *Flodigarry* (light

gray line, Figure 3.11E), which fall between ~0-2° SE. The resulting range of possible dips of the Flodigarry facies is between ~4° SE and 2° NW, and 95% of solutions fall between 3.8° SE and 1.4° NW, consistent with an approximately flat stratal geometry extending through VRR and Glen Torridon.

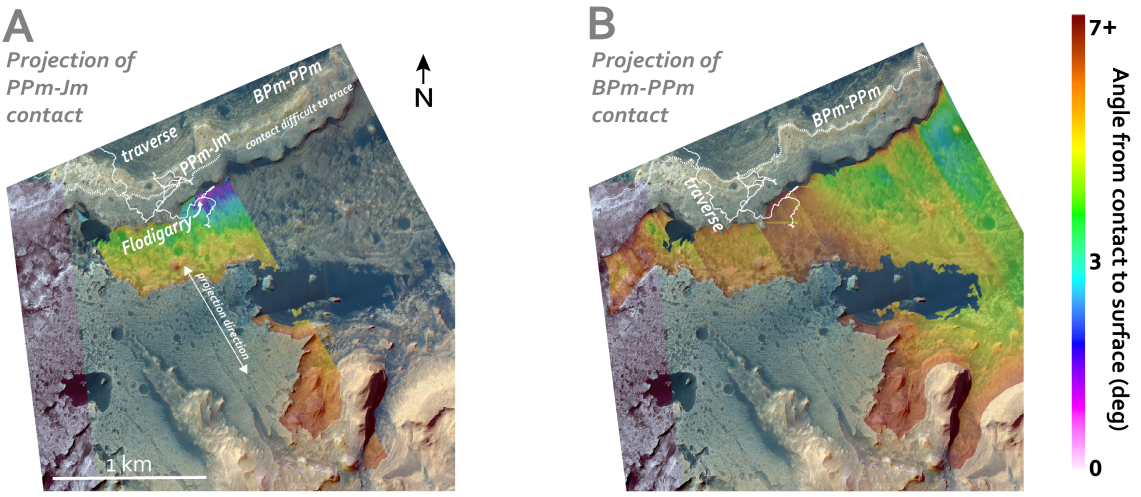

Figure 3.12. Map of the angle between the (**A**) PPm – Jm contact and surface and (**B**) BPm-Jm contact and surface projected along a line oriented toward 315° (arrows in (A)). The rover traverse is shown by the solid white lines. Angles are positive if they dip NW. The Flodigarry target is highlighted in (A).

3.5.2.2 Dip Constraints from the Projection of Contact Elevations

The strata that comprise VRR extend southward into the Glen Torridon trough where they are overlain by younger strata. This can be confirmed in situ due to the identification of the *Flodigarry* target in Glen Torridon and is also supported for the BPm, which is seen from HiRISE to extend several hundred meters into Glen Torridon west of the Greenheugh pediment where the positive topography of VRR tapers out (Figure 3.A4). The extent of other VRR member lithologies in Glen Torridon may additionally constrain regional dips. The projections developed in 3.5.2.1 can be extended to calculate the angle between the major member contacts and points throughout Glen Torridon. The BPm – PPm and PPm – Jm contacts on VRR were identified using a combination of ground-based and orbital mapping (Edgar et al., 2020) and traced in HiRISE images. For each point in a region of Glen Torridon,

the angle between each point and the BPm – PPm and PPm – Jm contacts along an approximate NW-striking (315°) dip angle was calculated (Figure 3.13).

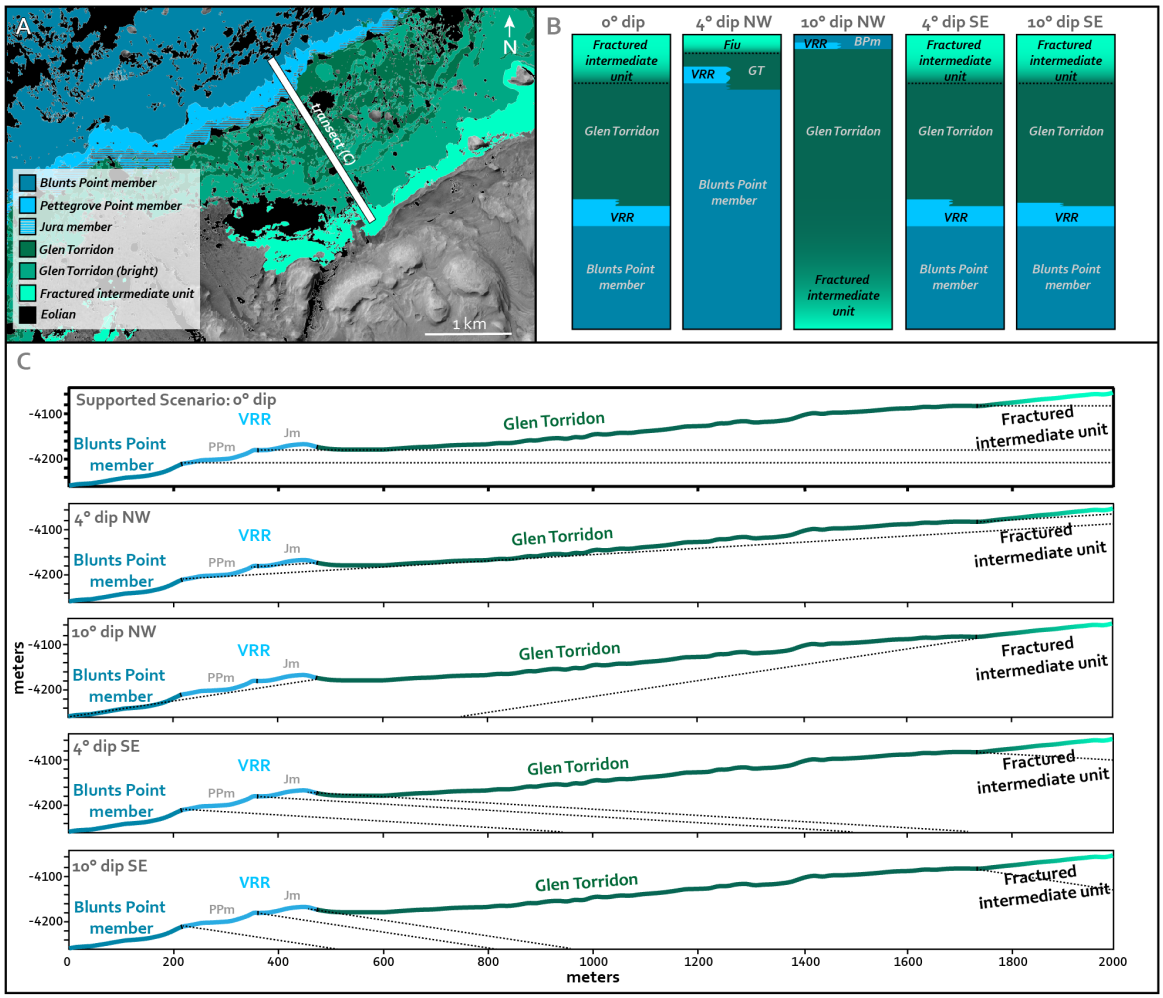

Figure 3.13. (**A**) Geological map showing the Blunts Point, Pettegrove Point, and Jura members, Glen Torridon, and the sulfate-bearing (fractured-intermediate) unit. Map adapted from Stack et al. (2017). (**B**) Notional stratigraphic columns for different regional dips along the white transect in (A). Unit thicknesses within the columns are approximately to scale. (**C**) Elevation profile along the white transect in (A). Dashed lines denote the projection of each unit under the surface following the regional dip cases in (B).

In most portions of Glen Torridon, including along the rover traverse, the BPm would be exposed if it dipped more than ~5-7° NW (Figure 3.13B). East and west of the rover traverse, where the trough is slightly deeper, the required dips for exposure decrease to ~2.5-

3° NW. The BPm, which is typified by mudstone characteristic of much of the Murray formation (Fedo et al., 2018), has not been identified in the area south of VRR along the rover's future traverse from either rover- or orbiter-based images, or east of the rover's location in deeper parts of the Glen Torridon trough. Assuming the BPm contiguously underlies the Glen Torridon strata, its absence from most mapped regions suggests the member can dip no more than ~2.5-3° NW. The magnitude of this constraint may vary slightly due to post-depositional deformation, and angle estimates grow increasingly uncertain farther from VRR, but values of <~2.5-3° are common throughout the mapped region. In most portions of the Glen Torridon trough, Jm strata would be exposed only if they dipped more than ~0-3.5° NW (Figure 3.13A). Although Curiosity has traversed this full range of angles, strata lithologically similar to the lower Jm have only been identified at one location – *Flodigarry* – which is located precisely where the angle between the PPm – Jm contact and Glen Torridon is the lowest (Figures 3.11A, 3.12A). Other strata along the first several hundred meters of the rover's traverse through Glen Torridon are interpreted as Jm, but do not share the same characteristics as the Flodigarry facies. If PPm or Jm dips are more than ~1-2° NW, Flodigarry strata should be identifiable across a several hundred-meter swath of the Glen Torridon trough. Collectively, results are consistent with regionally flat- or near-flat-lying stratal geometry for the Murray formation.

3.6 Discussion

3.6.1 Collective Interpretation of Dip Measurements

The uncertainty of most Mastcam-based plane fits is too large to yield a well-constrained dip and dip azimuth. The large uncertainties result primarily from the combination of poor bedding exposures (i.e. short extents in $\bar{x}_1$ and $\bar{x}_2$) and large stereo errors. In several scenes, however (section 3.5.1.2), the stacked plane fits are well-constrained to a range of a few degrees of dip and ~15-60° of dip azimuth. Any attitude differences between these beds in excess of the reported uncertainties are likely real. Such outcrop-dependent attitude differences are common, and no single regional attitude is contained in the solution space of every stacked trace. For example, the stacked solutions

from sols 1829, 1866, and 1944 are relatively well-constrained and do not overlap. The (up to 100°) different orientation of these beds is probably not primary due to their association with apparent secondary deformation processes, but rather the result of weathering, gravity-driven motion or rotation of blocks, and localized post-depositional deformation that could result from multiple processes including impact cratering or differential compaction. Crossbeds deposited by some types of migrating bedforms could yield a wide range of primary dip azimuths including those in which the contacts bound an extreme of the field of observations (e.g. Rubin and Carter, 2006), although crossbeds were not positively identified on VRR (Edgar et al., 2020). In tandem with uncertainties stemming from the error structure of the traces, structural variation within VRR yields a murky picture of dips at a regional scale based on in-situ bedding traces alone. Possible solutions for stacked dips in each member and member contact mostly range from ~2°N-10° S in the Jura member, ~2-10° S in the Pettegrove Point member, ~6°SE-~8°NW in the Blunts Point member, ~4-10°N on the BPm – PPm contact, and ~0-6° with variable azimuth on the PPm – Jm contact. The probability of solutions falling in this range is nonuniform, and most solutions sit near the middle of the range (Figure 2.10). That is, it is more likely that the true attitudes of most beds are closer to the middle of the uncertainty range than the extremities. Although the range of solutions is too variable collectively to confidently report an aggregate regional dip, they do not support regional dips greater than several degrees in any direction. There are beds on VRR that dip more than several degrees, but these solutions dip in multiple directions (Figures 3.9, 3.10), are discrepant from most member orientations. and likely arise from either high stereo errors (e.g. sol 2000), rotation (e.g. sol 1870), or post-depositional deformation, probably mostly impact cratering (e.g. sol 1944), which has a high retention rate at VRR.

Stratigraphic correlations between VRR member strata and Glen Torridon (section 3.5.1) further constrain the regional structural orientation. Correlation of the *Flodigarry* target with similar facies encountered by Curiosity in the lower Jm exposed on the northern flank of VRR constrain the dip of the Flodigarry facies to between ~3°SE and 2°NW (section 3.5.1.1). Projections of the BPm – PPm and PPm – Jm contacts SE indicate that Curiosity

would have already encountered BPm strata in Glen Torridon if the dip were more than ~5°NW. Furthermore, BPm strata may be visible from orbit elsewhere in the Glen Torridon trough if the regional dip is more than ~2-3°NW, assuming lateral continuity (section 3.5.1.2). No BPm strata have been identified in Glen Torridon east of the Greenheugh Pediment, although it is possible that BPm strata are not identifiable in HiRISE images. A similar exercise with the PPm – Jm contact indicates that Curiosity should have already encountered Jm strata if the regional dip is flat, which it did at *Flodigarry*. Collectively, regional stratigraphic correlations are consistent with dips between ~2°SE and 2°NW.

3.6.2 Comparison with Orbiter-derived Dip Measurements

Previous studies have measured the attitude of features on VRR (Fraeman et al., 2013) and elsewhere on lower Mt. Sharp (Milliken et al., 2010, Stack et al., 2013, Kite et al., 2013, 2016) using orbiter-based images and DEMs (Table 3.2). Orbiter-derived dips on Mount Sharp generally range from 2-8° NW. In the BPm and VRR, Fraeman et al. (2013) report dips of 6.3-7.8° NW and 5.7-14.1° predominantly NW, respectively. These are consistent with HiRISE-derived attitudes generated for the BPm – PPm and PPm – Jm contacts in this study (contacts shown in Figure 3.12), which dip 7.30° toward 334.4° and 6.6° toward 332.1°, respectively. Beds measured along the PPm – Jm contact in Mastcam images mostly dip shallowly S or WNW, unlike the HiRISE-based contact (section 3.5.2, Table 3.1).

Although orbiter-based dip measurements of VRR member boundaries are well-constrained due to their long trace extents along both principal components and are consistent between studies, they are at odds with the interpretation of regional dips as flat (section 3.6) and with measurements of strata on member boundaries that do not uniformly dip northward. The discrepancy between regional bedding attitudes and orbiter-based measurements may indicate that features measured in HiRISE, which are mostly VRR member boundaries, do not represent primary bedding, and thus are discordant with strata. This discordancy could have multiple non-exclusive explanations: 1) the topographic ledges along each VRR member boundary could result from differential diagenesis (Fraeman et al., 2020), in which

case the attitude of traces along the boundaries would not represent primary stratigraphy; 2) VRR member boundaries may have undergone significant post-depositional deformation that skewed their attitude from the primary regional structural orientation; and 3) the members might retain lateral facies variations that change in elevation. In the first case, stratigraphic correlations between VRR members and Glen Torridon strata would be complicated by the possibility that VRR members are predominantly defined by diagenetic processes, in which case VRR members might not extend far south of the ridge despite regionally flat strata. In the second case, local deformation along the member boundaries could simultaneously explain steep dips of varying direction measured in situ on member boundaries and the fact that member boundaries do not follow elevation contours. In the third case, elevation variation along member boundaries could arise from primary processes such as deposition on preexisting lakebed topography in the form of low-relief depositional lobes, mounds, or channels. It is difficult to evaluate this scenario due to the limited spatial extent of rover observations. In addition to the aforementioned mechanisms, the attitudes of individual beds along the member contacts as measured in Mastcam images might be skewed toward the north relative to other outcrops on VRR due to downslope rotation, although this process would not bias orbiter-based measurements of the member boundaries. Other orbiter-based measurements of putative lower Mt. Sharp strata (Table 3.2) are not necessarily subject to the same confounding conditions present on VRR, but measurements of VRR member attitudes highlight the possibility that orbital and in situ attitude measurements do not necessarily record the structural orientation of bedding.

3.6.3 Constraints on Stratigraphy of the Mt. Sharp group

In-situ bed orientation measurements and regional stratigraphic correlations jointly constrain the geometry of strata, and therefore the stratigraphic relationship between units in the Mt. Sharp group. Figure 3.13 shows five notional stratigraphic models based on different scenarios for regional dips: 0° dip, 4° NW dip, 4° SE dip, 10° NW dip, and 10° SE dip. The 0° dip case (i.e. if the Mt. Sharp group strata are flat) is supported by regional stratigraphic correlations (sections 3.5.1.1 and 3.5.1.2) and broadly consistent with the collection of

individual and stacked bedding plane fits (sections 3.5.1 and 3.5.2). Under dip ~0°, the upper part of VRR is stratigraphically equivalent to the lower portions of Glen Torridon (Figure 3.13C). If contiguous, no BPm and few PPm strata would be expected to outcrop in Glen Torridon, although Jm strata would be expected to outcrop in the trough, which matches observations. Along the traverse in Figure 3.13A, VRR and Glen Torridon would be ~60 m and ~120 m thick, respectively. If dips are flat throughout the Mt Sharp group, the rover's elevation gain directly corresponds to the stratigraphic thickness of the traversed members.

A 4° NW dip and slightly shallower NW dips are more consistent with most orbiter-based dip measurements (Table 3.1, also see section 3.6.1) and some individual and stacked bed fits on VRR, especially those on the BPm – PPm contact (Table 3.1, sections 3.5.1 and 3.5.2), but inconsistent with regional stratigraphic correlations and most stacked bed fits. In the 4° NW dip case, the upper BPm would be stratigraphically equivalent to Glen Torridon in most portions of the Glen Torridon trough and, because the dip would be close to the 5-6° regional slope, Glen Torridon would be thin (<20 m thick) relative to the overlying and underlying units. In this case, the BPm would outcrop in portions of the Glen Torridon trough, which is not observed. If the dip were 10° NW, which is inconsistent with all measurements, the conventional age relationship for the Mt. Sharp group would reverse (strata would be older up section). A 4° SE dip and shallower SE dips is inconsistent with most in-situ dip measurements and poorly supported by regional stratigraphic correlations. In the 4° SE dip case, the Jm would be stratigraphically equivalent to lower portions of Glen Torridon and units in the Mt. Sharp group would have comparable thicknesses greater than those in the 0° dip case. If the dip were 10° SE, which is inconsistent with all measurements, Glen Torridon and the sulfate-bearing (fractured intermediate) unit would be stratigraphically thick compared to VRR.

3.6.4 Implications for Depositional Environment

Knowledge of the orientation of the Mt. Sharp group also carries implications for understanding how sediment accumulation in Gale crater contributed to the formation of lower Mt. Sharp. Mechanisms for mound formation that invoke erosion to present

morphology may be supported by flat-lying or shallowly dipping strata (e.g. Andrews-Hanna et al., 2010; Day et al., 2016; Kite et al., 2013; Malin and Edgett, 2000), whereas if the mounds grew in place on preexisting topography (Kite et al., 2013, 2016), the constituent bedding should be closer to the regional dip.

The interpretation that dips within VRR and BPm are effectively flat supports the notion that, at least near the Glen Torridon region, strata were deposited horizontally on an equipotential surface or shallowly dipping and subsequently eroded to their present form (Grotzinger et al., 2015), and hence the strata traversed by the Curiosity rover up through VRR did not directly contribute to the construction of Mt. Sharp via anticompensational stacking. Even the steepest northward dips allowed by regional stratigraphic correlations (~2° NW, section 3.5) are significantly shallower than the 5-6° regional slope, requiring significant erosion to account for the discrepancy between the primary layer orientations and modern slope. This is consistent with the lacustrine hypothesis for accumulation of much of the Murray formation (Fedo et al., 2017; Grotzinger et al., 2015; Rivera-Hernandez et al., 2020; Stack et al., 2019). Flat dips in the Mt. Sharp group do not necessarily dispute the possibility that the bulk of Mt Sharp formed by the accretion of draping strata in a mound shape (e.g. see hybrid model in Grotzinger et al., 2015, their Figure 8), as downslope layer orientation measurements in Gale crater are, with the exception of measurements on VRR in Fraeman et al., 2013, limited to the sulfate unit and above (Table 3.2; Kite et al., 2016). Anticompensational stacking is supported by many orbiter-based layer orientation measurements on sedimentary mounds, including in Gale crater above Glen Torridon, that show downslope bedding attitudes (Kite et al., 2016). Curiosity will eventually reach the sulfate-bearing unit where it can evaluate whether the layer orientations are consistent with anticompensational stacking, but quantitative rover-based assessments of layer orientations above Glen Torridon are not yet possible.

3.7 Conclusions and Imaging Recommendations

We have presented the first in situ constraints on the orientation of Mt. Sharp group strata using a combination of measurements made from stereo Mastcam images and regional

stratigraphic correlations. Bed orientations were measured in the Blunts Point, Pettegrove Point, and Jura members of the Murray formation. We implemented the PCA-based analytical approach of Quinn and Ehlmann (2019b) in conjunction a Monte Carlo bootstrapping technique to account for non-uniform stereo errors and a variance-based framework for computing statistically based stereo errors. Even in with relatively low plane fit uncertainty, true variations in strata orientation, likely predominantly due to post-depositional rotation or deformation (e.g. impact cratering), make it difficult to tightly constrain regional orientations by averaging the attitudes of bedding measured in situ at different sites. In situ measurements constrain regional attitudes to be within several degrees of horizontal. Regional stratigraphic correlations of rock targets within the so-called "Flodigarry facies", a package of rocks at the base of the Pettegrove Point – Jura Member contact, constrain dips to be between ~3° SE and 2° NW regionally. The absence of lithologies matching the Pettegrove Point member within the areas of Glen Torridon explored thus far by the Curiosity rover constrains dips to be no more than a few degrees NW or indicates that the strata are unrecognizable or laterally discontinuous. As the rover continues its traverse through Glen Torridon, the identification or absence of lithologies matching the Blunts Point member may further constrain regional structural orientation, as its presence in Glen Torridon would suggest dips are regionally higher than we predict.

Overall, the results of this study suggest that the strata comprising the Blunts Point, Pettegrove Point, and Jura members are approximately horizontal, consistent with sediment deposition on a flat, equipotential surface. At least part of the Glen Torridon trough is stratigraphically equivalent to the Jura member of VRR. There is a discrepancy between the orientation of VRR member boundaries as measured from HiRISE, where they dip ~6-7° N, and the dip constraints in this study, indicating that the member boundaries and the strata that comprise them are discordant. This discordancy may arise from the possibility that VRR members are distinguished primarily by diagenetic processes that did not follow strata boundaries, in which case stratigraphic correlations between VRR members and strata in the Glen Torridon trough must be treated cautiously, as member correlations and stratigraphic correlations may differ.

This study also highlights potential improvements to imaging strategies that could benefit MSL, Mars2020, and future rover missions with stereo imaging capabilities. The greatest challenge in deriving accurate rover-based attitude measurements, apart from confidence that the observed orientations are primary, is the poor ratio of plane extent (described by the $\bar{x}_1 - \bar{x}_2$ plane) to the error in the plane fit $\bar{x}_3$, which results from a combination of limited outcrop exposure and the small stereo baseline of the Mastcams and Navcams. Even scenes with relatively long bedding exposures can yield highly uncertain fits if traces fall predominantly along a single principal component axis. The uncertainty of plane solutions can be improved by shortening the distance to targets to reduce the range error (typically to distances of less than 10 m), stacking multiple bed traces from a single scene to increase the sampling extent in the $\bar{x}_1 - \bar{x}_2$ plane, or collecting stereo images of the same target from multiple positions (i.e. multiple baseline stereo imaging).

As Curiosity continues its traverse of Glen Torridon, we expect that the methods described here will be utilized to validate the interpretation of the regional structural orientation of the Mt. Sharp group as flat, and eventually to characterize the orientation of layers in the sulfate-bearing strata.

3.8 Acknowledgments

Mastcam images presented in this paper are archived in the Planetary Data System (pds.nasa.gov). Archives of all Mastcam stereo products will be available via the NASA Planetary Data System (PDS) through the Mastcam Stereo Analysis and Mosaics (MSAM) project (Deen et al., 2018). All derived bed trace products are archived at CaltechDATA (doi:10.22002/D1.1318). The software used to fit bedding planes is archived at CaltechDATA (Attitude, doi:10.22002/D1.1211, https://data.caltech.edu/records/1211). We are grateful to the Mars Science Laboratory Project engineering and science teams, as well as MSL team members who participated in tactical and strategic operations, for their diligent efforts required to collect the data presented here. Thanks to the MSL sed-strat working group, Kevin Lewis, Maddie Turner, and Edwin Kite for their input that improved the material presented in this manuscript. We also thank David Rubin and an anonymous

reviewer for their input. B.L.E. acknowledges support from the MSL Participating Scientist Program. A portion of this research was carried out at the Jet Propulsion Laboratory, California Institute of Technology, under a contract with the National Aeronautics and Space Administration.

Appendix

Text A1 provides additional details on how confidence intervals are created in the variance-limited framework. Figures A1-A3 and Table A1 in the supporting information portray in situ bed orientation measurements of the same targets presented in the main text, but with the different stereo error cases discussed in section 3.2.3 (1σ and 5σ). The 1σ case, in which stereo errors are assumed to typically be large relative to trace extents, likely overestimate the contribution of stereo errors to uncertainty and should be treated only as examples of how large stereo errors can skew the average dip solution. Figure A4 provides an example of the Blunts Point member extending into the Glen Torridon region west of the rover's traverse.

Text 3.A1

Confidence intervals are created by applying the Fisher ($F_{a,d,n-d}$) statistical distribution as

$$\mathbf{h} = \boldsymbol{\lambda} + \mathbf{a}\mathrm{F}_{\mathrm{a,d,n-d}}\boldsymbol{\sigma}_{\boldsymbol{\lambda}}, \qquad (2.A1)$$

where $\mathbf{h}$ denotes the hyperbolic error space of the plane, $\boldsymbol{\lambda}$ remains the PCA eigenvectors, $\mathbf{a} = [-\mathbf{1}. -\mathbf{1}, \mathbf{1}]$ controls the direction along which errors are applied, and $\boldsymbol{\sigma}_{\boldsymbol{\lambda}}$ is the standard error of the eigenvectors, expressed in the noise variance framework (Quinn and Ehlmann, 2019) as

$$\boldsymbol{\sigma}_{\boldsymbol{\lambda}}^{\mathbf{2}} = \frac{4\boldsymbol{\lambda}\boldsymbol{\lambda}_{\mathbf{3}}}{n-2} \qquad (2.A2)$$

for sample size n.

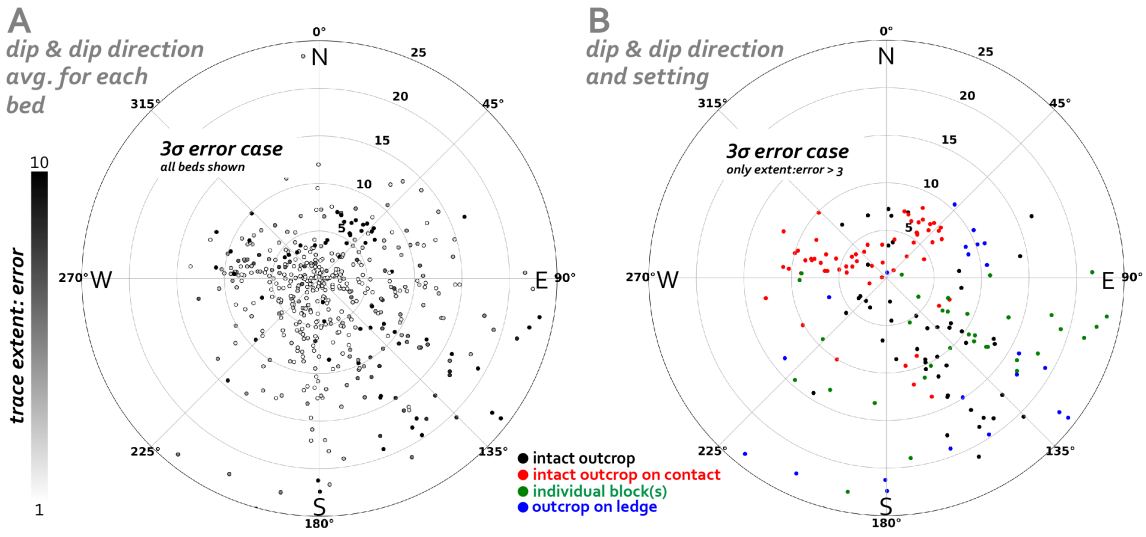

Figure 3.A1. (**A**) Average dip angle and dip direction of every bed measured in this study using the 3σ stereo error case. Errors, which are often significant, are shown in Figure 9. Each point represents the average solution for one bedding plane. Points are shaded according to the minimum ratio of the spatial extent of the trace along $\bar{\mathbf{x}}_1$ or $\bar{\mathbf{x}}_2$ to errors along those axes (i.e. white points have small traces relative to the magnitude of errors). (**B**) Classification of the solutions from (A) with traces that exceed a spatial extent to error ratio of 3 along both principal components, according to whether the bed is part of an intact outcrop, an intact outcrop on a contact, an outcrop on the side of a ledge (defined here as a regional slope >20°), or an individual block.

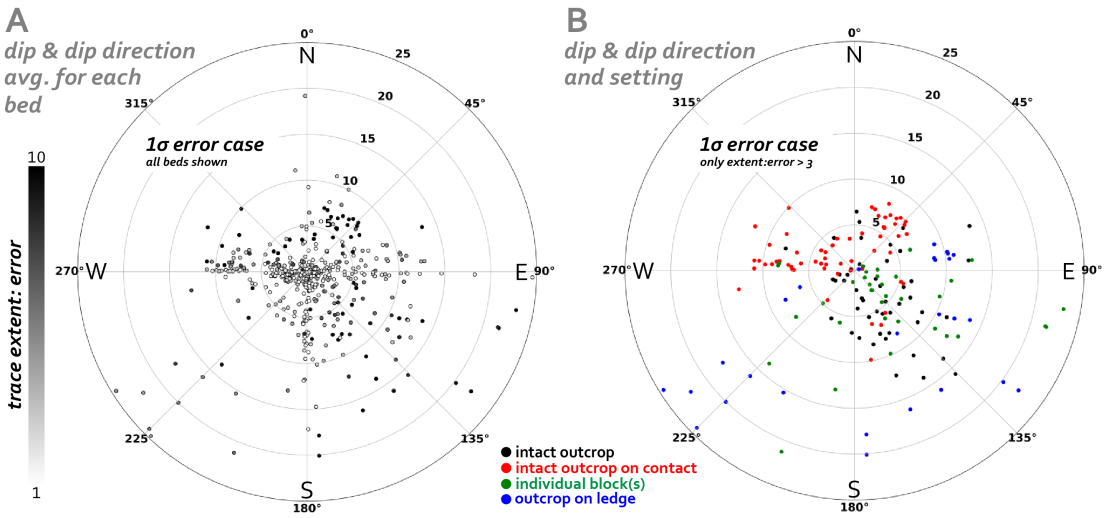

Figure 3.A2. (**A**) Average dip angle and dip direction of every bed measured in this study using the 1σ stereo error case. Errors, which are often significant, are shown in Figure 3.9. Each point represents the average solution for one bedding plane. Points are shaded according to the minimum ratio of the spatial extent of the trace along $\bar{\mathbf{x}}_1$ or $\bar{\mathbf{x}}_2$ to errors along those axes (i.e. white points have small traces relative to the magnitude of errors). (**B**) Classification of the solutions from (a) with traces that exceed a spatial extent to error ratio of 3 along both principal components, according to whether the bed is part of an intact outcrop, an intact outcrop on a contact, an outcrop on a regional slope >20°, or an individual block.

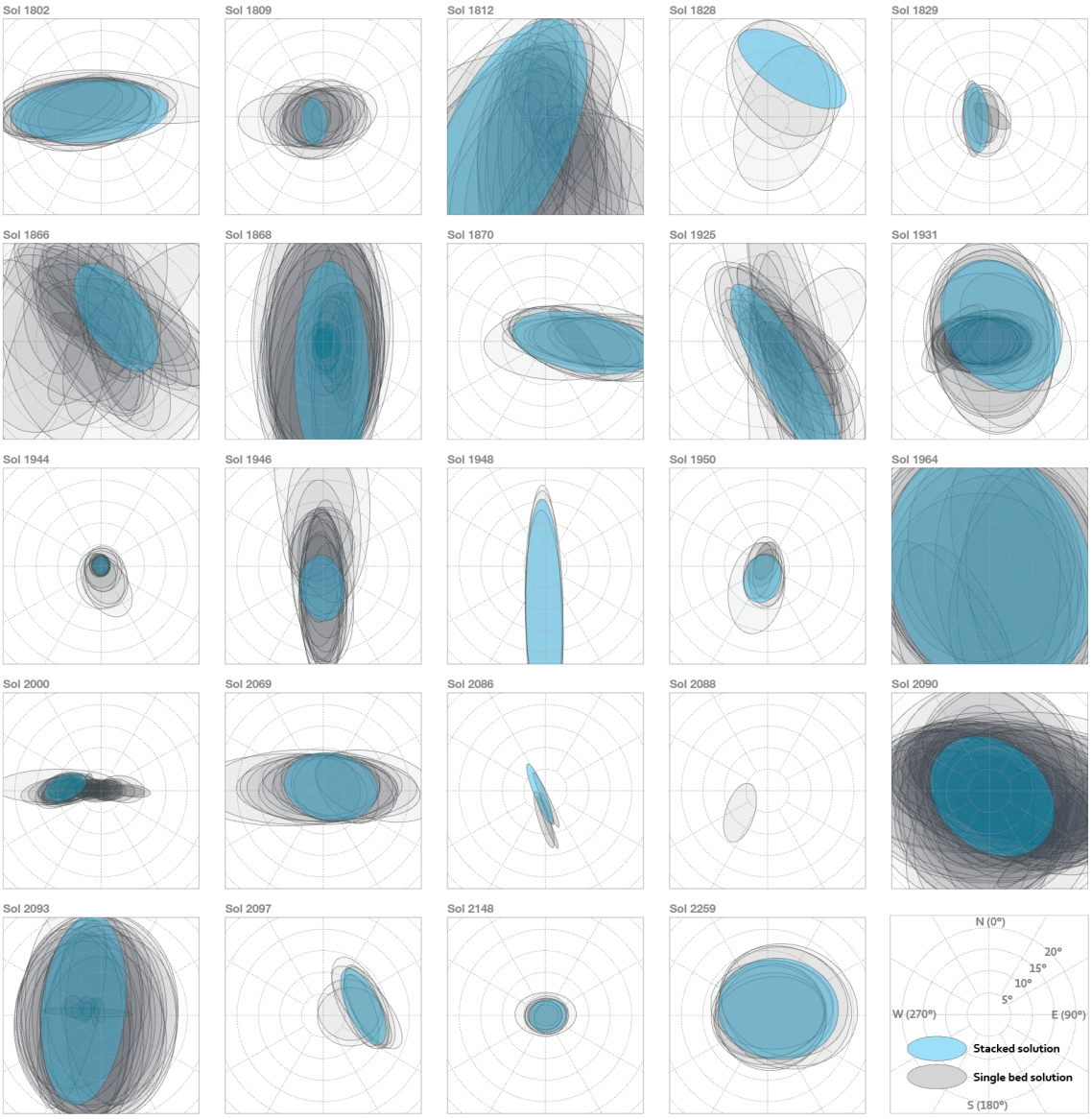

Figure 3.A3. Range of possible dip and dip azimuth solutions at different sites, grouped by sol. Gray ellipses denote the solution space of individual bed traces. Blue ellipses denote the solution space of stacked traces from that sol. Not all individual traces shown were necessarily used to produce the stacked solutions for a given sol. All single bed solutions shown had trace extent to error extent ratios of at least five along the first and second principal component axes. Using 1σ error case.

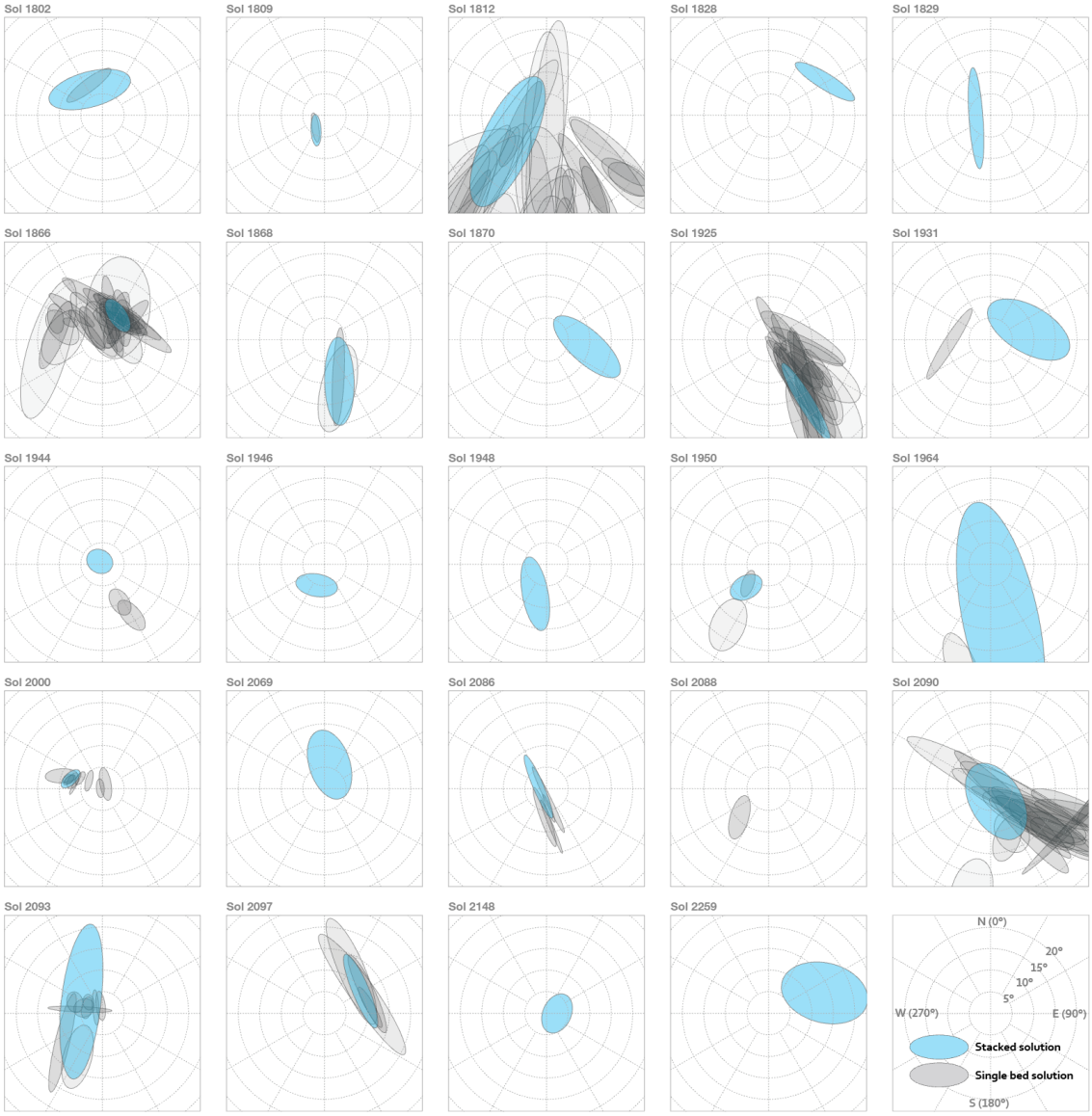

Figure 3.A4. Range of possible dip and dip azimuth solutions at different sites, grouped by sol. Gray ellipses denote the solution space of individual bed traces. Blue ellipses denote the solution space of stacked traces from that sol. Not all individual traces shown were necessarily used to produce the stacked solutions for a given sol. All single bed solutions shown had trace extent to error extent ratios of at least five along the first and second principal component axes. Using 5σ error case.

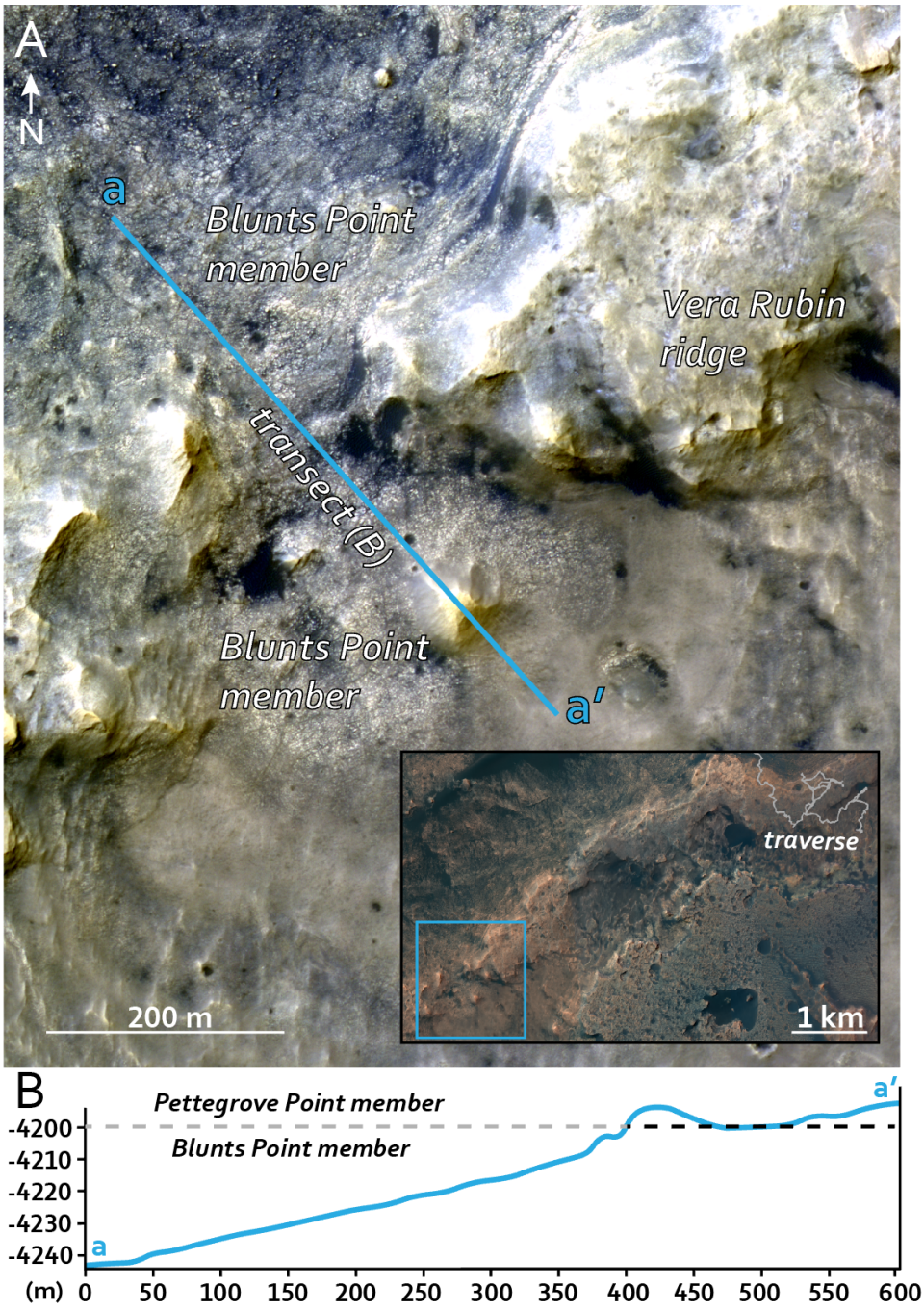

Figure 3.A5. (**A**) Erosional window in Vera Rubin ridge several km west of the Curiosity rover where the Blunts Point member is seen extending into Glen Torridon. (**B**) Transect from (a) showing a remnant portion of the Pettegrove Point member overlying the Blunts Point member on either side.

Table 3.A1. DIP MEASUREMENTS OF VRR MEMBER CONTACTS FROM HIRISE AND STACKED DIP MEASUREMENTS FROM STEREO MASTCAM IMAGES ON VRR (1σ STEREO ERROR CASE)

Sol or ID	Member	Outcrop Type	Regional Slope	Regional Dip Direction	n	L (m)	Dip	Dip Direction	θ_{min}	θ_{min}	Rake	Second PC to Error Ratio
Traces of VRR member contacts from HiRISE												
BPm – PPm contact	BPm – PPm	-	-	-	352	3873	7.30°	334.4°	0.30°	3.74°	91.3°	-
PPm – Jm contact	PPm – Jm	-	-	-	140	1076	6.56°	332.1°	0.22°	1.11°	71.7°	-
Joint fitting of parallel bedding planes on VRR												
1802	BPm	Intact	18.9°	32.0°	1119	0.51	3.04°	294.8°	7.21°	18.27°	62.05°	3.86
1809	BPm – PPm	Intact	18.5°	7.6°	1689	0.14	2.08°	237.6°	4.49°	5.49°	59.45°	8.35
1812	PPm (on ledge)	Intact	20.6°	353.9°	1262	0.06	9.88°	239.7°	14.00°	30.32°	124.09°	14.30
1828	PPm	Intact	8.0°	316.0°	468	0.21	12.62°	27.3°	5.92°	14.33°	5.60°	6.76
1829	PPm (on ledge)	Blocks	36.3°	327.6°	827	0.13	3.13°	265.7°	2.85°	8.00°	179.66°	2.96
1866	PPm – Jm	Intact	18.7°	10.0°	1781	0.25	6.64°	32.1°	7.14°	14.11°	25.17°	33.08
1868	PPm – Jm	Intact	12.4°	3.8°	320	0.20	6.65°	163.2°	8.64°	24.85°	105.89°	4.40
1870	Jm	Intact	15.3°	330.4°	808	0.11	8.84°	91.8°	6.77°	16.82°	81.73°	2.72
1925	Jm	Intact	14.3°	337.1°	1615	0.13	8.90°	151.1°	6.00°	24.05°	89.34°	14.90
1931	Jm	Blocks	18.5°	351.6°	-	-	-	-	-	-	-	-
1944	Jm	Intact	15.7°	79.6°	878	0.79	0.13°	326.0°	1.85°	2.13°	60.41°	4.21
1946	Jm	Intact	18.3°	92.8°	1436	0.18	5.12°	182.9°	5.13°	7.66°	81.72°	2.95
1948	Jm	Blocks	12.8°	257.3°	348	0.84	11.24°	181.3°	4.27°	26.95°	87.45°	1.88
1950	Jm	Intact	17.9°	261.8°	527	0.47	3.07°	201.6°	4.25°	5.68°	97.27°	4.77
1964	Jm	Block	8.0°	346.2°	419	0.04	1.40°	178.1°	23.33°	29.89°	74.47°	2.71
2000	PPm – Jm	Intact	18.5°	355.8°	1576	0.25	0.39°	312.2°	2.46°	3.37°	136.83°	4.20
2069	BPm	Intact	18.3°	340.9°	1459	0.74	1.98°	63.2°	7.77°	10.93°	126.79°	3.19
2086	BPm	Intact	18.0°	336.1°	517	0.87	1.47°	241.4°	1.32°	7.42°	6.62°	16.90
2088	BPm	Block	19.7°	357.8°	-	-	-	-	-	-	-	-
2090	BPm	Block	-	-	1190	0.06	1.45°	154.5°	12.22°	15.76°	66.99°	5.87
2093	BPm – PPm	Intact	18.0°	344.7°	614	0.36	2.34°	301.7°	1.30°	3.83°	141.93°	14.87
2097	BPm – PPm (on ledge)	Intact	24.1°	32.3°	659	0.46	9.53°	77.8°	3.77°	9.53°	12.38°	6.54
2148	BPm – PPm (on ledge)	Intact	48.0°	358.4°	502	0.13	0.51°	98.1°	3.83°	4.30°	71.55°	1.51
2259	Jm	Blocks	6.6°	54.4°	720	0.16	2.87°	57.9°	11.70°	13.99°	52.79°	2.04

Table 3.A2. NAME OF MASTCAM MOSAICS USED IN THIS STUDY

Sol	Mosaic number(s)
1802	9300, 9302
1809	9337, 9338
1812	9354
1828	9456
1829	9461, 9462
1866	9753
1868	9766
1870	9772
1925	10045
1931	10081
1944	10158
1946	10168
1948	10180
1950	10206
1964	10272
2000	10489
2069	10984
2086	11111
2088	11129
2090	11137
2093	11164
2097	11330
2148	11541
2259	12090

References

Abarca, H., Deen, R., Hollins, G., Zamani, P., Maki, J., Tinio, A., et al. (2019). Image and data processing for InSight lander operations and science. *Space Science Reviews*, 215(2), 1–53. https://doi.org/10.1007/s11214-019-0587-9.

Alexander, D. & Deen, R. (2017). Mars Science Laboratory project software interface specification (SIS); camera & LIBS experiment data record (EDR) and reduced data record (RDR) data products, version 4.0. JPL doc. D-38107, data set MSL-M-NAVCAM-2-EDR-V1.0, NASA planetary data system.

Andrews-Hanna, J. C., Zuber, M. T., Arvidson, R. E., & Wiseman, S. M. (2010). Early Mars hydrology: Maridiani playa deposits and the sedimentary record of Arabia Terra. *Journal of Geophysical Research*, 115, E06002. https://doi.org/10.1029/2009je003485

Arvidson, R. E., Ashley, J. W., Bell, J. F. III, Chojnacki, M., Cohen, J., Economou, T. E., et al. (2011). Opportunity Mars Rover mission: Overview and selected results from Purgatory ripple to traverses to Endeavour crater. *Journal of Geophysical Research*, 116, E00F15. https://doi.org/10.1029/2010JE003746.

Banham, S. G., Gupta, S., Rubin, D. M., Watkins, J. A., Sumner, D. Y., Edgett, K. S., et al. (2018). Ancient Martian aeolian processes and palaeomorphology reconstructed from the Stimson formation on the lower slope of Aeolis Mons, Gale crater, Mars. *Sedimentology*, 65(4), 993–1042. https://doi.org/10.1111/sed.12469.

Barnes, R., Gupta, S., Traxler, C., Ortner, T., Bauer, A., Hesina, G., et al. (2018). Geological analysis of Martian rover-derived digital outcrop models using the 3-D visualization tool, planetary robotics 3-D viewer—Pro3D. *JGR: Planets*, 5, 285–307. https://doi.org/10.1002/2018EA000374.

Bell, J. F. III, Godber, A., McNair, S., Caplinger, M. A., Maki, J. N., Lemmon, M. T., et al. (2017). The Mars Science Laboratory Curiosity rover Mastcam instruments: Preflight and in-flight calibration, validation, and data archiving. *Earth and Space Science*, 4, 396–452. https://doi.org/10.1002/2016EA000219

Bennett, K., Fox, V. K., Bryk, A. B., Fedo, C., Vasavada, A. R., Dehouck, E., et al. (2019). Results from the Curiosity rover's traverse through the clay-bearing Glen Torridon region in Gale crater. *AGU Fall Meeting*. P33B-01.

Bennett, K., Rivera-Hernandez, F., Tinker, C., Horgan, B., Fey, D. M., Edwards, C., et al. (2020). MAHLI at Vera Rubin ridge, Gale crater, Mars: Fine-scale features reveal extensive diagenesis. *JGR: Planets*. In press.

Day, M., & Kocurek, G. (2016). Observations of an aeolian landscape: From surface to orbit

in Gale Crater. *Icarus*, 280, 37–71. https://doi. org/10.1016/j.icarus.2015.09.042.

Deen, R., Zamani, P., Abarca, H., Maki, J. (2019). InSight project software interface specification (SIS); Camera experiment data record (EDR) and reduced data record (RDR) data products. v.3.3. JPL D-56937. NASA Planetary Data System.

DiBiase, R. A., Limaye, A. B., Scheingross, J. S., Fischer, W. W., & Lamb, M. P. (2013). Deltaic deposits at Aeolis Dorsa: Sedimentary evidence for a standing body of water on the northern plains of Mars. *Journal of Geophysical Research*, 118, 1285–1302. https://doi.org/ 10.1002/jgre.20100.

Edgar, L. A., Gupta, S., Rubin, D. M., Lewis, K. W., Kocurek, G. A., Anderson, R. B., et al. (2017). Shaler: A fluvial sedimentary deposit on Mars. *Sedimentology*, 65(1), 96–122. https://doi.org/10.1111/sed.12370.

Edgar, L., Fedo, C. M., Gupta, S., Banham, S. G., Fraeman, A. A., Grotzinger, J. P., et al. (2020). A lacustrine paleoenvironment recorded at Vera Rubin Ridge, Gale crater: Overview of the sedimentology and stratigraphy observed by the Mars Science Laboratory Curiosity rover. *JGR: Planets*, 125, e2019JE006307. https://doi.org/10.1029/2019JE006307.

Fedo, C., Fedo, C., Grotzinger, J. P., Edgar, L. A., Fox, V. K., Bennett, K. A., et al. (2019). Connecting lower Mount Sharp strata: How does the clay-bearing unit in Glen Torridon relate to the Murray formation, Gale crater, Mars. *AGU Fall Meeting*. P31A-3422.

Fedo, C., Grotzinger, J.P., Bryk, A., Edgar, L. A., Bennett, K., Fox, K., et al. (2020). Ground-based stratigraphic correlation of the Jura and Knockfarril Hill members of the Murray formation, Gale crater: Bridging the Vera Rubin ridge-Glen Torridon divide. *LPSC 51*. Abstract 2345.

Fedo, C., Grotzinger, J. P., Gupta, S., Fraeman, A., Edgar, L., Edgett, K., et al. (2018). Sedimentology and stratigraphy of the Murray formation, Gale Crater, Mars. *LPSC 49*. Abstract 2078.

Fox, V., Bennett, K. A., Bristow, T., Ehlmann, B., House, C., Fairén, A. G., et al. & the MSL Science Tea (2019). Exploring the clay-bearing unit with the Curiosity rover. *LPSC 50*. Abstract 2826.

Fraeman, A. A., Edgar, L. A., Rampe, E. B., Thompson, L., Frydenvang, J., Bryk, A., Fedo, C. M., et al. (2020). The origin of Vera Rubin ridge: Overview and results from Curiosity's exploration campaign. In review.

Fraeman, A. A., Arvidson, R. E., Catalano, J. G., Grotzinger, J. P., Morris, R. V., Murchie, S. L., et al. (2013). A hematite-bearing layer in Gale Crater, Mars: Mapping and

implications for past aqueous conditions. *Geology*, 41(10). https://doi.org/10.1130/G34613.1.

Fraeman, A. A., Ehlmann, B. L., Arvidson, R. E., Edwards, C. S., Grotzinger, J. P., Milliken, R. E., et al. (2016). The stratigraphy and evolution of lower Mount Sharp from spectral, morphological, and thermophysical orbital data sets. *JGR: Planets*, 121, 1713–1736. https://doi.org/10.1002/2016JE005095.

Fueten, F., Stesky, R. M., & MacKinnon, P. (2005). Structural attitudes of large scale layering in Valles Marineris, Mars, calculated from Mars Orbiter Laser Altimeter data and Mars Orbiter camera imagery. *Icarus*, 175(1). https://doi.org/10.1016/j.icarus.2004.11.010.

Goudge, T. A., Milliken, R. E., Head, J. W., Mustard, J. F., & Fassett, C. I. (2017). Sedimentological evidence for a deltaic origin of the western fan deposit in Jezero crater, Mars and implications for future exploration. *Earth and Planetary Science Letters*, 458. https://doi. org/10.1016/j.epsl.2016.10.056.

Grotzinger, J. P, & Milliken, R. (2012). The sedimentary rock record of Mars: Distribution, origins, and global stratigraphy. In J. P. Grotzinger & R. Milliken (Eds.), Sedimentary geology of Mars (Vol. 102, pp. 1–48). Tulsa, OK: SEPM.

Grotzinger, J. P., Sumner, D. Y., Kah, L. C., Stack, K., Gupta, S., Edgar, L., et al., & MSL Science Team (2014). A habitable fluvio-lacustrine environment at Yellowknife Bay, Gale Crater, Mars. *Science*, 343(6169), 1242777. https://doi.org/10.1126/science.1242777.

Grotzinger, J. P., Gupta, S., Malin, M. C., Rubin, D. M., Schieber, J., Siebach, K., et al. (2015). Deposition, exhumation, and paleoclimate of an ancient lake deposit, Gale crater, Mars. *Science*, 350(6257). https://doi.org/10.1126/science.aac7575.

Gwizd, S., Fedo, C., Grotzinger, J., Edgett, K., Rivera-Hernandez, F., Stein, N. (2019). Depositional history of the Hartmann's Valley member, Murray formation, Gale crater, Mars. *LPSC 49*. Abstract 2150.

Hayes, A. G., Grotzinger, J. P., Edgar, L. A., Squyres, S. W., Watters, W. A., & Sohl-Dickstein, J. (2011). Reconstruction of eolian bed forms and paleocurrents from cross-bedded strata at Victoria Crater, Meridiani Plaum, Mars. *Journal of Geophysical Research*, 116, E00F21. https://doi.org/10.1029/2010JE003688.

Hurowitz, J. A., Grotzinger, J. P., Fischer, W. W., McLennan, S., Milliken, R. E., Stein, N., et al. (2017). Redox stratification of an ancient lake in Gale crater, Mars. *Science*, 356(6341). https://doi.org/10.1126/science.aah6849.

Hynek, B. M., & Phillips, R. J. (2008). The stratigraphy of Meridiani Planum, Mars, and implications for the layered deposits' origin. *Earth and Planetary Science Letters*, 274(1–2). https://doi.org/10.1016/j.epsl.2008.07.025.

Kite, E. S., Lewis, K. W., Lamb, M. P., Newman, C. E., & Richardson, M. I. (2013). Growth and form of the mound in Gale Crater, Mars: Slope wind enhanced erosion and transport. *Geology*, 41(5). https://doi.org/10.1130/G33909.1.

Kite, E. S., Sneed, J., Mayer, D. P., Lewis, K. W., Michaels, T. I., Hore, A., & Radkin, S. C. R. (2016). Evolution of major sedimentary mounds on Mars: Buildup via anticompensational stacking modulated by climate change. *JGR: Planets*, 121, 2282–2324. https://doi.org/10.1002/2016JE005135.

Le Deit, L., Hauber, E., Fueten, F., Pondrelli, M., Pio Rossi, A., & Jaumann, R. (2013). Sequence of infilling events in Gale Crater, Mars: Results from morphology, stratigraphy, and mineralogy. *JGR: Planets*, 118, 2439–2473. https://doi.org/ 10.1002/2012JE004322.

Lewis, K. W., & Aharonson, O. (2006). Stratigraphic analysis of the distributary fan in Eberswalde crater using stereo imagery. *Journal of Geophysical Research*, 111, E06001. https://doi.org/10.1029/2005JE002558.

Lewis, K. W., Aharonson, O., Grotzinger, J. P., Kirk, R. L., McEwen, A. S., & Suer, T. A. (2008). Quasi-periodic bedding in the sedimentary rock record of Mars. *Science*, 322(1532). https://doi.org/10.1126/science.1161870.

Lewis, K. W., & Aharonson, O. (2014). Occurrence and origin of rhythmic sedimentary rocks on Mars. *JGR: Planets*, 119, 1432–1457. https://doi.org/10.1002/2013JE004404.

Lewis, K. W., Aharonson, O., Grozinger, J. P., Squyres, S. W., Bell, J. F., Crumpler, L. S., & Schmidt, M. E. (2008). Structure and stratigraphy of home plate from the Spirit Mars exploration rover. *Journal of Geophysical Research*, 113, E12S36. https://doi.org/10.1029/ 2007JE003025.

Lewis, K.W. and Turner, M.L. (2019). Geologic structure of the Vera Rubin Ridge, Gale Crater, Mars. *LPSC 50*. Abstract 2216.

Lewis, K.W., Turner, M.L., and Stack, K.M. (2020). Implications of non-horizontal stratigraphy at Mount Sharp, Gale Crater, Mars. *LPSC 51*. Abstract 2544.

Maki, J., Thiessen, D., Pourangi, A., Kobzeff, P., Litwin, T., Scherr, L., et al. (2012). The Mars Science Laboratory engineering cameras. *Space Science Reviews*, 170(1-4), 77–93. https://doi.org/10.1007/s11214-012-9882-4.

Malin, M. C., & Edgett, K. S. (2000). Sedimentary rocks of early Mars. *Science*, 290, 1927–1937. https://doi.org/10.1126/science.290.5498.1927.

Malin, M. C., Ravine, M. A., Caplinger, M. A., Shaemi, F. T., Schaffner, J. A., Maki, J. N., et al. (2017). The Mars Science Laboratory (MSL) Mast cameras and descent imager: I. Investigation and instrument descriptions. *Earth and Space Science*, 4, 506–539. https://doi.org/10.1002/2016EA000252.

Metz, J., Grotzinger, J., Okubo, C., & Milliken, R. (2010). Thin-skinned deformation of sedimentary rocks in Valles Marineris, Mars. *Journal of Geophysical Research*, 115, E11004. https://doi.org/10.1029/2010JE003593.

Milliken, R. E., Grotzinger, J. P., & Thomson, B. J. (2010). Paleoclimate of Mars as captured by the stratigraphic record in Gale Crater. *Geophysical Research Letters*, 37, L04201. https://doi.org/10.1029/2009GL041870.

Minitti, M. E., Malin, M. C., van Beek, J. K., Caplinger, M., Maki, J. N., Ravine, M., et al. (2019). Distribution of primary and secondary features in the Pahrump Hills outcrop (Gale crater, Mars) as seen in a Mars Descent Imager (MARDI) "sidewalk" mosaic. *Icarus*, 328, 194–209. https://doi.org/10.1016/j.icarus.2019.03.005.

Okubo, C. H. (2010). Structural geology of Amazonian-aged layered sedimentary deposits in southwest Candor Chasma, Mars. *Icarus*, 207(1). https://doi.org/10.1016/j.icarus.2009.11.012.

Okubo, C. H., Lewis, K. W., McEwen, A. S., & Kirk, R. L. (2008). Relative age of interior layered deposits in southwest Candor Chasma based on high-resolution structural mapping. *Journal of Geophysical Research*, 113, E12002. https://doi.org/10.1029/2008JE003181.

Quinn, D. P., & Ehlmann, B. L. (2019a). The deposition and alteration history of the northeast Syrtis Major layered sulfates. *JGR: Planets*, 124, 1743–1782. https://doi.org/10.1029/2018JE005706.

Quinn, D. P., & Ehlmann, B. L. (2019b). A PCA-based framework for determining remotely sensed geological surface orientations and their statistical quality. *Earth and Space Science*, 6, 1378–1408. https://doi.org/10.1029/2018EA000416.

Rapin, W., Ehlmann, B. L., Dromart, G., Schieber, J., Thomas, N. H., Fischer, W. W., et al. (2019). An interval of high salinity in ancient Gale crater lake on Mars. *Nature Geoscience*, 12(11), 889–895. https://doi.org/10.1038/s41561-019-0458-8.

Rivera-Hernandez, F., Sumner, D. Y., Mangold, N., Stack, K. M., Forni, O., Newsom, H., et al. (2019). Using ChemCam LIBS data to constrain grain size in rocks on Mars: Proof

of concept and applications to rocks at Yellowknife Bay and Pahrump Hills, Gale crater. *Icarus*, 321, 82-98. https://doi.org/10.1016/j.icarus.2018.10.023.

Rivera-Hernandez, F., Sumner, D. Y., Mangold, N., Banham, S. G., Edgett, K. S., Fedo, C. M., et al. (2020). Grain size variations in the Murray formation: Stratigraphic evidence for changing depositional environments in Gale crater, Mars. *JGR: Planets*, 125, e2019JE006230. https://doi.org/10.1029/2019/JE006230.

Rubin, D.M. & Carter, C.L. (2006). Bedforms and cross-bedding in animation: Society for Sedimentary Geology (SEPM) Atlas Series.

Siebach, K. L., Fedo, C. M., Edgar, L. E., Edgett, K., Grotzinger, J. P., Fraeman, A. A., et al. (2019). Overview of Gale crater stratigraphy and sedimentology from 6 years of roving with Mars Science Laboratory. *LPSC 50*. Abstract 2132.

Squyres, S. W., Grotzinger, J. P., Arvidson, R. E., Bell, J. F. III, Calvin, W., Christensen, P. R., et al. (2004). In situ evidence for an ancient aqueous environment at Meridiani Planum, Mars. *Science*, 306(5702), 1709–1714. https://doi.org/10.1126/science.1104559.

Stack, K. E., Sun, V. Z., Arvidson, R. E., Fedo, C., Day, M., Bennett, K., et al. (2019). Origin of linear ridges in the clay-bearing unit of Mount Sharp, Gale Crater, Mars. *LPSC 50*. Abstract 1210.

Stack, K. M., Cofield, S. M., & Fraeman, A. A. (2017). Geologic map of the MSL Curiosity rover extended mission traverse of Aeolis Mons, Gale Crater, Mars. LPSC 48. Abstract 1889. Stack, K. M., Grotzinger, J. P., & Milliken, R. E. (2013). Bed thickness distributions on Mars: An orbital perspective. *JGR: Planets*, 118, 1323–1349. https://doi.org/10.1002/jgre.20092

Stein, N., Grotzinger, J. P., Schieber, J., Mangold, N., Hallet, B., Newsom, H., et al. (2018). Desiccation cracks provide evidence of lake drying on Mars, Sutton Island member, Murray formation, Gale Crater. *Geology*, 46(6), 515–518. https://doi.org/10.1130/G40005.1.

Turner, M.L. & Lewis, K.W. (2019). Geologic structure of the Vera Rubin ridge and clay-bearing Glen Torridon region, Gale crater, Mars. *AGU Fall Meeting*. P31A-3424.

Watters, W. A., Grotzinger, J. P., Bell, J., Grant, J., Hayes, A. G., Li, R., et al. (2011). Origin of the structure and planform of small impact craters in fractured targets: Endurance crater at Meridiani Planum, Mars. *Icarus*, 211(1). https://doi.org/10.1016/j.icarus.2010.08.030.

Williams, R. M. E., Grotzinger, J. P., Dietrich, W. E., Gupta, S., Sumner, D. Y., Wiens, R. C., et al. (2013). Martial fluvial conglomerates at Gale Crater. *Science*, 340(6136), 1068–1072. https://doi.org/10.1126/science.1237317.

Chapter 4

DESICCATION CRACKS PROVIDE EVIDENCE OF LAKE DRYING ON MARS, SUTTON ISLAND MEMBER, MURRAY FORMATION, GALE CRATER

N. Stein[1], J.P. Grotzinger[1], J. Schieber[2], N. Mangold[3], B. Hallet[4], H. Newsom[5], K.M. Stack[6], J.A. Berger[7], L. Thompson[8], K.L. Siebach[9], A. Cousin[10], S. Le Mouélic[3], M. Minitti[11], D.Y. Sumner[12], C. Fedo[13], C.H. House[14], S. Gupta[15], A.R. Vasavada[6], R. Gellert[16], R. C. Wiens[17], J. Frydenvang[18], O. Forni[10], P. Y. Meslin[10], V. Payré[19], and E. Dehouck[10]

[1]Division of Geological and Planetary Sciences, California Institute of Technology, Pasadena, California 91125, USA

[2]Department of Geological Sciences, Indiana University, Bloomington, Indiana 47405, USA

[3]Laboratoire Planétologie Géodynamique, UMR6112 CNRS/Université Nantes, Nantes, France

[4]Department of Earth and Space Sciences, University of Washington, Seattle, Washington 98105, USA

[5]Institute of Meteoritics and Department of Earth and Planetary Sciences, University of New Mexico, Albuquerque, New Mexico 87131, USA

[6]Jet Propulsion Laboratory, California Institute of Technology, Pasadena, California 91109, USA

[7]Department of Earth Sciences, University of Western Ontario, London, ON N6A 5B7, Canada

[8]Planetary and Space Science Centre, University of New Brunswick, NB E3B 5A3, Canada

[9]Department of Geosciences, Stony Brook University, Stony Brook, New York 11795, USA

[10]Institut de Recherche en Astrophysique et Planétologie, Université de Toulouse, UPS-CNRS-OMP, Toulouse, France

[11]Planetary Science Institute, Tucson, Arizona 85719, USA

[12]Department of Earth and Planetary Sciences, University of California, Davis, California 95616, USA

[13]Department of Earth and Planetary Sciences, University of Tennessee, Knoxville, Tennessee 37996, USA

[14]Department of Geosciences and Penn State Astrobiology Research Center, The Pennsylvania State University, University Park, Pennsylvania 16802, USA

[15]Department of Earth Science and Engineering, Imperial College London, London SW7 2AZ, UK

[16]Department of Physics, University of Guelph, Guelph, ON N1G 2W1, Canada

[17]Los Alamos National Laboratory, Los Alamos, New Mexico 87544, USA

[18]Natural History Museum of Denmark, University of Copenhagen, Copenhagen, Denmark

[19]Université de Lorraine, 54000 Nancy, France

This chapter was published as:

Stein, N.T. et al. (2018), Desiccation cracks provide evidence of lake drying on Mars, Sutton Island member, Murray formation, Gale crater. *JGR: Planets*, 46, 515-518. https://doi.org/10.1130/G40005.1.

4.1 Abstract

Mars Science Laboratory (MSL) Curiosity rover data are used to describe the morphology of desiccation cracks observed in ancient lacustrine strata at Gale crater, Mars, and to interpret their paleoenvironmental setting. The desiccation cracks indicate subaerial exposure of lacustrine facies in the Sutton Island member of the Murray formation. In association with ripple cross-stratification and possible eolian cross-bedding, these facies indicate a transition from longer-lived perennial lakes recorded by older strata to younger lakes characterized by intermittent exposure. The transition from perennial to episodically exposed lacustrine environments provides evidence for local to regional climate change that can help constrain Mars climate models.

4.2 Introduction

Reconstructions of ancient habitable environments on Mars increasingly depend on detailed analysis of sedimentary facies recording aqueous environments. Over the past decade, the Mars Exploration Rover Opportunity encountered ancient eolian, fluvial, and lacustrine environments deposited in hypersaline, acidic, sulfate- and hematite-enriched playas formed in interdune depressions at Meridiani Planum (e.g. Grotzinger et al., 2005). This setting contrasts with the clay- and magnetite-bearing, moderate pH, perennial lacustrine facies in Gale crater (Grotzinger et al., 2014, 2015; Hurowitz et al., 2017; Rampe et al., 2017). Suites of sedimentary structures, facies associations, and authigenic and diagenetic mineral assemblages were essential to recognize these paleoenvironmental settings. Previously, potential martian desiccation cracks were identified in multiple sedimentary deposits from orbit (e.g., El-Maarry et al., 2014) and in situ by rovers (Grotzinger et al., 2005, 2014).

The kilometers-thick sedimentary succession in Gale crater provides an opportunity to observe changes in surface environments over extended periods in martian history. Studies of basal strata in the informally named Murray formation demonstrated the presence of long-lived perennial lakes in Gale crater at ca. 3.6–3.2 Ga (Grotzinger et al.,

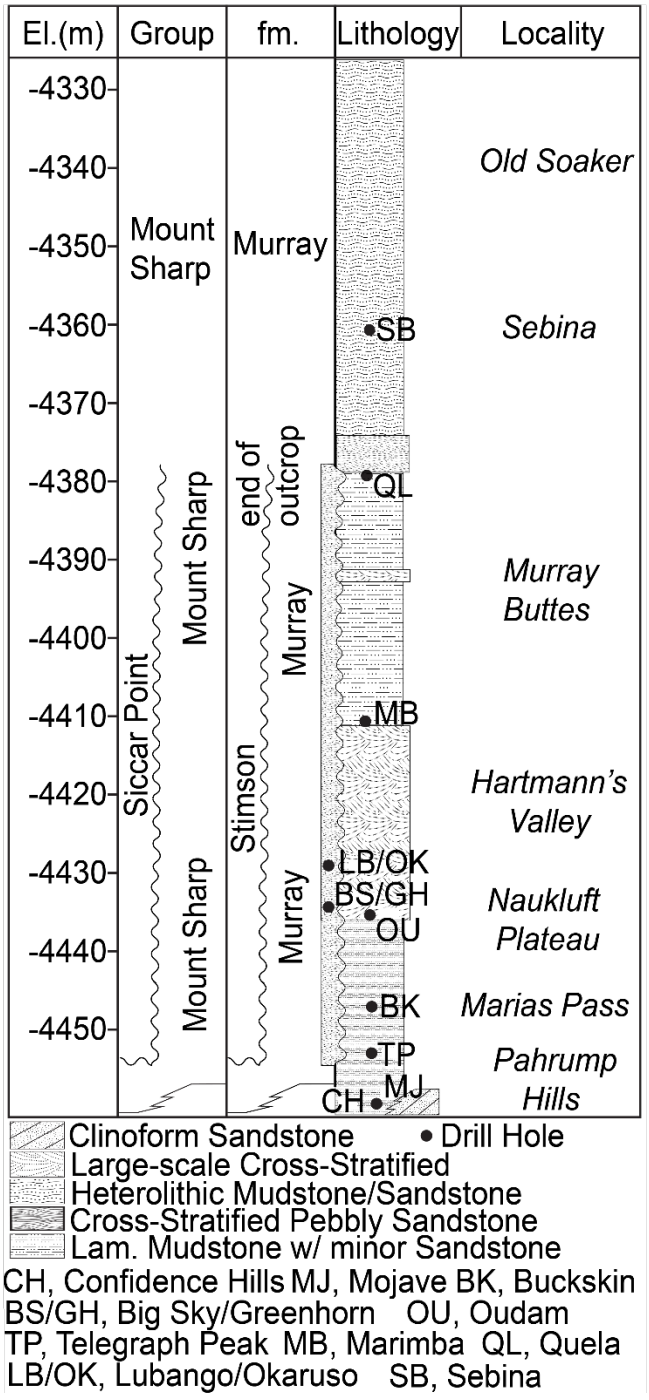

Figure 4.1. Stratigraphic column for the sedimentary facies of the Murray formation, Mars. Old Soaker (OS) rock slab is in the heterolithic facies of the Sutton Island member of the Murray formation. El.—elevation; Lam.—laminated.

2014, 2015; Hurowitz et al., 2017). Recent facies observations at higher stratigraphic levels (Fedo et al., 2017) may record an evolution of the environment over time. Here we present in situ evidence for lithified desiccation cracks in the Murray formation, indicating that the lakes may have partially dried in its younger history.

During Sols 1555–1571, Curiosity investigated a series of distinctive centimeter-scale reticulate ridges on the surfaces of several slabs of rock that expose bedding planes in the Sutton Island member of the Murray formation. Their morphology and composition is characterized to determine if they formed via desiccation and to examine implications for the deposition of associated strata.

4.3 Geologic Setting

As of Sol 1700, the Curiosity rover has explored more than 200 m of strata consisting of fluvial, deltaic, lacustrine, and eolian sediments (Williams et al., 2013; Grotzinger et al., 2014, 2015; Banham et al., 2016; Edgar et al., 2017) represented by the Bradbury group, the interfingering and overlying Murray formation (Mount Sharp group), and the unconformably overlying Stimson formation (Siccar Point group) (Fig. 4.1). The first ~25-m-thick Murray interval consists dominantly of finely laminated mudstones with minor siltstones and sandstones of lacustrine origin (Grotzinger et al., 2015). It is overlain by an ~25-m-thick interval with decimeter- to meter-scale cross-stratification that suggests sediment transport as large bedforms or in channels (Fedo et al., 2017), followed by >30 m of finely laminated red/purple-hued mudstone with intervals of very fine sandstone, consistent with sediment accumulation in subaqueous lacustrine environments (Grotzinger et al., 2015; Fedo et al., 2017). These younger strata, comprising the Sutton Island member of the Murray formation, expose broken and tilted slabs of bedrock, including finely laminated red mudstones, centimeter-scale ripple cross-laminated mudstone, decimeter-scale cross-stratification, and massively bedded intervals of siltstone (Fedo et al. 2017).

4.4 Old Soaker Campaign

The focus of the investigation is an ~80-cm-long, 40-cm-wide rock slab called "Old Soaker" (OS) that exposes a bedding plane with a red surface marked by a network of ridges that form polygons (Fig. 4.2A). The red mudstone is ~1 cm thick and overlies a gray sandstone bed containing bedding-parallel seams of calcium sulfate ($CaSO_4$). OS and a similar nearby slab called "Squid Cove" (SC) were imaged with the Mast Camera (Mastcam) and the Mars Hand Lens Imager (MAHLI) to characterize the geometry and fill of the ridges. Their elemental compositions were examined with the rover's ChemCam Laser Induced Breakdown Spectrometer (LIBS) and Alpha-Particle X-Ray Spectrometer (APXS).

4.4.1 Methods

The geometries of the polygonal ridges were determined using MAHLI images to evaluate whether their shape is consistent with desiccation. Images of ridges and their junctions were traced to calculate vertex angle distributions, widths of ridges and the polygons they form, and ridge surface area. A three-dimensional (3-D) model of OS was generated from 76 MAHLI images processed using photogrammetry software. The grain sizes of the red and gray beds were measured with ~16 μm/pixel MAHLI images.

4.5 Results

4.5.1 Morphology of the Ridges and Surrounding Beds

The red surfaces of OS and SC are covered by networks of arcuate ridges with up to 5 mm of positive relief that define predominantly four-sided and some five-sided, 0.5–3.5-cm-wide polygons (Figs. 4.2B and 4.3A). Red surfaces of adjacent slabs also show raised

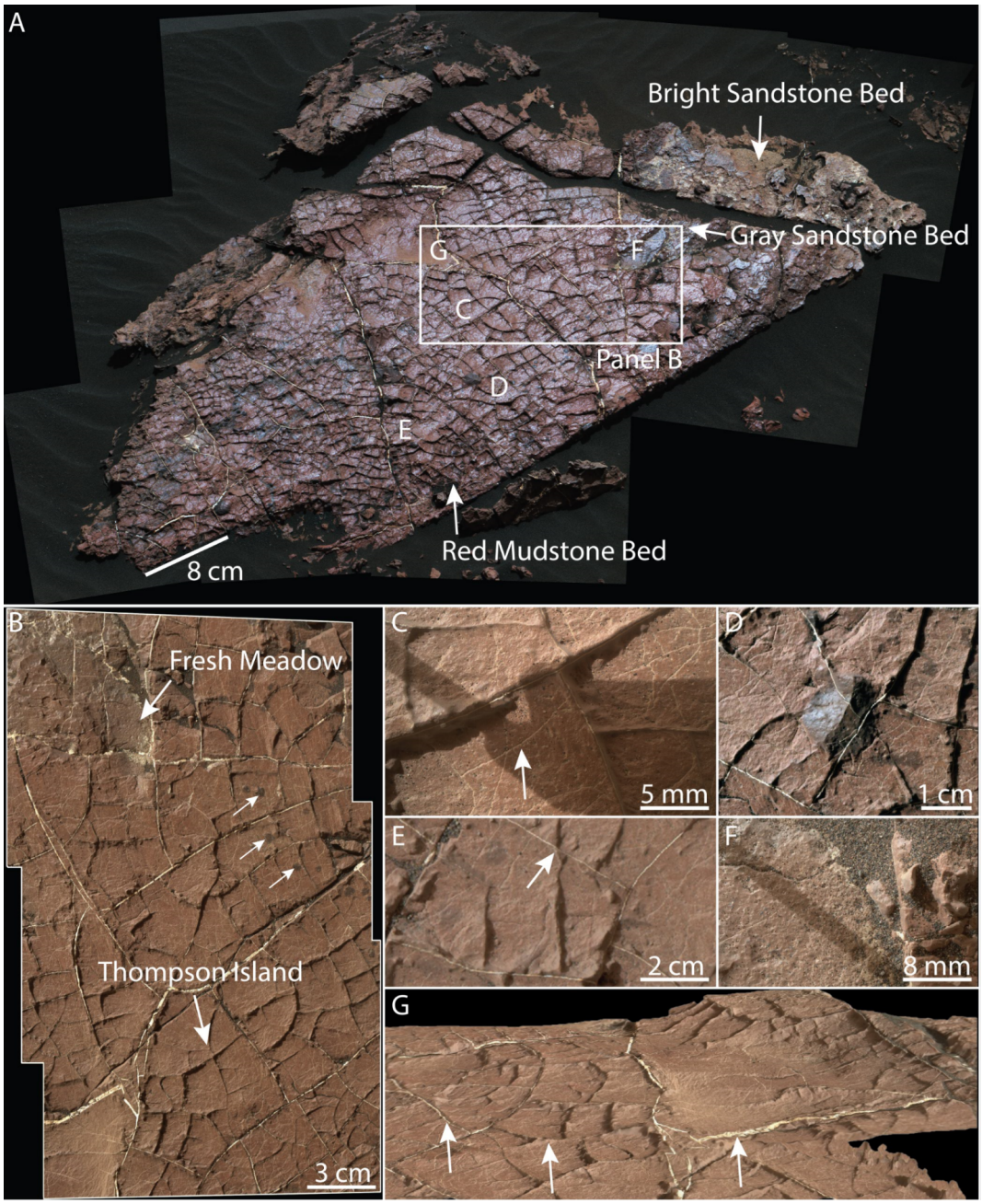

Figure 4.2. Mastcam (sol 1555) and Mars Hand Lens Imager (MAHLI) images of Old Soaker (OS) rock slab, Mars. (**A**) A network of raised ridges forms closed polygons on a red bed on OS. White calcium-sulfate ($CaSO_4$) veins follow many of the ridges. Ridgeless gray beds underlie the red bed. (**B**) Mosaic of nadir MAHLI images of OS. Arrows point to alpha-particle X-ray spectrometer (APXS) targets shown in Table 4.2, and examples of dark spots. Illumination from upper left. (**C**) Partly shadowed MAHLI image of Thompson Island. White arrow denotes a sub-millimeter-wide fracture in a polygon. (**D**) MAHLI image shows ridges terminating on a gray patch. Illuminated from left. (**E**) MAHLI image

shows a $CaSO_4$ vein cross-cutting a ridge (arrow). Illuminated from upper left. (**F**) MAHLI image of the gray bed (target Fresh Meadow). Illuminated from upper left. (**G**) 3-D view of the red bed showing ridges tapering off into a depression. Left arrow: $CaSO_4$ vein on side of ridge; middle arrow: typical polygon-forming ridge; right arrow: $CaSO_4$ vein.

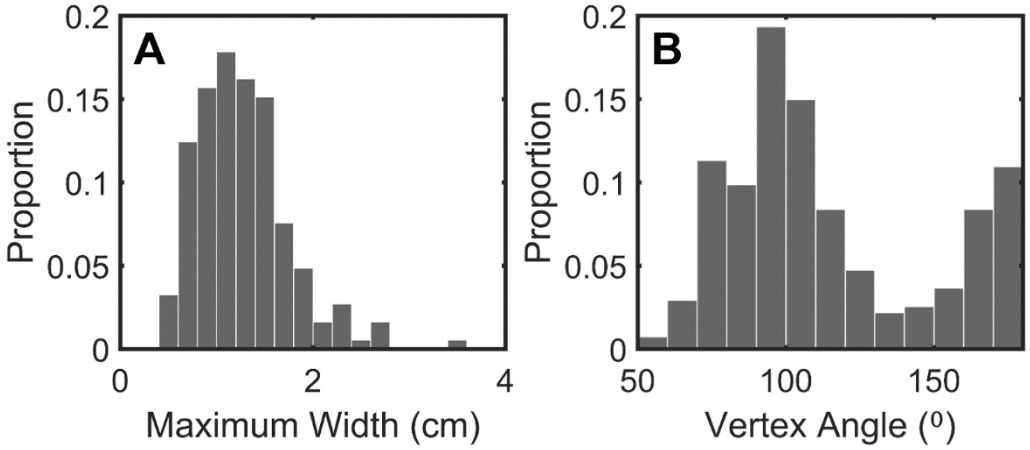

Figure 4.3. Distribution of the maximum width of polygons (**A**) and vertex angles (**B**) formed by ridges on Old Soaker rock slab, Mars.

Table 4.1. CHEMCAM MEASUREMENTS ON AND AROUND OLD SOAKER ROCK SLAB, MARS

Target	No. Points or Targets	SiO_2	TiO_2	Al_2O_3	FeO	MgO	CaO	Na_2O	K_2O	Sum of oxides (wt%)	Comments
Murray mudstones	88 targets	52.4	0.98	12.3	19.0	5.5	2.7	2.7	1.2	96.8	Sol 1410–1520
	std. dev.	2.1	0.05	1.4	1.0	1.1	0.9	0.4	0.3	2.3	
Red layer (3)	70 points	51.6	0.95	13.9	19.0	5.9	1.8	3.0	0.9	97.0	–
	std. dev.	1.6	0.07	1.5	1.5	0.6	0.4	0.4	0.4	2.5	
Gray layer (2)	12 points	49.8	0.93	11.7	19.1	5.8	1.4	2.8	2.2	93.9	Slightly low sum. One Cl line.
	std. dev.	1.4	0.15	1.7	0.9	0.7	0.5	0.5	0.5	1.9	
Bright layer (1)	12 points	39.8	0.86	8.8	12.5	3.0	17.1	1.5	0.4	84.0	Frequent S lines. Local F. Low
	std. dev.	5.2	0.30	1.8	2.2	0.6	3.4	0.4	0.3	5.7	sum.
Dark ridges	13 points	47.6	0.94	11.3	19.3	4.8	1.6	2.4	1.8	89.9	Low total. High H line.
	std. dev.	2.4	0.19	0.9	0.7	0.7	0.9	0.3	0.5	3.0	
Gilley Field Dark	3 points	44.1	0.86	10.4	24.6	4.4	1.2	2.6	0.4	88.4	Low total.
Spot	std. dev.	2.0	0.01	0.7	4.0	0.6	0.1	0.2	0.1	1.0	
Light vein	1 point	2.5	0.20	0.7	5.6	2.7	31.2	0.5	0.0	43.5	Multiple S lines.

Note: Targets consist of multiple points. Points on each feature are obtained at various locations and averaged to give a mean chemistry close to bulk chemistry. The quantification is obtained from comparison with laboratory data on Earth. Volatiles difficult to identify with laser ablation techniques (S, Cl, P) are not quantified. Oxide wt% sums are not normalized, such that low totals highlight the presence of volatiles. Standard deviations are calculated from the number of points of each category to display the variability inside each category.

Table 4.2. KEY APXS MEASUREMENTS ON OLD SOAKER ROCK SLAB, MARS

Target	Na_2O	MgO	Al_2O_3	SiO_2	P_2O_5	SO_3	Cl	K_2O	CaO	TiO_2	Cr_2O_3	MnO	FeO_T	Ni	Zn	Br
Thompson Island	2.62	5.96	9.13	44.80	1.00	6.29	2.38	0.83	3.75	1.01	0.32	0.18	21.39	749	645	1352
Error (±)	0.14	0.17	0.19	0.54	0.07	0.08	0.03	0.04	0.04	0.03	0.01	0.01	0.26	40	20	40
Fresh Meadow	3.22	5.86	7.54	34.04	0.87	13.34	2.51	2.29	3.95	0.75	0.33	0.20	24.83	477	405	927
Error (±)	0.14	0.17	0.19	0.43	0.05	0.15	0.04	0.07	0.04	0.03	0.01	0.01	0.26	25	15	30

Note: Alpha-particle X-ray spectrometer (APXS) oxide wt% or ppm concentration of two representative measurements on Old Soaker. "Thompson Island" was acquired on the red bed (Sol 1566, SH –41.6 °C, FWHM (full width at half maximum) 146 eV, duration 8:09:16). Fresh Meadow was acquired on the underlying gray bed (Sol 1570, SH –20.7 °C, FWHM 169 eV, duration 1:26:11).

ridges spanning an area of a few square meters. The ridges range in length from a few centimeters to ~0.3 m and mostly meet orthogonally, forming T-junctions (Fig. 4.3B). The ridges are made of red-to-gray sediment similar in color to the surrounding bed (Figs. 4.2B and 4.2C) and comprise ~20% of OS's surface. No grains in the ridges or surrounding surface are resolved in MAHLI images (Fig. 4.2C), indicating a maximum grain size of coarse silt. $CaSO_4$ veins distinct from ridge material follow most, but not all, of the ridges (Figs. 4.2B and 4.2C) and in some cases cross-cut the ridges (e.g., Fig. 4.2E). Sub-millimeter-wide fractures occur within the polygons (Fig. 4.2C). Gray, semi-circular, millimeter-scale patches dot the red beds on OS and SC. They can show raised relief and in places are cross-cut by veins (Figs. 4.2B and 4.2D).

Some very fine sand grains and millimeter-scale concretions or embedded grains are visible in MAHLI images of the gray bed at OS (Fig. 4.2F). The ridges taper off within millimeter-scale depressions in the red mudstone at OS (Fig. 4.2G). Fractures associated with the ridges of the SC slab penetrate the red mudstone and terminate at the boundary with the underlying gray sandstone (Fig. 4.4). The gray beds appear to lack ridges (Figs. 4.2A and 4.2F).

4.5.2. Composition Measurements at Old Soaker and Squid Cove

ChemCam analysis of OS identified three distinct bed compositions (Fig. 4.2A): (1) a lowermost bright sandstone with no ridges and a composition consistent with cementation of sandstones by calcium sulfates; (2) a gray bed with comparatively high K_2O abundance relative to the bright sandstone (1.5–2.5 wt%); and (3) an overlying red mudstone compositionally similar to other Murray mudstones (Table 4.1) (Mangold et al.,

2017). APXS measurements of OS show that the red mudstone bed is similar in composition to average Murray bedrock, but is two to three times richer in Cl (2–3 wt%) and Br (1150–1430 ppm). The gray bed (target "Fresh Meadow") is distinct from the overlying red bed, with relatively enriched K_2O, SO_3, Na_2O, and FeO_T and depleted TiO_2, SiO_2, and Al_2O_3 (Table 4.2).

ChemCam observation points on the ridges validate that their composition is distinct from $CaSO_4$ vein fill and close to that of the gray bed, with lower Al_2O_3 and SiO_2, high H emission lines, and higher K_2O abundances than the red bed. The presence of strong H lines on the ridges indicates the presence of a significant component of hydrous phases absent from the red layer. The dark patches (target "Gilley Field"; Table 4.1) in the red bed are enriched in FeO (up to 27 wt%) and MnO (0.7 wt%) relative to the surrounding rock. The bright veins are similar to $CaSO_4$ veins encountered since the beginning of the mission (Table 4.1) (Nachon et al., 2017).

4.6 Discussion

Proposed formation mechanisms for the ridges must account for several observations: (1) ridges form polygonal networks with T-junctions and continuous arcuate shapes; (2) the ridges in the red mudstone beds correspond to fractures that penetrate those beds; (3) the fractures are restricted to the red beds and terminate at the boundary with coarser underlying material; (4) the fractures are filled with very fine-grained sediment; (5) $CaSO_4$ veins run along many but not all of the ridges, in some cases cross-cut the ridges, and, unlike the ridges, cut all beds in exposed cross sections; and (6) the ridges are compositionally similar to the underlying gray bed. The most likely fracturing mechanisms include desiccation, synaeresis, and hydraulic fracturing.

4.6.1 Origin of the Ridges

Shrinkage cracks form in response to tensile stresses within sediment that result from contraction due to moisture or heat loss (Shorlin et al., 2000). When stress exceeds

local tensile strength, materials fracture and cracks begin to grow orthogonal to the direction of maximum tensile stress, typically resulting in a polygonal pattern (Sletten et al., 2003). In uniform material, new cracks will turn to converge with other cracks orthogonally, resulting in junctions mostly near 90° (Shorlin et al., 2000) as observed at OS and SC (Fig. 4.3). Abundant T-junctions show that sediments dried to completion, possibly in a single event, rather than undergoing multiple wetting and drying cycles that tend to form 120° junctions (Goehring et al., 2010).

Desiccation cracks form at the sediment-air interface and are preserved in the rock record through sediment infill from overlying strata (Plummer and Gostin, 1981). The compositional and color similarity of the ridges to the average Murray formation, which is predominantly comprised of silt-sized grains or smaller, suggests that the ridges are comprised of sediment. Ridge-forming sediment at OS and SC is indistinguishable from the surrounding bed based on grain size alone, so this observation is not definitive evidence for sediment infill from an overlying bed.

Sulfate-mineralized fractures attributed to hydraulic fracturing are prevalent throughout the Murray formation (Grotzinger et al., 2014, 2015; Caswell and Milliken 2017; Young and Chan, 2017), and $CaSO_4$-filled veins also run along most of the OS ridges, so burial-related hydraulic fracturing may be considered a potential mechanism for

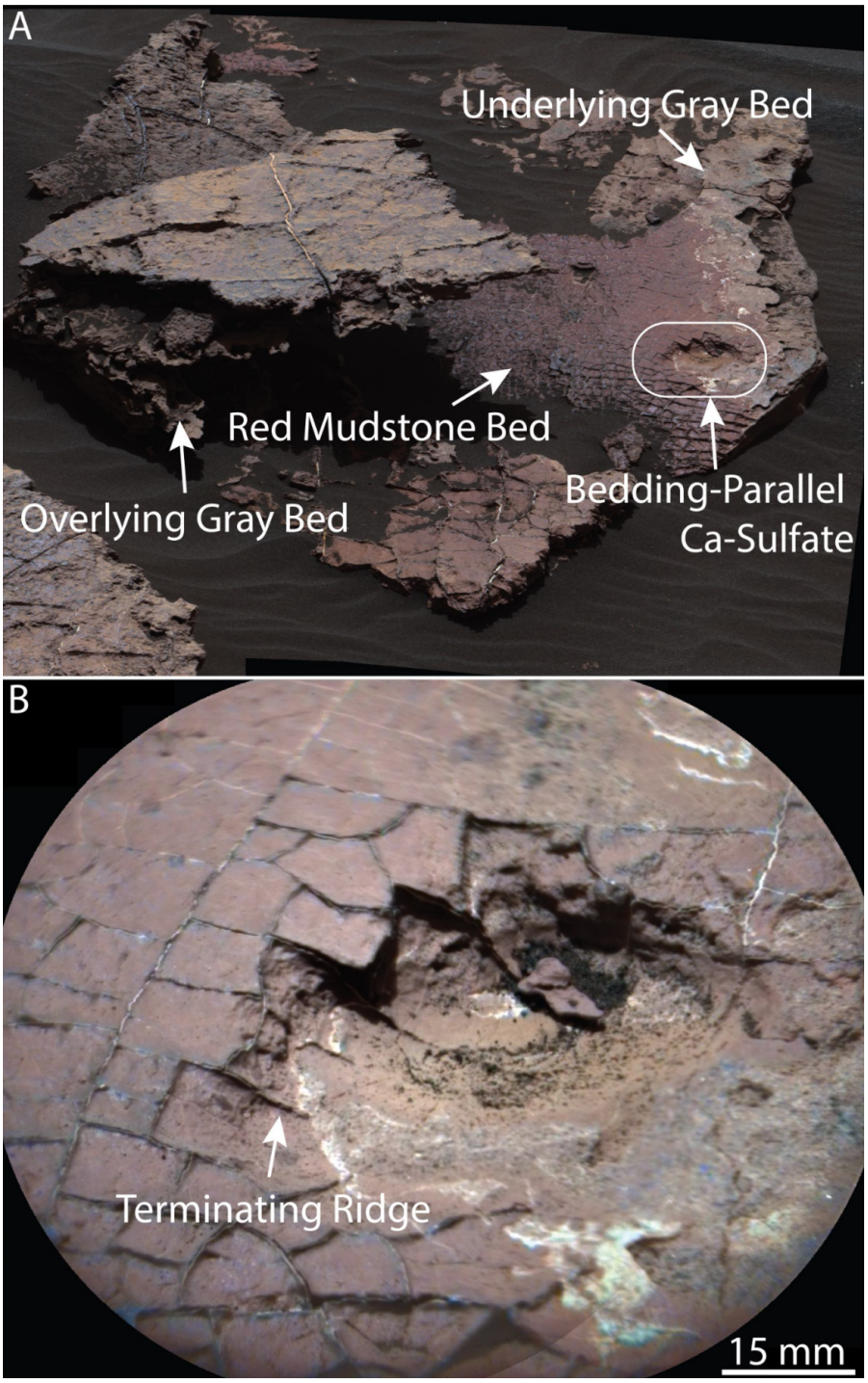

Figure 4.4. (**A**) Mastcam image of Squid Cove (SC) rock slab, Mars (sol 1555). Ridges form polygons in a thin red bed. (**B**) Colorized ChemCam RMI mosaic of the contact between the red and gray beds on SC (white box, frame A). Fractures penetrate the red bed and terminate at the boundary with the underlying gray bed. Illumination from upper left.

the origin of the ridges. However, cross-cutting relationships indicate that the ridges and their infilling materials were lithified prior to the formation of sulfate-filled fractures; sulfate-filled fractures cross-cut some ridges and are not visible along all ridges (Figs. 4.2C and 4.2E). Moreover, hydraulic fracturing should yield relatively consistent fracture orientations (Hubbert and Willis, 1972), which are not observed at OS or SC. Zones of weakness created by early sediment-filled fractures were likely overprinted by burial-related stresses (Caswell and Milliken, 2017), followed by precipitation of calcium sulfates.

The ridges are restricted to the red surfaces and their associated fractures terminate at the boundary with the underlying sandstone, consistent with desiccation of a thin mud layer. This style of termination is inconsistent with synaeresis cracking or hydraulic fracturing, which in the latter case would also be expected to cross-cut the bedding planes (Hubbert and Willis, 1972; Plummer and Gostin, 1981; Young and Chan, 2017). The 0.5–3.5 cm length scale of the polygons on OS and SC is consistent with a millimeter- to centimeter-thick deformable layer, similar to the observed thickness of the red mudstone bed and analogous to terrestrial experiments (e.g. Shorlin et al., 2000). Variation in polygon size across slabs may be due to changes in basal friction, bed thickness, or impurities. The cracks are parallel-sided (do not taper downward) in profile (Fig. 4.4), which can occur if the coupling between the desiccated and underlying beds is low enough to not affect the fractures (Shorlin et al., 2000).

4.6.2 Lithification of Ridges

The ridges likely formed via desiccation of a surficial mud layer and filling by sediment sourced from an overlying bed. Although the ridges and underlying gray bed are compositionally similar, the occurrence of interstratified gray and red beds suggests that a gray mudstone originally covered the cracked red mudstone and acted as a source of fracture fill material. Diagenesis associated with later fluids may account for their current similar compositions. Sulfates and other salts may have formed during desiccation as evaporites and/or after the fractures lithified. After deposition, the Murray formation was

buried under up to several kilometers of sediment that likely provided sufficient overburden pressure to generate hydraulic fractures (Caswell and Milliken, 2017; Young and Chan, 2017). These fractures likely propagated along pathways of reduced strength produced by the desiccation cracks, and in some cases cross-cut polygons. These fracture networks then acted as conduits for fluid precipitation of $CaSO_4$ cements.

4.7 Conclusions and Implications for Gale Crater Paleolakes

Recognition of distinct suites of sedimentary structures is a powerful tool in interpreting Mars paleoenvironmental history as it has been for Earth. The Murray formation is interpreted to record a transition from long-lived (~10^5–10^7 yr) perennial lacustrine conditions observed in the basal Murray (Grotzinger et al., 2015; Hurowitz et al., 2017) to episodically exposed conditions recorded by the desiccation-cracked surfaces in the Sutton Island member of the Murray. The predominance of T-junctions at OS and SC indicates a single drying event rather than multiple cycles of wetting and drying. The identification of desiccation cracks is an important facies attribute of the Murray formation that suggests a history of oscillating lake levels that led to intermittent exposure and possible evaporative diagenesis. The drier conditions may represent a temporal transition from deeper lacustrine facies dominated by suspension fallout to shallower lakes with more common traction deposition and desiccation. The Sutton Island member is ~70 m stratigraphically higher than the Pahrump Hills member, but is also >1 km closer to the center of the Gale lake basin. This suggests the exposed lake facies are not basin margin facies, but rather lowstand facies which represent lake level oscillations.

4.8 Acknowledgments

We are indebted to the Mars Science Laboratory (MSL) project engineering and science teams, and MSL team members who participated in tactical and strategic operations, for their efforts that were vital in collecting the data presented. Thanks to S. Kattenhorn, K. Benison, and K. Herkenhoff for reviews that improved this manuscript. Some of this research was performed at the Jet Propulsion Laboratory, California Institute

of Technology (USA), under a contract with NASA. This material is based upon work supported by the National Science Foundation Graduate Research Fellowship Grant No. DGE-1144469. These data are archived in the Planetary Data System (pds.nasa.gov).

References

Banham, S.G, Gupta, S., Rubin, D.M., Watkins, J.A., Sumner, D.Y., Edgett, K.S. et al. (2018). Ancient martian aeolian processes and palaeomorphology reconstructed from the Stimson formation on the lower slope of Aeolis Mons, Gale crater, Mars. *Sedimentology*, 65, 993-1042. https://doi.org/10.1111/sed.12469.

Caswell, T.E., & Milliken, R.E., (2017). Evidence for hydraulic fracturing at Gale crater, Mars: Implications for burial depth of the Yellowknife Bay formation. *Earth and Planetary Science Letters*, 468, 72–84, https://doi.org/10.1016/j.epsl.2017.03.033.

Edgar, L.A., Grotzinger, J.P., Hayes, A.G., Rubin, D.M., Squyres, S.W., Bell, J.F., et al. (2012). Stratigraphic architecture of bedrock reference section, Victoria Crater, Meridiani Planum, Mars, in Grotzinger, J.P., ed., Sedimentary Geology of Mars: Society for Sedimentary Geology Special Publications, 102, 195–209, https://doi.org/10.2110/pec.12.102.0195.

El-Maarry, M.R., Watters, W., McKeown, N.K., Carter, J., Noe Dobrea, E., Bishop, J.L., et al. (2014). Potential desiccation cracks on Mars: A synthesis from modeling, analogue-field studies, and global observations: *Icarus*, 241, 248, https://doi.org/10.1016/j.icarus.2014.06.033.

Fedo, C. et al. (2017). Facies analysis and basin architecture of the upper part of the Murray formation, Gale Crater, Mars. *LPSC 48*, Abstract 1689.

Goehring, L., Conroy, R., Akhter, A., Clegg, W.J., & Routh, A.F., (2010). Evolution of mud-crack patterns during repeated drying cycles. *Soft Matter*, 6, 3562–3567, https://doi.org/10.1039/B922206E.

Grotzinger, J.P., Arvidson, R.E., Bell, J.F., Calvin, W., Clark, B.C., Fike, D.A. et al. (2005). Stratigraphy and sedimentology of a dry to wet eolian depositional system, Burns formation, Meridiani Planum, Mars. *Earth and Planetary Science Letters*, 240, 11–72, https://doi.org/10.1016/j.epsl.2005.09.039.

Grotzinger, J. P., Sumner, D. Y., Kah, L. C., Stack, K., Gupta, S., Edgar, L., et al., & MSL Science Team. (2014). A habitable fluvio-lacustrine environment at Yellowknife Bay, Gale Crater, Mars. *Science*, 343(6169), 1242777. https://doi.org/10.1126/science.1242777.

Grotzinger, J.P., Gupta, S., Malin, M. C., Rubin, D.M., Schieber, J., Siebach, K. et al., (2015). Deposition, exhumation, and paleoclimate of an ancient lake deposit, Gale crater, Mars. *Science*, 350, https://doi.org/10.1126/science.aac7575.

Hubbert, M.K., & Willis, D.G. (1972). Mechanics of hydraulic fracturing. *Transactions of the American Institute of Mining and Metallurgical Engineers*, 210, 153–166. https://doi.org/10.2118.686-G.

Hurowitz, J.A., Grotzinger, J.P., Fischer, W.W., McLennan, S.M., Milliken, R.E., Stein, N. et al. (2017). Redox stratification of an ancient lake in Gale Crater, Mars. *Science*, 356, https://doi.org/10.1126/science.aah6849.

Mangold, N., Cousin, A., Meslin, P.-Y., Payre, V., Dehouck, E., Newsom, H.E., et al. (2017). ChemCam analysis of aqueous processes on polygonal cracks at Gale Crater, Mars. *LPSC 48*, Abstract 1908.

Nachon, M., Mangold, N., Forni, O., Kah, L., Cousin, A., Wiens, R.C. et al. (2017). Chemistry of diagenetic features analyzed by ChemCam at Pahrump Hills, Gale crater, Mars. *Icarus*, 281, 121–136, https://doi.org/10.1016/j.icarus.2016.08.026.

Plummer, P.S., & Gostin, V.A., (1981). Shrinkage cracks; Desiccation or synaeresis? *Journal of Sedimentary Petrology*, 51, 1147–1156.

Rampe, E.B., Ming, D.W., Blake, D.F., Bristow, T.F., Chipera, S.J., Grotzinger, J.P. et al. (2017). Mineralogy of an ancient lacustrine mudstone succession from the Murray formation, Gale crater, Mars. *Earth and Planetary Science Letters*, 471, 172–185, https://doi.org/10.1016/j.epsl.2017.04.021.

Shorlin, K.A., de Bruyn, J.R., Graham, M., & Morris, S.W. (2000). Development and geometry of isotropic and directional shrinkage-crack patterns. *Physical Review E: Statistical Physics, Plasmas, Fluids, and Related Interdisciplinary Topics*, 61, 6950–6957, https://doi.org/10.1103/PhysRevE.61.6950.

Sletten, R.S., Hallet, B., & Fletcher, R.C. (2003). Resurfacing time of terrestrial surfaces by the formation and maturation of polygonal patterned ground. *JGR: Planets*, 108, 8044, https://doi.org/10.1029/2002JE001914.

Williams, R.M.E., Grotzinger, J.P., Dietrich, W.E., Gupta, S., Sumner, D.Y., Wiens, R.C. (2013). Martian fluvial conglomerates at Gale Crater. *Science*, 340, 1068–1072, https://doi.org/10.1126/science.1237317.

Young, B.W. & Chan, M.A. (2017). Gypsum veins in Triassic Moenkopi mudrocks of southern Utah: Analogs to calcium sulfate veins on Mars. *JGR: Planets*, 122, 150–171. https://doi.org/10.1002/2016JE005118.

Chapter 5

THE FORMATION AND EVOLUTION OF BRIGHT SPOTS ON CERES

N. T. Stein[1], B. L. Ehlmann[1,2], E. Palomba[3,4], M. C. De Sanctis[3], A. Nathues[5], H. Hiesinger[6], E. Ammannito[7], C. A. Raymond[2], R. Jaumann[8], A. Longobardo[4], C. T. Russell[7]

[1]Division of Geological and Planetary Sciences, California Institute of Technology, Pasadena, CA, 91125.

[2]Jet Propulsion Laboratory, California Institute of Technology, Pasadena, CA, 91109.

[3]INAF-IAPS, Via del Fosso del Cavaliere 100, 00133 Rome, Italy.

[4]ASDC-ASI, Via del Politecnico, 00133 Rome, Italy.

[5]Max Planck Institute for Solar System Research, Justus-von-Liebig-Weg 3, 37077 Goettingen, Germany.

[6]Institut für Planetologie, Westf älische Wilhelms-Universität. Münster, Germany.

[7]Department of Earth, Planetary, and Space Sciences, University of California, Los Angeles, CA, 90095.

[8]DLR, Institute of Planetary Research, Rutherfordstraße 2 12489, Berlin, Germany.

This chapter was published as:

Stein, N.T. et al. (2019), The formation and evolution of bright spots on Ceres. *Icarus*, 320, 188-201. https://doi.org/10.1016/j.icarus.2017.10.014.

5.1 Abstract

The otherwise homogeneous surface of Ceres is dotted with hundreds of anomalously bright, predominantly carbonate-bearing areas, termed "faculae," with Bond albedos ranging from ~0.02 to >0.5. Here, we classify and map faculae globally to characterize their geological setting, assess potential mechanisms for their formation and destruction, and gain insight into the processes affecting the Ceres surface and near-surface. Faculae were found to occur in four distinct geological settings, associated predominantly with impact craters: 1) crater pits, peaks, or floor fractures (floor faculae), 2) crater rims or walls (rim/wall faculae), 3) bright ejecta blankets, and 4) the mountain Ahuna Mons. Floor faculae were identified in eight large, deep, and geologically young (asteroid-derived model (ADM) ages of $<420 \pm 60$ Ma) craters: Occator, Haulani, Dantu, Ikapati, Urvara, Gaue, Ernutet, and Azacca. The geometry and geomorphic features of the eight craters with floor faculae are consistent with facula formation via impact-induced heating and upwelling of volatile-rich materials, upwelling/excavation of heterogeneously distributed subsurface brines or their precipitation products, or a combination of both processes. Rim/wall faculae and bright ejecta occur in and around hundreds of relatively young craters of all sizes, and the geometry of exposures is consistent with facula formation via the excavation of subsurface bright material, possibly from floor faculae that were previously emplaced and buried. A negative correlation between rim/wall facula albedo and crater age indicates that faculae darken over time. Models using the Ceres crater production function suggest initial production or exposure of faculae by large impacts, subsequent dissemination of facula materials to form additional small faculae, and then burial by impact-induced lateral mixing, which destroys faculae over timescales of less than 1.25 Gyr. Cumulatively, these models and the observation of faculae limited to geologically young craters indicate relatively modern formation or exposure of faculae, indicating that Ceres' surface remains active and that the near surface may support brines in the present day.

5.2 Introduction

Ceres' surface is rather dark. The average geometric albedo measured by Dawn's Visible and Infrared spectrometer (VIR) at 0.55 μm is 0.094 ± 0.008, and the average bond albedo measured with the Framing Camera (FC) clear filter is 0.034 ± 0.001 (Ciarniello et al., 2016; Ammannito et al., 2016; Li et al., 2016). Ceres' dark surface materials, whose reflectance ranges between ~0.03 and 0.37 (Nathues et al., 2016), are a mixture of magnesium phyllosilicates, ammoniated phases, other low-albedo materials such as organic carbon and iron-bearing opaque phases, and small amounts of carbonates (King et al., 1992; De Sanctis et al., 2015; Ammannito et al., 2016). FC images show that the otherwise uniform-albedo dark surface is punctuated by bright regions associated primarily with impact craters. Here we use the term "facula" to refer to isolated bright spots, whereas more extensive bright regions surrounding impact craters are referred to as "bright ejecta." The material comprising faculae and bright ejecta is sometimes referred to as "bright material." The brightest and most extensive of these regions, Cerealia Facula and Vinalia Faculae, are in the central pit and floor of Occator crater and were visible upon Dawn's approach to Ceres (Nathues et al., 2015, 2017). Cerealia Facula has an average Bond albedo of 0.24 ± 0.01 (Li et al., 2016), and its spectra are consistent with a composition that includes significantly more abundant carbonate of different composition than the average surface (Na-rich instead of Ca, Mg-rich) as well as ammoniated salts such as NH_4Cl or NH_4HCO_3 (De Sanctis et al., 2016). At least two faculae contiguous with VIR detections of H_2O ice have been identified at latitudes higher than 30°N (Combe et al., 2016, 2017). A dedicated study of the composition of the faculae indicates that most of them are rich in Mg- or Na-carbonate (Carrozzo et al., 2017; Palomba et al., 2017), and thus they cannot be explained by meteoritic infall as is the case for some anomalously dark materials on Vesta (which would be considered brighter than average on the much darker surface of Ceres) (McCord et al., 2012; Reddy et al., 2012). Instead an endogenous origin is likely, perhaps due to the upwelling and crystallization of salts from brines or entrained altered solids that were brought to the surface (De Sanctis et al., 2016; Nathues et al., 2017).

Since Dawn's initial investigation of Occator crater, the FC has imaged the entire illuminated surface at a resolution of ~35 m/pixel in clear filter. These images have revealed the presence of hundreds of faculae and bright ejecta associated with impact craters. By characterizing the mechanisms by which bright materials are emplaced, we can better understand the composition and structure of the subsurface and the processes that shape Ceres' surface. Here we detail a comprehensive global mapping of bright materials using high resolution FC data and a new classification scheme to characterize their geologic setting. Results are used to investigate potential mechanisms for the formation and destruction of faculae and the processes that modify them over time.

5.3 Identification and Mapping of Faculae

Faculae were identified using a photometrically corrected clear filter HAMO FC-based albedo mosaic and defined as regions with a Bond albedo at least 30% higher than that of surrounding pixels. The threshold of 30% was selected because it represents a typical spread of albedos about the mean for a given scene. Hence, an albedo 30% higher than the local average represents twice the typical variation in a scene. When reported, the area of faculae was computed on the basis of the total number of pixels surpassing this threshold. This is similar to the criterion adopted by Palomba et al. (this issue) to identify faculae in VIR images. Bond albedo measures the fractional power of electromagnetic radiation incident on a surface that is scattered back into space, whereas the geometric albedo is the ratio of surface brightness at zero phase angle to that of an idealized, flat Lambertian (diffusely scattering) surface. The Bond albedo is dominated by light scattered at a moderate range of phase angles well sampled by Dawn, and is hence less model-dependent than the geometric albedo, which relies on additional modeling assumptions due to the lack of some observations at small phase angles.

The Dawn FC has an angular resolution of 93.7 μrad/pixel (Sierks et al., 2011), yielding image pixel scales of up to ~35 m at Ceres. With the clear filter, Dawn FC is sensitive to wavelengths of light between ~400-1000 nm and peaking near 700 nm (Sierks et al., 2011). Because faculae on Ceres can be small and are often distributed at sub-km

scales, FC images offer means to identify small faculae based on albedo. Faculae were not mapped north or south of ~55° due to the difficulty of distinguishing true faculae from bright reflections on sun-facing crater rims. In the future, candidate faculae in these regions may be identified on the basis of an improved photometric correction that incorporates high resolution topographic information. Faculae were confirmed visually in order to remove spurious identifications. The facula catalog was cross-referenced with a VIR-based facula catalog produced by Palomba et al. (2017), although not all faculae identified in FC images were verified with VIR spectra to contain Na carbonates because many FC-identified faculae are below the spatial resolution of VIR. That is, the defining characteristic of faculae reported here is their albedo rather than a specific composition. Although Palomba et al. (2017) also identify faculae on the basis of albedo, the higher spatial resolution of the FC LAMO data (~35 m/pixel) relative to VIR LAMO data (~90-110 m/pixel) means the catalog presented here (included in the supplementary materials) reports more faculae, particularly spatially small rim/wall faculae.

Faculae were mapped onto a LAMO FC clear filter mosaic of the surface by morphologic type. Facula extent was mapped using the 30% threshold and tracked in a GIS database. Reported crater depths associated with some faculae were calculated from a photogrammetric FC digital elevation map (DEM), available in the PDS, as the average rim-to-floor depth of two transects in N-S and E-W directions.

5.4 Distribution and Classification of Faculae

There are at least 300 faculae or clusters of faculae in total, >200 of which are located on crater rims or walls. The albedo of the facula regions ranges from slightly below the average surface Bond albedo of 0.034 ± 0.001 to more than 0.5 in the central pit of Occator crater (Fig. 1) (Li et al., 2016). The lower portion of the range is set by the albedos of faculae adjacent to anomalously dark material or in regions with high incidence angles where there are errors in the photometrically corrected mosaic. It is possible that a small number of these dark faculae, which were not spatially extensive enough to be detected

with VIR, are not compositionally similar to the carbonate-bearing faculae and may instead be impactor material from bright asteroids.

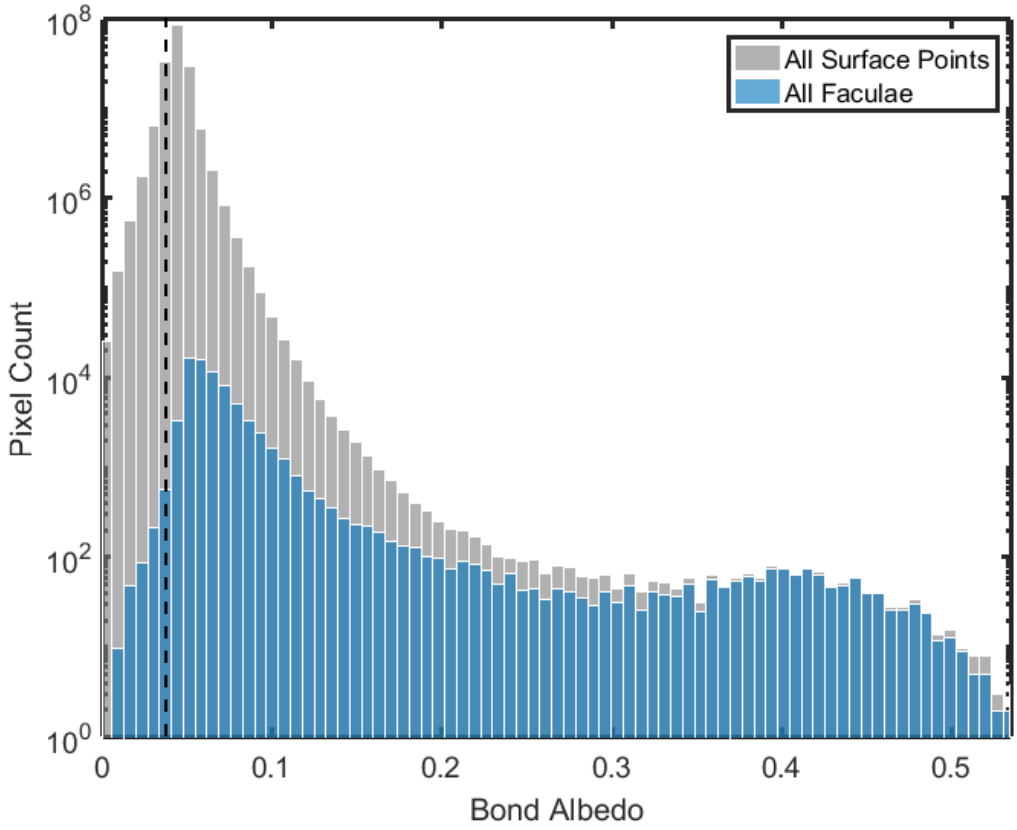

Figure 5.1. Comparison of the Bond albedo of all faculae and all points on the surface as seen by FC. Faculae are identified based on the difference in albedo compared to the surrounding region, as discussed in the text. The vast majority of surface points with Bond albedos > 0.1 that are not classified as faculae are due to reflections on sun-facing crater walls. The average Bond albedo of the surface is 0.034 ± 0.001 (dashed line) (Li et al., 2016). The peak near 0.4 is due to Cerealia Facula in Occator crater.

We group faculae into four geologic settings (Fig. 5.2): 1) central pit or peak complexes or floor fractures within large craters ("floor faculae"), 2) crater rims and walls ("rim/wall" faculae), 3) within ejecta, including the rims or walls of small craters in ejecta blankets ("bright ejecta"), and 4) the mountain Ahuna Mons. With the exception of Ahuna Mons, all faculae occur in or around impact craters. (Fig. 5.3). By latitude, the faculae are relatively evenly distributed within the ±55° latitude bounds of our study area and are

prevalent throughout both Vendimia Planitia and Hanami Planum. There is no clear correlation between facula concentration and crustal thickness, although the extensive Cerealia Facula is located in the thickest portion of the crust (Ermakov et al., 2017). Faculae appear associated with many, but not all (see sections 5.4.1.1 and 5.4.2.1), of the least-degraded craters and with some older basins. In this manuscript, we focus on the characteristics of faculae-containing craters, i.e., settings 1-3 above.

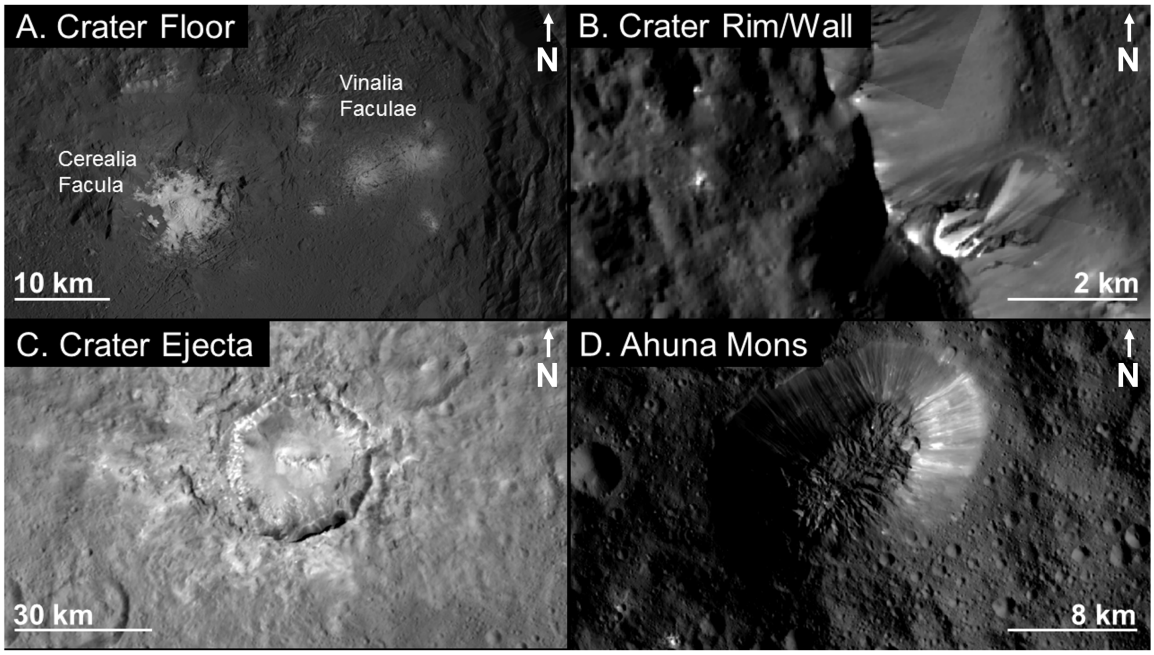

Figure 5.2. LAMO and HAMO FC images of examples of the four geologic settings of faculae. (**A**) Cerealia and Vinalia Faculae in Occator crater are examples of pit/peak and floor fracture associated faculae and are the brightest faculae on Ceres. (**B**) Faculae emanating from near the top of the southwestern wall of Dantu crater. Bright-toned material can be seen streaking down toward the crater floor. (**C**) Haulani crater, which in addition to floor and rim/wall faculae has a large, high albedo ejecta blanket. (**D**) Bright material streaks down the steep slopes of the mountain Ahuna Mons. North is up in all images.

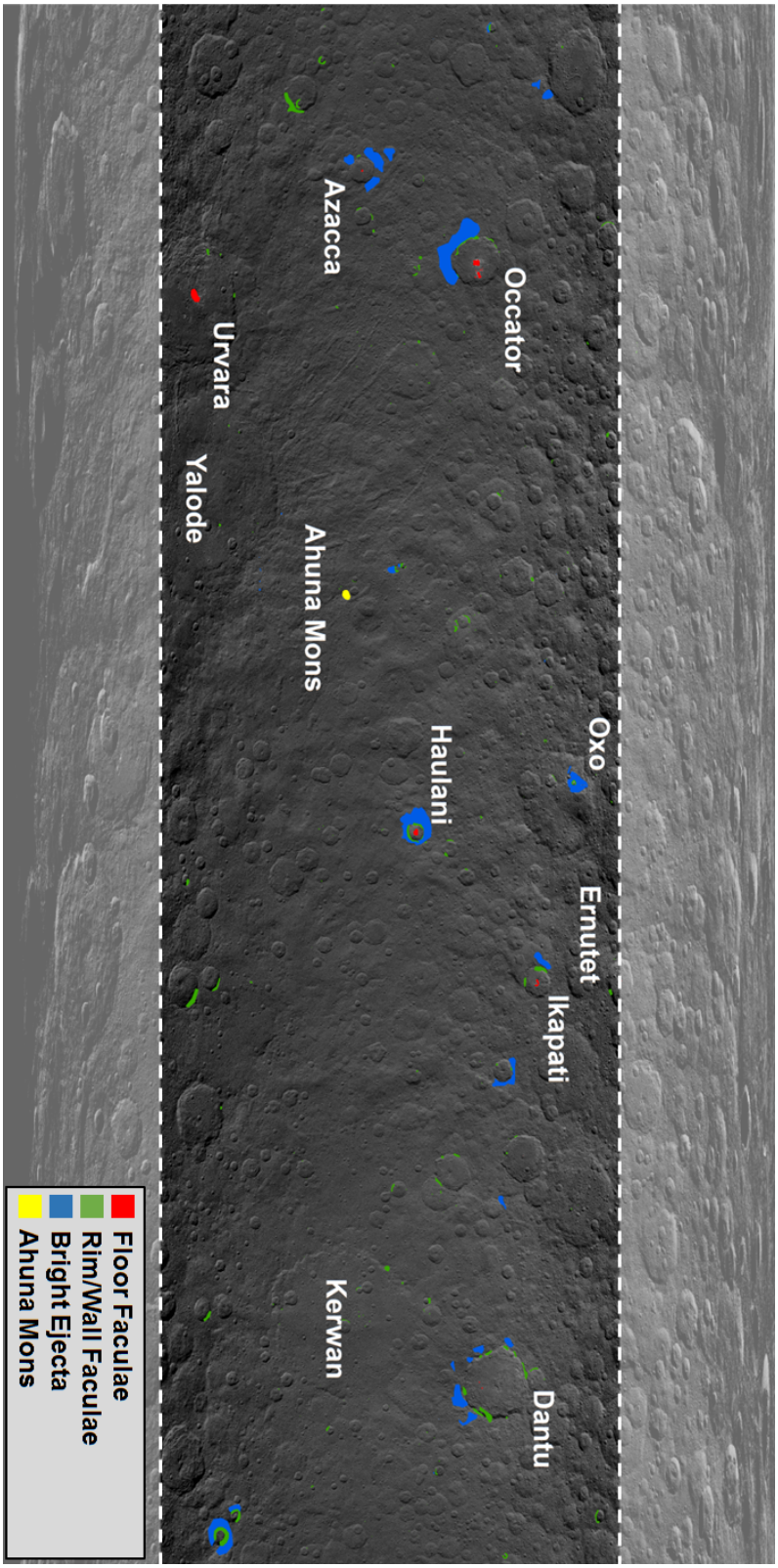
Occator
Azacca
Urvara
Yalode
Ahuna Mons
Haulani
Oxo
Ernutet
Ikapati
Dantu
Kerwan
Floor Faculae
Rim/Wall Faculae
Bright Ejecta
Ahuna Mons

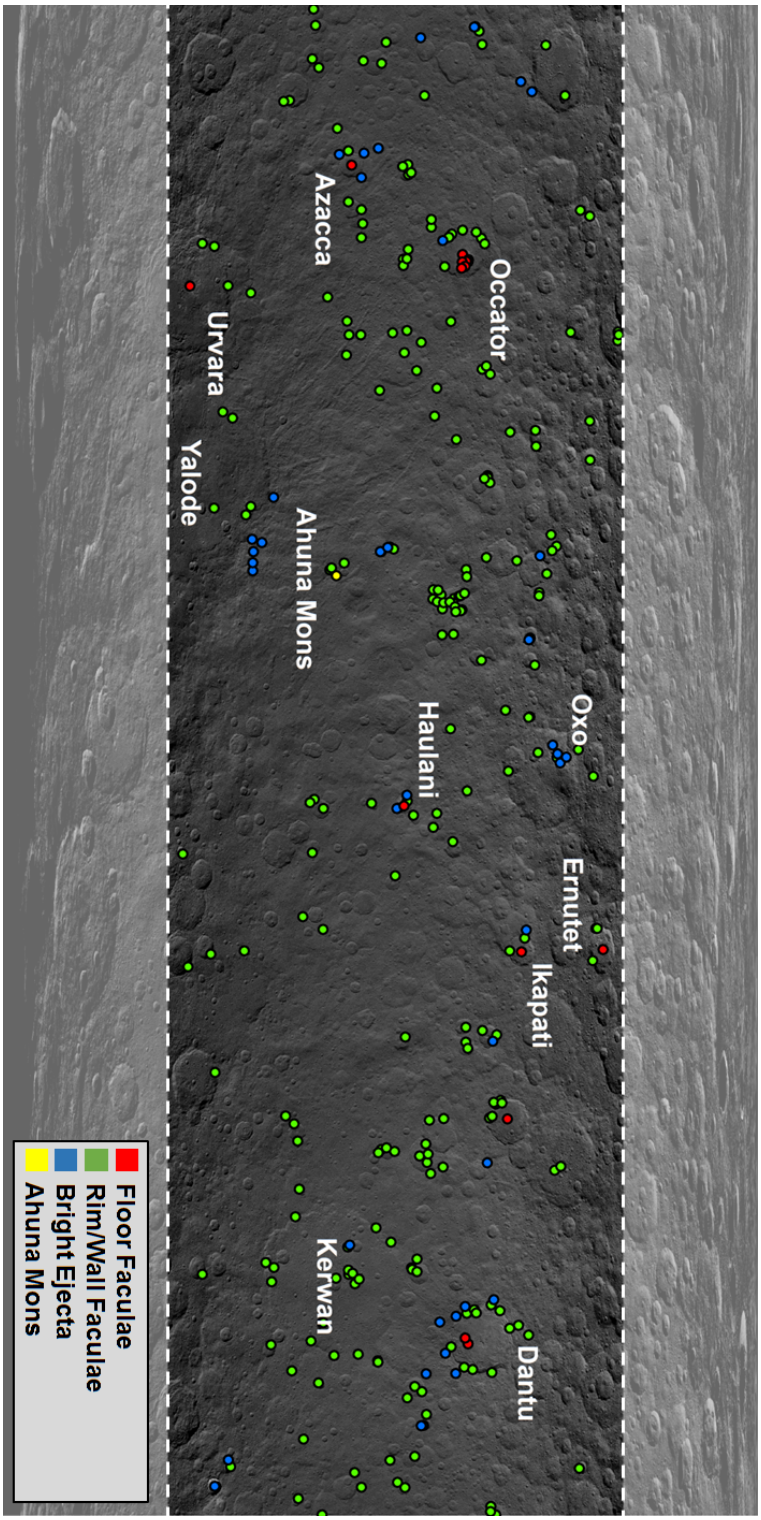

Figure 5.3. All faculae mapped onto a LAMO FC clear filter mosaic and classified by geologic setting. Facula extents are mapped in A (top). All facula locations are denoted as points in B (bottom).

5.4.1 Floor Faculae

5.4.1.1 Characteristics of Craters with Floor Faculae

Floor faculae are defined as faculae that occur within the central pit or peak complex of large craters or along crater floor fractures (Fig. 5.4), and are distinct from faculae exposed on the rim or wall of small craters contained within the floor of larger craters (e.g. in Fig. 5.4E,F). Floor faculae are observed in eight craters: Occator, Dantu, Haulani, Azacca, Ikapati, Gaue, Ernutet, and Urvara, and range in extent from <1 km^2 (Gaue) to >120 km^2 (Occator) (Table 5.1). Cumulatively these faculae span a total area of at least 375 km^2. Each of these craters is larger than the simple-to-complex crater transition diameter, which on Ceres occurs at diameters of 7.5 to 12 km (Hiesinger et al., 2016). The smallest of the craters exhibiting floor faculae is Haulani, with a diameter D of ~32 km, and the largest is Urvara with D ~163 km. Most large craters, including more than 90% of craters with D > 50 km and the largest crater on the surface (Kerwan, D = 283 km), do not contain floor faculae (Fig. 5.5A). An additional important parameter is crater depth, independent of diameter. Craters with floor faculae are among the deepest on the surface; 8 of the 28 deepest craters contain floor faculae, and 13 of the 28 deepest craters contain at least some type of bright material. Although the craters with floor faculae are not anomalously deep for their diameter relative to the average crater population, they are the deepest in their respective regions (Fig. 5.5B) with only one exception, Ernutet, which is adjacent to the deeper Ikapati crater, which also has floor faculae. Hence, crater depth is a stronger control on the presence of floor faculae than crater diameter alone. No craters shallower than 3 km contain floor faculae. No correlation exists between crater diameter or depth and the spatial extent of floor faculae.

Table 5.1. LIST OF ALL CRATERS WITH FLOOR FACULAE, THEIR DIMENSIONS, AND PRESENCE/TYPE OF FLOOR FRACTURES (BUCZKOWSKI ET AL., 2016) AND PITTED TERRAINS (SIZEMORE ET AL., 2017)

Crater Name	Diameter (km)	Approx. Depth (km)	Approx. Depth Diameter Ratio	Occurrence	Floor Fractures?	Pits?
Occator	92	4200	0.046	Central pit/dome and floor fractures	Class 1	Few
Dantu	125	5180	0.041	Floor fractures	Class 1	Abundant
Haulani	32	3050	0.095	Central peak	Class 1	Abundant
Ikapati	50	3560	0.071	Central peak complex	Class 1	Abundant
Gaue	89	4430	0.050	Central peak	Class 1	No
Azacca	50	3980	0.080	Central peak complex	Class 1	Few, degraded
Urvara	163	4500	0.028	Central peak	Possible class 4	Degraded
Ernutet	57	3250	0.057	Central peak	No	No

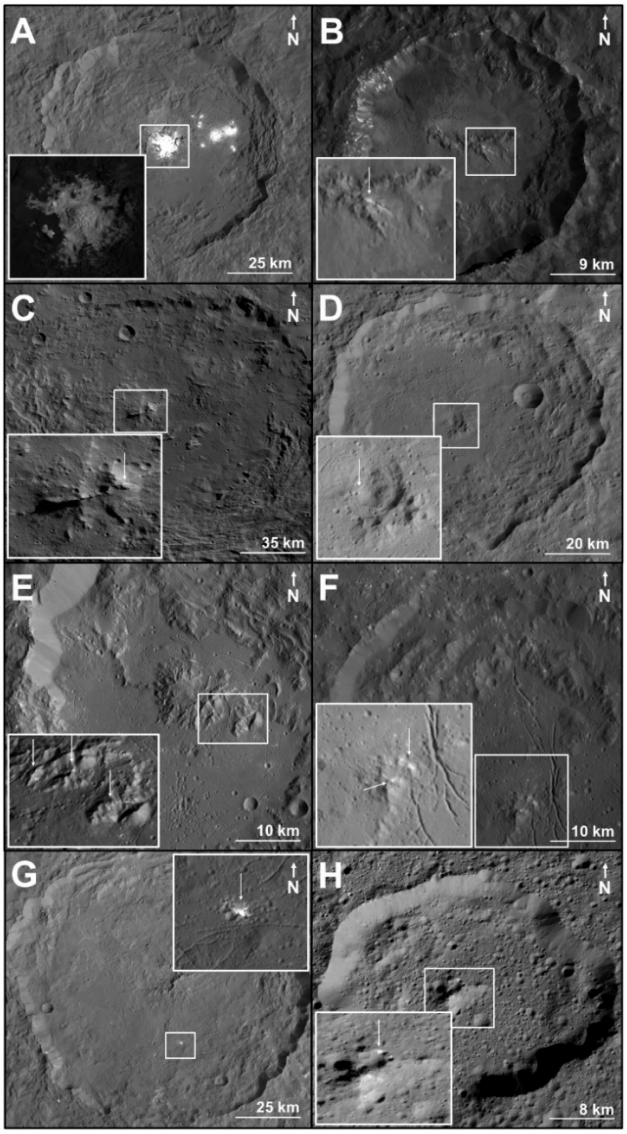

Figure 5.4. FC images of all craters with floor faculae. (**A**) Occator crater with an inset of Cerealia facula in Occator's central pit. Extensional fractures are visible on the 0.4 km tall central dome (Nathues et al., 2017). Small impact craters on this facula expose brighter underlying material. (**B**) Haulani crater. Bright material emanates from near the top of the central ridge alongside a lobate flow. Rim/wall faculae are also visible on the crater's western rim of the crater. (**C**) Urvara crater, which contains a large facula on its central ridge. (**D**) Gaue crater, which contains sparse and fairly dark faculae near its central pit. (**E**) Faculae in the central peak complex of Ikapati crater. Rim/wall faculae are also visible in small craters on the crater floor and along the western crater rim. (**F**) Faculae in the central peak complex of Azacca crater. Rim/wall faculae are also visible in small craters on the crater floor and along the western crater rim. (**G**) Dantu crater, which contains a large floor facula associated with concentric floor fractures. (**H**) Faculae on the central ridge of Ernutet crater. Rim/wall faculae are also visible on the western and southern crater rims.

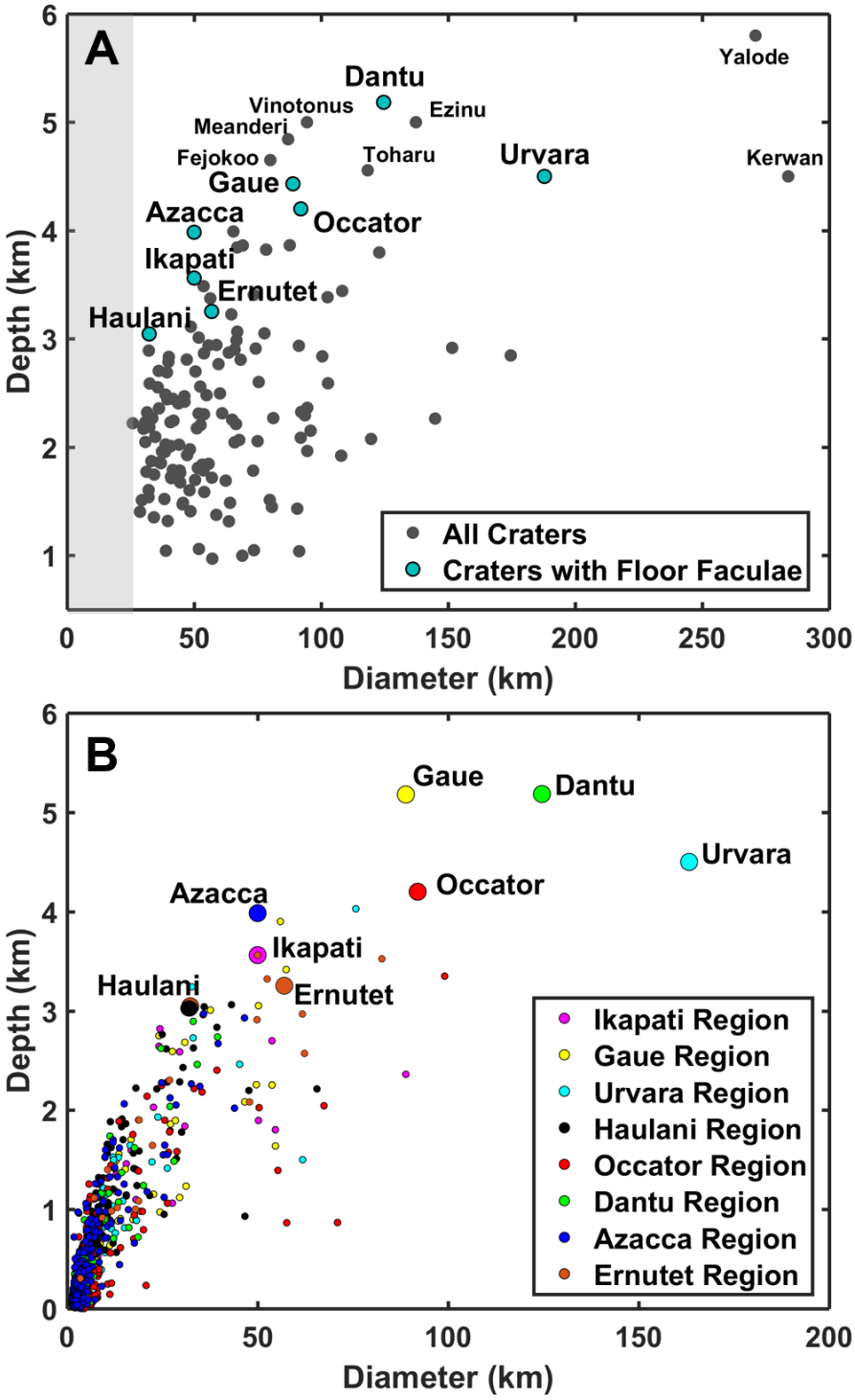

Figure 5.5. (**A**) Depth and diameter of the largest craters on Ceres (gray) with those that contain floor faculae indicated (cyan). (**B**) Depth and diameter of craters within a ~200 km radius of the craters with floor faculae. A ~200 km radius was selected under the assumption that the subsurface composition is relatively similar over that area.

Most of the floor facula-containing craters exhibit features consistent with the upwelling and outgassing of volatiles. Urvara, Dantu, Occator, Ikapati, Azacca, and Haulani contain pitted terrains on their floors consistent with post-impact outgassing of volatiles (Denevi et al., 2012; Sizemore et al., 2017). Dantu and Ikapati contain the largest examples of pitted terrains on the surface. Occator, Azacca, Gaue, Dantu, Haulani, and Ikapati contain fractures on their floor that are morphologically similar to class I lunar Floor-Fractured Craters (FFCs), whose formation is attributed to doming resulting from magmatic intrusion (Schultz, 1976; Jozwiak et al., 2015; Buczkowski et al., 2016).

The craters with floor faculae generally exhibit morphologically immature features including steep crater sides and well-defined central peak/pit complexes. Crater size-frequency distribution (CSFD) measurements indicate that the craters with floor faculae are relatively young. ADM crater ages range from <6 Ma for Haulani to 110 ± 7.2 Ma for Urvara and 420 ± 60 Ma for Ernutet, the two oldest craters with floor faculae (Schmedemann et al., 2016; Pasckert et al. 2017). FC color images show that the floor facula craters occur in spectrally blue regions, which have a negative spectral slope over the visible wavelengths relative to the average surface, consistent with their young age (Jaumann et al., 2016; Nathues et al., 2016; Schmedemann et al., 2016; Stephan et al., 2017). Floor formation ages of the floor facula craters are known in some cases to be significantly younger than crater formation ages, indicating extensive and sometimes long-lasting post-impact activity (Nathues et al., 2016).

5.4.1.2 Characteristics of Floor Faculae

The floor faculae are typically, though not exclusively, associated with central pit or peak complexes (Fig. 5.4A-F, H) and exhibit an array of morphologies. The brightest and most extensive is Cerealia Facula in the ~3.5 km wide, 0.6 km deep central pit of Occator crater (Jaumann et al., 2017; Nathues et al., 2017). A dome in the center of the pit consisting of bright material rises 0.4 km above the surrounding terrain and exhibits extensional tectonic fractures (Nathues et al., 2017). The average Bond albedo of Cerealia Facula is 0.24 ± 0.01 and increases to more than 0.5 in the center of the dome. Small craters

in Cerealia Facula appear to expose brighter underlying material (Fig. 5.4A). A cluster of several faculae (Vinalia Faculae) lies on the eastern floor of Occator along an extensive fracture system (Nathues et al., 2017). These faculae are on average significantly darker than Cerealia Facula, with a Bond albedo of 0.11 ± 0.04.

In Haulani crater, faculae with an albedo of 0.085 ± 0.01 are exposed near the top of a central mountain ridge and streak downslope alongside smooth, lobate landslide materials that are mass wasting toward the crater floor (Fig. 5.4B). The crater floor contains numerous pits, flows, and floor fractures as well as diffuse bright material. Extensive faculae are also exposed along the rim. Faculae in Azacca, Gaue, Urvara, and Ikapati also occur along central ridges or peak complexes (Fig. 5.4C-F), but are not directly associated with lobate flows as in Haulani. Gaue, Urvara, and Ikapati also contain smooth floor materials that may be sourced from post-impact extrusion of volatile-rich material (Pasckert et al., 2016; Sizemore et al., 2017). In Dantu crater, faculae with an average albedo of 0.11 ± 0.02 occur along crater floor fractures rather than in the central pit/peak complex and are the most spatially extensive floor faculae outside of Occator crater (Fig. 5.4G). The faculae in Ernutet (Fig. 5.4H) and Gaue (Fig. 5.4D) are less extensive than those in other craters and although they occur in central peak complexes, they may be associated with small impact craters below the limit of FC resolution, and hence may have formed by a process distinct from the other floor faculae.

We found no clear correlation between crater formation age and albedo of floor faculae; the central facula of Haulani (albedo 0.085 ± 0.01), the youngest of the craters (<6 Ma, Schmedemann et al., 2016) with floor faculae, is significantly darker than Occator's Cerealia and Vinalia Faculae (albedos of 0.24 ± 0.01 and 0.11 ± 0.04, respectively). Crater count-based formation age estimates for Occator crater are 34 ± 2 Ma (Nathues et al., 2017) and 23.7 ± 1.1 Ma (Neeseman et al., this issue). The Haulani floor facula is also darker than the floor faculae in the 72-150 Ma Dantu crater (albedo 0.11 ± 0.02), but brighter than the faculae in the older Azacca crater (albedo 0.07 ± 0.01) (Fig. 5.6).

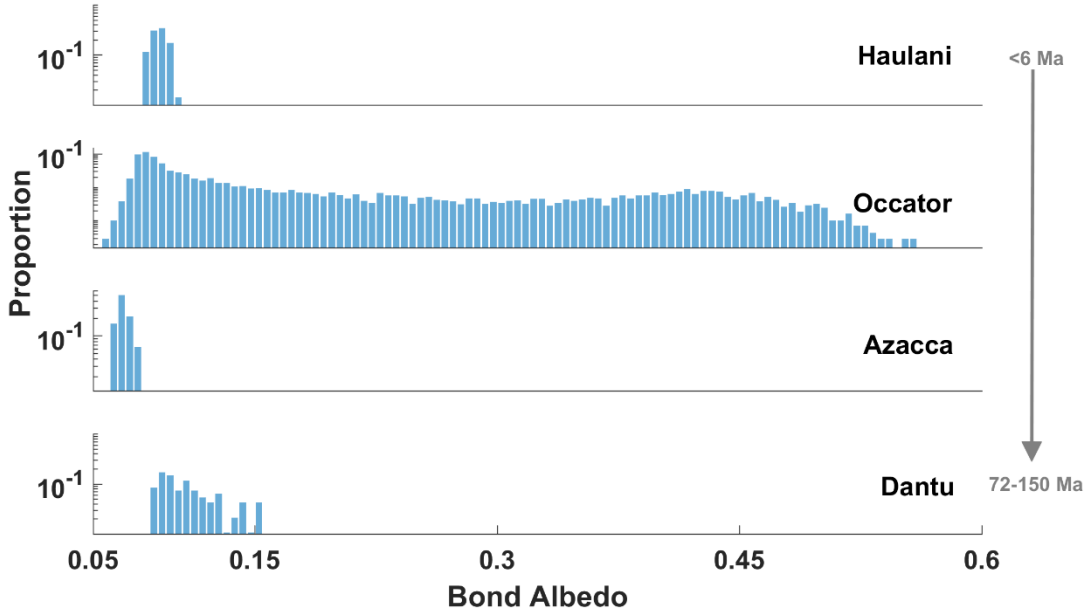

Figure 5.6. Albedo distribution of the largest floor faculae in approximate order of crater age (Neeseman et al., this issue; Schmedemann et al., 2016; Nathues et al., 2017; Pasckert et al. 2017), increasing from top to bottom. There is no obvious correlation between crater age and floor faculae albedo; Cerealia (0.24 ± 0.01) and Vinalia (0.11 ± 0.04) Faculae in Occator crater are brighter on average than those in Haulani (0.085 ± 0.01) despite Occator's older age. The floor faculae in Dantu crater (0.11 ± 0.02) are significantly brighter than those in Azacca (0.07 ± 0.01), despite Dantu being significantly older.

5.4.2 Rim/Wall Faculae

5.4.2.1 Characteristics of Craters with Rim/Wall Faculae

Rim/wall faculae and collections of bright material occur along the rims or walls of craters, typically within ~100-200 m of the uppermost surface (Fig. 5.2B). By number and extent, they are the most common facula class, occurring in more than 150 craters with D > 1 km and covering at least 1,100 km^2 cumulatively. The craters containing rim/wall faculae are often clustered together in small groups. Unlike floor faculae, rim/wall faculae occur in craters of all sizes, including the smallest resolvable craters (~100 m diameter) in LAMO FC images, and most frequently occur in simple craters (Fig. 5.7A). The distribution of craters with rim/wall faculae is, however, skewed toward larger diameters relative to Ceres' average crater population (Fig. 5.7B). Rim/wall faculae also occur

preferentially in craters that are anomalously deep for their diameter (Fig. 5.7C). The high d/D of craters with rim/wall faculae indicates that on average they are relatively young. Not all fresh craters contain rim/wall faculae, but faculae are not observed in any highly degraded craters.

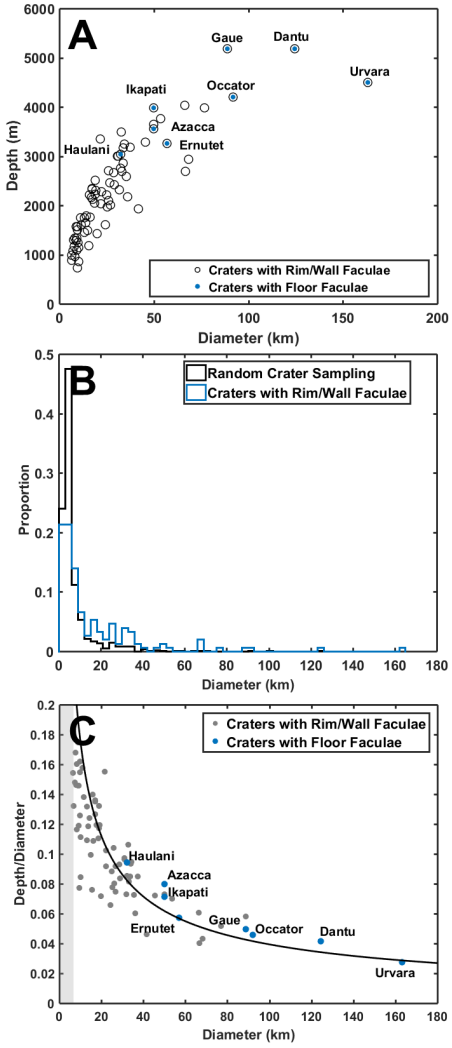

Figure 5.7. (**A**) Depth and diameter of > 5 km diameter craters that contain floor faculae (blue circles) and rim/wall faculae (black circles). (**B**) Comparison of the diameter of craters with rim/wall faculae (blue) to a random sample of more than 1,000 craters (black) from ±55° latitude. (**C**) The depth/diameter of craters with rim/wall faculae (black and blue) as a function of diameter compared with a curve representing the average depth/diameter of morphologically fresh craters on Ceres (black). On average, the depth/diameter of craters with rim/wall faculae is close to that of other morphologically fresh craters, consistent with a young crater age.

Some of the most extensive rim/wall faculae occur in craters with floor faculae such as Haulani and Dantu, and all craters with floor faculae also contain rim/wall faculae. Additionally, the floors of craters with floor faculae also contain many small craters with rim/wall faculae. Many craters with extensive rim/wall faculae, such as Haulani (Fig. 5.5B), Kupalo (Fig. 5.8A), Juling (Fig. 8A), Oxo (Fig. 5.8B), and Ikapati (Fig. 5.8C) also contain bright ejecta blankets (see section 5.4.3). Some of the brightest and most extensive rim/wall faculae occur in the adjacent and geologically young Juling (D = 20 km) and Kupalo (D = 26 km) craters (Fig. 5.8A).

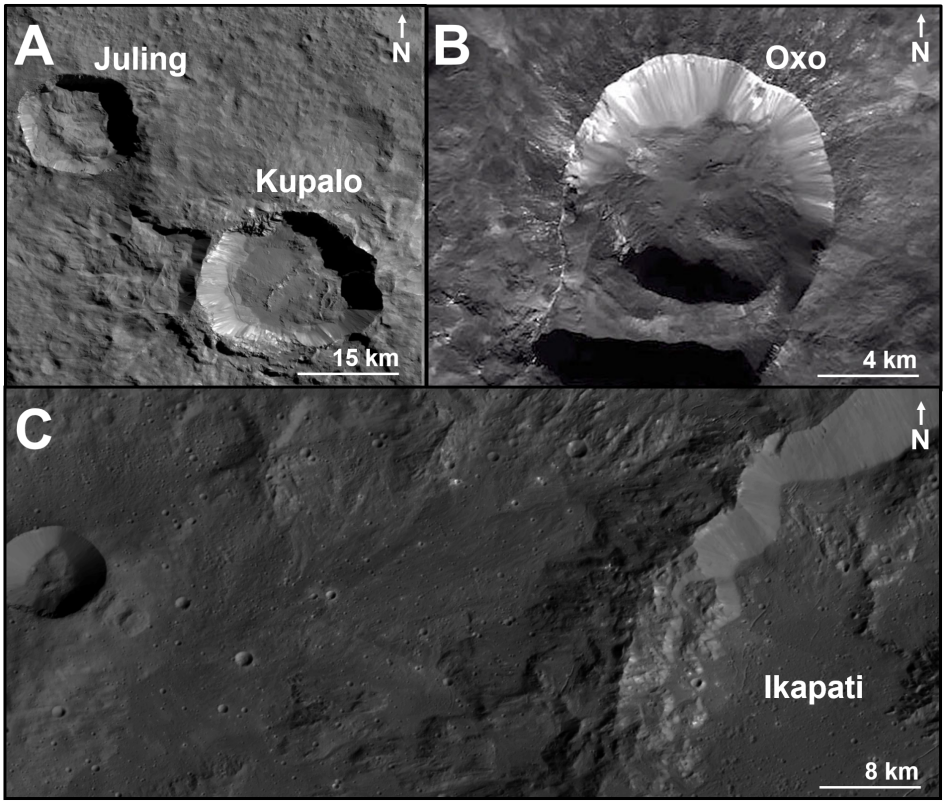

Figure 5.8. (**A**) Juling and Kupalo craters contain some of the brightest and most extensive rim/wall faculae on Ceres. Both craters formed within the last few Myr. Their spatial extent and temporal proximity indicate that they may expose the same previously formed facula. (**B**) Oxo crater contains the brightest faculae outside of Occator crater and is one of the youngest craters on the surface (190 ka (1σ +100 ka, -70 ka)) (Nathues et al., 2017b). It also contains some exposed H_2O ice (Combe et al., 2016). (**C**) In addition to containing rim/wall faculae, Ikapati crater has a large ejecta blanket on its western side that is dotted with small craters that contain rim/wall faculae that are brighter than the surrounding blanket (white arrows).

5.4.2.2 Characteristics of Rim/Wall Faculae

Rim/wall faculae typically occur as isolated <1 km diameter bright regions that emanate from the shallow subsurface and streak down crater walls. In some large craters, faculae are observed near the base of crater walls or even on crater floors, but closer examination reveals that these actually occur on the rims of smaller, later impacted craters. In some craters such as Kupalo (Fig. 5.8A), faculae are more extensive and occur in discontinuous clusters that line portions of the crater rim at equal depth. The faculae frequently streak down crater walls, darkening with lateral distance down a topographic gradient (Fig. 5.2B). In smaller craters such as Oxo (Fig. 5.8B), bright material that lines the entire crater rim as well as portions of the crater floor was likely excavated instead of forming upon impact, as the floor bright material is contiguous with bright ejecta. Most rim/wall faculae occur in small craters within bright ejecta blankets, which likely expose even brighter underlying material (e.g., Fig. 5.8C).

Rim/wall faculae have an average Bond albedo of 0.10 ± 0.01, significantly lower than the average floor facula albedo of 0.18 ± 0.02, but this difference in averages is primarily attributable to Occator's spatially extensive and exceptionally bright Cerealia Facula, without which the average floor facula albedo drops to 0.089 ± 0.01. Without Oxo, which contains by far the brightest rim/wall facula, the average rim/wall facula albedo is 0.07 ± 0.01. Many rim/wall faculae are brighter than floor faculae in other craters. Within the same crater, however, rim/wall faculae are darker than the floor faculae (Fig. 5.9). In contrast to the non-correlation between albedo and crater formation age for floor faculae, there is a negative correlation between rim/wall facula albedo and crater age with younger craters containing brighter faculae on average (Fig. 5.9). The different trends in albedo between floor and rim/wall faculae are interpreted to result from activity in the floor faculae

that potentially significantly post-dates crater formation (see section 5.5.1.1), making floor faculae brighter than the parent crater age might suggest.

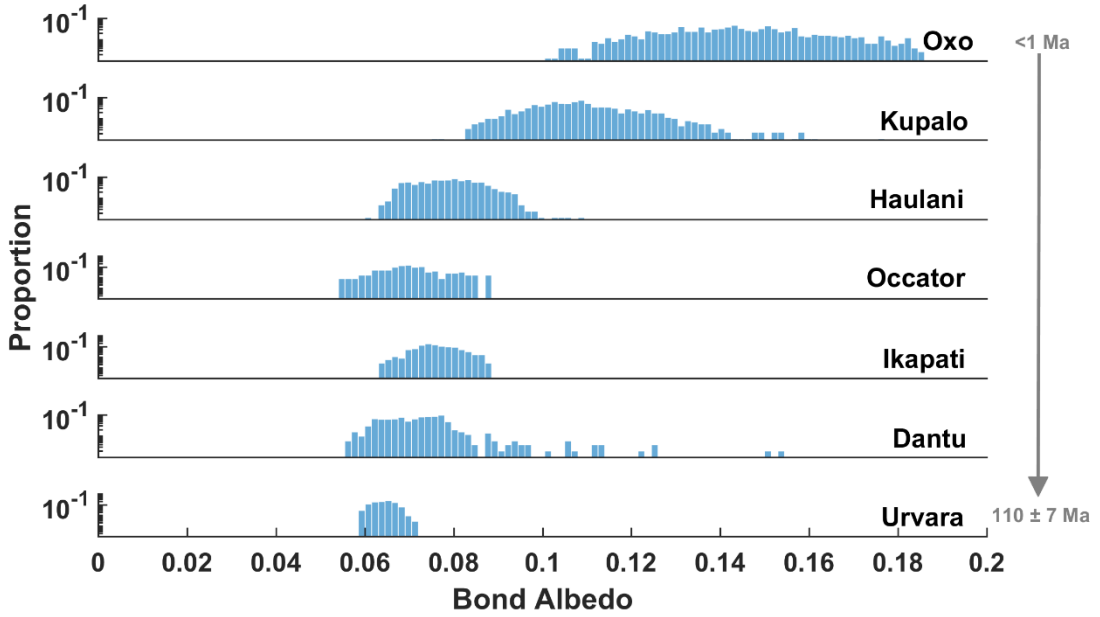

Figure 5.9. Albedo distribution of the most extensive rim/wall faculae in approximate order of crater age (Neeseman et al., this issue; Schmedemann et al., 2016; Nathues et al., 2017; Pasckert et al. 2017), increasing from top to bottom. There is a negative correlation between crater age and the albedo of rim/wall faculae. Oxo, which is < 1 Ma, contains the brightest faculae (0.014 ± 0.02) outside of Occator crater.

5.4.3 Bright Ejecta

Many craters with floor and/or rim/wall faculae exhibit bright ejecta blankets. These bright ejecta are only associated with craters that also contain rim/wall faculae, and they occur around craters of all sizes. Although there is no preferred overall orientation of the bright ejecta, they are preferentially on the sides of craters where rim/wall faculae are most prominent, such as at Juling and Kupalo (Fig. 5.8A). Around somewhat older craters such as Dantu and Ikapati, bright ejecta contain within them small craters with rim/wall faculae that expose brighter underlying material (Fig. 5.8C). The ejecta are on average

darker than rim/wall and floor faculae, perhaps because of partial mixing with average surface material (Fig. 5.10).

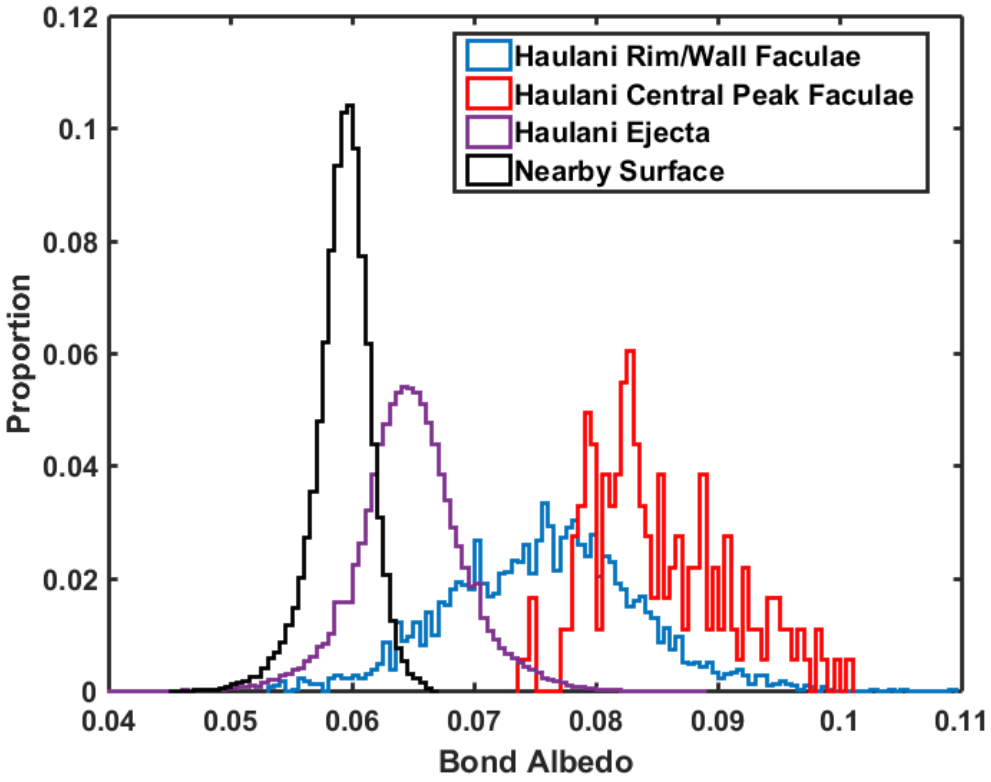

Figure 5.10. Albedo distribution of different types of faculae in and around Haulani crater. The darker, left-skewed distribution of the rim/wall faculae (blue) as compared to the floor faculae (red) indicates that they were not deposited contemporaneously as part of the same process. Similar albedo trends are observed in Occator and Ikapati.

5.4.4 Ahuna Mons

Ahuna Mons is a ~5 km-high, 17 km-wide mountain near Ceres' equator and the most prominent mountain on the surface (Fig. 5.2D). The summit is concave downward and contains troughs, ridges, and hummocky terrains, while the mountain flanks are at the angle of repose and contain bright material that streaks downward from the summit. On the east face of Ahuna Mons, bright material appears to emanate from the top of the mountain and streak ~4 km to its base, likely because of gravity-driven motion. On the

north flank, similar streaks of bright material appear to emanate from ~1-2 km above the surface on the side of the mountain and streak to the surface. Several small craters on the south flank and top of Ahuna Mons expose rim/wall faculae. Previous modeling by Ruesch et al. (2016) indicates that Ahuna Mons was emplaced by the formation of a cryovolcanic dome, likely from extrusions of hydrated salts with low eutectic temperatures and thermal conductivities. The bright streaks likely run out due to gravity-driven regolith motion. No similar faculae are observed on any other mountains independent of rim/wall faculae in impact craters.

5.4.5 Composition of Faculae

Palomba et al. (2017) and Carrozzo et al. (2017) investigated the composition of faculae using VIR spectra and found significant variations in the abundance of ammoniated clays and the depth and position of 3.4 and 4 μm carbonate absorption bands across the surface. Most faculae contain Mg-Ca carbonates similar in composition to Ceres' average surface carbonates, mixed with dark components and hydrated and ammoniated compounds (Palomba et al., 2017). Several regions including Oxo, Occator, Azacca, Kupalo, Ernutet, Dantu, Haulani, Baltae Catenae, and Ahuna Mons contain some Na carbonate associated with bright material (Zambon et al., 2017; Carrozzo et al., 2017). The rim/wall faculae are compositionally similar to many floor faculae, but the dominant carbonate tends to be Mg-Ca carbonate whereas floor faculae and the most extensive rim/wall faculae (e.g. in Oxo and Kupalo) typically contain at least some Na-carbonate (Carrozzo et al., 2017; Palomba et al., 2017). Water ice detections in Oxo crater (Combe et al., 2016; Nathues et al., 2017b) and other H_2O-containing craters (Carrozzo et al., 2017; Combe et al., 2017) are sometimes contiguous with the carbonate-bearing faculae.

5.5 Potential Facula Formation Mechanisms

Apart from Ahuna Mons, the formation of faculae is clearly associated with impact events, although the formation mechanisms behind the different types of faculae are likely distinct. The occurrence of floor faculae in exceptionally deep craters is consistent with

their formation via A) impact-induced heating and upwelling of volatile-rich materials, B) excavation/upwelling of heterogeneously distributed brines or their precipitation products, or C) a combination of both processes with some variation by location. The occurrence of rim/wall faculae in craters of all sizes cannot be explained by impact-induced heating or upwelling, and hence their formation requires the induction of a separate formation mechanism, likely the excavation of previously emplaced faculae, such as buried floor faculae or exposed brine layers or lenses. Here we evaluate different facula formation mechanisms in the context of the number of faculae and morphological observations discussed in sections 5.3 and 5.4.

5.5.1 Floor Facula Formation

The formation of floor faculae is clearly associated with impact events, and the formation process must allow for the transport of volatiles from the subsurface to the surface. Below about 40° latitude in both hemispheres, Ceres' surface is largely devoid of water ice and other volatiles at ~1 m depth (Prettyman et al. 2016), but the shallow subsurface is likely a mixture of 30-40% ice by volume with an intermixed silicates, salts, and clathrates (Bland et al., 2016). Previously, De Sanctis et al. (2016) proposed that natrite (Na_2CO_3), likely the predominant carbonate of many floor faculae, and accompanying ammonium-bearing species could have formed by the interaction of NaCl and NH_3 in solution. The maximum modeled temperature of Ceres' outer crust (Castillo-Rogez and McCord, 2010; Hayne and Aharonson, 2015) is as high as -30°C, below the eutectic points of NaCl (-21°C), NH_4Cl (-22°C), NH_4HCO_3 (-17°C), and $NaHCO_3$ (-6°C), the likely Ceres salts, in water.

5.5.1.1 Facula Formation via Impact-Induced Heating

One potential mechanism for the production of the facula source fluids is impact-induced heating in large craters (De Sanctis et al., 2016). Crater impact models by Bowling

et al. (this issue) indicate that material near the center of moderate-to-large impact craters could be heated to more than 270 K, in excess of the eutectic temperature of the salts, and

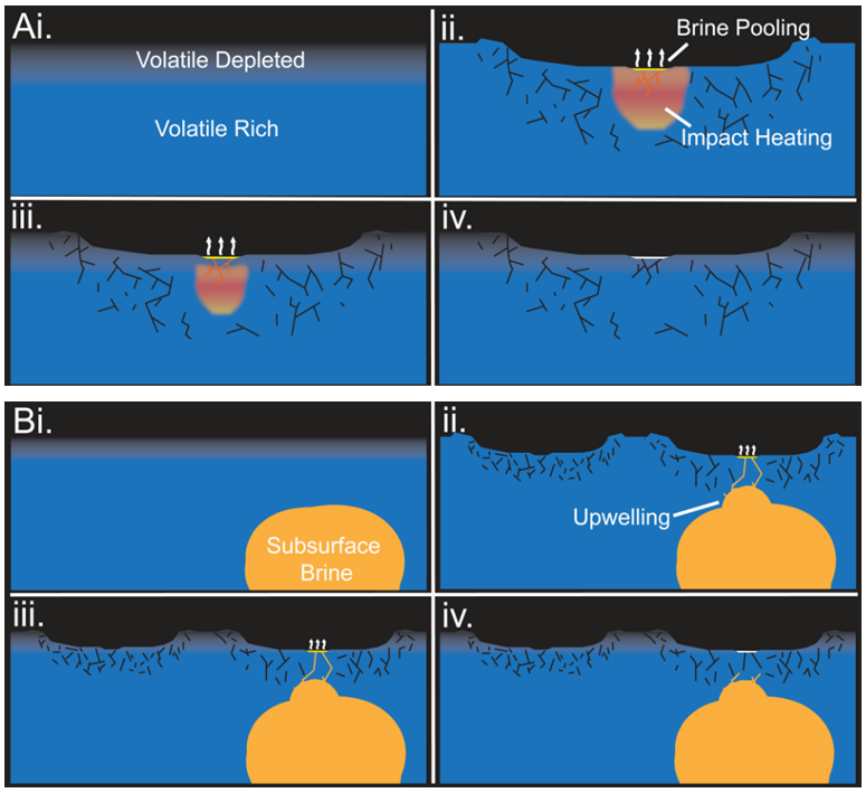

Figure 5.11. Schematic of two possible floor faculae formation mechanisms. Top: Faculae formation via impact-induced heating and upwelling of subsurface volatiles. (**Ai**) The steady-state surface is split into two layers: a volatile-rich subsurface and a shallow, volatile-depleted near-surface. (**Aii**) A large impact mixes volatile-depleted and volatile-rich materials in the subsurface (red) and heats subsurface volatiles. A volatile-rich slurry rises to the surface along impact-induced fractures and pools in a central pit. (**Aiii**) Volatiles near the surface sublimate. (**Aiv**) Sublimation ceases and a bright deposit of salts (facula) remains in the central pit. The subsurface cools. Bottom: Faculae formation via the upwelling of spatially heterogeneous subsurface volatiles due to impact-induced stresses. (**Bi**) A steady-state surface as in Ai but with a volatile-rich slurry (orange) at depth. The distribution of the heated material is laterally heterogeneous. (**Bii**) Some large impacts sample the already existing volatile-rich slurry, which may either rise to the surface along impact-induced fractures as shown or as a plume. (**Biii**) Near-surface volatiles sublimate. (**Biv**) Sublimation ceases and a bright deposit of salts (facula) is left in the central pit. Similar sized nearby craters might not generate faculae due to the heterogeneous nature of the subsurface.

that this heated material could be sourced from depths in excess of 20 km in an Occator-sized crater. Such a formation scenario is outlined in Fig. 5.11A. In this scenario, Ceres' near-surface is volatile-depleted and consists of a mixture of low-albedo materials, magnesium phyllosilicates, ammoniated phyllosilicates, and carbonates, with no more than a few wt% H_2O. The deeper subsurface is enriched in volatiles, especially ice. Heating from a large impact could produce a volatile-rich brine in the subsurface that rises to the surface along impact-induced fractures and pools in a central pit or travels laterally along crater floor or subsurface fractures (Fig. 5.11Aii.). The volatile-rich material would quickly sublimate (Fig. 5.11Aiii.), leaving a bright lag deposit of salts on the crater floor (Fig. 5.11Aiv.).

Models indicate that a heated subsurface region with a characteristic length scale of 10 km should cool on a timescale of < 3 Ma (Bowling et al., this issue), significantly less than the age of Occator crater, suggesting the formation of faculae could be limited to the period shortly following crater emplacement. It is unclear, however, whether the formation of all floor faculae is contemporaneous with crater formation; Nathues et al. (2017) derived a model age of 4.0 ± 0.1 Myr for Cerealia Facula, significantly younger than Occator itself (~20-35 Myr). Crater count-based facula ages rely on accurate identification of the spatial extent of already small faculae that may have been larger in the past, and should be treated as an approximate upper age bound. Additionally, the possible detection of a diurnal haze layer above Occator crater (Nathues et al., 2015; Thangjam et al., 2016) may indicate ongoing outgassing activity associated with the faculae, though its presence is debated (Schröder et al., 2016). Moreover, the lack of correlation between floor facula albedo and crater age may also indicate that their formation is not contemporaneous with crater formation as would be expected if faculae darken equally over time due to lateral mixing. Hence, the upwelling of material in Occator and other floor facula craters may have persisted for or occurred at least several Myr after impact. Impact heating models must account for the apparent discrepancy between facula and crater ages. Periods of more than ~1 Myr after impact may be too long if the extrusion of brines is controlled by impact-derived heat alone (Bowling et al., this issue), although upwelling derived from a reservoir of pre-existing volatiles could account for long-lasting post-impact activity.

5.5.1.2 Facula Formation by Upwelling of Extant Brines from Depth

Cerealia Facula and Ahuna Mons provide a clear indication of recently upwelled subsurface material (De Sanctis et al., 2016; Ruesch et al., 2016; Nathues et al., 2017). The other floor facula craters also exhibit numerous features consistent with the upwelling of subsurface volatiles such as pitted terrains and floor fractures that are similar to the geometry found in Type 1 lunar floor-fractured craters. Hence, the formation of floor faculae could equally be explained if subsurface temperatures exceed modeled values in at least some locations, allowing volatile-rich brines to exist at depth. Subsequent large impacts could heat these brines further and allow them to travel to the surface along impact-induced fractures (e.g. Fig. 5.11B) or to rise in plumes as an isostatic response to crater formation. Such a scenario could also allow for upwelling and outgassing activity long after crater formation. Similar processes may have been involved in the formation of Ahuna Mons and its faculae.

In either scenario or a combination of both, the varied compositions of the floor faculae coupled with the lack of floor faculae in several large, deep craters indicates the formation of floor faculae is sensitive to lateral variations in subsurface composition or ice abundance, possibly on the spatial scale of the craters themselves (10s-100s of km). Such heterogeneity may be implied by observed variations between the relative abundances of phyllosilicates and ammoniated species (Ammannito et al., 2016). Previous investigations of viscous relaxation by Bland et al. (2016) indicate that Ceres' subsurface ice content may vary by as much as 5-10 volume percent over short length scales. Similar heterogeneities in subsurface temperature or composition could explain the lack of floor faculae in some young, deep craters.

The association of floor facula-containing craters with features consistent with upwelling materials coupled with the young age of Cerealia Facula relative to Occator

suggests that the upwelling of extant subsurface brines likely plays an integral role in facula formation and may be complemented by impact-induced heating.

5.5.2 Rim/Wall Facula and Bright Ejecta Formation

Key observations of rim/wall faculae include darkening with age and their association with impact craters. The occurrence of rim/wall faculae in many shallow, small-diameter craters is inconsistent with their formation via impact-induced heating or plume activity. Some large craters such as Haulani, Dantu, and Occator contain floor and rim/wall faculae in addition to bright ejecta, which raises the prospect that all types of bright material were emplaced simultaneously by the same mechanism. It is apparent, however, that the rim/wall faculae are darker than floor faculae contained within the same crater, indicating that they were emplaced earlier rather than contemporaneously by the same formation process (e.g., for Haulani, Fig. 5.10). Bright ejecta blankets have a lower albedo than rim/wall and floor faculae contained in the same crater.

Several observations indicate rim/wall faculae formed via the excavation of previously emplaced faculae: 1) rim/wall faculae occur preferentially in larger diameter craters, as would be expected if new craters were exposing buried bright material because larger craters intersect a greater surface area; 2) craters with rim/wall faculae are frequently clustered together over length scales of 5-50 km, consistent with the existence of heterogeneously distributed subsurface deposits of bright material; and 3) all craters with bright ejecta, whose formation is contemporaneous with impact excavation, also contain rim/wall faculae. Previously emplaced floor faculae could have formed via impact-facilitated processes (see section 5.5.1) and been later buried by material emplaced by subsequent impacts or subsurface faculae may have already existed at depth from subsurface reactions of volatile-rich brines (Fig. 5.12A). Subsequent impacts of any size that intersect previously emplaced faculae would expose them again along their crater rim and partially disseminate the material as bright ejecta (Fig. 5.12B). The association of bright ejecta blankets with rim/wall facula-containing craters, as well as the preferential distribution of bright ejecta on crater sides with rim/wall faculae, indicates that the material

comprising these two types of faculae is generated simultaneously by the same mechanism. Subsequently, rim/wall faculae would darken, likely due to space weathering and/or lateral mixing (see section 5.6) as indicated by the negative correlation between crater age and rim/wall facula albedo. Eventually the rim/wall faculae are likely buried due to lateral mixing from subsequent impacts (Fig. 5.12C). Due to the heterogeneous distribution of previously emplaced faculae, not all new impacts would produce rim/wall faculae or bright ejecta.

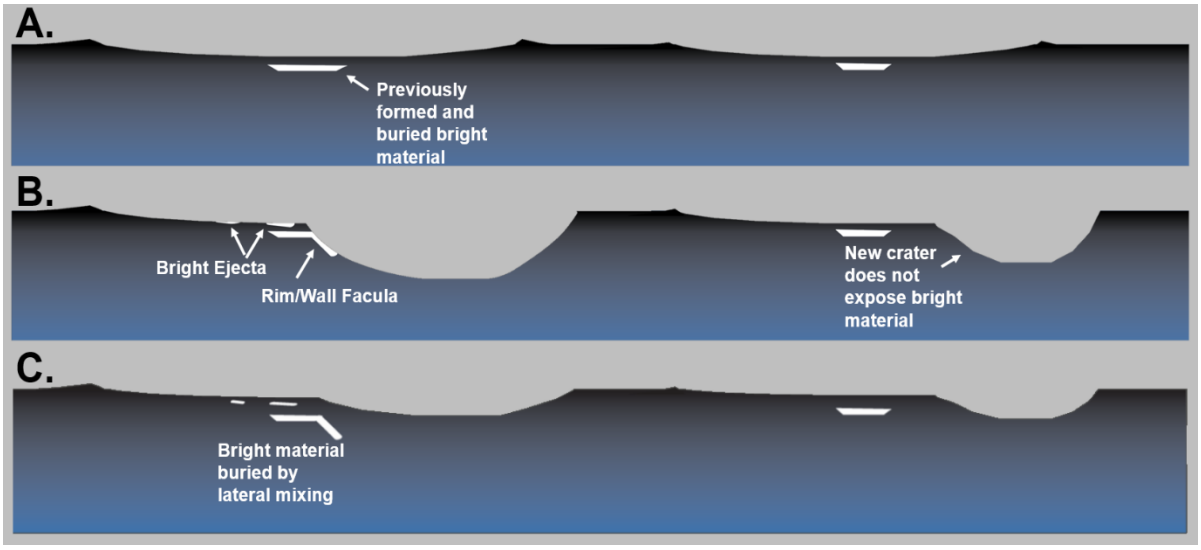

Figure 5.12. Schematic of the favored formation mechanism for rim/wall faculae and bright ejecta blankets. (**A**) Faculae formed due to previous impacts (Figure 5.10) are shallowly buried by mostly dark materials disseminated by subsequent impacts. (**B**) New impacts may partially intersect previously emplaced faculae and expose them as rim/wall faculae or disseminate them as bright ejecta (left). Not all new impacts will intersect buried bright material (right). (**C**) Eventually rim/wall faculae and bright ejecta are buried due to a combination of space weathering and burial by lateral mixing.

In the following sections, we examine key aspects of this hypothesized scenario: the timescales for darkening and removal of faculae from the Ceres surface (section 5.6)

and whether the current number of craters with rim/wall faculae is consistent with their formation via excavation using a simple impact cratering model (section 5.7).

5.6 Darkening and Disappearance of Faculae

The occurrence of floor faculae in exceptionally deep, morphologically fresh craters located in spectrally blue regions indicates that they are geologically young. Recent CSFD measurements by Schmedemann et al. (2016) estimate that the oldest of the floor facula craters has a formation age of ≤ 420 Ma. The presence of numerous older, shallower D > 50 km craters (Fig. 5.4), which may have viscously relaxed to their present state (Bland et al., 2016), and which lack faculae, raises the prospect that at least some of these craters once contained floor faculae that subsequently disappeared from the surface. A similar inference can be drawn for rim/wall faculae, which occur preferentially in anomalously deep and presumably young craters. The lack of rim/wall faculae in degraded craters indicates that either the faculae are a geologically recent phenomenon or that they disappear from the surface over time scales of several hundred Myr. Additionally, a gradual darkening mechanism for the rim/wall faculae is implied by the negative correlation between rim/wall facula albedo and parent crater age. The lack of such a correlation for the floor faculae is interpreted to result solely from the mismatch between floor faculae age and parent crater age due to post-impact activity and is not interpreted to result from a difference in the darkening process.

Possible mechanisms for the disappearance of faculae include gradual devolatilization or chemical alteration, darkening and thus disappearance due to space weathering, or burial via impact-induced lateral mixing. Chemical alteration is unlikely as the known bright constituents of faculae (carbonates and NH_4-salts) are stable at the temperatures and pressures of Ceres' surface. Fresh craters on Ceres are spectrally blue and exhibit distinct optical properties compared to older surface regions, indicating that some process of space weathering or regolith gardening homogenizes the surface (Pieters et al., 2016a). A different group of surface and space weathering processes including lateral mixing, micrometeorite bombardment and contamination, thermal cycling, and

sublimation likely dominate on Ceres as compared to inner solar system bodies that experience the formation of nanophase metallic iron ($npFe^0$) or other nanophase particles (Pieters et al., 2016b). Of these processes, lateral mixing by emplacement of typical Ceres surface materials is most likely to significantly lower the albedo of faculae over relevant timescales.

We estimated the timescale over which impact-induced lateral mixing and direct impacts are expected to bury or disseminate newly emplaced faculae by using the Ceres crater production function (Hiesinger et al., 2016). A grid with the surface area of Ceres was populated randomly with craters of diameters and frequencies sourced from the crater production function in million year time steps. During each time step the grid was populated with a new set of craters. Ejecta thrown by new craters were assumed to completely bury surface material within a characteristic radius, taken here to be between zero and two crater diameters across. The area covered directly by new craters or their ejecta, which represents a region within which faculae would be removed, was calculated during each time step.

Models were run after 3 Ga, after any enhanced early bombardment and over a time period where the cratering production function was similar to the modern production rate. Results show that in the limit of no lateral mixing – i.e. all ejecta are lost to space and faculae are only directly disseminated by impacts – 50% of faculae would be removed from the surface within ~1.25 Ga (Fig. 5.13). This represents an upper bound on the average facula removal time from lateral mixing alone. In a more reasonable scenario where ejecta bury surface material within one crater radius, this time decreases to only ~300 Ma. The facula removal time would decrease further if the burial radius increased or if other processes like space weathering play a role in removal or darkening of the faculae. Hence, the burial or direct dissemination of faculae by impacts provides a viable mechanism for

their removal from the surface over timescales of several hundred Ma, consistent with the observed age range of the floor facula craters.

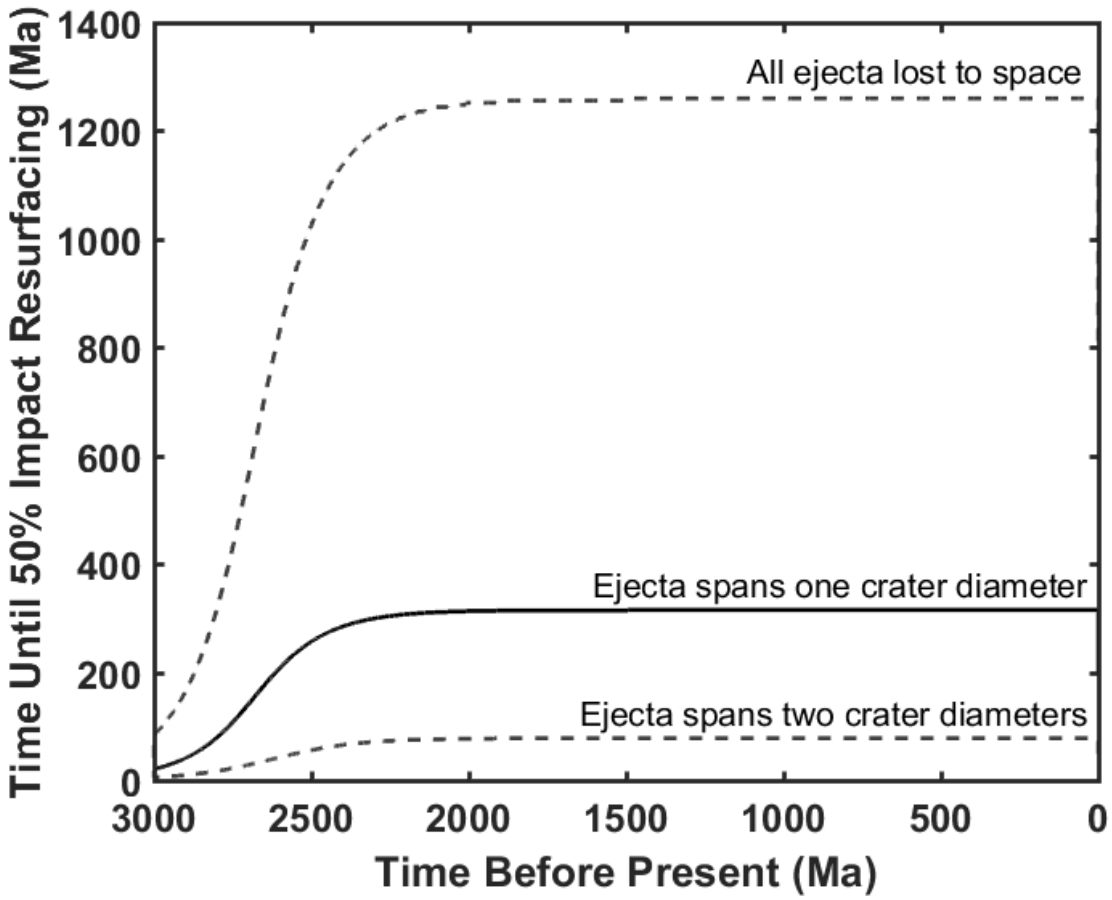

Figure 5.13. Simulated time until a given point on Ceres' surface has a 50% probability of being either directly impacted or buried by impact ejecta at different time periods before the present. The central line assumes that all ejecta are emplaced within a single crater radius. The upper bound denotes the case in which there is not ejecta blanket (i.e. all material is lost to space). The lower bound denotes the case in which the diameter of the ejecta blanket is twice that of the crater. The removal time decreases in the past due to the increased impact rate.

5.7 Facula Formation and Excavation Model

Under the hypothesis that impacts create crater floor or near-subsurface faculae with destruction timescales like those above, we next calculated the expected number of

faculae produced over Ceres' geologic history and exposed at the surface today. Starting at t=4.5 Ga, a grid with the surface area of Ceres A was populated in Myr time steps with a crater population sourced from the Ceres crater production function f (Hiesinger et al., 2016). During each time step t_i a total of $\boldsymbol{A\sum_{d=1}^{250} f(t_i, D)}$ craters were placed at random positions on the grid. Several rules were applied:

- Craters above a cutoff diameter D_c produced a circular floor facula of diameter D_f in the crater center that was carried to the next time step.

- In subsequent time steps if a new crater completely overlaid a previously emplaced facula, the facula was disseminated as bright ejecta and removed from subsequent time steps.

- If a new crater only partially intersected or was contained completely within a previously emplaced facula, a rim/wall facula was created and carried to the next time step. The portion of the previously emplaced floor facula directly intersected by the new crater was disseminated as bright ejecta and removed from subsequent time steps.

- If a new crater completely overlaid a previously emplaced rim/wall facula, the rim/wall facula was disseminated as bright ejecta, and the rim/wall facula was removed from the simulation.

In addition to destruction by direct impact, the gradual disappearance of faculae was modeled by including a condition whereby any rim/wall faculae remaining after time $\boldsymbol{t_r}$ were removed from the surface. The simulation was run for each combination of parameters $\boldsymbol{d_c}$ (50-100 km), D_f (1-10 km), and $\boldsymbol{t_r}$ (50-2000 Myr). The range of D_f was selected to mirror the size of faculae observed on the surface, and the range of t_r was selected to incorporate the timescales calculated in section 5.6. The range of crater diameters D_c was selected because larger craters produce floor faculae more frequently than smaller craters, although it is likely unrealistic for every crater with $D > D_c$ to produce

a facula, as many large and deep craters do not contain faculae. The small number of craters with floor faculae makes this parameter difficult to estimate accurately.

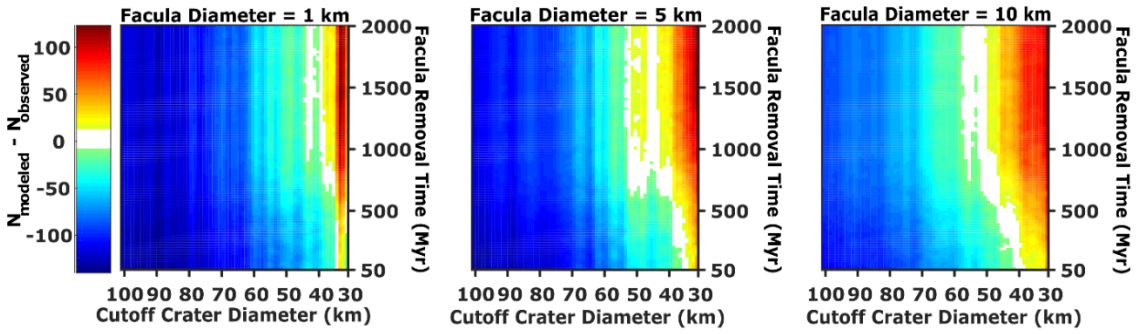

Figure 5.14. Difference beteween the modeled and the observed number of craters with rim/wall faculae for a range of facula removal times (t_r), cutoff crater diameters (D_c) for facula production, and facula diameters (D_f) of 1, 5, and 10 km. Model results reproduce the observed number of craters with rim/wall faculae for a wide range of t_r and D_f, if D_c is between 30-100 km.

Results show that the model reproduced the currently observed number of craters with rim/wall faculae for a wide range of D_f and t_r input parameters and a more restricted range of D_c (Fig. 14). If no $\boldsymbol{t_r}$ is imposed, the modeled number of craters with rim/wall faculae greatly exceeds the <200 currently observed. For example, for D_c =75 km, D_f = 10 km, and no t_r, the final number of craters with rim/wall faculae exceeds 10^4 (Fig. 15). For the same combination of parameters and t_r of 250, 500, and 1000 Myr, the simulated number of craters with rim/wall faculae drops to ~50, 100, and 300, respectively, similar to the observed number. This indicates that the observed number of craters with rim/wall faculae can be explained by the excavation of previously emplaced faculae if they are created by large impacts, distributed by smaller impacts, and removed from the surface over timescales of < 1 Gyr. Results also show that there were likely more faculae in the past due to the higher impact rate.

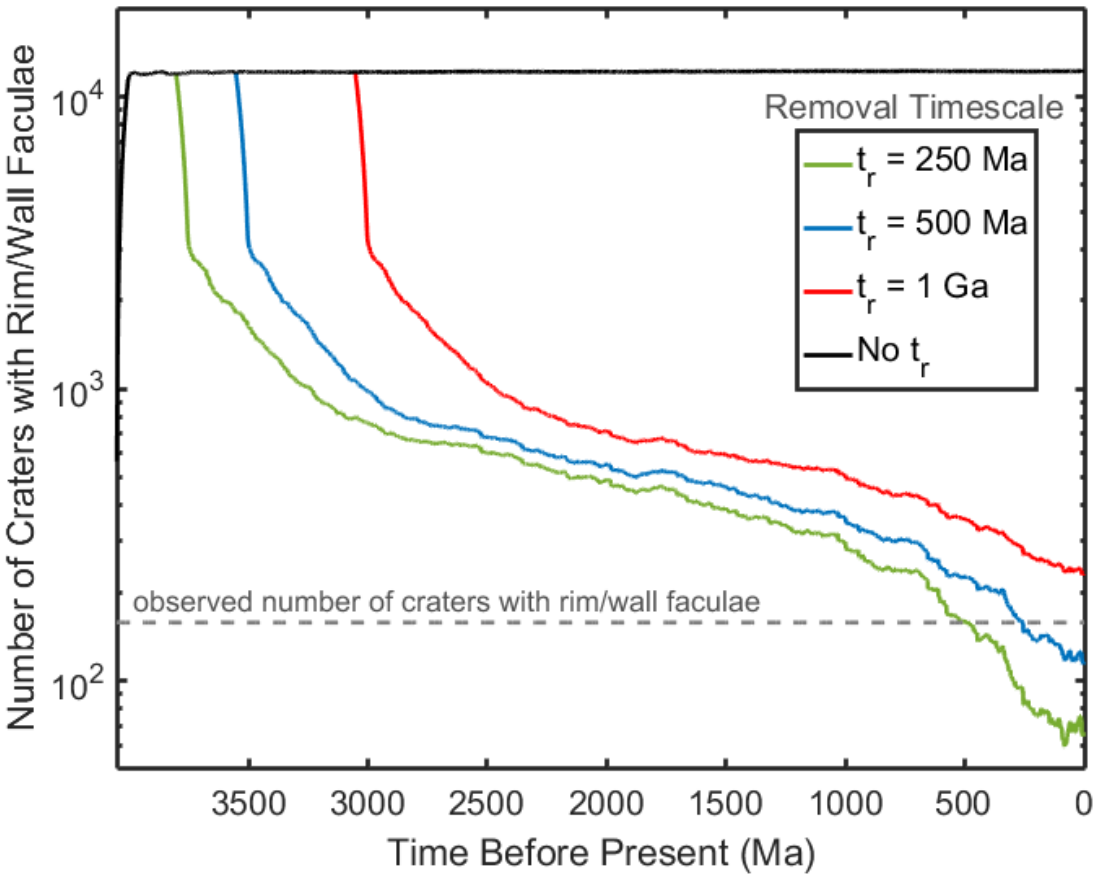

Figure 5.15. Simulated number of craters with rim/wall faculae as a function of time for a cutoff crater diameter for faculae production, D_c = 75 km, and initial faculae diameter D_f = 10 km. The top black line denotes the number of craters with rim/wall faculae if no cutoff time is imposed for facula removal by lateral mixing of dark material (t_r=0; i.e. faculae are only removed via direct impacts). The colored lines denote the modeled number of craters with rim/wall faculae if new faculae are removed on a characteristic timescale to simulate the combined effects of darkening due to space weathering and/or burial via lateral mixing. The dashed line denotes the number of craters currently observed with rim/wall faculae independent of ejecta blankets (154 craters).

5.8 Conclusions

Images from the Dawn Framing Camera were used to classify, identify, and map all faculae on the surface of Ceres. Faculae were found to fall into four distinct geological classes: 1) crater pits, peaks, or floor fractures (floor faculae), 2) crater rims or walls (rim/wall), 3) bright ejecta blankets, and 4) the mountain Ahuna Mons. Faculae occur

almost exclusively in or around impact craters. Floor faculae occur in large, deep, and young craters that often contain crater floor fractures and pitted terrains, consistent with the upwelling and degassing of volatiles. The geometry of craters with floor faculae is consistent with their formation via the impact-induced heating and upwelling of subsurface volatiles, the upwelling of volatile-rich brines along impact-induced fractures or as low-density plumes, or some combination of these processes. The association of floor faculae craters with features consistent with upwelling materials and the young age of floor faculae relative to their parent craters indicate that the impact-initiated upwelling of extant subsurface brines may be the favored crater floor faculae formation mechanism. Variations in the composition and albedo of floor faculae, coupled with the abundance of large and deep craters without floor faculae, indicates that their formation may be dependent on lateral variations in subsurface ice and/or brine abundance, composition, and temperature that only allow faculae to form in some regions of Ceres.

Rim/wall faculae were found to occur in relatively young craters of all sizes, and the geometry of rim/wall faculae and the craters that contain them is consistent with their formation via the excavation of faculae that were previously emplaced either as floor faculae that were subsequently buried or by the reaction of subsurface brines. Bright ejecta are interpreted to form by the same mechanism on the basis of their strong association with rim/wall faculae. Models using the Ceres crater production function indicate that faculae are likely to be destroyed, buried by impact-induced lateral mixing, or directly disseminated by impacts on timescales of less than several hundred Myr, consistent with the young age of the rim/wall- and floor facula-containing craters. Space weathering also may play an active role in the speeding the darkening of faculae over Myr timescales. A 4.5 Gyr computational model of facula production and destruction indicates that the observed number of craters with rim/wall faculae is consistent with the formation of floor

faculae in large craters, dissemination by impact to form rim/wall faculae, and removal from the surface over <1 Ga timescales.

Data collectively point to a relatively modern formation or exposure of faculae, indicating that Ceres' surface remains active and the near surface may support brines in the present day. Faculae currently exposed on the surface continue to evolve due to the combined effects of space weathering and lateral mixing. Faculae were likely forming at even greater rates in the geologic past, and warmer subsurface temperatures and higher impact rates would have promoted near-surface brines with greater frequency than today. Rim/wall faculae expose these relicts of alteration as a window into Ceres' past aqueous alteration. Although the original formation of faculae is clearly associated with impact processes, it remains unclear whether portions of the subsurface are warm enough to exceed the eutectic temperatures of the progenitor species of faculae or if heating is instead provided directly by impacts. Future analysis of the floor faculae, and particularly observations of whether some or all floor faculae remain active in present day, may allow this distinction to be made.

5.9 Acknowledgments

We are indebted to the Dawn mission team for their efforts in collecting the data used in this paper, as well as to members of the FC and VIR teams for their helpful discussions. A portion of this work was performed at the Jet Propulsion Laboratory, California Institute of Technology, under contract to NASA. Thanks to M. Landis and V. Reddy for reviews that improved this manuscript. This material is based upon work supported by the National Science Foundation Graduate Research Fellowship Grant No. DGE-1144469. VIR is funded by the Italian Space Agency and was developed under the leadership of INAF-Istituto di Astrofisica e Planetologia Spaziali, Rome, Italy. The instrument was built by Selex-Galileo, Florence, Italy. This work was supported by the

Italian Space Agency grant. Data used are available in the supplement material or archived in the Planetary Data System (pds.nasa.gov).

References

Ammannito, E., DeSanctis, M.C., Ciarniello, M., Frigeri, A., Carrozzo, F.G., Combe, J.-P., et al. (2016). Distribution of phyllosilicates on the surface of Ceres. Science. 353, 1006. https://doi.org/10.1126/science.aaf4279.

Bowling, T., Ciesla, F., Davidson, T., Scully, J., Castillo-Rogez, J., & Marchi, S. (2018). Post-impact thermal structure and cooling timescales of Occator crater on Asteroid 1 Ceres. *Icarus*, 320, 110-118. https://doi.org/10.1016/j.icarus.2018.08.028.

Buczkowski, D.L., Schmidt, B.E., Williams, D.A., Mest, S.C., Scully, J.E.C., Ermakov, A.I., et al. (2016). The geomorphology of Ceres. *Science*. 353, aaf4332. https://doi.org/10.1126/science.aaf4332.

Carrozzo, F.G., De Sanctis, M.C., Ammannito, E., Castillo-Rogez, J., Ehlmann, B.L., Ciarniello, et al. (2017). Nature, formation, and distribution of carbonates on Ceres. *Science Advances*, 4. https://doi,org/10.1126/sciadv.1701645.

Castillo-Rogez, J.C. & McCord, T.B. (2010). Ceres' evolution and present state constrained by shape data. *Icarus*, 205, 443–459. https://doi.org/10.1016/j.icarus.2009.04.008.

Ciarniello, M., De Sanctis, M.C., Ammannito, E., Raponi, A., Longobardo, A., Palomba, E., et al. (2017). Spectrophotometric properties of dwarf planet Ceres from the VIR spectrometer on board the Dawn mission. Astronomy and Astrophysics. 598, A130. https://doi.org/10.1051/0004-6361/201629490.

Combe, J.-P., McCord, T.B., Tosi, F., Ammannito, E., Carrozzo, F.G., De Sanctis, M.C., et al. (2016). Detection of local H_2O exposed at the surface of Ceres. *Science*, 353, aaf3010. https://doi.org/10.1126/science.aaf3010.

Combe, J.P., Raponi, A., Tosi, F., De Sanctis, M.C., Ammannito, E., Carrozzo, et al. (2017). Exposed H_2O-rich areas on Ceres detected by Dawn. *LPSC 48.* Abstract 2568.

Denevi, B.W., Blewett, D.T., Buczkowski, D.L., Capaccioni, F., Capria, M.T., De Sanctis, M.C., et al. (2012). Pitted terrain on Vesta and implications for the presence of volatiles. *Science*, 338(6104), 246-249. https://doi.org/10.1126/science.1225374.

De Sanctis, M.C., Ammannito, E., Raponi, A., Marchi, S., McCord, T.B., McSween, H.Y., et al. (2015). Ammoniated phyllosilicates with a likely outer Solar System origin on (1) Ceres. *Nature*, 528, 241–244. https://doi.org/10.1038/nature16172.

De Sanctis, M.C., Raponi, A., Ammannito, E., Ciarniello, M., Toplis, M.J., McSween, H.Y., et al. (2016). Bright carbonate deposits as evidence of aqueous alteration on (1) Ceres. *Nature*, 536, 1–4. https://doi.org/10.1038/nature18290.

Ermakov, A.I., Fu, R.R., Castillo-Rogez, J.C., Raymond, C.A., Park, R.S., Preusker, F., et al. (2017). Constraints on Ceres' internal structure and evolution from its shape and gravity measured by the Dawn spacecraft. *JGR: Planets*, 122. https://doi.org/10.1002/2017JE005302.

Hayne, P. O., and O. Aharonson. (2015). Thermal stability of ice on Ceres with rough topography, *JGR: Planets*, 120, 1567–1584. https://doi.org/10.1002/2015JE004887.

Hiesinger, H., Marchi, S., Schmedemann, N., Schenk, P., Pasckert, J.H., Neesemann, A., et al. (2016). Cratering on Ceres: Implications for its crust and evolution. *Science,* 353, aaf4759-aaf4759. https://doi.org/10.1126/science.aaf4759.

Jozwiak, L.M., Head, J.W., Zuber, M.T., Smith, D.E., & Neumann, G.A. (2012). Lunar floor-fractured craters: Classification, distribution, origin and implications for magmatism and shallow crustal structure. *J. Geophys. Res. E Planets*, 117, 1–23. https://doi.org/10.1029/2012JE004134

King, T. V., Clark, R. N., Calvin, W. M., Sherman, D. M., & Brown, R. H. (1992). Evidence for ammonium-bearing minerals on Ceres. *Science*, 255, 1551–1553. https://doi.org/10.1126/science.255.5051.1551.

Li, J.Y., Reddy, V., Nathues, A., Corre, L. Le, Izawa, M.R.M., Cloutis, E.A., et al. (2016). Surface Albedo and Spectral Variability of Ceres. *Astrophys. J.*, 817, L22. https://doi.org/10.3847/2041-8205/817/2/L22.

McCord, T.B., Combe, J-Ph., McSween, H., Jaumann, R., Reddy, V., Tosi, F., et al. and the Dawn Team. (2012). Dark material on Vesta: Adding carbonaceous volatile-rich materials to planetary surfaces. *Nature,* 491, 83-86. https://doi:10.1038/nature11561.

Nathues, A., Hoffmann, M., Schaefer, M., Le Corre, L., Reddy, V., Platz, T., et al. (2015). Sublimation in bright spots on (1) Ceres. *Nature*, 528, 237–240. https://doi.org/10.1038/nature15754.

Nathues, A., Hoffman, M., Platz, T., Thangjam, G.S., Cloutis, E.A., Reddy, V., et al. (2016). FC colour images of dwarf planet Ceres reveal a complicated geological history. *P&SS*, 134, 122-127. https://doi.org/10.1016/j.pss.2016.10.017.

Nathues, A., Platz, T., Thangjam, G., Hoffmann, M., Mengel, K., Cloutis, E.A., et al. (2017). Evolution of Occator Crater on (1) Ceres. *Astron. J.*, 153, 112. https://doi.org/10.3847/1538-3881/153/3/112.

Nathues, A., Platz, T., Hoffmann, M., Thangjam, G., Cloutis, E. A., Applin, D. M. et al. (2017). Oxo Crater on (1) Ceres – Geologic history and the role of water ice. *Astrophys. J.*, 154, 84. https://doi.org/10.3847/1538-3881/aa7a04.

Palomba, E., Longobardo, A., De Sanctis, M.C., Stein, N.T., Ehlmann, B., Galiano, et al. (2017). Compositional differences among Bright Spots on the Ceres surface. *Icarus*, https://doi.org/10.1016/j.icarus.2017.09.020.

Pasckert, J.H., Hiesinger, H., Williams, D.A., Crown, D.A., Mest, S.C., Buczkowski, et al. (2016). Geologic mapping of the Ac-H-2 Coniraya quadrangle of Ceres from NASA's Dawn mission. *LPSC 47*. Abstract 1450.

Pieters, C.M., Ammannito, E., Ciarniello, M., De Sanctis, M.C., Hoffmann, M., Jaumann, R., et al. (2016). Surface processes and space weathering on Ceres. *LPSC 47*. Abstract 1383.

Pieters, C.M. & Noble, S.K. (2016). Space weathering on airless bodies. *JGR: Planets*, 121. 1865-1884. https://doi.org/10.1002/2016JE005128.

Prettyman, T.H., Yamashita, N., Toplis, M.J., McSween, H.Y., Schorghofer, N., Marchi, S., et al. (2016). Extensive water ice within Ceres aqueously altered regolith: Evidence from nuclear spectroscopy. *Science*, 6765, 1–11. https://doi.org/10.1126/science.aah6765.

Reddy, V., Le Corre, L., O'Brien, D.P., Nathues, A., Cloutis, E.A., Durda, D.D., et al. (2012). Delivery of dark material to Vesta via carbonaceous chondritic impacts. *Icarus*, 221(2), 544-559. https://doi.org/10.1016/j.icarus.2012.08.011.

Ruesch, O., Platz, T., Schenk, P., McFadden, L.A., Castillo-Rogez, J.C., Quick, L.C., et al. (2016). Cryovolcanism on Ceres. *Science*, 353, aaf4286-aaf4286. https://doi.org/doi:10.1126/science.aaf4286.

Schmedemann, N., Kneissl, T., Neesemann, A., Stephan, K., Jaumann, R., Krohn, K., et al. (2016). Timing of optical maturation of recently exposed material on Ceres. *Geophys. Res. Lett.*, 43, 11,987-11,993. https://doi.org/10.1002/2016GL071143.

Schröder, S.E., Maue, T., Gutiérrez Marqués, P., Mottola, S., Aye, K.M., Sierks, H., et al. (2013). In-flight calibration of the Dawn Framing Camera. *Icarus,* 226, 1304–1317. https://doi.org/doi:10.1016/j.icarus.2013.07.036.

Schultz, P.H. (1976). Floor-fractured lunar craters. *Moon*, 15, 241-273. https://doi.org/10.1007/BF00562240.

Sierks, H., Keller, H.U., Jaumann, R., Michalik, H., Behnke, T., Bubenhagen, F., et al. (2011). The Dawn Framing Camera. *Space Science Reviews*, https://doi.org/10.1007/s11214-011-9745-4.

Sizemore, H. G., Platz, T., Schorghofer, N., Prettyman, T. H., De Sanctis, M. C., Crown, D. A., et al. (2017). Pitted terrains on (1) Ceres and implications for shallow subsurface volatile distribution. *Geophys. Res. Lett.* 44, 6570-6578. https://doi.org/10.1002/2017GL073970.

Stephan, K., Jaumann, R., Krohn, K., Schmedemann, N., Zambon, F., Tosi, F., et al. (2017). An investigation of the bluish material on Ceres. *Geophys. Res. Lett.*, 1660–1668. https://doi.org/10.1002/2016GL071652.

Thangjam, G., Hoffmann, M., Nathues, A., Li, J.Y. & Platz, T. (2016). Haze at Occator Crater on Dwarf Planet Ceres. *The Astrophysical Journal Letters*, 833, L25. https://doi.org/10.3847/2041-8213/833/2/L25.

Zambon, F., Raponi, A., Tosi, F., De Sanctis, M. C., McFadden, L. A., Carrozzo, F. G.,et al. (2017). Spectral analysis of Ahuna Mons from Dawn mission's visible-infrared spectrometer. *Geophys. Res. Lett.* 44, 97-104. https://doi.org/10.1002/2016GL071303.

Chapter 6

NA-CARBONATE EXPOSURES REVEAL RECENT, WIDESPREAD MOBILIZATION OF MATERIAL IN CERES' SHALLOW SUBSURFACE

N. Stein[1], B. L. Ehlmann[1,2], D.J. Stevenson[1], J. Castillo-Rogez[2], C.A. Raymond[2]

[1]Division of Geological and Planetary Sciences, California Institute of Technology, Pasadena, California 91125, USA

[2]Jet Propulsion Laboratory, California Institute of Technology, Pasadena, California 91109, USA

6.1 Abstract

Most of the Na-carbonate on Ceres surface is excavated material on the rims and walls of impact craters, but its source is uncertain. We map the distribution and extent of exhumed Na-carbonate with Dawn's Visible and Infrared Imaging Spectrometer (VIR), revealing a strong spatial correlation between domes and some shallow subsurface Na-carbonate deposits. Using Monte Carlo impact models, we constrain the timing of emplacement of the shallow subsurface Na-carbonate and establish that large deposits were likely emplaced in the last ~1 Ga and probably within the last few hundred Ma. The spatial association of Na-carbonate deposits and domes indicates that they form by the same or related processes. We demonstrate that a combination of processes including diapirism driven by Rayleigh-Taylor instabilities and solid-state deformation due to differential loading could mobilize Na-carbonate-bearing ices to the shallow subsurface without the recent presence of brines.

6.2 Introduction

One of the greatest revelations of the Dawn mission at Ceres was the observation of multiple surface features consistent with recent and potentially ongoing geological activity. Two prominent formations most conspicuously reveal Ceres' active state: Occator crater and Ahuna Mons. The ~92 km diameter Occator impact crater contains central bright, km-scale diameter deposits rich in Na-carbonate and ammoniated salts (De Sanctis et al., 2016) termed faculae with crater chronology ages of <20 Ma (Nathues et al., 2017; Neesemann et al., 2019). The faculae post-date the crater and likely formed from the extrusion of impact-heated brines (De Sanctis et al., 2016; Nathues et al., 2017, 2019; Ruesch et al., 2017; Zolotov et al., 2017) sourced from the shallow subsurface or possibly a deeper reservoir (Quick et al., 2019, Hesse and Castillo-Rogez, 2018). Ahuna Mons is a ~4 km high mountain – the most prominent on Ceres – with similar bright streaks of Na-carbonate mass wasting from its sides (Ruesch et al., 2016). Explanations for the formation of Ahuna Mons include the extrusion of brines from a deep source (Ruesch et al., 2016; 2019) or

surface deformation arising from solid-state flow akin to terrestrial salt tectonics (Bland et al., 2019).

It is now clear that these features are not unique; Ceres' surface is dotted with hundreds of Na-carbonate exposures (Carrozzo et al., 2017; Palomba et al., 2017; Stein et al., 2017) and dozens of putative domes (Sori et al., 2017; 2018; Sizemore et al., 2018), hinting that the processes that formed Occator crater's faculae and Ahuna Mons are spatially pervasive. Critical questions about these features remain. When did they form? What is their provenance? Are Na-carbonate deposits and domes formed by the same or related processes? Answers to these questions are central to understanding the history of recent geological activity on Ceres and its place as a target of astrobiological interest.

To address these questions, we focus on the most common class of Na-carbonate exposures on Ceres: those that occur on crater rims and walls (Stein et al., 2017). Crater rim/wall Na-carbonate deposits are observed in hundreds of young craters and range in scale from tens of meters to tens of kilometers, even larger than the central facula in Occator crater (Cerealia Facula). As in Occator crater, these once precipitated from brines, forming salts that include NH_4Cl and Na-carbonates, such as $Na_2CO_3 \cdot 10H_2O$, $Na_2CO_3 \cdot 2H_2O$, and/or $NaHCO_3$ (Castillo-Rogez et al., 2019; De Sanctis et al., 2016; Raponi et al., 2018; Zolotov et al., 2017).

Two potential sources of the Na-carbonate exposed on crater rims have been considered (Stein et al., 2017): 1) heating of ices during the formation of the parent crater and 2) exposure of Na-carbonate that formed in a previous impact and precipitated in the subsurface or was shallowly buried by lateral impact mixing. Because many rim/wall Na-carbonates either occur in craters too small for impact-induced brine formation or are too distant from the materials that would have heated sufficiently to form brines (Bowling et al., 2018), and because they are typically associated with Na-carbonate-enriched ejecta, scenario 1 is ruled out. It is instead inferred that the rim Na-carbonate exposures result from the impact-driven excavation of shallowly buried Na-carbonate (Stein et al., 2017). In evaluating the plausibility of scenario 2, Stein et al. (2017) posited that the current number

of crater wall Na-carbonate exposures is consistent with the expected number of previous large impactors that could plausibly have generated Na-carbonate deposits in an Occator-like process that were subsequently exhumed. Although parsimonious with our understanding of the processes forming Occator crater's Na-carbonate deposits, this explanation does not fully satisfy the observations because many large rim/wall Na-carbonate deposits do not sit in any discernible pre-existing Occator-sized (or larger) impact basin. Thus, the rim/wall Na-carbonate exposures present another Ceres mystery: there are globally widespread but spatially heterogeneous collections of shallow subsurface Na-carbonate – sometimes large (10s of km) – with unknown provenance and depositional timing.

Because shallow subsurface Na-carbonate deposits represent the largest collection of material that might have been recently mobilized to Ceres' surface, the rim/wall Na-carbonate exposures may be pivotal in characterizing recent geological activity on Ceres. Here we investigate two remaining scenarios for the emplacement of shallow subsurface Na-carbonate: 1) exposure of the precipitation products of brines that have been in Ceres' shallow subsurface since its differentiation and 2) exposure of shallowly buried Na-carbonate mobilized to the surface from the deep crust or upper mantle by brine upwelling and/or solid state deformation. We map the distribution and extent of exhumed Na-carbonate using images from Dawn's Visible and Infrared Imaging Spectrometer (VIR) instrument and relate them to the distribution of domes. We then use Monte Carlo impact models to constrain the timing of emplacement of the shallow subsurface Na-carbonate. We then evaluate potential mechanisms for the mobilization of Na-carbonate and simultaneous emplacement of domes and proximal shallow subsurface Na-carbonate deposits.

6.3 Distribution and Extent of Crater Rim/wall Na-carbonate

Na-carbonate is exposed patchily at hundreds of sites on Ceres (Carrozzo et al., 2017; Palomba et al., 2017). Most exposures occur on crater rims where bright Na-carbonate-bearing material was excavated by the impact and/or subsequent erosion and

wasted down crater walls (Stein et al., 2017). FC images show that the bright material typically wastes from depths of 10s-100s of m below the crater rim, though sometimes deeper, indicating that it was previously shallowly buried. In this study, we investigated spatially significant (>5 km extent) crater rim/wall bright spots to determine their composition. Calibrated (level 1b) VIR IR images (De Sanctis et al., 2015) at up to 100 m/px spatial resolution were denoised and thermally corrected. Na-carbonates were identified by a shift from the surface average ~3.95 µm carbonate band position (indicative of Mg- or Mg-Ca carbonates) to ~4.0 µm (Na-carbonates) (Figure 6.1A) (De Sanctis et al., 2016; Carrozzo et al., 2017).

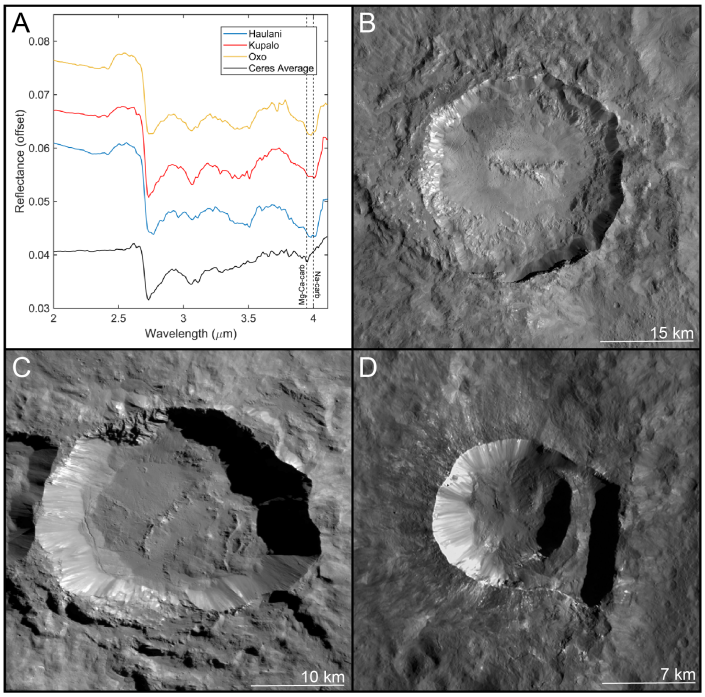

Figure 6.1. (**A**) Thermally corrected VIR reflectance spectra of bright material on the rim of Haulani crater (**B**), Kupalo crater (**C**), and Oxo crater (**D**) as well as the Ceres-average spectrum.

Rim/wall Na-carbonates >1 km across were identified on the rims and walls of 41 craters, 27 of which have exposures that cover nearly contiguous spans of 5-32 km, including Haulani (Figure 6.1B), Azacca, Ikapati, Kupalo (Figure 6.1C), Dantu, and Oxo (Figure 6.1D) (Table 6.1). All large rim/wall bright spots were found to have Na-carbonate. Most deposits are exposed by morphologically fresh craters. Those that have been dated

have recent asteroid-derived model ages (Table 6.1), consistent with the prediction that surface Na-carbonate deposits are buried by lateral mixing over periods of 100s of Ma (Stein et al., 2017). Several of the craters including Gaue, Dantu, Ikapati, Azacca, Urvara, Kupalo, Juling, and Haulani exhibit geomorphologic indicators of high subsurface ice content such as central pit craters, lobate landslides and ejecta, pitted materials, scarps, and floor fractures (Sizemore et al., 2018). Oxo crater, the youngest surveyed with an age of only ~190 ka (Nathues et al., 2017b) (Figure 6.1D), is the sole crater with infrared absorptions from H_2O ice, co-occurring with hydrated Na-carbonates (Combe et al., 2016). Hydrated Na-carbonates have also been observed in the <2.7 Ma Haulani crater (Tosi et al., 2018).

6.4 Constraints on the Ages of Near-surface Na-carbonates

Impacts constantly expose and mix Ceres' surface. Fresh exposures of Na-carbonate are subsurface deposits that were not previously removed or mixed beyond recognition. To investigate the longevity of near-subsurface Na-carbonate deposits, we ran a series of Monte Carlo simulations to model the destruction timescale of buried Na-carbonate. The objective of the model was to predict the largest contiguous deposit of Na-carbonate persisting in the shallow subsurface (and could thus be exposed on a crater rim) as a function of time as material is excavated by impacts. A grid with the surface area of Ceres A was populated in 1 Myr time steps with a crater population sourced from the asteroid-derived Ceres crater production function f (Marchi et al., 2016). 1 km thick cylinders with diameters of 1 to 150 km, representing buried Na-carbonate, were placed at random positions on the grid at a depth of 0 m. During each time step t, $A\sum_{d=1}^{250} f(t_i, d)$ craters with diameter d and diameter-dependent depth (Stein et al., 2017) were placed at random positions in the grid. Material directly intersected by the craters was removed from subsequent timesteps and the surface elevation was adjusted. The redistribution of Na-carbonates by impact ejecta was not considered because Na-carbonate-bearing ejecta are more mixed than and easily discernible from primary crater rim Na-carbonate exposures. The simulation was run >1,000 times for each cylinder diameter to build statistics.

Table 6.1. CRATER RIM NA-CARBONATE EXPOSURES >5 KM

Parent Crater	Longitude	Latitude	Na-carbonate exposure size (km)	Parent crater age (Ma)	Inside older crater?	Geomorphic indicators of high ice content?	Distance to closest dome (km)
Oxo	0	42.2	9	0.19 ± 0.1, 0.07	Y	N	57
Kupalo	172.2	-41.0	25	<4.5	N	Y	191
Haulani	9.4	4.6	32	1.7-2.7	N	Y	36
Juling	167.2	-35.7	15	<2.5	Y	Y	141
Azacca	-143.9	-7.5	10, 12	76 ± 10	N	Y	60
Dantu	142.0	24.2	8	72-150	N	Y	40
Ikapati	42.43	34.0	32	19-43	Y	Y	223
Ernutet	42.0	50.8	18	420 ± 60	Y	N	198
Unnamed	-159.6	-20.6	9	-†	Y	N	171
Urvara	-121.8	-43.2	7	130-240	N	Y	87
Unnamed	-47	-45	10	-	Y	N	78
Belun	-5.3	-34.5	6	-	Y	N	112
Unnamed	23.9	-42.6	9	-	Y	N	113
Gaue	83.2	27.0	13, 17	-	N	Y	18
Unnamed	135	-37.0	16	-	Y	N	226
Xevioso	-49.4	0.3	7	-	N	N	47
Unnamed	-51	1.8	10	-	N	N	37
Halki	-25.6	24.3	5	-	N	N	35
Telepinu	-26.7	26.0	6	-	N	N	26
Rao	119.0	8.1	8	-	N	N	41
Kait	-6	0	7	-	Y	N	80
Takel	-80.6	50.0	7	-	Y	N	127
Unnamed	158.5	-21.5	12	-	Y	N	52
Unnamed	161.7	-18.1	7	-	Y	N	24
Unnamed	118.0	-26.3	6	-	Y	N	143
Unnamed	-175.0	23.0	15	-	Y	N	281
Unnamed	-42.5	18.5	10	-	N	N	11
Ahuna Mons*	-44.1	-10.5	18	<70 ± 20	N	Y	0
Occator*	-120.2	19.8	9	21 ± 0.4	N	Y	0

*Notable Na-carbonate exposures not on crater rims. Ages from Schmedemann et al., 2016; Williams et al., 2017; Nathues et al., 2017b.

†Dashes denote craters whose ages have not been reported.

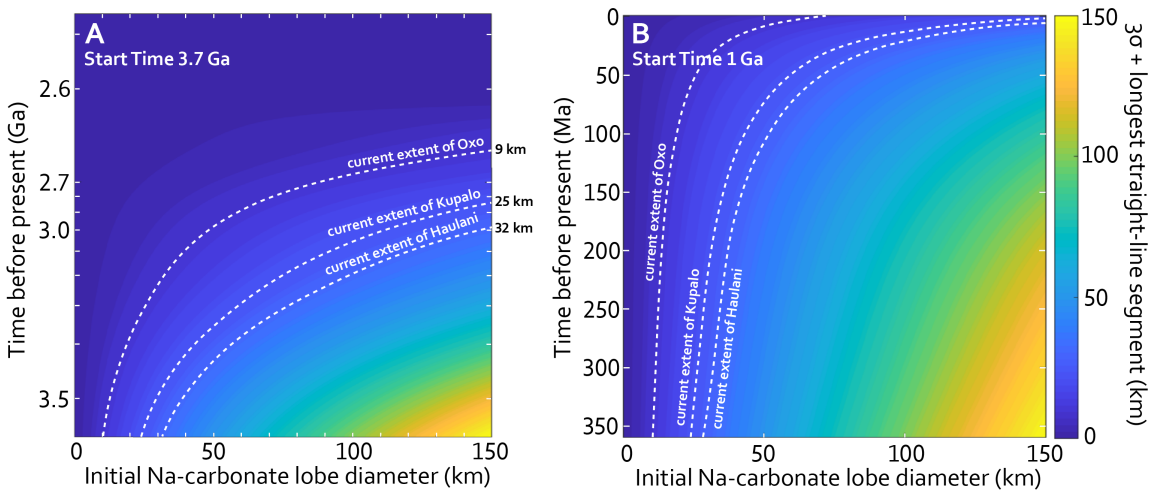

Figure 6.2. (**A**) Simulated maximum lateral extent (reporting mean + 3σ value) of shallowly buried Na-carbonate as a function of time and the initial deposit diameter for material deposited 3.7 Ga. White contours denote the modern lateral extent of contiguous or nearly contiguous Na-carbonate deposits exposed on the rims of Haulani crater, Kupalo crater, and Oxo crater. (**B**) Simulation with identical parameters for material deposited 1.0 Ga.

The first set of simulations considered near-surface Na-carbonate deposited at the end of the Late Heavy Bombardment (LHB, 3.7 Ga) (Figure 6.2A). Results show that to 3σ confidence, a single subsurface Na-carbonate deposit of 32 km – the largest observed today on Ceres – would not exist 500 Myr later, i.e. it could not exist at 3.2 Ga, even if it started with a large diameter of 150 km because bombardment would have segmented the deposit. Deposits at the scale of that exposed by Oxo (9 km) would have been destroyed by ~2.7 Ga. Hence, all current exposures of Na-carbonate must have been emplaced in the shallow subsurface well after the end of the LHB. Only in scenarios with emplacement beginning 1 Ga or later (Figure 6.2B) can deposits survive to the present at the 3σ limit, and deposits 20-30 km in size would require initial sizes >~150 km. The mean solutions require typical emplacement ages of several hundred Ma or less for the largest rim exposures. Hence, the models strongly exclude the possibility that crater rim exposures are the precipitation products of brines that have been in the shallow subsurface since differentiation. Model results constrain the large Na-carbonate exposure to have formed or been mobilized to the shallow (upper few hundred m) subsurface within the last ~1 Ga.

6.5 Distribution of Shallow Subsurface Na-carbonate Relative to other Crater Features

The surface distribution of large Na-carbonate deposits was compared with the location of older impact basins, domes, and isostatic gravity anomalies to further constrain depositional processes.

Large (>5 km) Na-carbonate exposures are commonly, through not exclusively, in planitiae previously identified as putative ancient impact basins (Marchi et al., 2016) and other topographic lows. Excluding the three large putative ancient impact basins (Marchi et al., 2016), which are too old to be the direct source of large, intact deposits of shallowly buried Na-carbonate, 12 of the large Na-carbonate rim exposures are not inside of any discernible older impact basin that could have provided exogenous heating to produce brines that concentrated Na-carbonate (Table 1, Figure 6.3A).

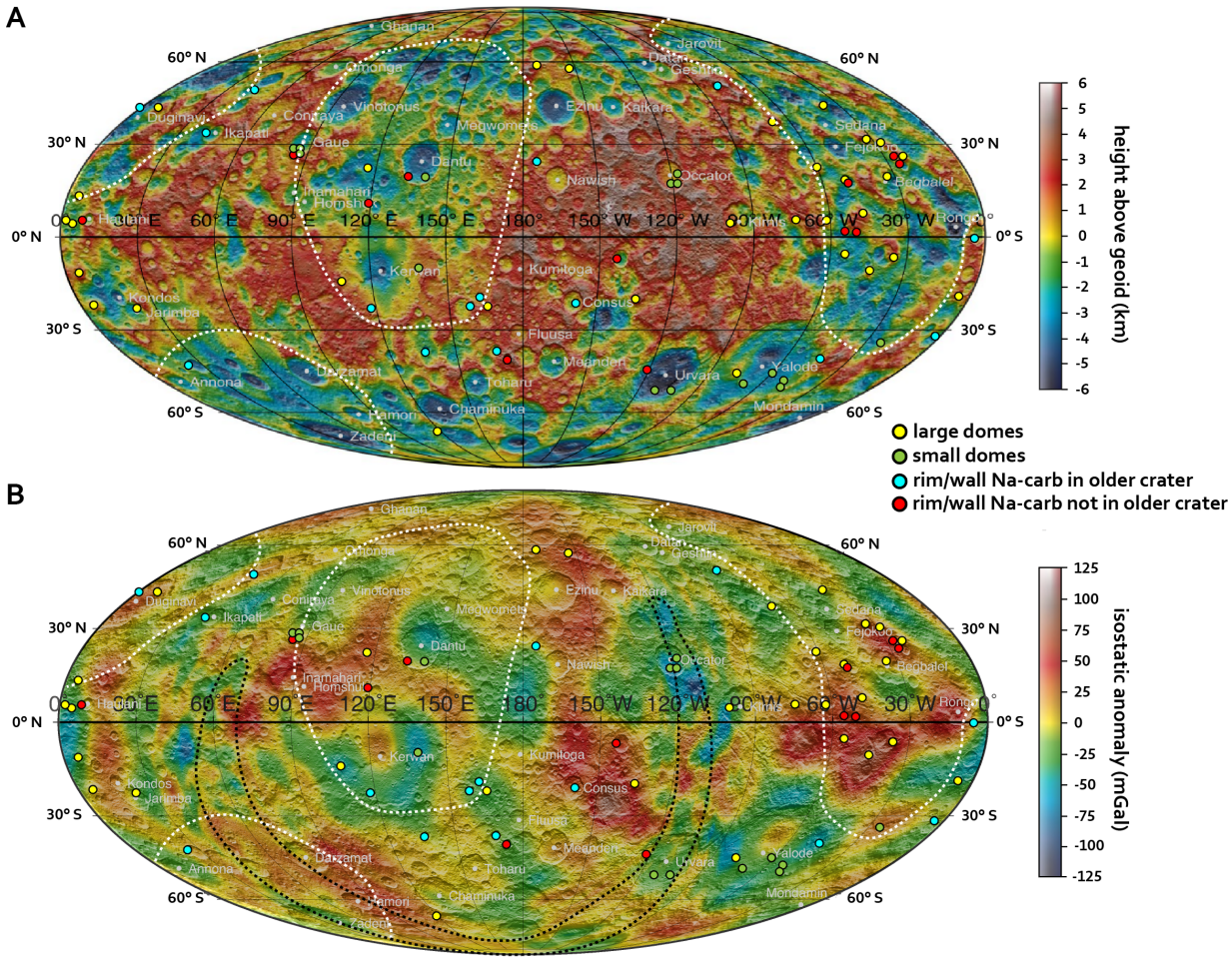

Figure 6.3. (**A**) Ceres topography map overlain with all crater rim Na-carbonate deposits with lateral extents >5 km and all large and small domes mapped by Sizemore et al. (2018) and Sori et al. (2018). Small domes are defined in Sizemore et al. (2018). (**B**) The same features overlain onto the combined LAMO-XM2 isostatic gravity anomaly map. White dashed lines denote the approximate boundaries of putative ancient impact basins reported by Marchi et al. (2016). The black dashed line denotes the swath of XM2 gravity data with degree strength >30. Both base maps were produced by Park et al. (2020). VIR observations are limited above or below ~60° latitude.

Domes are one of the most conspicuous geomorphic signs of endogenic activity on Ceres. There are at least 37 putative large domes (Sizemore et al., 2018; Sori et al., 2018) and 16 putative small domes or mounds (Sizemore et al., 2018). The large domes range in diameter from 20-100 km and rise 2-4 km above the surrounding terrain (Sori et al., 2018). Domes are concentrated in the putative ancient impact basins (Figure 6.3A), and nearly all are close to an older or nearly contemporaneous impact basin. 31 domes are on

a crater floor or directly on a crater rim and all but three of the remaining domes are within 30 km of a crater rim. Ahuna Mons is the only dome mantled by Na-carbonate, which streaks down its sides (Ruesch et al., 2016; Zambon et al., 2017). Liberalia Mons, which is intersected by the Na-carbonate-bearing Xevioso crater, is directly associated with Na-carbonate (Zambon et al., 2019). No other domes are directly intersected by young craters. Despite the limited exposure of Na-carbonate on domes, there is a clear spatial relationship between domes and large crater rim Na-carbonate exposures that are not inside of older basins (excluding planitiae); 10 out of 12 such Na-carbonate exposures are closer to domes than ~85% of all surface points (Figure 6.4). Most of these exposures are in a large planitium east of Hanami Planum that also contains at least 13 large domes (Figure 6.3A). Kupalo crater, which exposes more than 25 km of Na-carbonate on its rim and is not inside an older basin, is an outlier at ~191 km from the closest mapped dome, but intersects a prominent topographic high that may be a previously unmapped dome.

Domes are in regions exhibiting a wide range of isostatic gravity anomalies (Figures 3B, 5). Generally, positive isostatic anomalies may be due to a combination of subsurface mass excess, thin crust, or lower subsurface porosities, whereas negative isostatic anomalies are commonly attributed to excess subsurface ice (Ermakov et al., 2017). Ahuna Mons is near the center of a strong positive isostatic gravity anomaly that indicates a subsurface mass concentration interpreted by Ruesch et al., (2019) as a mantle plume and the source of fluids that formed Ahuna Mons. Similarly, the 3.8 km tall Cosecha Tholus near Oxo crater is in the vicinity of a strong positive isostatic gravity anomaly modeled by Park et al. (2020) to result from a mid-crust mass excess. Most large crater rim Na-carbonate deposits that are not inside older craters are associated with positive isostatic gravity anomalies (Figure 6.3B, Figure 6.5). Some craters with large Na-carbonate rim exposures, such as Ikapati crater, are associated with negative isostatic gravity anomalies that may signal excess subsurface ice (Park et al., 2020), though not all craters with geomorphologic indicators of high subsurface ice content (Sizemore et al. 2018) are near negative anomalies.

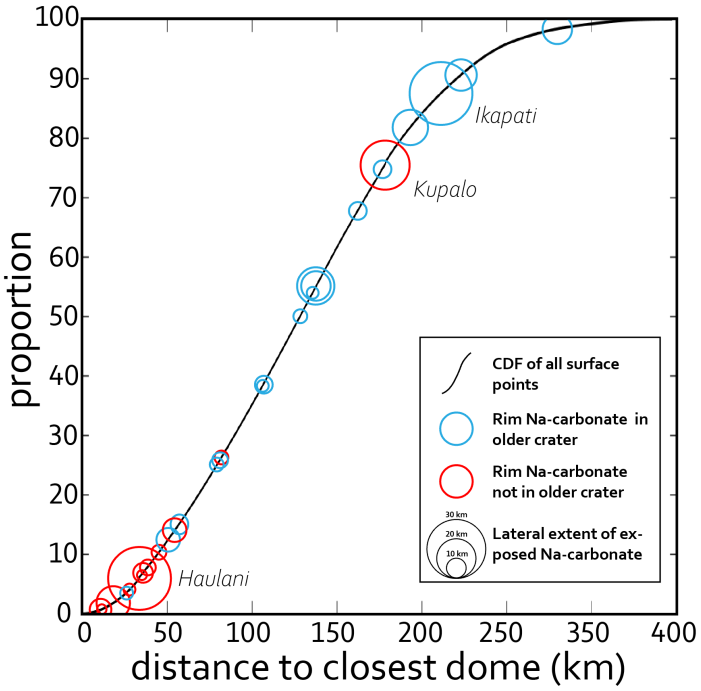

Figure 6.4. Cumulative distribution function of the distance from every surface point to the closest dome catalogued by Sizemore et al. (2018) and Sori et al. (2018). Circles represent large rim Na-carbonate exposures. Circle size represents the relative lateral extent of the exposures.

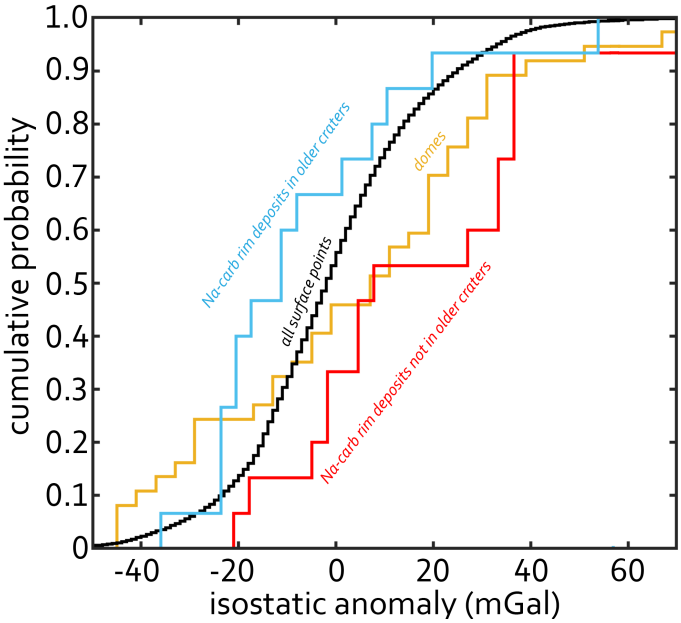

Figure 6.5. Cumulative distribution function of the isostatic gravity anomaly of all surface points compared with that of domes and large crater rim Na-carbonate deposits.

6.6 Previously Proposed Mobilization Mechanisms on Ceres

The close spatial association of domes and large Na-carbonate deposits (Figures 6.3, 6.4) suggests that the same process(es) that formed Ceres' domes may have brought Na-carbonate to the shallow subsurface or that the conditions that favor dome formation also promote mobilization and deposition of Na-carbonate. Moreover, the lack of older impact basins associated with some deposits necessitates that at least some of the largest Na-carbonate exposures, such as in Haulani and Kupalo craters, are sourced from material that was recently mobilized to the shallow subsurface. Here we review the viability of previously proposed dome formation mechanisms and whether they could simultaneously explain large, recent subsurface Na-carbonate deposits.

Cryovolcanic extrusion akin to the formation of dacitic domes on Earth is the most cited formation mechanism for Ahuna Mons (Ruesch et al., 2016, 2019) and has been extended to other domes (Sori et al., 2017, 2018). Ruesch et al. (2019) proposed that Ahuna Mons resulted from freezing pressure-driven extrusion of a dense, salt-rich slurry of brine and solid particles from a regional mantle uplift beneath Ahuna Mons where brines may persist in small quantities (Castillo-Rogez et al., 2019; Fu et al., 2017). Other domes with smaller aspect ratios were proposed by Sori et al. (2017, 2018) to have formed over the last several 100 Myr via brine extrusion and viscously relaxed to their present morphology. Slurry extrusion explains several observations, namely the presence of Na-carbonate on Ahuna Mons and its qualitative similarity to the morphology of terrestrial dacitic domes, but it must overcome some challenges. Chiefly, the domes lack clear flow textures diagnostic of extrusive volcanic origin (Bland et al., 2019; Sizemore et al., 2018). Furthermore, their progenitor fluids must rise from an inferred depth of ~30 km without freezing, requiring ascent velocities $>10^{-5}$ m s^{-1} (Ruesch et al., 2019) and conduits > 10 m diameter (Quick et al., 2019). A formation mechanism for large conduits is unclear. Although deep fractures from nearby impacts have been proposed (Sizemore et al., 2018), it is difficult to reconcile mobilization through ancient fractures with the recent emplacement constraints of subsurface Na-carbonate proposed in this study. Large, crust-

throughgoing fractures formed during the basin-forming impacts are a tantalizing source of conduits that could simultaneously explain the association between domes and basins, but the relatively young dome ages (Sori et al., 2018) and impact modeling (section 6.4) constrain most mobilization to within the last several hundred Ma, likely well after the formation of such fractures. Lastly, extrusion cannot easily explain why brines sometimes form large, shallow Na-carbonate deposits without topographic expression proximal to domes. Collectively, these challenges suggest that brine extrusion alone may not explain the formation of all domes and large subsurface Na-carbonate deposits.

Bland et al. (2019) advanced an alternative model for the formation of Ceres' domes that invokes the solid-state flow of ices. In this model, differential loading drives solid-state deformation of relatively low-viscosity, low-density (LVLD) material (water ice) analogous to terrestrial salt doming. Impact-driven lateral overburden variation was proposed to drive upward subsurface solid-state ice flow to form domes with geometries consistent with the observed domes. An advantage of the solid-state flow model is that it permits the ice that forms the domes to sit in the shallow subsurface for billions of years before an impact introduces an overburden variation, consistent with impact models in section 6.3 that permit material to persist several km below the surface for >1 Ga. One challenge that the solid-state model faces is that they must (and perhaps can, see section 6.7.2) account for the simultaneous shallow emplacement of large-shallow Na-carbonate deposits proximal to domes. Additionally, the solid-state model requires an abundance of shallow subsurface ice within a few km of the surface.

A challenge shared by both formation mechanisms is that many (though not all) Na-carbonate deposits, especially those proximal to domes, are associated with positive isostatic gravity anomalies, which may indicate a mass excess rather than a deficit caused by high subsurface ice content required for the solid-state model. The extrusion model faces the same issue as the slurry's ice content is expected to be higher (>40 vol%) than average crust material (Bland et al., 2017; Prettyman et al., 2017; Ruesch et al., 2019; Sori et al., 2018). In either case, subsurface anomalies at the scale of domes and large Na-

carbonate deposits might be unresolved in Dawn gravity data. LAMO gravity data vary from ~82-105 km resolution, well above the scale of most domes, whereas XM2 data have a resolution of ~37-51 km but do not cover regions with any domes or large Na-carbonate deposits (Figure 6.3B).

Mobilization mechanisms should also account for the prevalence of domes and large Na-carbonate rim exposures in basins. The putative basin-forming impacts could have partially exhumed ice-rich Na-carbonate bearing material, created fractures that acted as conduits for brines to pool in the shallower subsurface, or provided the perturbation necessary to initialize RT instabilities and diapirism. Regardless of the precise mechanism that deposited LVLD material within a few km of the surface, ancient impacts also likely wrought conditions favorable to mobilization. Namely, positive isostatic gravity anomalies in planitiae indicate that the crust is likely thinner (~30 km) and perhaps denser than average in those regions (Ermakov et al., 2017). Moreover, the impacts could have destabilized clathrates in the crust to for weaker water ice (Castillo-Rogez et al., 2018).

6.7 Diapirism and Solid-state Deformation as Source of Domes and Subsurface Na-carbonate Deposits

The constraint that large Na-carbonate deposits were mobilized to within a few hundred m of the surface <1 Ga indicates that the mobilization of their parent material, and perhaps that of at least some domes, may occur in a multistep process. Here we propose a scenario in which low density, low viscosity Na-carbonate-bearing water ice (hereafter referred to as LVLD material) is 1) mobilized from the upper mantle or lower crust to within a few km of the surface by brine extrusion or solid state diapirism and then 2) impact-driven solid-state deformation drives this material farther toward the surface to form domes and large shallow subsurface Na-carbonate deposits.

6.7.1 Mobilization of Material from the Deep Crust

We assume that the putative dome- and Na-carbonate exposure-forming LVLD material is a mixture of water ice and a few vol% $NaHCO_3$, Na_2CO_3, or hydrated Na-carbonates. Hydrated Na-carbonates are a plausible phase in LVLD material due to their relatively low density (2.25 g/cm^3 for $Na_2CO_3 \cdot H_2O$, 1.51 g/cm^3 for $Na_2CO_3 \cdot 7H_2O$, and 1.46 g/cm^3 for $Na_2CO_3 \cdot 10H_2O$ compared to 2.54 g/cm^3 for Na_2CO_3) and greater stability with depth relative to Na_2CO_3 (Zolotov et al., 2001). Additionally, the youngest Na-carbonate rim exposures likely contain hydrated Na-carbonates (Haulani crater) or both hydrated Na-carbonates and H_2O (Oxo crater) (section 6.2), indicating that this might occur in other craters rim walls prior their to sublimation and dehydration. Moreover, Castillo-Rogez et al. (2018) modeled the freezing of a putative Ceres ocean with a starting fluid composition in equilibrium with mineralogy observed by De Sanctis et al. (2015) and found that water ice and a few vol% $NaHCO_3$ and/or hydrated Na-carbonates should have precipitated with water ice between ~267K and ~247K. The freezing models also indicate that ~90 vol% of water would first freeze between 273-267K, trapping Na-carbonate beneath 10s of km of ice. Hence, any LVLD material in the upper few km of the subsurface must have been mobilized after Ceres' ocean froze.

Previous work (Quick et al., 2019; Raymond et al., 2020; Ruesch et al., 2019) has proposed that brines could have risen from the deep crust or upper mantle through pore space or impact-induced fractures. Bland et al., 2019, proposed that this process or preexisting heterogeneities could accumulate LVLD material at depths of a few km (Bland et al., 2019). Another possibility is that the mobilization of LVLD material is an entirely solid-state process driven by diapiris that start as Rayleigh-Taylor (RT) instabilities. RT instabilities can form when less dense material underlies a denser material. Vertical displacement on the boundary between the fluids grows because the rising material is buoyant relative to the crustal material it is displacing. Ceres' outer crust is a mixture of hydrated silicates, salts and/or clathrates, and <~35% water ice by volume (Castillo-Rogez et al., 2018; Bland et al., 2016; Ermakov et al., 2017; Fu et al., 2017). Regional changes in surface composition (Ammannito et al., 2016; Combe et al., 2016), impact crater morphology (Bland et al., 2016), geomorphic features (Hughson et al., 2019; Sizemore et

al., 2018), and gravity anomalies associated with mass variations beneath some craters (Bland et al., 2018; Ermakov et al., 2017; Park et al., 2020) imply significant variations in crustal composition, raising the possibility of large collections of unstable ice-rich material in the crust that could give rise to RT instabilities. Here we evaluate whether RT instabilities can plausibly give rise to ice diapirs in Ceres' crust and whether ice diapirs could transport LVLD material to within a few km of the surface.

RT instabilities develop when

$$\eta_{crit} < \eta_{ice}, \tag{6.1}$$

where η_{ice} is the viscosity of the buoyant material, most plausibly predominantly water ice, and η_{crit} is the critical viscosity that allows a perturbation to grow to an amplitude greater than the characteristic length scale over which viscosity varies significantly (eq. 6.3). Following the assumptions of Rubin et al. (2014), η_{crit} is approximated as

$$\eta_{crit} = \left[(\varphi - 1)^{1/n} \frac{C_{L\Delta\rho}}{2n}\right] \left(\frac{Z_0}{L}\right)^{(n-1)/n} \Delta\rho g L \tau, \tag{6.2}$$

where $\Delta\rho$ is the density difference between the crust and the upwelling material, g is the acceleration due to gravity (~0.27 m/s^2), Z_0 is the amplitude of an initial disturbance (e.g. displacement from an impact), τ is the maximum timescale over which the instability operates, and φ is a quantity that relates the stress and strain rate. $C_{L\Delta\rho}$ is a dimensionless quantity that depends on the geometry and rheology of the layers and was found to be ~0.76 (Molnar et al., 2002) for viscous rock and ice overlying an inviscid layer where L<< the thickness of the upper layer, which is true in this scenario. Finally, L is calculated as

$$L = \frac{nRT_0}{Q} \frac{T_0}{|dT/dz|}, \tag{6.3}$$

where R and T_0 are the gas constant and temperature at the interface between the ice and the crust, respectively. Q is the activation energy (49 kJ mol^{-1}). The geothermal gradient of

the crust is taken as ~2K/km (Hesse and Castillo-Rogez, 2018), but is poorly constrained. Higher geothermal gradients would generally make it easier for RT instabilities to develop and would also permit instabilities higher in the crust.

To determine the conditions for instability in Ceres' crust, the effective viscosity-temperature profile of pure water ice was calculated for effective shear stress σ and strain rate $\dot{\varepsilon}$ as

$$\eta_{ice} = \frac{\sigma}{2\dot{\varepsilon}}. \tag{6.4}$$

The strain rate was estimated with empirical parameters compiled in Rubin et al. (2014) and Fu et al. (2017) as

$$\dot{\varepsilon} = \dot{\varepsilon}_{diff} + \left(\frac{1}{\dot{\varepsilon}_{basal}} + \frac{1}{\dot{\varepsilon}_{gbs}}\right)^{-1} + \dot{\varepsilon}_{disl}, \tag{6.5}$$

which accounts for several flow mechanisms in ice including diffusional glow, grain boundary sliding, basalt-slip-accommodated grain boundary sliding, and dislocation creep. The quantities were modeled with a power-law form described in Rubin et al. (2014).

Assuming a surface temperature of 150 K and 2K/km thermal gradient, a water ice RT instability could develop at depths below ~10 km over several hundred Ma following an initial 1 km perturbation (Figure 6.6A). Comparatively, methane clathrate hydrate, which may be abundant in parts of the crust (Castillo-Rogez et al., 2018), is not as prone to RT stabilities because of its high viscosity and would be unstable only in the lowest parts of the crust (Figure 6.6A).

Bland et al. (2018) estimated that buoyancy-driven diapirs could reach depths of 10-20 km before stalling, assuming the overlying material has an average crust density of 1287 kg/m^3. We revisited the depth to which diapirs rise in the crust while permitting a wider range of density contrasts possible in Ceres' heterogeneous crust to establish whether

diapirism can bring LVLD within a few km of the surface. The ascent velocity v of a spherical diapir was modeled from Marsh (1982) as

$$v = \frac{2\Delta\rho g d^2}{3A\mu_1} \tag{6.6}$$

in which d is the thickness of the shear zone surrounding the diapir, taken as the diapir radius, A is an exponential factor of viscosity variation, calculated as $\ln\frac{\mu}{\mu_1}$, μ_1 is the smallest value of viscosity in the shear zone, and $\Delta\rho$ is the density contrast between the diapir and surrounding material. This equation accounts for heat exchange from the warm diapir into the surrounding wall rock, which would depress the viscosity and ease ascent. We solved for v in time steps assuming depth-invariant density and a linear viscosity profile from 10^{25} Pas at the surface to 10^{21} Pas at the base of the crust (Fu et al., 2017). Step duration was adjusted dynamically with velocity to account for changing parameters and was of order 10^5 – 10^7 years per step after 10^6 years of modeled time. We assessed whether it is appropriate to disregard heat exchange by solving the 1D heat conduction equation numerically during each step as

$$\rho c_p \frac{dT}{dt} = \lambda\left(\frac{d^2T}{dx^2}\right) \tag{6.7}$$

$$T_i^{n+1} = T_i^n + \Delta t \frac{\lambda}{\rho c_p}\left(\frac{T_{i+1}^n - 2T_i^n + T_{i-1}^n}{(\Delta x)^2}\right), \tag{6.8}$$

where T_i^n is the temperature of cell i at time step n, c_p is the specific heat of ice, λ is thermal conductivity, and x is the distance outward from the diapir. Results indicate that the exterior of diapirs <50 km in diameter cool effectively instantaneously relative to the time step duration, and after several time steps for 100 km diapirs. Hence, the depth to which diapirs rise was instead modeled for an endmember case assuming no heat exchange as

$$v = \frac{2}{9}\frac{\Delta\rho g d^2}{\mu}, \tag{6.9}$$

where the viscosity in the shear zone, μ, follows the aforementioned linear profile. Diapir ascent was modeled for a range of density contrasts between 0 and 1200 kg/m^3.

After ~1 Ga, diapirs with diameters of 25 to 50 km effectively stall ~8-15 km below the surface and 100 km diapirs stall ~6-2 km below the surface depending on the density of the overlying material (Figure 6.6B). The final depth of 100 km diapirs may be slightly shallower due to heat exchange during ascent. The results are independent of the depth at which the diapirs start because the ascent is controlled by viscosity and density contrast. Hence, water ice diapirism could plausibly mobilize LVLD material from Ceres' mid to lower crust to within several km of the surface.

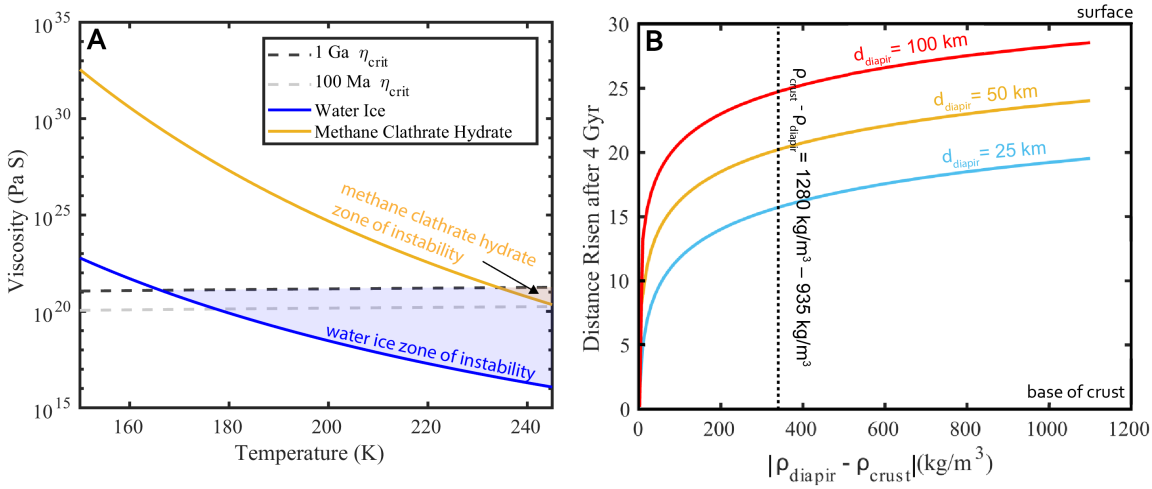

Figure 6.6. (**A**) Estimated conditions for a Rayleigh-Taylor instability to develop in Ceres' crust over 10^5 – 10^6 yr for a 1 km perturbation considering low density layers of water ice or methane clathrate hydrate. (**B**) Distance that diapirs of varying diameters would rise after 4 Ga as a function of density contrast, starting from the base of a 30 km thick crust. For reference, the dashed line is the average crustal density minus that of water ice.

6.7.2 Mobilization of Na-carbonate-bearing Ices from the Shallow Subsurface

The mobilization of subsurface LVLD material through differential loading can account for the formation of domes inside of crater rims (section 6.6), but must also account

for 1) the significant number of domes that are immediately adjacent to but outside of crater rims, and 2) the emplacement of very shallow Na-carbonate-bearing ices proximal to domes. These scenarios may be rectified by further consideration of processes akin to terrestrial salt tectonics. Salt tectonics is driven primarily by differential loading induced by gravitational forces, thermal gradients, or forced displacement of the boundaries of a salt body, and more rarely buoyancy (Hudec and Jackson, 2007). These processes are closely tied to regional deformation, typically either compressional, extensional, or transtensional, that are likely uncommon on Ceres. On Ceres, impact craters are the most probable source of differential loading that drives reactive piercement (Bland et al., 2019), but large impacts likely also produce listric extensional faults that extend well beyond their rim and provide a fault along which LVLD material could flow due to overburden pressure and perhaps buoyancy, yielding positive surface deformation akin to terrestrial thrust piercements (Hudec and Jackson, 2007). LVLD material could also advance along shallow surface-parallel impact fractures well beyond the parent crater where future impacts could expose the LVLD material, which would sublimate and dehydrate to leave an Na-carbonate-enriched lag. Hence, solid-state deformation due to differential overburden and impact-induced fractures can plausibly explain the observed distribution of domes relative to craters, the close spatial association of domes and large shallow subsurface Na-carbonate deposits, and their recent emplacement.

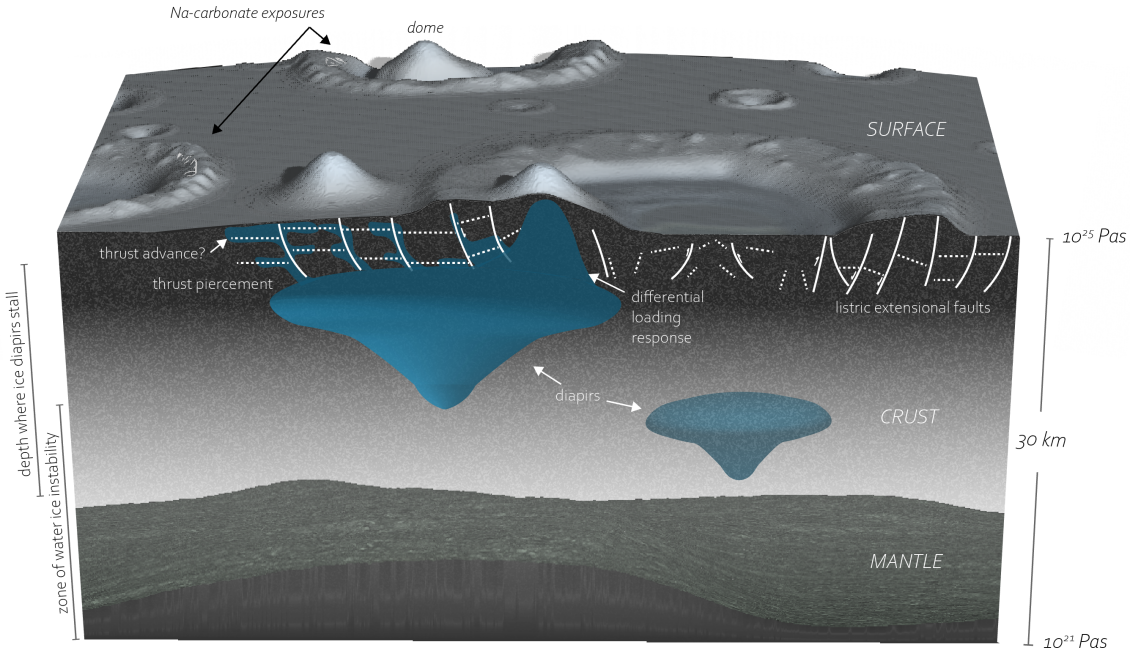

Figure 6.7. Schematic of solid-state mobilization of Na-carbonate-bearing water ice from the deep crust to the shallow subsurface. Diapirism could bring LVLD material from the deep crust to within a few km of the surface. Lateral overburden pressure variation from impacts could drive solid-state deformation of the LVLD material to form domes. Overburden pressure may drive the propagation of LVLD material along listric extensional faults and surface-parallel fractures in the shallow subsurface, where it may subsequently be exposed by an impact and sublimate to leave an Na-carbonate-bearing lag deposit.

6.8 Conclusions

Crater rim/wall carbonate exposures occur with nearly contiguous lateral extents of up to 32 km and sizes of 5-32 km in 27 discrete craters. Model results show that for the persistence of large, shallow subsurface Na-carbonate deposits to the present, either they must have initially been >150 km or they were emplaced in the last ~1 Ga and probably within the last few hundred Ma. Some large Na-carbonate rim/wall deposits inside of older basins could plausibly be sourced from exogenic heating in an Occator-like process, but large deposits not in older basins require mobilization of Na-carbonate-bearing material from deeper in the crust or upper mantle.

The close spatial association of some large Na-carbonate deposits and domes indicates that they form by the same process or related processes. Furthermore, both are

relatively more prevalent in ancient basins than expected from a random distribution. Potential sources for the mobilization of deep Na-carbonate-bearing material include extrusion of brines or solid-state deformation. Recent and widespread brine transport faces some challenges, namely brines require recent crust-throughgoing fractures whose source is unclear and extrusion alone cannot easily explain the association of shallow Na-carbonate deposits without topographic expression near domes. Brines cannot be ruled out as the source of some or all domes and large subsurface Na-carbonate deposits. Here, we proposed a two-step process that does not require the recent presence of shallow subsurface brines and can simultaneously explain the formation of domes and large proximal Na-carbonate deposits: 1) hydrated Na-carbonate-bearing water ice below basins is mobilized from the upper mantle or lower crust to within a few km of the surface by brine extrusion or solid state diapirism; and 2) subsequent impacts produce differential loading and extensional faults that permit solid-state deformation, which forms domes around craters as well as shallow sheets of Na-carbonate bearing material that can later be exposed as crater rim/wall bright spots. Regardless of how they were emplaced, the shallow subsurface Na-carbonate deposits are another indication of recent and widespread endogenic activity on Ceres.

References

Ammannito, E., DeSanctis, M.C., Ciarniello, M., Frigeri, A., Carrozzo, F.G., Combe, J.-P., et al. (2016). Distribution of phyllosilicates on the surface of Ceres. Science. 353, 1006. https://doi.org/10.1126/science.aaf4279.

Bland, M.T., Raymond, C.A., Schenk, P.M., Fu, R.R., Kneissl, T., Jan Hendrik, P., et al. (2016). Composition and structure of the shallow subsurface of Ceres revealed by crater morphology. *Nature Geoscience*, 9, 538-542. https://doi.org/10.1038/ngeo2743.

Bland, M.T., Ermakov, A.I., Raymond, C.A., Williams, D.A., Bowling, T.J., Preusker, F., et al. (2018). Morphological indicators of a mascon beneath Ceres's largest crater, Kerwan. *Geophys. Res. Lett.*, 45. https://doi.org/10.1002/2017GL075526.

Bland, M.T., Buczkowski, D.L., Sizemore, H.G., Ermakov, A.I., King, S.D., Sori, M.M., et al. (2019). Dome formation on Ceres by solid-state flow analogous to terrestrial salt

tectonics. *Nature Geoscience*. 12, 797-801. https://doi.org/10.1038/s41561-019-0453-0.

Bowling, T., Ciesla, F., Davidson, T., Scully, J., Castillo-Rogez, J., & Marchi, S. (2018). Post-impact thermal structure and cooling timescales of Occator crater on Asteroid 1 Ceres. *Icarus*, 320, 110-118. https://doi.org/10.1016/j.icarus.2018.08.028.

Carrozzo, F.G., De Sanctis, M.C., Ammannito, E., Castillo-Rogez, J., Ehlmann, B.L., Ciarniello, et al. (2017). Nature, formation, and distribution of carbonates on Ceres. *Science Advances*, 4. https://doi,org/10.1126/sciadv.1701645.

Castillo-Rogez, J.C. & McCord, T.B. (2010). Ceres' evolution and present state constrained by shape data. *Icarus*, 205, 443–459. https://doi.org/10.1016/j.icarus.2009.04.008.

Castillo-Rogez, J.C., Neveu, M., McSween, H.Y., Fu, R.R., Toplis, M.J., & Prettyman, T. (2018). Insights into Ceres's evolution from surface composition. *Meteorics and Planetary Science*, 1-24. https://doi.org/10.111/maps.13181.

Castillo-Rogez, J.C., Hesse, M.A., Formisano, M., Sizemore, H., Bland, M., Ermakov, et al. (2019). Conditions for the long-term preservation of a deep brine reservoir in Ceres. *Geophysical Research Letters*, 46. https://doi.org/10.1029/2018GL081473.

Combe, J.-P., McCord, T.B., Tosi, F., Ammannito, E., Carrozzo, F.G., De Sanctis, M.C., et al. (2016). Detection of local H_2O exposed at the surface of Ceres. *Science*, 353, aaf3010. https://doi.org/10.1126/science.aaf3010.

De Sanctis, M.C., Ammannito, E., Raponi, A., Marchi, S., McCord, T.B., McSween, H.Y., et al. (2015). Ammoniated phyllosilicates with a likely outer Solar System origin on (1) Ceres. *Nature*, 528, 241–244. https://doi.org/10.1038/nature16172.

De Sanctis, M.C., Raponi, A., Ammannito, E., Ciarniello, M., Toplis, M.J., McSween, H.Y., et al. (2016). Bright carbonate deposits as evidence of aqueous alteration on (1) Ceres. *Nature*, 536, 1–4. https://doi.org/10.1038/nature18290.

Ermakov, A.I., Fu, R.R., Castillo-Rogez, J.C., Raymond, C.A., Park, R.S., Preusker, F., et al. (2017). Constraints on Ceres' internal structure and evolution from its shape and gravity measured by the Dawn spacecraft. *JGR: Planets*, 122. https://doi.org/10.1002/2017JE005302.

Fu, R.R., Ermakov, A.I., Marchi, S., Castillo-Rogez, J.C., Raymond, C.A., Hager, B.H., et al. (2017). The interior structure of Ceres as revealed by surface topography. *Earth and Planetary Science Letters*. 476, 153-164. https://doi:10.1016/j.epsl.2017.07.053.

Hesse, M.A. & Castillo-Rogez, J.C. (2018). Thermal evolution of the impact-induced cryomagma chamber beneath Occator crater on Ceres. *Geophysical Research Letters*. 46. https://doi.org/10.1029/2018GL080327.

Hiesinger, H., Marchi, S., Schmedemann, N., Schenk, P., Pasckert, J.H., Neesemann, A., et al. (2016). Cratering on Ceres: Implications for its crust and evolution. *Science,* 353, aaf4759-aaf4759. https://doi.org/10.1126/science.aaf4759.

Hudec, M.R. & Jackson, M.P.A. (2007). Terra infirma: Understanding salt tectonics. *Earth-Science Reviews*, 82, 1-28. *https://doi.org/10.1016/j.earscirev.2007.01.001*.

Hughson, K.H.G., Russell, C.T., Schmidt, B.E., Chilton, H.T., Sizemore, H.G., Schenk, P.M., et al. (2019). Fluidized appearing ejecta on Ceres: Implications for the mechanical properties, frictional properties, and composition of its shallow subsurface. *J. Geophys. Res.*, 124. https://doi.org/doi:10.1029/2018JE005666.

Marchi, S., Ermakov, A.I., Raymond, C.A., Fu, R.R., O'Brien, D.P., Bland, M.T., et al. (2016). The missing large impact craters on Ceres. *Nature Communications*, 7. https://doi.org/10.1038/ncomms12257.

Molnar, P., Houseman, G.A., & Conrad, C.P. (2002). Rayleigh-Taylor instability and convective thinning of mechanically thickened lithosphere: Effects of non-linear viscosity decreasing exponentially with depth and of horizontal shortening of the layer. *Geophysical Journal International*, 133. https://doi.org/10.1046/j.1365-246X.1998.00510.x.

Nathues, A., Hoffmann, M., Schaefer, M., Le Corre, L., Reddy, V., Platz, T., et al. (2015). Sublimation in bright spots on (1) Ceres. *Nature*, 528, 237–240. https://doi.org/10.1038/nature15754.

Nathues, A., Platz, T., Thangjam, G., Hoffmann, M., Mengel, K., Cloutis, E.A., et al. (2017). Evolution of Occator Crater on (1) Ceres. *Astron. J.*, 153, 112. https://doi.org/10.3847/1538-3881/153/3/112.

Nathues, A., Platz, T., Hoffmann, M., Thangjam, G., Cloutis, E. A., Applin, D. M. et al. (2017). Oxo Crater on (1) Ceres – Geologic history and the role of water ice. *Astrophys. J.*, 154, 84. https://doi.org/10.3847/1538-3881/aa7a04.

Nathues, A., Platz, T., Thangjam, G., Hoffmann, M., Scully, J.E.C., Stein, N., et al. (2019). Occator crater in color at highest spatial resolution. *Icarus*, 320, 24-38. https://doi.org/10.1016/j.icarus.2017.12.021.

Neesemann, A., van Gasselt, S., Schmedemann, N., Marchi, S., Walter, S.H.G., Preusker, F., et al. (2019). The various ages of Occator crater, Ceres: Results of a comprehensive synthesis approach. *Icarus*, 320, 60-82. https://doi.org/10.1016/j.icarus.2018.09.006.

Palomba, E., Longobardo, A., De Sanctis, M.C., Stein, N.T., Ehlmann, B., Galiano, A., et al. (2017). Compositional differences among Bright Spots on the Ceres surface. *Icarus*. https://doi.org/10.1016/j.icarus.2017.09.020.

Park, R.S., Konopliv, A.S., Ermakov, A.I., Castillo-Rogez, J.C., Fu, R.R., Hughson, K.H.G., et al. (2020). Evidence of non-uniform crust of Ceres from Dawn's high-resolution gravity data. *Nature Astronomy*. https://doi.org/10.1038/s41550-020-1019-1.

Prettyman, T.H., Raymond, C.A., Scully, J.E.C., Sizemore, H.G., Sori, M.M., Vaughan, et al., (2020). Evidence of non-uniform crust of Ceres from Dawn's high-resolution gravity data. *Nature Astronomy*. https://doi.org/10.1038/s41550-020-1019-1.

Prettyman, T.H., Yamashita, N., Toplis, M.J., McSween, H.Y., Schorghofer, N., Marchi, S., et al. (2016). Extensive water ice within Ceres aqueously altered regolith: Evidence from nuclear spectroscopy. *Science*, 6765, 1–11. https://doi.org/10.1126/science.aah6765.

Quick, L.C., Buczkowski, D.L., Ruesch, O., Scully, J.E.C., Castillo-Rogez, J., Raymond, C.A., Schenk, P.M., et al. (2019). A possible brine reservoir beneath Occator crater: Thermal and compositional evolution and formation of the Cerealia dome and Vinalia Faculae. *Icarus*, 320, 119-135. https://doi.org/10.1016/j.icarus.2018.07.016.

Raponi, A., De Sanctis, M.C., Carrozzo, F.G., Ciarniello, M., Castillo-Rogez, J.C., Ammannito, E., et al. (2018). Mineralogy of Occator crater on Ceres and insight into its evolution from the properties of carbonates, phyllosilicates, and chlorides. *Icarus*. 320. https://doi.org/10.1016/j.icarus.2018.02.001.

Raymond, C.A., Ermakov, A.I., Castillo-Rogez, J.C., Marchi, S., Johnson, B.C., Hesse, M.A., et al. (2020). Impact-driven mobilization of deep crustal brines on dwarf planet Ceres. *LPSC 50*, Abstract 2621.

Rubin, M.E., Desch, S.J., & Neveu, M. (2014). The effect of Rayleigh-Taylor instabilities on the thickness of undifferentiated crust on Kuiper Belt Objects. *Icarus*, 236, 122-135. https://doi.org/10.1016/j.icarus.2014.03.047.

Ruesch, O., Platz, T., Schenk, P., McFadden, L.A., Castillo-Rogez, J.C., Quick, L.C., et al. (2016). Cryovolcanism on Ceres. *Science*, 353, aaf4286-aaf4286. https://doi.org/10.1126/science.aaf4286.

Ruesch, O., Quick, L.C., Landis, M.E., Sori, M.M., Cadek, O., Broz, P., et al. (2019). Bright carbonate surfaces on Ceres as remnants of salt-rich water fountains. *Icarus,* 320, 39-48. https://doi.org/10.1016/j.icarus.2018.01.022.

Ruesch, O., Genova, A., Neumann, W., Quick, L.C., Castillo-Rogez, J.C., Raymond, C.A., et al. (2019). Slurry extrusion on Ceres from a convective mud-bearing mantle. *Nature Geoscience*. 12, 505-509. https://doi.org/10.1038/s41561-019-0378-7.

Schmedemann, N., Kneissl, T., Neesemann, A., Stephan, K., Jaumann, R., Krohn, K., et al. (2016). Timing of optical maturation of recently exposed material on Ceres. *Geophysical Research Letters*. 43. https://doi.org/10.1002/2016GL071143.

Sizemore, H. G., Platz, T., Schorghofer, N., Prettyman, T. H., De Sanctis, M. C., Crown, D. A., et al. (2017). Pitted terrains on (1) Ceres and implications for shallow subsurface volatile distribution. *Geophys. Res. Lett.* 44, 6570-6578. https://doi.org/10.1002/2017GL073970.

Sizemore, H.G., Schmidt, B.E., Buczkowski, D.A., Sori, M.M., Castillo-Rogez, J.C., Berman, D.C., et al. (2018). A global inventory of ice-related morphological features on dwarf planet Ceres: Implications for the evolution and current state of the cryosphere. *JGR: Planets*, 124. https://doi.org/10.1029/2018JE005699.

Sori, M.M., Bryne, S., Bland, M.T., Bramson, A.M., Ermakov, A.I., Hamilton, C.W., Otto, K.A., et al. (2017). The vanishing cryovolcanoes of Ceres. *Geophysical Research Letters*. 44. https://doi.org/10.1002/2016GL072319.

Sori, M.M., Sizemore, H.G., Byrne, S., Bramson, A.M., Bland, M.T., Stein, N.T., et al. (2018). Cryovolcanic rates on Ceres revealed by topography. *Nature Astronomy*. 2, 946-950. https://doi.org/10.1038/s41550-018-0574-1.

Stein, N.T., Ehlmann, B.L., Palomba, E., De Sanctis, M.C., Nathues, A., Hiesinger, H., et al. (2017). The formation and evolution of bright spots on Ceres. *Icarus,* 320, 188-201. https://doi.org/10.1016/j.icarus.2017.10.014.

Williams, D.A., Buczkowski, D.L., Mest, S.C., Scully, J.E.C., Platz, T., & Kneissl, T. (2017). Introduction: The geologic mapping of Ceres. *Icarus,* 316, 1-13. https://doi.org/10.1016/j.icarus.2017.05.004.

Zambon, F., Raponi, A., Tosi, F., De Sanctis, M. C., McFadden, L. A., Carrozzo, et al. (2017). Spectral analysis of Ahuna Mons from Dawn mission's visible-infrared spectrometer. *Geophys. Res. Lett.*, 44, 97-104. https://doi.org/10.1002/2016GL071303.

Zambon, F., Carrozzo, F.G., Tosi, F., Ciarniello, M., Combe, J. Ph. Frigeri, A., et al. (2019). Mineralogical analysis of quadrangle Ac-H-10 Rongo on the dwarf planet Ceres. *Icarus*, 318, 219-229. https://doi.org/10.1016/j.icarus.2017.09.021.

Zolotov, M.Y. & Shock, E.L. (2001). Composition and stability of salts on the surface of Europa and their oceanic origin. *Journal of Geophysical Research*. 106, 32815-32827. https://doi.org/10.1029/2000JE001413.

Zolotov, M.Y. (2017). Aqueous origins of bright salt deposits on Ceres. 2017. *Icarus,* 296, 289-304. https://doi.org/10.1016/j.icarus.2017.06.018.

Chapter 7

SUMMARY, IMPLICATIONS, AND OUTSTANDING QUESTIONS

In this thesis, I used a range of remote sensing techniques to characterize past habitable environment on three bodies. Altogether, this work has 1) provided deep understanding of environmental controls on the texture and distribution of microbial mats; 2) contextualized Murray formation strata relative to the structure of Gale crater; 3) identified definitive evidence of intermittent subaerial exposure in an ancient martian lacustrine facies; and 4) placed quantitative constraints on the timing of endogenic processes on Ceres and refined our understanding of the processes that drive recent activity. Below, I synthesize findings presented in this thesis and discuss the key outstanding questions that follow.

7.1 Controls on Modern Microbial Mat Fabrics

The identification and characterization of microbial textures is one of the primary means to probe the fossil record for ancient life (e.g. Knoll, 2015; Schopf, 2006). Commonly, the interpretation of ancient mats relies on the preservation of textures that arose syndepositionally from the interaction of mats with environmental factors such as hydrodynamics, desiccation, and physical sediment dynamics (Schieber et al., 2007), yet to aid the interpretation of these textures in the sedimentary carbonate record it is crucial to identify the processes that determine the morphology of modern microbial mats. Our work on Little Ambergris set out to answer a few major questions. 1) which processes determine the surface morphology of microbial mats on Little Ambergris Cay? 2) what is the response of microbial mats to variations in water depth, subaerial exposure time, and sedimentation? 3) How did widespread, luxuriant microbial mats, which are rare globally today and perhaps throughout Phanerozoic time, develop in such a high-energy environment that involved formation of active sand shoals? This study also benefitted from the integration of UAVs with in-situ and satellite-based observations, which permitted quantification of mat responses to environmental perturbations at a scale and resolution that was previously impossible.

The key finding of this work is that the texture and distribution of the microbial mats on Little Ambergris Cay are controlled not by microbial community composition or ecological succession, but by subaerial exposure during quiescent periods and hydrodynamic forces and sedimentation during storm events. We identified three distinct mat morphotypes that are nearly segregated into separate elevation ranges that correspond to different water depths and thus different daily subaerial exposure time. Using high resolution photogrammetric DEMs coupled with facies maps produced from a combination of UAV-based orthomosaics and in-situ mapping, we demonstrated that the mat textures and the spatial distribution of mats are sensitive to minute differences in elevation; nearly all mats are within ~25 cm of the mean water level and average daily subaerial exposure time differs by as much as 15 hours over elevation changes of 5 cm.

Fortuitously, the uninhabited Little Ambergris was struck by the eye wall of Category 5 Hurricane Irma one month after our second field season on the island, providing an unprecedented opportunity to measure the response of microbial mats to overriding storm events. In addition to identifying and characterizing the resulting suite of unique microbially influenced textures, we now better understand the role powerful storms play in the mechanical weathering and distribution of mats in the island's interior basin. Sedimentation is a key control; in parts of the basin, thick, recurring storm deposits smother underlying mats, whose component filamentous microbes are unable to migrate upward and thus rapidly decay. Elsewhere, thinner sediment deposits are quickly penetrated by underlying motile microorganisms and recolonized. Mechanical weathering during storms rips up broad tracts of mats in the interior basin, whereas mats protected by the baffling effects of dense mangrove forests are not threatened and instead grow to be thick and luxuriant.

Finally, ^{14}C ages from sediment cores collected in the interior basin indicate that portions of the interior have been restricted for more than 2000 years, perhaps allowing mats to grow during that time. The development of a restricted environment was permitted by the convergence of persistent trade wind-driven waves in the lee of the adjacent Big Ambergris cay, which has a Pleistocene bedrock core that created an energy barrier. Rapid lithification

of carbonate sediment permitted the development and accretion of a bedrock rim. Quick cementation, which might be rarer in high-energy siliciclastic environments, likely played a crucial role in stabilizing the bedrock rim against storm overprinting.

7.1.1 Implications for the Identification of Ancient Microbialites and Future Applications of UAVs as Novel Remote Sensing Platforms

The lack of preserved microbial mats in sediment cores suggests that none of the microbial mats on Little Ambergris will enter the rock record. Hence, Little Ambergris serves as an example of a productive ecosystem with low preservation potential and highlights that there may be scant evidence of microbial processes preserved from similar ancient environments. This need not be the case for all ancient environments, however. Preservation can occur when cement precipitation rates exceed net dissolution, which could occur when evaporation and/or photosynthesis create enough carbonate mineral supersaturation (Present et al., 2020). Additionally, understanding the role of environmental processes in controlling microbial textures will improve interpretations of similar textural signatures that are preserved from ancient environments. Continued observation of the recovery of microbial mats on Little Ambergris will improve our understanding of the long-term response of microbial mats to sedimentation and overriding storm events.

This work highlighted the utility of UAVs as novel platforms for remote sensing. UAVs offer several advantages or outright unique capabilities compared to more traditional methods of field geology and remote sensing, including: 1) high mobility (capable of covering multiple km^2 per flight); 2) diverse and rapidly interchangeable instrument payload capacity; 3) ease of autonomy; 4) potential for repeated surveys with high temporal frequency; and 5) low expense. In the geosciences, UAVs are typically equipped with a GPS and color camera to produce orthomosaics and photogrammetric DEMs at spatial and temporal resolutions far superior to those available via satellite-based imaging. Other common instruments include light detection and ranging (LiDAR), point and imaging spectrometers, and magnetometers, but effectively any sufficiently light instrument can be mounted on a UAV.

It is not unreasonable to anticipate that UAVs will soon become an integral platform for planetary geology. Indeed, the helicopter Ingenuity that is planned for deployment from the Perseverance rover in 2021 and the planned Dragonfly mission to Titan highlight the exciting prospects for drone use in planetary science. As mission platforms, UAV payloads can also be adapted to permit ground-based measurements. Mission-based applications of UAVs are not limited to planetary science; work is underway to house drones in self-maintaining enclosures at remote field sites where they can respond to mission plans uploaded via satellite, autonomously collect data, and return and downlink data without direct human intervention. Such an architecture provides several unique capabilities including the capacity for rapid response to stochastic events, long-term baseline measurements, and measurements in high-risk conditions. These systems are already technologically feasible at relatively low cost. Hence, it is likely that UAVs will play an increasingly prevalent and diverse role in the terrestrial geology and planetary science.

7.2 The Depositional History of the Murray formation, Gale crater, Mars

The major goals of the Mars work presented in this thesis were to: 1) quantify the structural orientation of the Murray formation to refine its relationship with other sedimentary units in Gale crater; 2) assess textural evidence of drying in the Murray formation and interpret its significance for characterizing the depositional setting of the Murray formation.

In Chapter 4, we applied a PCA-based regression method to stereo Mastcam images to measure the structural orientation of Murray formation strata. Through these measurements and regional stratigraphic correlations, we constrained the dip of the Murray formation in the Blunts Point, Pettegrove Point, and Jura members to be within a few degrees of horizontal, consistent with approximately flat strata deposited on an equipotential surface. Results also indicate that at least the lowest part of the clay-bearing unit in the Glen Torridon region is stratigraphically equivalent to the Jura member of Vera Rubin ridge, raising questions about why VRR and lower Glen Torridon region are spectrally and topographically distinct. Finally, results show that the Murray formation did not contribute to the primary

formation of Aeolis Mons but predates the mound of sediment deposited around the central peak complex.

In chapter 5, we concluded that networks of reticulate ridges on the surface of several slabs in the Sutton Island member of the Murray formation are the remnants of desiccation cracks. The predominance of T-junctions on these slabs was interpreted to result from a single drying event rather that multiple cycles of wetting and drying. The identification of desiccation cracks is one of the few definitive textural markers of drying in the Murray formation and suggests a history of oscillating lake levels that led to intermittent exposure. The nature of the conditions that led to this drying are uncertain; the features are stratigraphically higher than the lacustrine strata identified in the Pahrump Hills member but significantly closer to the center of the Gale lake basin, suggesting that the desiccated lake facies are not basin margin facies and instead resulted from a lowstand. These results were subsequently corroborated by chemical evidence from Rapin et al. (2019) and Thomas et al. (2019).

7.2.1 Outstanding Questions and Potential Answers

What was the duration of the Gale crater lake(s)? Does the Murray formation record textural evidence of past climate variability? Does Gale crater record a definitive transition from a wet to dry climate?

Terrestrial analogs for sedimentation rates indicate that continuous lacustrine sedimentation could have occurred in the Murray formation for periods of at least 10^2 to 10^4 years (Grotzinger et al., 2015), and the total accumulation time required for Murray formation sediment, even if intermittent as indicated by textural evidence of drying (e.g. Fedo et al., 2018, Stein et al., 2018), could be $>10^7$ years (Grotzinger et al., 2015).

Most interpretations of Gale crater's lacustrine history (e.g. Grotzinger et al., 2015), estimates of lake lifetimes (Grotzinger et al., 2015), and even assessments of redox chemistry in Gale crater lakes (Hurowitz et al., 2017) depend on characterization of the pervasive, fine

lamination in the Murray fm. Despite this, little work has been done to quantify spatial variations in lamination thickness within the Murray formation to better constrain lake lifetimes and understand variability in sedimentation rates. In terrestrial settings, changes in the thickness of lacustrine deposits can be used as a paleoenvironmental indicator of interannual or longer-period climate variability due to temperature-driven sediment flux variations (e.g. Andrews and Trewin, 2010; Kemp, 1996; Pisarska-Jamrozy, 2013). Similarly, careful quantification of lamination thicknesses and their spatial variation in the Murray formation may act as a thus-far unseen lens into the climate conditions in the Gale crater region.

A quantitative survey of lamination thickness throughout the Murray formation could answer several outstanding questions, including: 1) is there any cyclic variability in lamination thickness or expression that can be correlated to interannual or longer-period climate variability?; 2) do lamination thickness variations correlate with compositional changes in support of redox-stratified conditions (e.g. Hurowitz et al., 2017); 3) do lateral variations in lamination expression coincide with textural evidence of drying and changes in sulfate and chloride in bedrock (e.g. Stein et al., 2019; Rapin et al., 2019; Thomas et al., 2019)?; 4) can estimates of lake lifetime be refined? Previous efforts to quantify lamination thickness variations in the Murray formation have been hampered by the difficulty of disentangling the orientation and viewing geometry of exposed rocks relative to the lamination, allowing characterization of only a sparse number of targets. The development of a PCA-based plane-fitting and error assessment algorithm (Quinn and Ehlmann, 2019) and its demonstrated effectiveness with stereo Mastcam images (Stein et al., 2020) indicate that it is feasible to robustly and systematically quantify lamination thickness throughout the Murray formation where the data exist. Consistent interannual variability could indicate differential sediment flux due to seasonal temperature variations (e.g. Huybers and Curry, 2006), whereas inferred decal-to-millennial variability could indicate the presence of large thermal buffers or even longer periodicity derived from orbital cycles (e.g. Hurowitz et al., 2017; Laskar et al., 2004; Lewis et al., 2008; Spalding et al., 2018).

Eventually, Curiosity will reach the sulfate-enriched unit, which signals a transition from the wetter environment recorded in the Bradbury group and much of the Murray formation to drier conditions. It remains to be seen what information about this transition is recorded in the sulfate unit strata. As in the Murray formation, the continued characterization of sedimentary textures and stratal relationships will be crucial in discerning the paleoenvironment and Gale crater's broader relevance to the history of the martian climate.

7.3 The Nature of Endogenic Geological Activity on Ceres

Dawn's observations at Ceres indicate that it once had a global ocean (Castillo-Rogez et al., 2020) and that brines may persist in the mantle (Fu et al., 2017). Moreover, the observation of multiple geologically-young surface features consistent with recent endogenic activity and possibly the presence of brines suggest Ceres is an active world. The source of the bright spots in Occator crater is understood to be, at least partially, brines that formed from impact heating and rose to the surface, precipitating bright Na-carbonate-rich salts (De Sanctis et al., 2016). The conundrum that remains regarding Occator crater is that the bright spots appear to post-date the crater by far longer than the expected lifetime of impact brines (<4 Ma, Bowling et al., 2018; Nathues et al., 2017; Neesemann et al., 2019). One possible explanation is that the Occator impact tapped into a deeper reservoir of extant brines (Hesse and Castillo-Rogez; 2018). The uncertainty surrounding the formation of the best-studied and most data-rich feature on Ceres highlights just how little is still understood about the dwarf planet. Indeed, the provenance of domes and other surface features indicative of recent activity is even less certain.

The major goals of the Ceres work presented in this thesis were thus to: 1) catalog and contextualize Na-carbonate deposits on Ceres; 2) constrain the timing of Na-carbonate deposits; and 3) identify and evaluate plausible sources for shallowly buried Na-carbonate and understand whether their formation required recent brines.

A key finding of Chapter 5 is that there are hundreds of Na-carbonate-bearing regions on Ceres. Some Na-carbonate deposits are in the floors of large craters and could have plausibly formed from the impact heating of endogenic material, but the great majority are on the rims and walls of craters. Many of these craters are too small for impact heating to have formed brines or too distant to have been transported from a central brine reservoir, indicating that the deposits already existed in the shallow crust before being exposed. Using a Monte Carlo impact model, we found that the bright spots must have been exposed within the last few hundred Ma before being buried due to impact-driven lateral mixing. Additionally, we found that the current number of crater rim Na-carbonate exposures is consistent with the expected number of previous large impactors that could have formed Occator-like deposits that were subsequently exhumed.

Chapter 6 addressed a problem that is immediately apparent at the end of Chapter 5: many large crater rim Na-carbonate exposures do not sit in any discernible impact basin that could have provided the heat to generate brines. Hence, Ceres' shallow subsurface has abundant material of aqueous origin but unknown provenance. We demonstrated that the excavated subsurface Na-carbonate deposits exposed on crater rims likely formed within the last ~1 Ga. Any material deposited earlier would have been disseminated by impacts. Additionally, we found that many of the large subsurface Na-carbonate deposits are anomalously close to domes, suggesting that they form by the same or related processes. Does this mean brines were recently widespread in Ceres' shallow subsurface? Our work demonstrates that mixtures of solid water ice and hydrated Na-carbonates can be transported from the lower crust to within a few km of the surface by diapirism, and differential loading from subsequent impacts could drive solid-state deformation that simultaneously generates domes and emplaces shallow Na-carbonate-bearing ices. This model does not definitively exclude brines but provides a plausible alternative mobilization mechanism. The degree to which brines vs. solid-state processes drive dome formation and the emplacement of shallow Na-carbonate remains an outstanding question.

7.3.1 Outstanding Questions and Potential Answers

What endogenic processes drive the formation of domes and emplacement of shallow Na-carbonate?

Chapter 6 establishes that large shallow Na-carbonate deposits, and plausibly domes, were mobilized to the shallow subsurface within the last ~1 Ga. More work is needed to discern whether the mobilization required brines, which is crucial to understanding the scope of recent aqueous activity on Ceres. There are two clear avenues for future progress in addressing this question with extant data: 1) refined geophysical modeling of loading-driven solid-state deformation and brine extrusion may refine the plausibility of either process simultaneously depositing domes and proximal shallow subsurface Na-carbonate; and 2) VIR data may be used to characterize the chemistry of bright spots outside of Occator crater and their variation in tandem with geologic context, providing additional insight into their formation.

What is Ceres' potential for past and present habitability?

It is believed that many of the solar system's large water-rich bodies once hosted or still host oceans. Oceans likely exist on several icy moons, including Europa (Carr et al., 1998), Ganymede (Kivelson et al., 2002), Enceladus (Roberts and Nimmo, 2008), and Titan (Iess et al., 2012). Several lines of evidence indicate that Ceres had an early global ocean (Castillo-Rogez et al., 2020), including (1) the crust structure and composition is consistent with outcomes of geochemical models of a freezing ocean (Castillo-Rogez et al., 2018); (2) Ceres accreted early and benefitted from enhanced ^{26}Al heating (Castillo-Rogez et al., 2010); (3) the hydrated and compositionally homogenous surface indicates pervasive global aqueous alteration (Ammannito et al., 2016). The ocean may have lasted for a few hundred million years or even still be present as a residual brine layer in the mantle or deep crust (Castillo-Rogez et al., 2020; Fu et al., 2017). Domes (Ruesch et al., 2016, 2019; Sori et al., 2017; 2018) and widespread shallow subsurface Na-carbonate deposits (this thesis) could

signal recent and ongoing mobilization of deep extant brines, but their provenance remains uncertain.

Additionally, some major elements essential for biology have been identified on Ceres' surface, including carbon in the form of carbonates and organic compounds (De Sanctis et al., 2017; Pieters et al., 2018) and nitrogen in ammonium (Ammannito et al., 2016; King et al., 1992). Other critical elements such as sulfur might be present but could not be identified with Dawn's instruments (Castillo-Rogez et al., 2020). Castillo-Rogez et al. (2020) identified several potential mechanisms to develop redox gradients in Ceres including serpentinization in impact melts, reactions between surface material and upwelling liquid, and endogenic radiolysis of water. If life did develop in Ceres, it would have faced an increasingly scarce energy supply, especially in colder near-surface environments. Despite this challenge, biosignatures such as lipid biomarkers could be transported to the surface. Regardless of how they were mobilized, the shallow Na-carbonate deposits offer a window into the chemistry of the deep interior from which they are sourced. The same might be true of Cerealia Facula and Vinalia Faculae if the Occator impact formed a connection to a deep brine source (Hesse and Castillo-Rogez, 2018).

Prudent goals for future exploration at Ceres include confirming the existence of liquid water (past or present) in Ceres, identifying the source of endogenic activity that forms domes and Na-carbonate deposits, identifying and quantifying the abundance of CHNOPS, determining the nature and origin of its organic compounds, and characterizing redox conditions at the surface. If an energy-starved body like Ceres does retain liquid and conditions favorable for life, it would certainly be a positive sign for the prospects of habitability elsewhere in our solar system. For now, Ceres remains a tantalizing object that will continue to shape our view of ocean worlds.

References

Ammannito, E., DeSanctis, M.C., Ciarniello, M., Frigeri, A., Carrozzo, F.G., Combe, J.-P., et al. (2016). Distribution of phyllosilicates on the surface of Ceres. Science. 353, 1006. https://doi.org/10.1126/science.aaf4279.

Andrews, S.D. & Trewin, N.H. (2010). Periodicity determination of lacustrine cycles from the Devonian of Northern Scotland. *Scottish J. Geo*, 46(2). https://doi.org/10.1144/0036-9276/01-395.

Bowling, T., Ciesla, F., Davidson, T., Scully, J., Castillo-Rogez, J., & Marchi, S. (2018). Post-impact thermal structure and cooling timescales of Occator crater on Asteroid 1 Ceres. *Icarus*, 320, 110-118. https://doi.org/10.1016/j.icarus.2018.08.028.

Carr, M.H., Belton, M.J.S., Chapman, C.R., Davies, M.R., Geissler, P., Greenberg, R., McEwen, A.S. et al. (1998). Evidence for a subsurface ocean on Europa. *Nature*, 391, 363-365. https://doi.org/10.1038/34857.

Castillo-Rogez, J.C., Neveu, M., McSween, H.Y., Fu, R.R., Toplis, M.J., & Prettyman, T. (2018). Insights into Ceres's evolution from surface composition. *Meteorics and Planetary Science*, 1-24. https://doi.org/10.111/maps.13181.

Castillo-Rogez, J.C., Neveu, M., Scully, J.E.C., House, C.H., Quick, L.C. Bouquet, A. et al. (2020). Ceres: Astrobiological target and possible ocean world. *Astrobiology*. 20. https://doi/org/10.1089/ast.2018.1999.

De Sanctis, M.C., Raponi, A., Ammannito, E., Ciarniello, M., Toplis, M.J., McSween, H.Y., et al. (2016). Bright carbonate deposits as evidence of aqueous alteration on (1) Ceres. *Nature*, 536, 1–4. https://doi.org/10.1038/nature18290.

De Sanctis, M.C., Ammannito, E., McSween, H.Y., Raponi, A., Marchi, S., Capaccioni, F. et al. (2017). Localized aliphatic organic material on the surface of Ceres. *Science*. 355, 719-722. https://doi.org/10.1126/science.aaj2305.

Edgar, L. A., Gupta, S., Rubin, D. M., Lewis, K. W., Kocurek, G. A., Anderson, R. B., et al. (2017). Shaler: A fluvial sedimentary deposit on Mars. *Sedimentology*, 65(1), 96–122. https://doi.org/10.1111/sed.12370.

Fedo, C., Grotzinger, J. P., Gupta, S., Fraeman, A., Edgar, L., Edgett, K., et al. (2018). Sedimentology and stratigraphy of the Murray formation, Gale Crater, Mars. *LPSC 49*. Abstract 2078.

Grotzinger, J.P., Crisp, J., Vasavada, A.R., Anderson, R.C., Baker, C.J., Barry, R., et al. (2012). *Space Sci. Rev.* 170(1-4). 5-56. https://doi.org/10.1007/s11214-012-9892-2.

Grotzinger, J. P., Sumner, D. Y., Kah, L. C., Stack, K., Gupta, S., Edgar, L., et al., & MSL Science Team (2014). A habitable fluvio-lacustrine environment at Yellowknife Bay, Gale Crater, Mars. *Science*, 343(6169), 1242777. https://doi.org/10.1126/science.1242777.

Hesse, M.A. & Castillo-Rogez, J.C. (2018). Thermal evolution of the impact-induced cryomagma chamber beneath Occator crater on Ceres. *Geophysical Research Letters*. 46. https://doi.org/10.1029/2018GL080327.

Hurowitz, J. A., Grotzinger, J. P., Fischer, W. W., McLennan, S., Milliken, R. E., Stein, N., et al. (2017). Redox stratification of an ancient lake in Gale crater, Mars. *Science*, 356(6341). https://doi.org/10.1126/science.aah6849.

Huybers, J. & Curry, W. (2006). Links between annual, Milankovitch and continuum temperature variability. *Nature*, 441, 329-332. https://doi.org/10.1038/nature04745..

Iess, L., Jacobson, R.A., DUcci, M., Stevenson, D.J., Lunine, J.I., Armstrong, J.W. et al. (2012). The tides of Titan. *Science*. 337, 457-459. https://doi.org/10.1126/science.1219631.

Kemp, A.E.S. (1996). Palaeoclimatology and plaeoceanoraphy from laminated sediments. *Geo. Soc. Special Pub.*, 116. https://doi.org/10.1144/GSL.SP.1996.116.01.20.

Kivelson, M.G., Khurana, K.K., & Volwerk, M. (2002). The permanent and inductive magnetic moments of Ganymede. *Icarus*, 157, 507-522. https://doi.org/10.1006/icar.2002.6834.

Knoll, A.H. (2015). Paleobiological perspectives on early microbial evolution. *Cold Spring Harb. Perspect. Biol.*, 7. https://10.1101/cshperspect.a018093.

Laskar, J., Correia, A.C.M., Gastineau, M., Joutel, F., Levrard, B., & Robutel, P. (2004). Long term evolution and chaeotic diffusion of the insolation quantities of Mars. *Icarus*. 170, 343-364. https://doi.org/10.1016/j.icarus.2004.04.005.

Lewis, K. W., Aharonson, O., Grotzinger, J. P., Kirk, R. L., McEwen, A. S., & Suer, T. A. (2008). Quasi-periodic bedding in the sedimentary rock record of Mars. *Science*, 322(1532). https://doi.org/10.1126/science.1161870.

Milliken, R. E., Grotzinger, J. P., & Thomson, B. J. (2010). Paleoclimate of Mars as captured by the stratigraphic record in Gale Crater. *Geophysical Research Letters*, 37, L04201. https://doi.org/10.1029/2009GL041870.

Nathues, A., Platz, T., Thangjam, G., Hoffmann, M., Mengel, K., Cloutis, E.A., et al. (2017). Evolution of Occator Crater on (1) Ceres. *Astron. J.*, 153, 112. https://doi.org/10.3847/1538-3881/153/3/112.

Neesemann, A., van Gasselt, S., Schmedemann, N., Marchi, S., Walter, S.H.G., Preusker, F., et al. (2019). The various ages of Occator crater, Ceres: Results of a comprehensive synthesis approach. *Icarus*, 320, 60-82. https://doi.org/10.1016/j.icarus.2018.09.006.

Pieters, C.M., Nathues, A., Thangjam, G., Hoffmann, M., Platz, T., De Sanctis, M.C. et al. (2017). Geologic constraints on the origin of red organic-rich material on Ceres. *MAPS*, 53. https://doi.org/10.1111/maps.13008.

Pisarska-Jamrozy, M. (2013). Varves and megavarves in the Eberswalde valley (NE Germany) – A key for the interpretation of glaciolimnic process. *Sedimentary Geology*, 291, 84-96. https://doi.org/10.1016/j.sedgeo.2013.03.018.

Present, T.M., Grotzinger, J.P., Gomes, M.L., Trower, E.J., Stein, N.T., Lingappa, U.F. et al. (2020). Non-lithifying microbial ecosystem, Little Ambergris Cay, Turks and Caicos Islands. In prep.

Quinn, D. P., and Ehlmann, B. L. (2019b). A PCA-based framework for determining remotely sensed geological surface orientations and their statistical quality. Earth and Space Science, 6, 1378–1408. https://doi.org/10.1029/2018EA000416

Rapin, W., Ehlmann, B. L., Dromart, G., Schieber, J., Thomas, N. H., Fischer, W. W., et al. (2019). An interval of high salinity in ancient Gale crater lake on Mars. *Nature Geoscience*, 12(11), 889–895. https://doi.org/10.1038/s41561-019-0458-8.

Roberts, J.H. & Nimmo, F. (2008). Tidal heating and the long-term stability of a subsurfaces ocean on Enceladus. *Icarus*, 194, 675-689. https://doi.org/10.1016/j.icarus.2007.11.010.

Ruesch, O., Platz, T., Schenk, P., McFadden, L.A., Castillo-Rogez, J.C., Quick, L.C., et al. (2016). Cryovolcanism on Ceres. *Science*, 353, aaf4286-aaf4286. https://doi.org/10.1126/science.aaf4286.

Ruesch, O., Quick, L.C., Landis, M.E., Sori, M.M., Cadek, O., Broz, P., et al. (2019). Bright carbonate surfaces on Ceres as remnants of salt-rich water fountains. *Icarus,* 320, 39-48. https://doi.org/10.1016/j.icarus.2018.01.022.

Schopf, J.W. (2006). Fossil evidence of Archaean life. *Phil. Trans. of the Royal Society*, 361, 869-885. https://doi.org/10.1098/rstb.2006.1834.

Schieber, J., Bose, P.K., Eriksson, P.G., Banerjee, S., Sarkar, S., Altermann, W., et al. (2007). Atlases in Geoscience. Elsevier. 307p.

Sori, M.M., Bryne, S., Bland, M.T., Bramson, A.M., Ermakov, A.I., Hamilton, C.W., Otto, K.A., et al. (2017). The vanishing cryovolcanoes of Ceres. *Geophysical Research Letters*. 44. https://doi.org/10.1002/2016GL072319.

Sori, M.M., Sizemore, H.G., Byrne, S., Bramson, A.M., Bland, M.T., Stein, N.T., et al. (2018). Cryovolcanic rates on Ceres revealed by topography. *Nature Astronomy*. 2, 946-950. https://doi.org/10.1038/s41550-018-0574-1.

Spalding, C., Fischer, W.W., & Laughlin, G. (2018). An orbital window into the ancient sun's mass. *ApJ*., 869. https://doi.org/10.3847/2041-8213/aaf219.

Stein, N.T. et al. (2018). Desiccation cracks provide evidence of lake drying on Mars, Sutton Island member, Murray formation, Gale crater. *JGR: Planets*, 46, 515-518. https://doi.org/10.1130/G40005.1.

Stein, N.T. et al. (2020). Regional structural orientation of the Mount Sharp group revealed by in situ dip measurements and stratigraphic correlations on the Vera Rubin Ridge. *JGR: Planets*, 123. https://doi.org/10.1029/2019/JE006298.

Thomas, N.H., Ehlmann, B.L., Meslin, P.-Y., Rapin, W., Anderson, D.E., Rivera-Hernandez, F. et al. (2019). Mars Science Laboratory observations of chloride salts in Gale crater, Mars. *Geophysical Research Letters.*, 46. https://doi.org/10.1029/2019GL082764.